Realizing the Energy Transition with Distributed Photovoltaics: A Study of High PV Penetration Grid-Edge Network Dynamics.

Robert Pollak

Thesis submitted to the University of Ottawa
in partial Fulfillment of the requirements for the
MAS.c degree in Electrical & Computer Engineering

Faculty of Engineering
University of Ottawa

Abstract

This paper investigates the voltage and phase dynamics of a low inertia inverter based Microgrid in islanded operation. In such case, the network is less robust to disturbances due to the lack of associated inertia within an inverter. In islanded operation, the assumption of a stiff grid is no longer valid due to the voltage and phase adjustment based on conventional droop control have a resulting effect on the power flows throughout the network where voltage and frequency stability of the network may be compromised. Other approaches neglect the network dynamics when there are power imbalances in the system and how each node is affected and if the resulting increase in demand can be met with the available power generation. This paper uses the fact that the phase dynamics of coupled inverters that employ droop control closely resemble the phase dynamics proposed by the Kuramoto model. Using this model allows the network stability to be analyzed under the true nonlinear operation. It Is observed through the strong coupling impedance of the secondary distribution transmission lines and the implementation of proportional droop control will provide an appropriate means for rural and suburban neighborhoods to operate independently, given the proportional droop gain is tuned appropriately.

Table of Contents

List of Figures

Chapter 4: Low-Voltage Network Dynamic Performance

List of Tables

CHAPTER 1: Introduction

1.1. The Distribution Level High Penetration Problem

The electric power system (EPS) was originally designed in consideration of centralized generation with one-way power flows. Renewable energy has become essential to meet increasing energy demands in a clean and sustainable fashion, leading to a high penetration of distributed energy resources (DER) such as photovoltaic (PV) and wind power systems which are interfaced to the grid through inverters. When using DER, penetration is typically done at the distribution level and therefore introduces two-way power flow into the utility grid.

When distributed energy resources were first introduced into the distribution grid, it was not anticipated that DER would have significant impact on local EPS. Therefore, the assumption was that the frequency and voltage at the substation between the distribution and transmission grid would remain close to nominal no matter how these DER would contribute. Early standards for inverter technology were based on the "do no harm" principle where the DER should not actively regulate frequency or voltage at the point of common coupling (PCC) and thus would cease to energize the area EPS when voltage and frequency fell out of defined limits. With rapidly increasing amounts of DER in the utility grid, these strict operating requirements are eliminating the added benefits of increased DER penetration and may present negative effects on the bulk power system (BPS). Where BPS concerns are frequency regulation, utility/local level concerns are voltage regulation. The latest revision of interconnection standards, such as [1], now mandate DER flexibility in which these systems must meet certain voltage and frequency ride through requirements. The newest revision also mandates reactive power injection capability allowing DERs to regulate voltage at the PCC.

In islanded operation when a Microgrid is formed, frequency regulation becomes an added concern for the local utility/distributed resources. Due to the non-inertial based generation sources, the microgrid becomes very sensitive to load/generation changes and abnormal events, creating serious reliability issues within the EPS. System frequency is similar across the entire interconnection and is established by the balance between load and generation. So, any significant loss in DER will have an impact on the system frequency, requiring other resources to address the deviation. Furthermore, these events may cause voltage reduction on buses and challenge the capability of each DER unit to meet the demands at the PCC.

In order to handle such events, inverter interfaced DER typically employs a three-layer hierarchal control strategy. These layers are commonly referred to as primary, secondary and tertiary control. The separation of the layers is determined by the time-scale in which the control systems layer acts upon. The lowest layer, the primary control layer, operates on the time scale of milliseconds to seconds. The primary layer is responsible for ensuring voltage, frequency and angle stability during operation in either microgrid or grid tied mode. The secondary control layer addresses the voltage and frequency deviation caused by the short-term supply-demand imbalance on the network as a result of the action taken on the primary control layer. This secondary layer acts on the order of minutes to hours. Lastly, the tertiary control layer is an optimization and network power flow control layer that is responsible for ensuring optimal network operation and power flow requirements are met. This layer, the furthest layer away from the short-term network stability, operates on the scale of hours to even days.

Depending on whether the inverter is acting within a grid-tied or microgrid/nano-grid system, the level of concern of each layer varies significantly. Although a major emphasis is typically on the primary control layer of the inverter. This emphasis is re-enforced in the micro/nano-grid operational mode due to the sensitivity of the non-inertial based generation and the voltage and frequency ride-through time scales set out in the latest interconnection standard [1]. Thus, leaving very little opportunity for demand response actions to occur. This concern will be the main topic of discussion and will be expanded in great detail throughout the remainder of the thesis.

1.2. Structure of the Electrical Power System (EPS)

Moving from traditional coal/gas/oil-based generation to renewable generation requires a massive shift in grid technologies at each level within the EPS [2]. As the environment becomes a more important and dominant role on today's political agenda, and the decreasing cost of PV and battery storage, it is likely that the majority share of the energy market will shift to renewable based sources. In recent light of the COVID-19 pandemic kickstarting the digital shift in society; the role of the EPS is now more important than ever. The mass adoption of electric vehicles will further increase the importance of the EPS as the demand is expected to double by 2030. This majority shift places new challenges on BPS and local/utility power system operators that requires significant advances in many different aspects of the grid.

Renewable sources of generation such as solar and wind are volatile stochastic generation sources with significant variation across multiple time scales. For example, significant shading from cloud coverage can drop the power output of PV generation up to 75% instantaneously. Depending on how wide spread the cloud coverage is and the wind speed, the impact on a micro/nano-grid can compromise the stability of the network and lead to a tightening of operational capabilities. The responsibility to handle such event would be the concern of the primary control system. In a grid connected cloud coverage scenario, the network is less vulnerable to such event due to the support from other generation sources on the system. At the local utility level, the impact of such event would be compensated by the secondary and tertiary control system of nearby DER clusters, if capable. Any frequency or voltage deviation would be addressed by the secondary control layer and a prolonged coverage event would have the local utility push optimal control strategies within the tertiary layer to manage the power flow throughout the local network to compensate. Furthermore, during a sunrise or sunset scenario, PV based generation would experience a prolonged ramping effect. This effect would be controlled and compensated by the secondary and tertiary control layers. During hot summer days, demand from induction motor-based air conditioners is significant and typically lead to voltage instability at the local level. With the newly mandated injection capabilities of [1], the hosting capacity of the feeder can be increased dramatically. If enough DER is carried on the feeder, any instantaneous high current draw from the starting of an air conditioning motor can be absorbed by the local DER and voltage stability can be maintained and deviation compensated for. An important role of the primary and secondary control layers.

These generation sources and disturbances operate in a probabilistic manor and require a significant shift in generation and demand prediction technologies. Information must be conveyed back to the local utility operator and BPS operator with a high degree of accuracy in order for proper generation management to be performed. In order to achieve high-accuracy demand prediction; prediction must be done at the grid-edge. Optimal scale battery storage systems are fundamental in the transition to a renewable based generation majority and serve as the intermediary resource in short-time scale supply demand imbalances. This is especially important in micro/nano grid interconnections when aforementioned disturbance events take place and it is required for an intermediary resource to compensate until the disturbance is cleared.

Distributed renewable energy generation typically has a low energy density in which multiple generation sources are aggregated at a small interconnection ~~power station~~ or point of connection. Cost is a major challenge when it comes to mass renewable generation adoption. In order to reduce the cost of these generation sources, renewable generation stations are commonly connected at the distribution level due to their inherent low energy density. This along with the increasing penetration of consumer rooftop solar, also known as prosumers, are creating a paradigm shift in the conventional structure of the electrical power system.

Figure 1.1 demonstrates a typical EPS structure, which is divided into three parts: generation, transmission and distribution. Typically, the generation sector is divided into a number of private companies which is regulated by the industry regulator. The BPS operator (Independent System Operation, ISO) is independent of the generation sources and tends to be one monopoly company, which manages the transmission system and is regulated by an industry regulator. The BPS operator is a monopoly due to the importance that the transmission system plays within overall power system integrity as it is a highly interacting and complicated mechanism. Any action within the demand and supply within the power system influences all the components within the transmission system [2]. As the DER penetration continues to climb, distribution networks can become net exporters of power therefore increasing the BPS complexity as power flows between large distribution networks. This places further emphasize on the communication between local utility operators and the bulk power system operators.

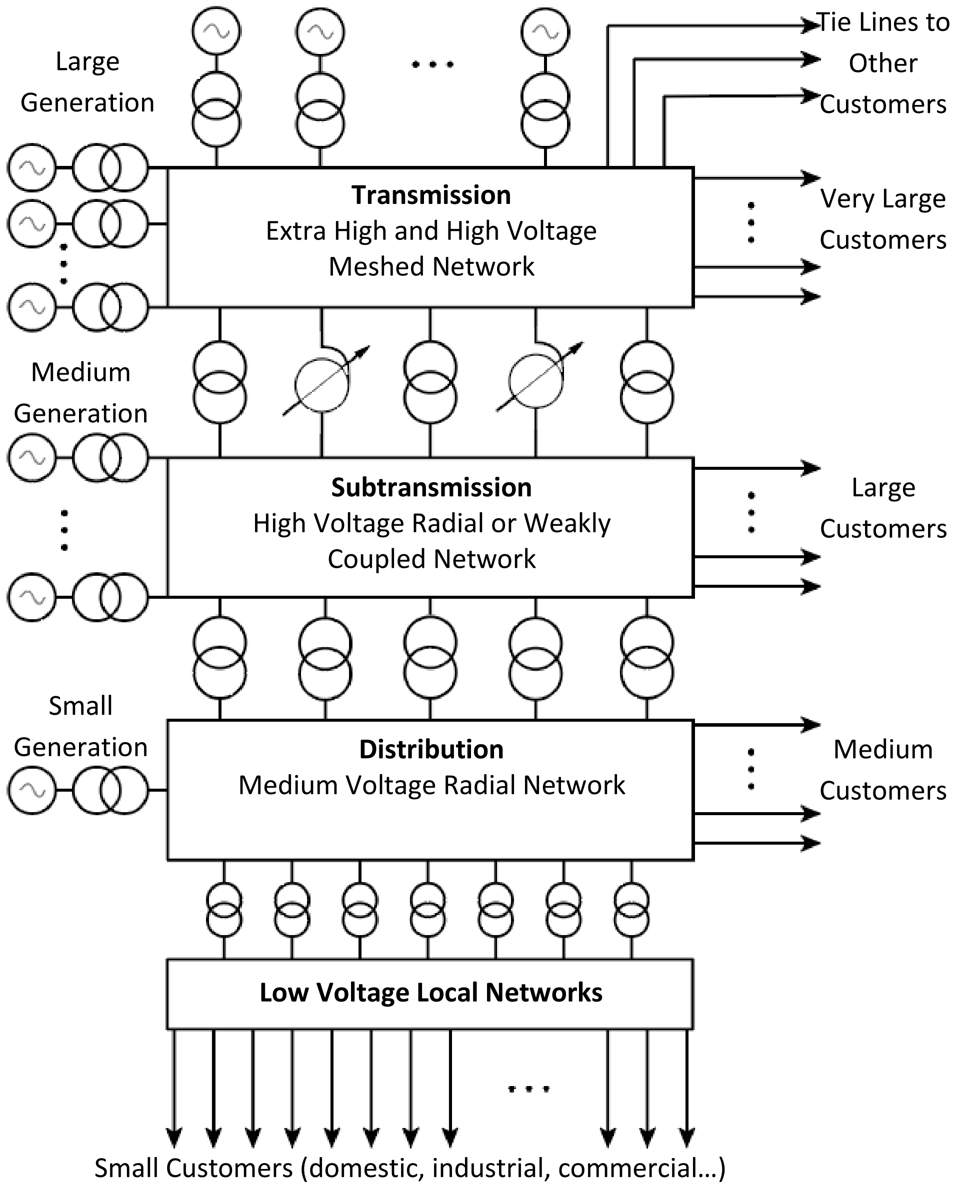

Figure 1.1: Conventional Structure of an Electrical Power System (EPS) [2]

The distribution is split into separate distribution companies which own and manage the distribution networks in given areas. These companies are known as wire businesses [2]. Retail energy is handled by competing supply companies but in some cases is solely owned and managed by the distribution company. With the increase in the amount of DER penetration at the grid edge, the local utility/ distribution company now carries much more concern when it comes to managing the local EPS.

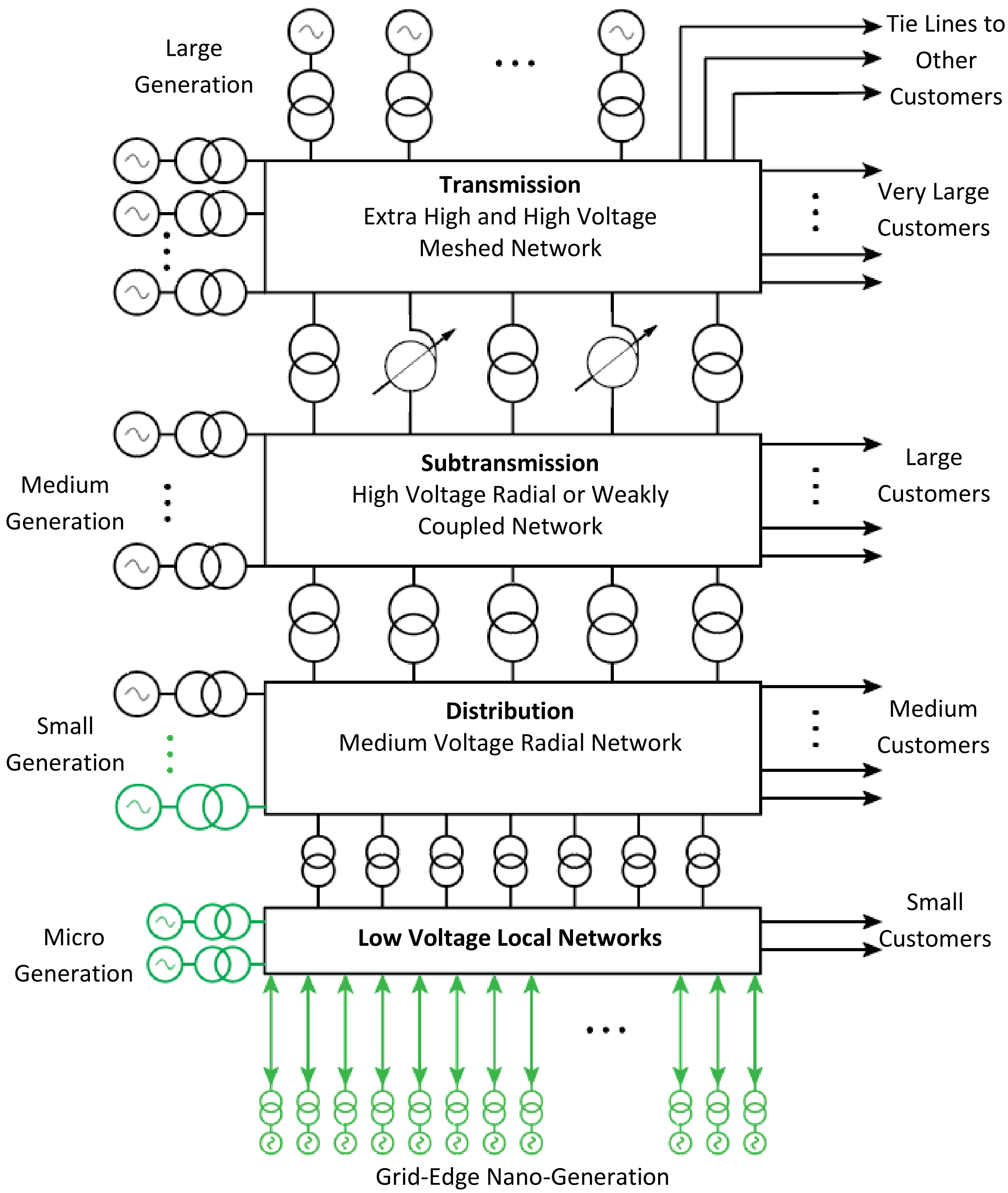

Figure 1.2: Modern Structure of an Electrical Power System (EPS)

Figure 1.2 highlights the adjustment in the structure of the conventional EPS that accounts for the increase in generation within the local EPS. Micro generation sources consist of medium-large scale PV power plants, battery storage systems and wind power plants connected to the distribution stations.

Nano-generation sources capture the prosumers located at the grid-edge. These prosumers can be visualized as neighborhoods of interconnected homes which have rooftop PV and small-scale wind generation located on their properties, behind their PCC. Neighborhoods of interconnected homes now become highly interacting small-scale power networks which are heavily influenced by the behaviors of the consumers and prosumers within their networks. Subject to the behavior of the individuals, the small-scale networks can become net exporters of power in which dynamic power flows between adjacent networks of interconnected homes vary in time. This rapid growth in DER has changed the operational picture for Local EPS's utilities. As the distribution networks begin to become net exporters of power and the power flow reversing direction, many technical challenges have been created. This has led to major short-term technical problems within the local EPS which consists of: protection system settings, voltage drops, congestion management and etc… [2].

This large-scale adoption of distributed energy resources and the now realized impact of DER on frequency stability, has transformed the local utilities role into one similar to that of the of a BPS operator. However, while similar, it is important to note the inherent differences between DER and EPS is the number and level of interactions between generation sources. Meaning, from a traditional standpoint, the local EPS operator was concerned with the maintenance and planning of the local EPS, due to the passive network. This added role of BPS operator mentality has created a high level of management complexity that is associated with the sheer scale of interconnects and generation sources at the grid-edge in comparison to that of a BPS operator. This has led to a drastic change in the mentality of the local EPS operators in which their concerns have shifted from only planning and maintenance (reactive operations) to include local power system and power flow management, stability and security (proactive operations).

The proactive operations of the local utility differ from that of what a BPS operator examines. This is due to the inherent differences in dynamics between the transmission network and the low voltage network. At the BPS level, the generation sources consist of deterministic, slow acting, large inertia rotating machinery which are resilient to small changes in demand. The interconnection between large generation sources is through high-voltage transmission lines which are dominated by the inductive impedance of the line. At the local level, we have stochastic, fast acting low inertia generation systems which are interconnected through transmission lines that are generally dominated by the resistive component of the line at the gride-edge (nano-generation) and inductive component at the direct distribution connection station (micro-generation). Therefore, the classical power system dynamics that are applied at the BPS level are not directly applicable within the low voltage electrical networks. As DER penetration grows at the grid-edge, these differences are becoming increasingly more significant in the overall EPS stability. The primary focus of this thesis is on the low-voltage network dynamics and will be expanded on in great detail throughout the remainder of this thesis.

1.2. Power System Stability

It is important to define power system stability and the relation with power system security as it is the main topic of discussion within this thesis. As the power system is a highly interacting complicated mechanism in which an action of any individual component (a power plant or a load) influences all the other components in the system. The definition of stability must be precisely defined and consistent across every aspect of the power system. This has been widely recognized and addressed by the IEEE/CIGRE Joint task force on stability terms and definitions. This joint task force defined power system stability as:

"Power system stability is the ability of an electric power system, for a given initial operating condition, to regain a state of operating equilibrium after being subjected to a physical disturbance, with most system variables bounded so that practically the entire system remains intact". – [3]

Power systems are nonlinear, their stability depends on both the initial conditions and the size of the disturbance. Their stability is classically connected with electromechanical phenomena and governed largely by this phenomenon. As DER penetration grows, the effects of the DER and their associated dynamics are changing the electromechanical governance. As aforementioned, distributed energy resources are primarily integrated within the distribution level of the EPS and are interfaced via inverters, which are non-inertial based generation sources. Due to the fast-acting control systems that govern the operation of the inverter, these DER have more impact on a smaller time scale compared to the electromechanical dynamics of rotating machinery. This discussion will be expanded in the latter parts of this paper.

Regardless of the dynamics associated with their respective types of generation, the stability of the power system relies only on three fundamental components: (1) Nodal voltage angles, δ; (2) Frequency, f; (3) Nodal voltage magnitudes, V. Due to the fundamental importance of these components, power system stability is defined by and classified as follows: (i) Power angle stability; (ii) Frequency stability; and (iii) Voltage stability; demonstrated in figure 1.3. Voltage and frequency stability are separated into *short-term* and *long-term stability* whereas rotor angle or angle stability is purely a short-term phenomenon. This is due to the angle-frequency relationship within generators. The primary concern of EPS stability boils down to two major interactions: how will the EPS respond to a change in demand/generation, and how will it respond to various types of external disturbance phenomena. Each of these phenomena introduce a wide spectrum of dynamics within the EPS, each of which occurs on different time scales. Similarly, the way the EPS responds to these disturbances also covers a wide spectrum of dynamics and their associated time frames based on the interacting mechanism [2].

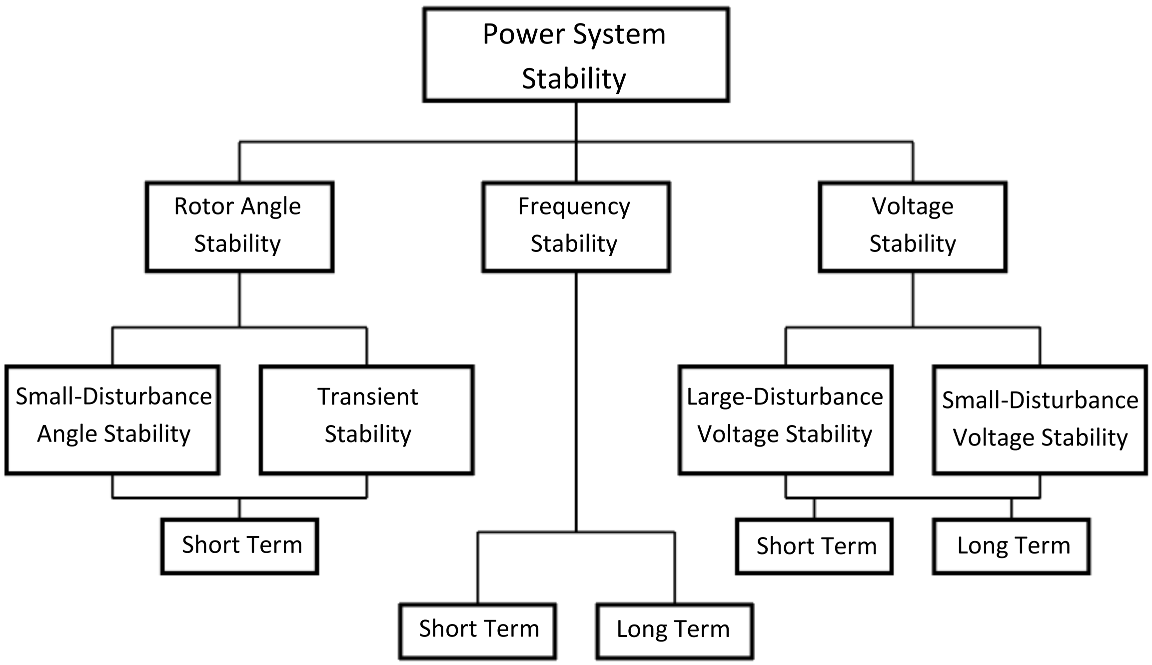

Figure 1.3: Classification of Power System Stability [4]

Classically, a change in sudden demand introduces fast dynamics into the system where conventionally there will be an imbalance in energy which results in a transient energy transfer between the rotating masses within the generators and the loads. Conventionally speaking, due to the large inertia, it would require a significant change in demand and/or generation in order for these fast dynamics to occur. Depending on the size and timescale of the disturbance, the slower acting electromechanical voltage and frequency control actions are needed to maintain system operations. The slowest of the imbalance disturbance response are the generation adjustments that are needed to address the slower aggregate daily demand variations. If BPS base load & intermediate connected [EMUO Terminology] generation plants cannot scale to meet these demand imbalances, they are then met with spinning reserves, non-spinning reserves (load-following), contingency reserves and peaker plants.

As society progresses to a more sustainable and renewable energy-based system, it is important to define attainable goals, which will accelerate this vision through current technology methods. The short-term goal would be to replace these spinning reserves and peakers (NGCC and IGCC plants) with renewable based generation sources. Currently, this is the role of modern connected PV and wind generation facilities. Unfortunately, due to the high variability, renewable plants still require assistance by spinning and non-spinning reserves, as they do not have the inherent ramping capability. This is why integration of large-scale battery storage systems are crucial within distribution system to eliminate the need of the non-renewable based sources.

How the system responds to the disturbances also introduces another spectrum of dynamics with their associated time frames. The fastest types of dynamics are the fast wave phenomena (wave effects, surges corresponding to the propagation of electromagnetic waves caused by lightning or switching operations) that occur within the high-voltage transmission lines. These are then followed by the electromagnetic changes within the electrical machines due to load imbalances, faults and etc.…. The electromagnetic dynamics translate into active power (rotor angle) oscillations amongst the interconnected electrical machines, these are relatively slow in comparison to the aforementioned fast-wave and electromagnetic dynamics. Finally, the slow prime mover and automatic generation controls will take effect to stabilize the power imbalance as well as the prime mover oscillations as the prime mover tries to achieve a steady state. These interactions of the machine windings as well as the protection systems take place in the orders of a millisecond to a second to stabilize. The slowest dynamics are the thermodynamic changes that result from steam-based power plants that are used to ramp up generation

The different phenomena play different roles in terms of the level of interaction within the network. The fast wave phenomena, due to lightning and switching overvoltages, occur almost exclusively in the network and basically do not propagate beyond the transformer windings due to their inherent de-coupling and voltage regulation capabilities. The electromagnetic phenomena mainly involve the generator armature and damper windings and partly the network. These electromechanical phenomena, namely the rotor oscillations and accompanying network power swings, mainly involve the rotor field, damper windings and the rotor inertia. As the power system network connects the generators together, this enables interactions between swinging generator rotors to take place. An important role is played here by the automatic voltage control and the prime mover control. Slightly slower than the electromechanics phenomena are the frequency oscillations, in which the rotor dynamics still play an important part, but are influenced to a much greater extent by the action of the turbine governing systems and the automatic generation control. Automatic generation control also influences the thermodynamic changes due to boiler control action in steam power plants [2].

With the shift in technologies and the growth of prosumers, there are many issues which need to be solved. As the distribution networks become increasingly more complicated, the BPS operators need to re-think BPS operation. Levels of abstraction are needed at the distribution level as they have now become highly interacting and too difficult for one to operate and manage independently. How can we model and analyze the aforementioned dynamics in the context of low-voltage networks with interconnected non-inertial based generation sources, where oscillator rotor swings do not exist? How does this play a role in local EPS stability? How does this play a role in local power quality? How does this contribute to overall BPS stability? These are the questions that will be further investigated throughout this study.

1.3. Power System Security

The proper understanding of the fundamental concepts in power system security is required to adequately assess the questions outlined for the purposes of this study. The following definitions will assist within the dynamic stability analysis of the resulting state after a disturbance and/or contingency within the network. The following is the definition of power system security which further outlines the differences between stability and security:

"Power system security is understood as the ability of the power system to survive plausible contingencies without interruption to customer service. Power system security and power system stability are related terms. Stability is an important factor of power system security, but security is a wider term than stability. Security not only includes stability, but also encompasses the integrity of a power system and assessment of the equilibrium state from the point of view of overloads, under- or overvoltage's and underfrequency." – [2]

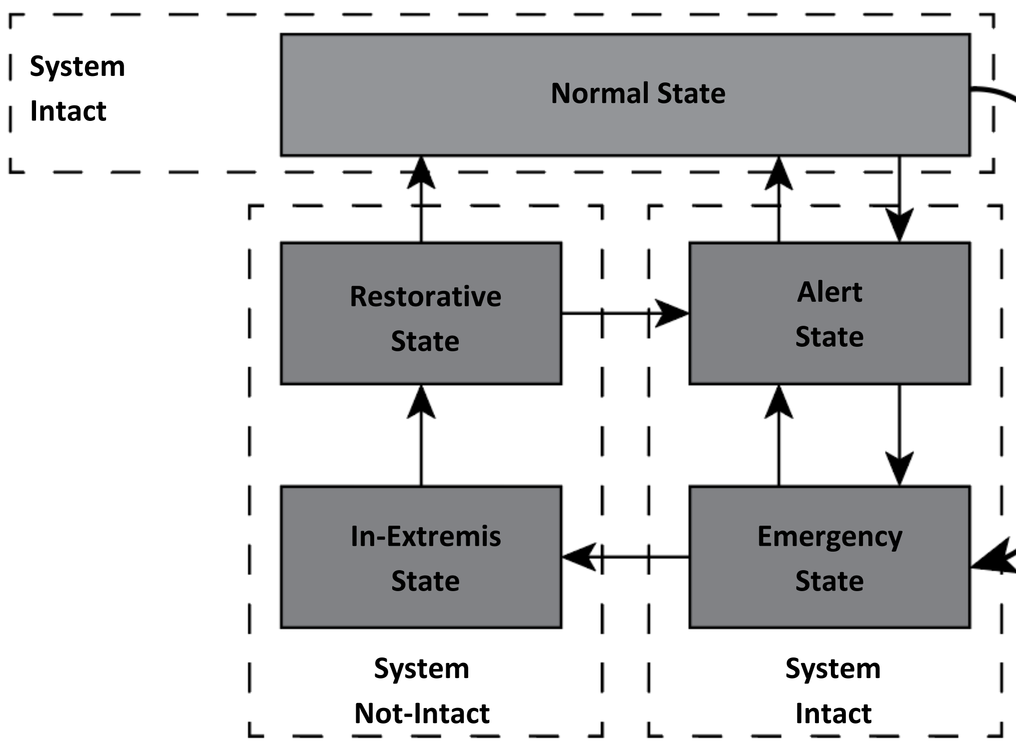

Figure 1.4: Power System Operating State Transition Map [4]

As referenced in figure 1.4, the five states are described as follows:

1) The *Normal State* – consists of when supply meets demand for all customers on the network. The power system is stable and can withstand conceivable contingencies as the three fundamental components (power angle, frequency and voltage magnitudes) for stability lie within their nominal operational boundaries.
2) The *Alert State* – arises when one or more of the fundamental components for power system operation exceed their nominal boundaries due to either a demand imbalance or a severe network contingency. The power system is still able to maintain operation without the failure of delivering energy to the customers. Preventative actions must be undertaken to restore the system to the normal state before another contingency may threaten power system stability further.
3) The *Emergency State* – The violation of the aforementioned boundaries are more severe and corrective actions MUST be taken in order to return to *alert state* then *normal state*. In this state, the power system is still intact and supplying customers but further contingencies severely threaten power system operation and customer service.
4) The *In-Extremis State* – The power system has undergone an extremis state after not enough corrective actions were undertaken to restore fundamental components to their nominal boundaries. This state requires severe corrective actions such as load shedding to prevent the system for undergoing fatal damage. An *in-extremis* state may be caused by a lack of synchronism, loss of generation, several faults and etc… Failure to take sufficient corrective action will result in a *blackout*.
5) The *Restorative State* – Is the intermediary remedy in returning the power system to the *normal state.* In this state, power system operators perform control actions to restore faults, system loads and reconnection of generation.

Analyzing and assessing power system security is divided into *static* and *dynamic* security. Dispatching centres are mainly concerned with *static* security analysis. This analysis is concerned with the power network pre-contingency states which are pre- and post-contingency analysis. Pre-contingency analysis consists of analyzing pre-contingency states such as available transfer capacity of the transmission network as well as network congestion identification. Post-contingency states are concerned with the verification of bus voltages and line power flow limits.

Dynamic security analysis is concerned with network operation in between these states. This analysis consists of our aforementioned fundamental components as well as the excursion of such components beyond their nominal operational boundaries during the transient periods. The follow are the typical criteria for dynamic security assessment:

1) Rotor (power) angle, voltage and frequency stability.
2) Voltage and frequency excursion during the transient state beyond nominal operational boundaries.
3) Power swing damping inside subsystems and between subsystem of interconnected networks.

Both *static* and *dynamic* security assessment strategies will be used in this thesis to assess the viability of low-voltage networks with high prosumer penetration. Although this thesis focuses and will emphasize *dynamic* security in greater detail using the aforementioned criteria.

1.4. Thesis Objective

This thesis takes a bottom-up approach in creating a secure electric power system that will facilitate the adoption and growth of mass renewable and sustainable energy generation penetration. A bottom-up approach is looking at each low-voltage network as a single interoperable node within the overall power system network. The more independent, robust and resilient each node is, the more robust and resilient the bulk power system becomes.

The objective of this thesis is to provide an in-depth security assessment of interconnected network of prosumers interacting within a low-voltage network neighborhood. All prosumers are interfaced through the grid through single-phase inverters that adhere to IEEE 1547-2018 interconnection standards. The security assessment will deliver static and dynamic analysis of the networks using IEEE 1547 interconnection requirements for the basis of stability evaluation. It will then be shown that a network of interconnected droop-controlled inverters closely resembles the Kuramoto model and the angle stability of the low-voltage network is strongly governed by the coupling impedance of the network. Based on this inherent relation, the coupling of the network will be extensively investigated within this thesis and the role of the coupling mechanism's effect on network stability.

1.5. Thesis Overview

Chapter 2 reviews the principal operation of inverters and will provide an in-depth review on: Inverter dynamics and modelling; Primary control system schema; Inverter to network synchronization mechanisms; and the IEEE 1547 interconnection and interoperability standards for inverters. This chapter will particularly focus on single-phase inverter operation as single-phase systems are most common in low voltage networks of interconnected homes. Discussions within this chapter can be carried over and modeled similarly in three-phase inverters through the use of DQ rotating reference frames. This concept will be briefly highlighted within this chapter.

Chapter 3 discusses the dynamics and modelling of components within low-voltage networks. The goal is to accurately describe the low-voltage network dynamics of an interconnected neighbourhood of prosumers. This consists of static and dynamic consumer load models; generation interfaces; network topologies; coupled oscillator dynamics; and stability analysis theory and criteria as set forth by IEEE 1547-

2018 standard.

Chapter 4 presents the stability and security analysis case study performed on the developed low-voltage network model from Chapter 3. Chapter 4 analyzes the dynamics of a low-voltage network of prosumers which all contain PV based generation and loads aggregated at their PCC (i.e disribution panel). Different types of loads will then be analyzed on the network and a static and dynamic security assesments are made based on IEEE 1547 requirements. This chapter further looks at the effect on network coupling and their inherent effect on security.

Chapter 5 concludes the thesis with a discussion of the results obtained in chapter 4. We will then give a final discussion on steps forward in terms of future research. Chapter 5 will be followed by a discussion on steps forward and potential future research.

CHAPTER 2: Single-Phase Inverter Operation

The focus of this thesis is concerned with low-voltage network dynamics associated with mass amounts of interconnected prosumers; modelling prosumers effectively is the objective of this chapter. As a majority of prosumers consist of rooftop PV being interfaced with the grid, this will be the basis of the control schemas discussed throughout this chapter. The prosumer PV adoption trend is likely to continue as PV costs drastically decline due to the economies of scale associated with consumer adoption. Typical rooftop PV systems are interfaced with the grid through string or multi-string inverters depending on the rooftop area. String inverters are typically within the 0.4-2kW range whereas multi-string inverters are within 1.5-10kW range.

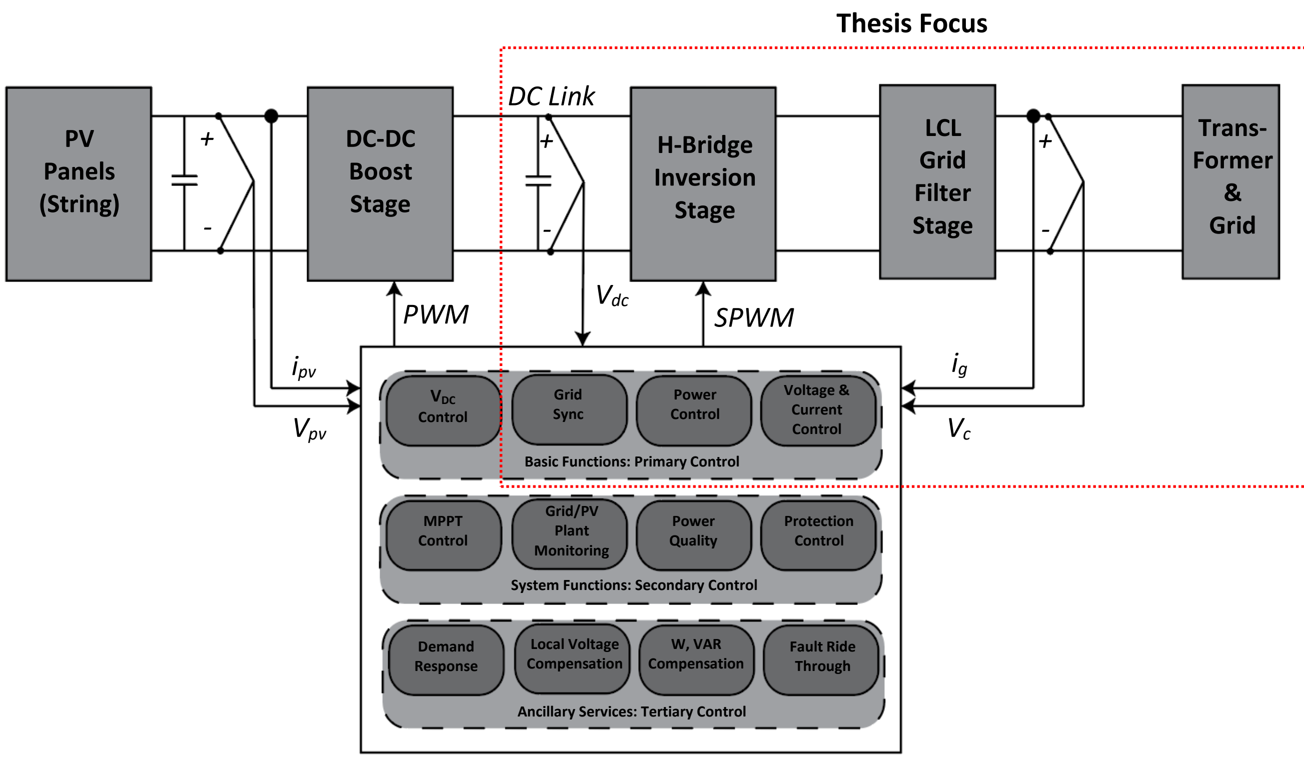

Figure 2.1: Generic Control Model for Prosumer Grid-Connected PV

This chapter describes a conventional single-phase grid connected inverter and their associated dynamics by providing; (I) high-level overview of inverter principle of operation; (II) detailed description and derivation of the inverter plant model; (III) The derivation and discussion of primary control loop dynamics; (IV) grid synchronization; (V) and a discussion of the most recent publication of the IEEE-1547-2018 interconnection standard. The discussion around the IEEE1547-2018 is particularly important due to the newly mandated interconnection and operation requirements for modern grid connected inverters today. A majority of the IEEE1547 standard applies within the short time scale and is thus the responsibility of the primary control layer to ensure a technically sound interconnection.

Due to the fast dynamics of the inverter, large technical interconnection requirements and mandatory injection capabilities, the primary control loop is critical to a technically sound interconnection and stability of the network. Thus, the need for a detailed discussion of the primary control loop. The concern of chapter is demonstrated in figure 2.1, highlighted in red. For the remainder of this work, the PV power optimization and Vdc control will be out of scope and a fixed and stable input power from the PV system will be assumed to the DC link. Further explanation of such assumption will be justified in the later parts of this chapter.

2.1. Single-Phase Inverter Operation

2.1.2 DC-DC H-Bridge Inversion Stage

The basic principle of operation of an inverter can be illustrated using the widely adopted H-bridge topology, shown in Fig 2.2 [5].The principle of this operation is the differential switching in which S_a, S_b^{low} and S_b, S_a^{low} switch coherently during the positive and negative half of the 60hz grid reference signal respectively. There are many circuit topology modifications that are made to the H-bridge circuit that are widely adopted in commercial inverter applications which improve overall H-bridge efficiency and can be found in the literature [5], [6], [7], [8].Depending on PV system specifications, the switches generally are high-power MosFET's or IGBT's. The switches nominal mode of operation is within the 20-60 kHz range in order to increase efficiency while reducing grid side harmonics as per the IEEE-1547 power quality requirements [1]. The higher the switching frequency; the smaller the inductor; the cheaper the inverter; the better the injected power quality.

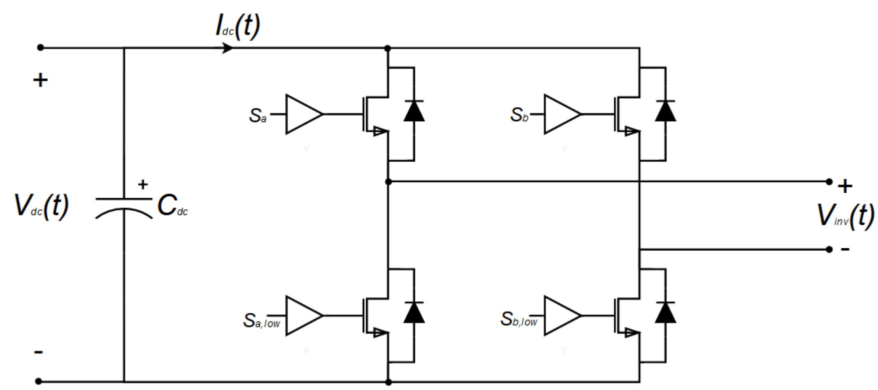

Figure 2.2: Basic Full-Bridge (H-Bridge) Inverter Circuit

Sinusoidal pulse width modulation (SPWM) is the most widely adopted gate control technique and is a fundamental block within the primary control loop. At a high-level, the generation of SPWM is done through a symmetrical sawtooth signal generator (operating at the fundamental gate switching frequency) being compared through an analog OR digital comparator to a grid reference signal. This comparison process is demonstrated by figure 2.3, the SPWM square wave output is high when the grid signal is greater than the symmetrical sawtooth wave signal and vice versa. The output of the aforementioned process is depicted by figure 2.4, (note: the frequency of the symmetrical sawtooth signal used to generate such SPWM is much higher than what was demonstrated in figure 2.3). The higher the SPWM frequency modulation is, the further the harmonics are on the frequency band. Thus, leading to greater filter attenuation and hence lower harmonics in the grid injected current. An important design consideration required to comply with the IEEE 1547 harmonic injection requirements. SPWM is discussed extensively in the literature [9], [10] and the discussion will be left to its basic principle here.

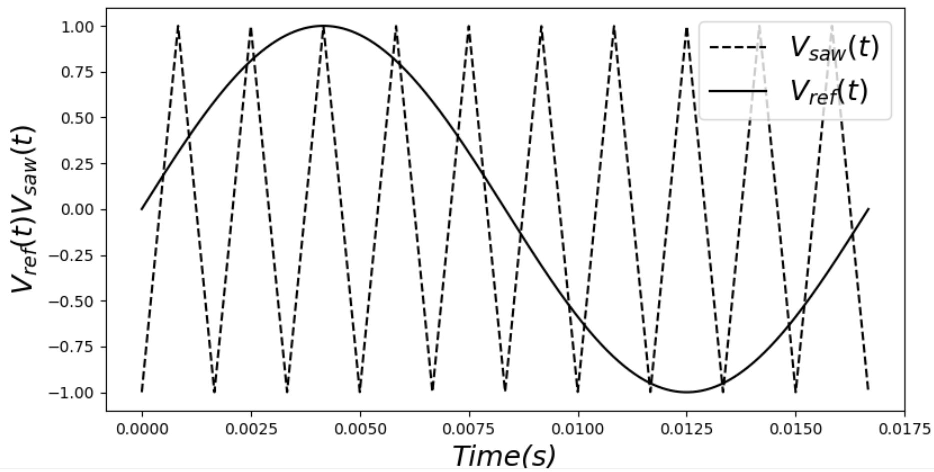

Figure 2.3: $V_{saw}(t)$ and $V_{ref}(t)$ SPWM Generation

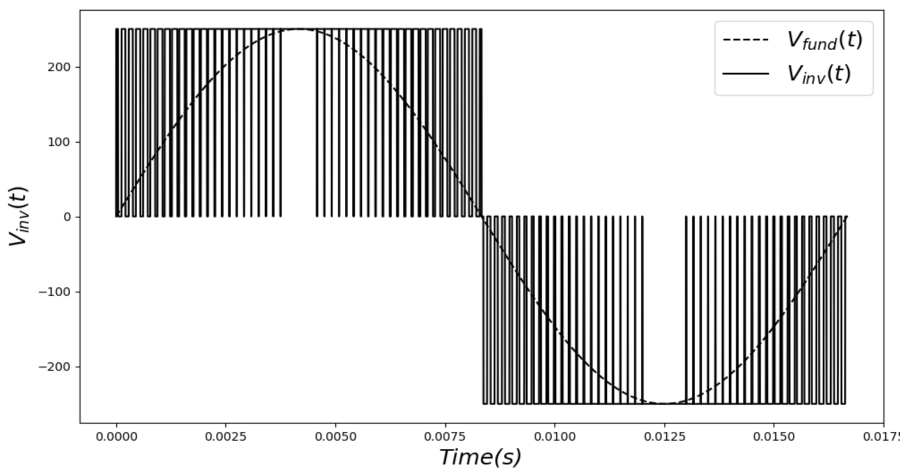

Figure 2.4: $V_{ref}(t)$ and $V_{SPWM}(t)$ Output Comparison

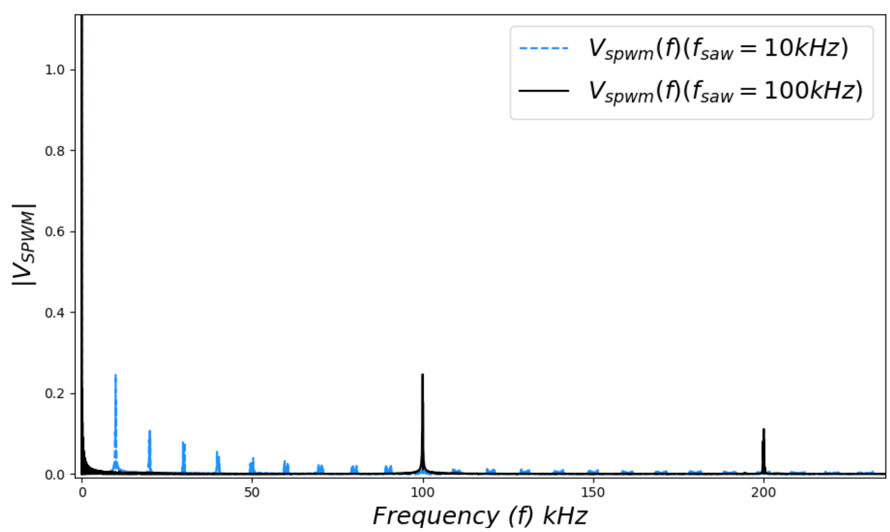

Figure 2.5: SPWM Harmonics at f_{saw}=10kHz & 100kHz

2.1.2 LCL Grid Filter Stage

The objective of the inverter output filter is to remove the high order harmonics that are generated around the multiples of the SPWM switching frequency and to leave the fundamental 60Hz sinusoidal grid voltage un-attenuated. Conventionally this is done with passive *LC* or *LCL* filters which are second and third order systems respectively.

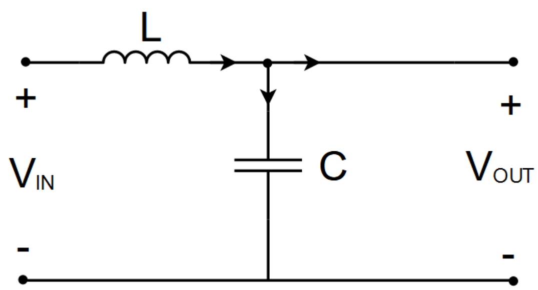

Figure 2.6: LC Filter

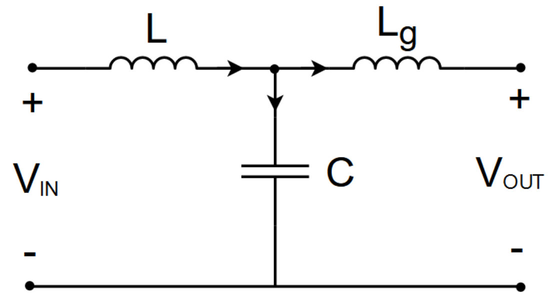

Figure 2.7: LCL Filter

Depending on performance and/or cost requirements of the system, the choice between the two different types of filters is made. In grid connected applications, the LC filter is not commonly used. This is due to the resonance frequency of the LC filter varying due to the varying inductive reactance of the grid. The grid filter should have a dominant inductive behavior to guarantee the proper operation of a voltage source inverter when connected to a voltage source type system such as the utility grid [11]. This dominant inductive behavior of the filter will allow the voltage source converter to mimic synchronous machines in which the active and reactive power may be controlled. Due to the additional inductor contained within the LCL filter, this filter provides a dominant inductive impedance and hence reduces the influence of the grid impedance on the inverter operation [14]. Thus, a crucial implication for advanced inverter functionality in high-penetration neighborhoods is to allow for local voltage control and microgrid frequency control.

Due to their inherent properties, the LCL filter will be the concern for the remainder of the thesis. The sizing and selection of the filter and capacitor are primarily based on harmonic attenuation, but further consideration is needed such as: the cut off frequency f_c, voltage THD, cost, resonance damping, efficiency, and power level [12], [13].

The resonance frequency of the LCL filter is:

$$f_{res} = \frac{1}{2\pi}\sqrt{\frac{L_f + L_g}{L_f L_g C_f}}. \tag{2.1}$$

This is the most important design criteria of the filter and should be significantly lower than the SPWM modulation switching frequency while providing enough bandwidth for the controller. It is recommended to select the cut-off frequency within $\frac{1}{3} \sim \frac{1}{2}$ of the switching frequency f_{sw} [14].

$$\frac{f_{sw}}{3} \leq f_c \leq \frac{f_{sw}}{2} \tag{2.2}$$

Due to the filters capacitive inductive and capacitive components, the filter resonates around the cut-off frequency. Figure 2.10-A demonstrates this resonance effect with the spike on the magnitude response bode plot trace of the LCL filter. This effect has the capability of amplifying major harmonic components that can reside within the load current resulting in a much higher THD. Such effects can also cause stability issues within the primary control loop. In practice, it is important to model the equivalent series resistances (ESR) R_L and R_C. The ESR components dampen higher-frequency oscillations and *LC* resonance around f_c resulting in better filter performance. It is common in practice to select *LC* components with modified and/or modify these values to increase the filter performance. The adjust LCL filter model is depicted in figure 2.8. The inherent trade-off of increasing ESR is potential power loss which are a particular issue for high-power applications in the MW range. For the remainder of this thesis, we will assume a third-order LCL filter to be used.

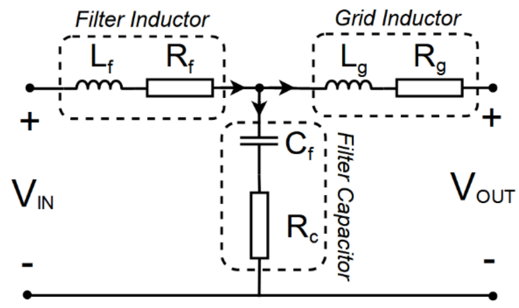

Figure 2.8: LCL Filter Model with ESR's

2.1.3 LCL Grid Filter Model

As there is a significant number of detailed literatures on grid connected LCL filter plant design, we will keep the mathematical model of the filter simple by assuming the inductance ESR is negligible. As aforementioned, it is common for designer to adjust the resistance (add active or passive damping) value. This is often done on the capacitor branch as this is not the major current carrying path. In this model we will combine the capacitor ESR with an external resistance and lump the values together as R_d, illustrated by figure 2.9 A & B.

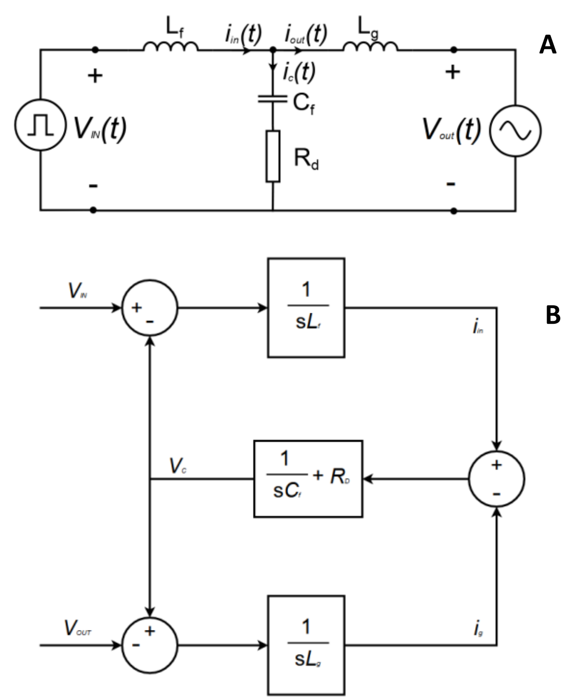

Figure 2.9: LCL Filter Model with Passive Capacitance Damping

By performing KVL in both loops and KCL at the central node and converting into the Laplace domain we obtain the following equations.

$$V_{in} = sL_f i_{in} + \left(\frac{1}{sC_f} + R_d\right) i_c \tag{2.3}$$

$$V_{out} = -sL_g i_{out} + \left(\frac{1}{sC_f} + R_d\right) i_c \tag{2.4}$$

Using the superposition theorem and substituting for i_c, the following transfer functions are obtained.

$$\left.\frac{I_{out}(s)}{V_{in}(s)}\right|_{V_{out}=0} = \frac{sC_f R_d + 1}{s^3 L_f L_g C_f + s^2 C_f R_d (L_f + L_g) + s(L_g + L_f)} \tag{2.5}$$

$$\left.\frac{I_{out}(s)}{V_{out}(s)}\right|_{V_{in}=0} = \frac{s^2 L_i C_f + sC_f R_d + 1}{s^3 L_f L_g C_f + s^2 C_f R_d (L_f + L_g) + s(L_g + L_f)} \tag{2.6}$$

Based on the IEEE 1547 Interconnection standard, the THD specifications are purely based on the maximum current distortion with no requirement on output voltage distortion. Therefore, the design of the LCL filter is based on Equation (2.5) and the transfer function of the LCL filter is

$$H_f(s) = \left.\frac{I_{out}(s)}{V_{in}(s)}\right|_{V_{out}=0} = \frac{sC_f R_d + 1}{s^3 L_f L_g C_f + s^2 C_f R_d (L_f + L_g) + s(L_g + L_f)}. \tag{2.7}$$

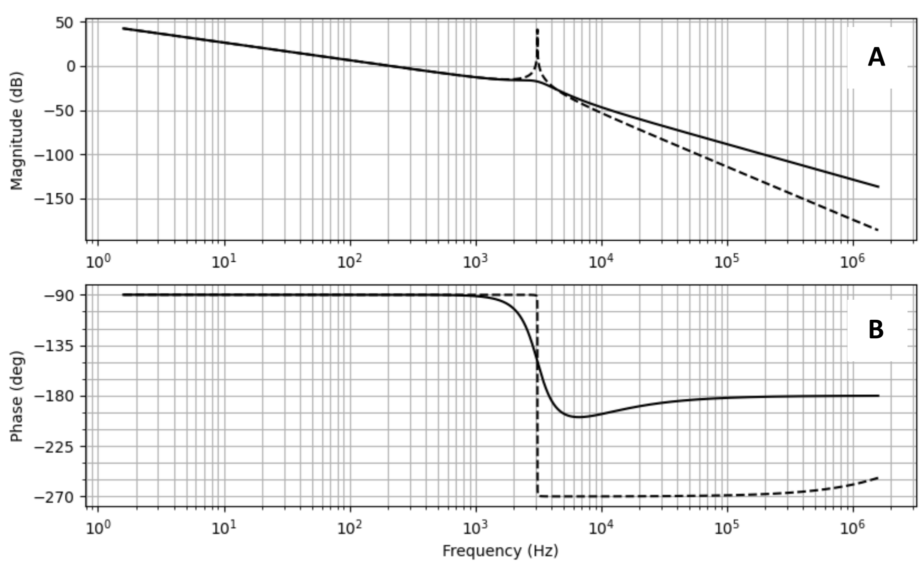

Figure 2.10: LCL Filter Bode Plot with R_d= 0.001 & 1Ω

Figure 2.10 plots the steady state frequency response of the LCL filter for two different values of capacitive damping resistance. The solid line represents the frequency response with damping resistance of 1 ohm whereas the dash line represents 1miliOhm damping. Comparing the frequency response of the two filter designs, there is an attenuation performance trade off past the resonant frequency of the filter. Note, to the left of the resonant frequency the attenuation is 20db/decade and to the right of the resonant frequency the attenuation is 40db/decade. Based on the addition of the damping mechanism within the filter, we can see that the filter nearly maintains a 20db/decade response. Therefore, the filter can effectively be modelled as an L filter, if simplicity is desired.

2.1.4 Single-Phase Inverter Plant Model

The plant which the control law is based upon is the LCL filter. Depending on the desired control law, inverters can either operate as a voltage source inverter (VSI) or a current source inverter (CSI). The choice of the control law will be expanded in the subsequent sections of this chapter and is purely based on overall system requirements. The complete inverter plant model can now be derived. The model will be represented in state space and due to the presence of three dynamic elements, our state vectors are of $\mathbb{R}^3$. We choose the inductor currents and the capacitor voltage as the state variables of the system $x = [i_{in} \quad i_{out} \quad u_c]^T$. The external inputs to the plant are the SPWM input voltage and the grid side voltage, $w = V_{in}$ and $u = V_{grid}$, respectively.

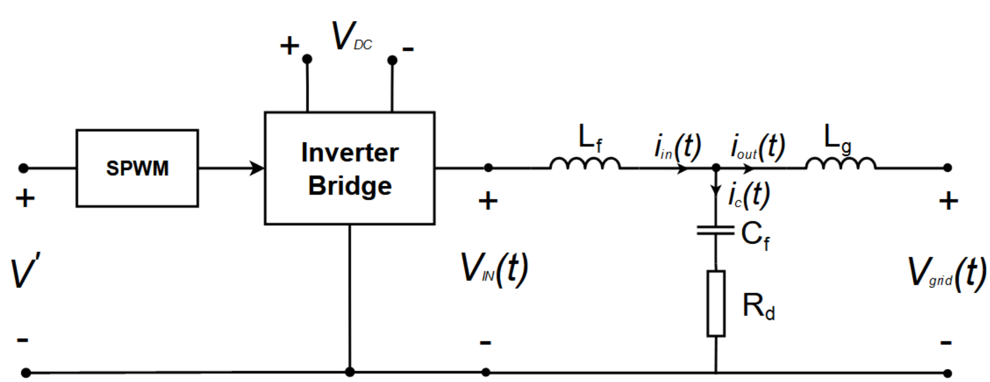

Figure 2.11: Inverter Plant Model

The plant, *P* is described by the following state equations:

$$\dot{x} = Ax + B_1 w + B_2 u \tag{2.8}$$

$$y = Cx + D_1 w + D_2 u \tag{2.9}$$

where,

$$A = \begin{bmatrix} -\frac{R_d}{L_f} & \frac{R_d}{L_f} & -\frac{1}{L_f} \\ \frac{R_d}{L_g} & -\frac{R_d}{L_g} & \frac{1}{L_g} \\ \frac{1}{C_f} & -\frac{1}{C_f} & 0 \end{bmatrix} \tag{2.10}$$

$$B_1 = \begin{bmatrix} \frac{1}{L_f} \\ 0 \\ 0 \end{bmatrix}, \quad B_2 = \begin{bmatrix} 0 \\ -\frac{1}{L_g} \\ 0 \end{bmatrix} \tag{2.11}$$

and

$$\begin{bmatrix} \dot{i_{in}} \\ \dot{i_{out}} \\ \dot{V_c} \end{bmatrix} = \begin{bmatrix} -\frac{R_d}{L_f} & \frac{R_d}{L_f} & -\frac{1}{L_f} \\ \frac{R_d}{L_g} & -\frac{R_d}{L_g} & \frac{1}{L_g} \\ \frac{1}{C_f} & -\frac{1}{C_f} & 0 \end{bmatrix} \begin{bmatrix} i_{in} \\ i_{out} \\ V_c \end{bmatrix} + \begin{bmatrix} \frac{1}{L_f} \\ 0 \\ 0 \end{bmatrix} V_{in} + \begin{bmatrix} 0 \\ -\frac{1}{L_g} \\ 0 \end{bmatrix} V_{out}. \tag{2.12}$$

The output of the inverter, *y,* depends on the control loop we are designing and the desired tracked output signal. In order to design the current and voltage control loops using classical control techniques, the state space representation must be transformed into a transfer function using the transfer function matrix (2.13) .

$$Y(s) = \boldsymbol{C}(sI - \boldsymbol{A})^{-1}\boldsymbol{B}U(s) + \boldsymbol{D}U(s) \tag{2.13}$$

The matrix C is dependent on the desired tracked output variable; A current controller, C = [0 1 0] or [1 0 0]; A voltage controller, C=[0 0 1]. The matrix D is the combination of the input column vectors D1 and D2.

2.2. Single-Phase Inverter Primary Control Loops

Modern single and three-phase inverters are now mandated by IEEE 1547-2018 [1] to have active and reactive power injection capabilities. Therefore, all modern inverters must act as VSI's to allow for local load, local EPS, and grid support capabilities. The VSI controls the AC current i_{in} through the switching function and by acting as a current source. Through AC current control, the VSI can change and control the DC value, V_{dc}, of the capacitor. Therefore, the DC capacitor is charged to a voltage sufficient to ensure the basic function of a VSI (Voltage is constant independent of the loading current).

Modern inverters adopt multiloop control strategies which consist of: 1) Fast acting inner current control loop; 2) Outer voltage control loop. Illustrated in figure 2.13. Current control is employed in order for the VSI to regulate current injection to control active and reactive power injection. The current reference is generated by the outer voltage control loop which is responsible for controlling the power exchange with a load, micro-grid and/or main grid depending on the connected system and system operating state [11]. The W, VAR injection control signals are generated through the widely-adopted droop control method which will be further detailed in the latter parts of this thesis.

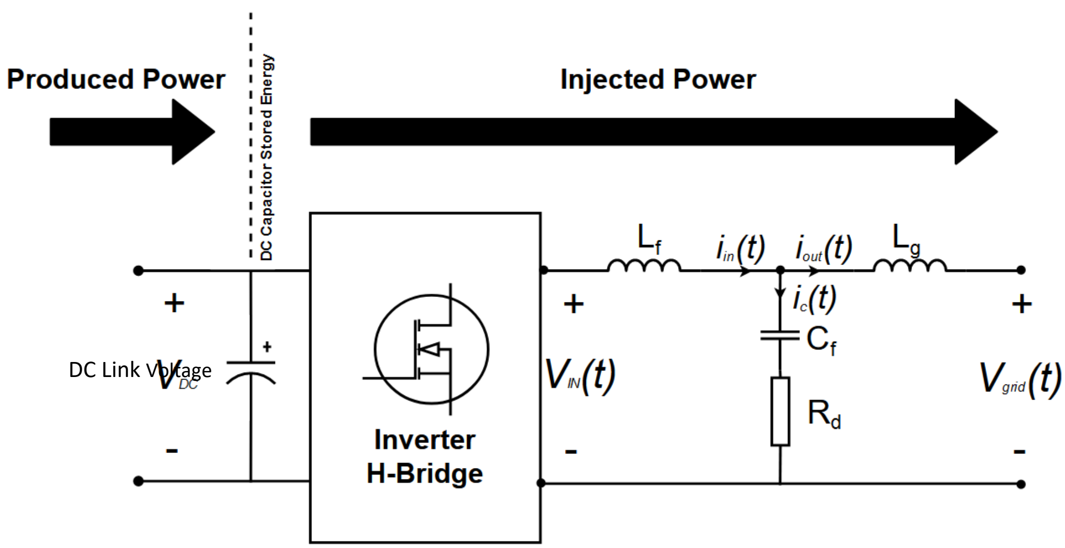

Figure 2.12: DC to AC Side Inverter Power Flow [11]

The DC link voltage, depicted in figure 2.12, is an important discussion point as it serves as the intermediary between the production of energy from the PV side and the injected energy into the local load, micro-grid, and/or grid. The DC link is subject to transient conditions due to production and loading imbalances. An increase in produced PV power will introduce a voltage overshoot while the contrary will produce a voltage undershoot. The DC link voltage control is achieved through the control of the power exchanged with grid/load OR through the control of the DC/DC converter. This thesis is concerned with the former of these two cases. Control of the DC link through the power exchange of the load is due to the increase in active and reactive power injection to the grid with respect to that produced by the PV system. Thus, it is performed through either AC reference commands through the current control loop or through the AC voltage across the LCL filter capacitor [11]. This thesis will focus on the control of the DC link voltage through the control of the AC voltage across the LCL filter which is performed through the widely accepted droop control. The inner current control loop is to regulate, limit and achieve short settling times while the outer control loop's objective is to maintain optimum regulation and stability.

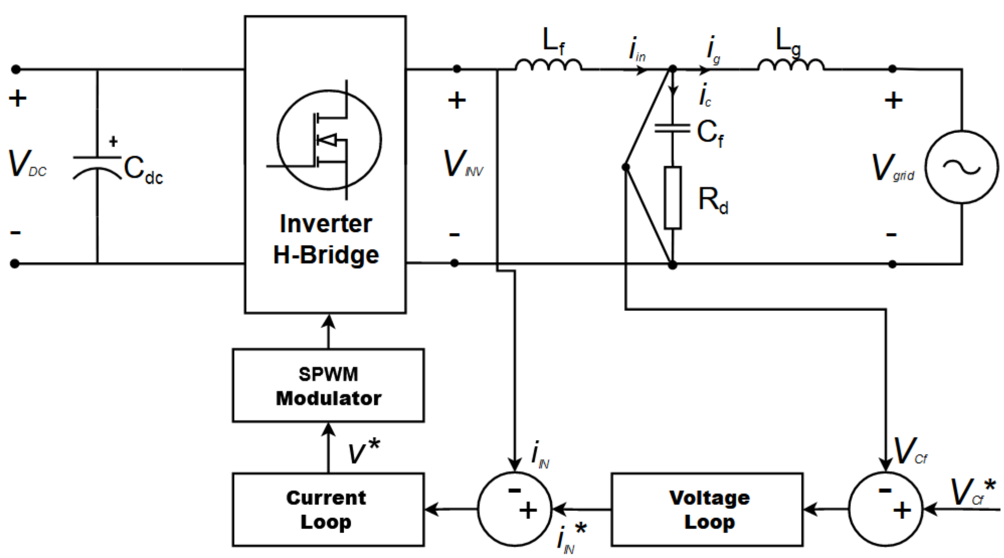

Figure 2.13: Voltage Source Inverter Fast -Acting Inner Control Loops

2.2.1 Single-Phase Current Control Loop

The inner current control provides fast acting current regulation from the reference signal that is generated from the voltage control loop. The control loop controllers may be designed in one of two ways: 1) Utilizing a Proportional Resonant (PR) controller, allowing fast-acting control in the time domain [15], [16], [17] or; 2) Through the use of a PI controller based on the Clark-Park ($\alpha\beta - dq$) rotating reference frame transformation, transforming the time-varying signals into DC quantities [2], [11], [18], [19]. The use of transforming the time varying signals into DC quantities allows us to employ well established classical control principles along with coherent single-phase and three-phase basis design fundamentals. The Clark-Park transformation transforms three-phase abc reference frame vectors to two-phase $\alpha\beta$ stationary reference frame vectors, allowing the three spatially separated vectors to be described as two. The $\alpha\beta$ frame is then rotated at a synchronous speed ω and is denoted as the dq frame.

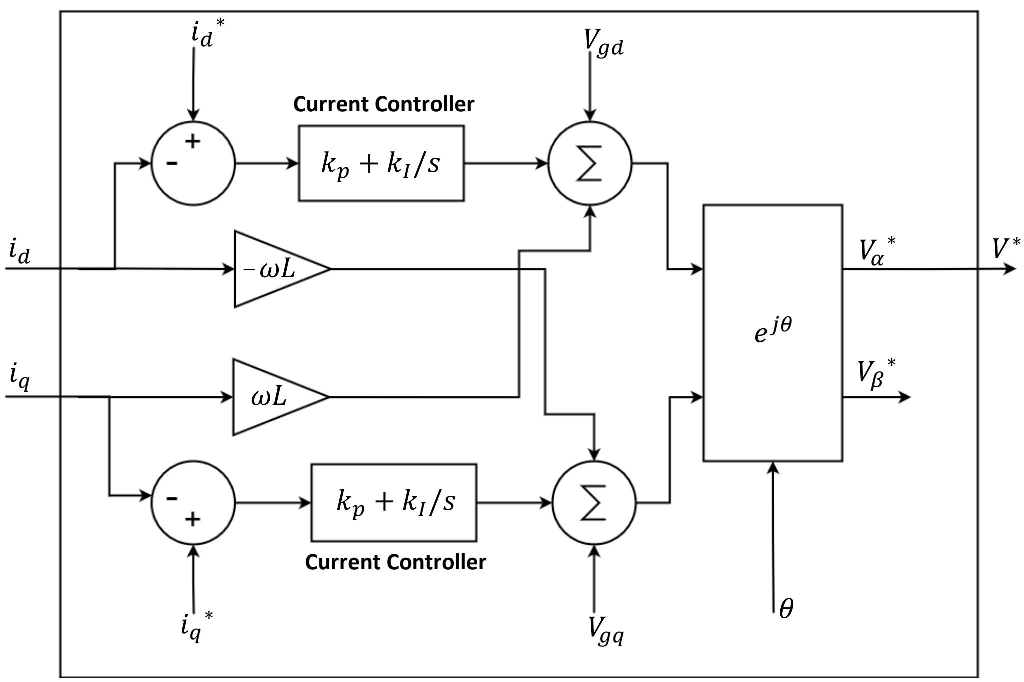

Figure 2.14: Single-Phase Inverter Current Control Loop

In a single-phase system, the use of a rotating frame is not possible unless a virtual system is coupled to the real frame to simulate a two-phase ($\alpha\beta$) environment. This virtual system is implemented through the use of a virtual phase delay block to create a virtual quadrature component. Thus, the single-phase system can be described as a two-phase system and transformed to the final synchronous dq reference frame.

The control loop of the transfer function is designed based on the state-space matrix (2.13). Open loop transfer functions will be denoted by $G(s)$ and the subscript $(\cdot)_i(s)$ will explicitly refer to the open loop transfer function of the current loop. Using the inverter H-bridge current as the output of the plant, $C = [1 \quad 0 \quad 0]$ and $B = B_1 = \left[\frac{1}{L_f} \quad 0 \quad 0\right]^T$. The open loop transfer function, $G_i(s)$ of the plant is,

$$G_i(s) = \frac{I_{in}(s)}{V_{in}(s)} = \frac{1}{L_f s} \frac{\left(s^2 + \frac{R_d}{L_g} + z_{LC}{}^2\right)}{\left(s^3 + \frac{R_d}{L_g}\frac{(L_f + L_g)}{L_g} s + \omega_{res}{}^2\right)}, \tag{2.14}$$

where $\omega_{res}{}^2 = \frac{L_f + L_g}{L_f L_g C_f}$ and $z_{LC}{}^2 = \frac{1}{L_g C_f}$. The current controller employed in the feedforward path is a proportional integral (PI) controller to ensure a fast response with zero steady state error. The feedforward PI controller transfer function is,

$$G_{i,PI}(s) = k_{pc} + \frac{k_{ic}}{s}. \tag{2.15}$$

The complete open loop transfer function of the current controller is,

$$G_{cc}(s) = G_{ic}(s) G_{if}(s)\,. \tag{2.16}$$

The complete open loop transfer function of the current control system is denoted by the subscript $(\cdot)_{cc}(s)$. Figure 2.14 illustrates the complete current control PI *dq* design within the feedforward path. It is important to note the feedforward de-coupling of the i_d and i_q variables that reduce the cross-coupling effect of the *dq* transformation of the variables.

2.2.2 Single-Phase Voltage Control Loop

As aforementioned in section 2.2.1 and demonstrated in figure 2.13, the current loop reference commands are generated from the outer voltage loop. The current control loop represented by figure 2.13, 2.14 and equation (2.16) is extended with an outer voltage control loop to form a multiloop control design. The voltage control loop follows a reference command, ${V_{ref}}^*$, generated from sensed inverter/grid conditions. The ${V_{ref}}^*$ command will be expanded in more detail in the later sections of this chapter. Based on classical control theory, the outer voltage loop can be imposed on the inner current control loop by cascading the unity feedback closed current control loop with a voltage controller. In order to create uniformity amongst the control system, the voltage control loop is designed and implemented within the *dq* reference frame. The design of the outer voltage control loop is illustrated in figure 2.15

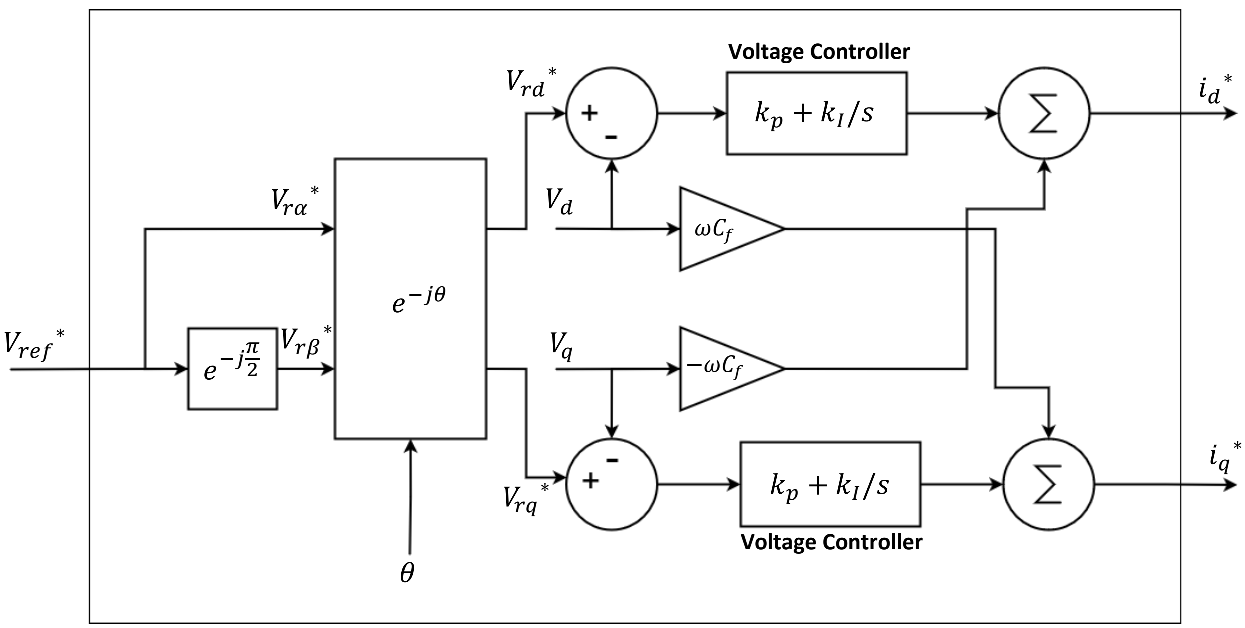

Figure 2.15: Single-Phase Inverter Voltage Control Loop

Based on figure 2.15, the reference command received from higher level control loops is transformed into its two-phase $\alpha\beta$ equivalent and rotated at the grid reference signal speed $e^{-j\theta}$ to create the DC reference command input to the voltage controller. Similar to that of current controller, the sensed output V_d and V_q variables are de-coupled by being feedforward to the output of the PI voltage controller.

The plant in which the voltage controller is designed upon, is the aforementioned closed loop unity feedback current controller scaled by the LCL grid output capacitor C_f. The open loop voltage plant transfer function, $G_v(s)$, where the subscript $(\cdot)_v(s)$ denotes the voltage is,

$$G_v(s) = \frac{V_c(s)}{V_{in}(s)} = \frac{G_{cc}(s)}{1 + G_{cc}(s)} \frac{1}{C_f(s)}. \tag{2.14}$$

In order to drive a fast voltage control response with no steady-state error, PI controller is employed in the feedforward path with an open loop transfer function $G_{v,PI}(s)$ where the subscript $(\cdot)_{v,PI}(s)$ represents the PI controller,

$$G_{v,PI}(s) = k_{vp} + \frac{k_{vi}}{s} \tag{2.15}$$

And the open loop transfer function of the voltage control loop being

$$G_{vc}(s) = G_{vc}(s) G_{vf}(s)\,. \tag{2.16}$$

The aforementioned reference command for the voltage loop is generated from the highest-level control loop within primary control, droop control. Droop control is responsible for adjusting the output voltage magnitude and frequency of the reference signal to the voltage control loop.

2.2.2 Droop Control

Droop control is commonly employed within large synchronous machines allowing voltage and frequency regulation based on sensed grid conditions as well as the capability of sharing the load amongst generators. Its goal is for the rotating machine to ramp up its mechanical rotating speed and/or field current in order to increase or reduce active and reactive power injection into the grid based on their respective droop curve settings. Taking this control methodology and applying it within the power electronics space allows inverters to participate in active voltage and frequency regulation at the grid edge and to provide low-voltage networks the ability to operate in a microgrid setting with the inverters sharing the load amongst one another without any communication [20], [21], [22]. Inverters mimic the actions of rotating machines by adjusting output voltage amplitude and frequency with respect to their defined droop curve. The active and reactive power ramp is a predefined curve (droop curve) with a given slope so that sensed values will indicate the increase or curtailment of power output of the generator. The droop settings employed within the inverters are defined through the power-flow characteristic of the transmission line and invert output impedance which connects the DER to the local area EPS. This coupling is illustrated in figure 2.16

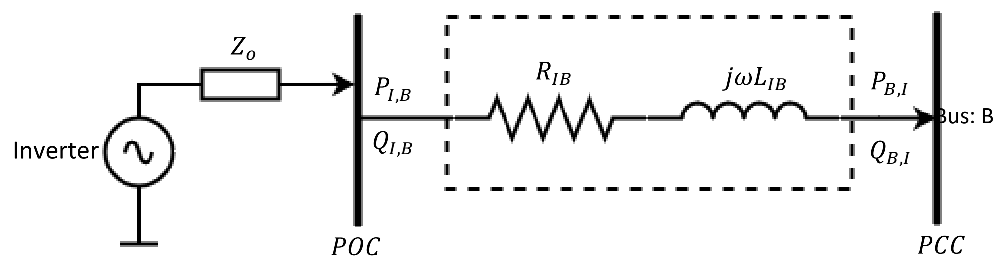

Figure 2.16: Inverter to Network Coupling

The point at which the inverter terminals connect to the local system and loads is denoted as the point of coupling (POC). The point of common coupling (PCC) is where this area EPS connects to the bulk EPS. This terminology is specifically defined in the IEEE 1547-2018 standard and will be expanded within subsequent sections of this chapter. The active and reactive power notation in figure 2.16 uses a directional notation where the subscript $(\cdot)_{I,B}$ represents the power transmitted from the sending end of the transmission line to the receiving end (POC to PCC) and $(\cdot)_{B,I}$ represents the inverse. The subscript, $(\cdot)_{IB}$, without a comma represents the coupling between two buses and is a non-directional representation. Z_o denotes the output impedance of the inverter. The feeder line is the transmission line between the POC and PCC. The power flow characteristics through the inverter output impedance and the feeder line are determined by the current injection from the switches terminals into the network (PCC) bus represented by

$$I_{I,B} = \frac{E_I e^{j\theta_I} - E_B e^{j\theta_B}}{Z_{IB} e^{j\delta_{IB}}} = Y_{IB} e^{-j\delta_{IB}} (E_I e^{j\theta_I} - E_B e^{j\theta_B}). \tag{2.17}$$

The apparent power that is injected/received by the network bus is governed by

$$S_{B,I} = E_B e^{j\theta_B} I_{IB}{}^{*} = Y_{IB} \left(E_B E_I e^{j(\theta_B - \theta_I + \delta_{IB})} - E_B{}^2 e^{j\delta_{IB}} \right). \tag{2.18}$$

Expanding (2.18) into its rectangular form we obtain,

$$\begin{gathered} S_{B,I} = Y_{IB} E_I E_B [\cos(\theta_B - \theta_I + \delta_{IB}) + j \sin(\theta_B - \theta_I + \delta_{IB})] \\ -Y_{IB} E_B{}^2 \, (\cos(\delta_{IB}) + j \sin(\delta_{IB})). \end{gathered} \tag{2.19}$$

Therefore, the active and reactive power injection into the network PCC is governed by

$$P_{B,I} = Re\{S_{B,I}\} = Y_{IB} E_B (E_I \cos(\theta_B - \theta_I + \delta_{IB}) - E_B \cos(\delta_{IB})) \tag{2.20}$$

and

$$Q_{B,I} = Im\{S_{B,I}\} = Y_{IB} E_B (E_I \sin(\theta_B - \theta_I + \delta_{IB}) - E_B \sin(\delta_{IB})). \tag{2.21}$$

Depending on the dominant impedance properties of the coupling transmission line we obtain the active and reactive power injection properties defined in Table 2.1.

SYSTEM IMPEDANCE	*DOMINANT INDUCTIVE* $\boldsymbol{\delta_{IB} \cong \pi/2}$	*DOMINANT RESISTIVE* $\boldsymbol{\delta_{IB} \cong 0}$	*COMPLEX IMPEDANCE* $\boldsymbol{Y_{IB} e^{-j\delta_{IB}}}$
ACTIVE POWER	$Y_{IB} E_B E_I \cos(\theta_B - \theta_I)$	$Y_{IB} E_B (E_I \cos(\theta_B - \theta_I) - E_B)$	*Eq'n (2.20)*
REACTIVE POWER	$Y_{IB} E_B (E_I \sin(\theta_B - \theta_I) - E_B)$	$Y_{IB} E_B E_I \sin(\theta_B - \theta_I)$	*Eq'n (2.21)*

Table 2.1: Transmission Line Impedance-Power Flow Relationship

Table 2.1 demonstrates that a resistive dominated coupling impedance has $V - W$ and $f - VAR$ characteristics whereas an inductive dominated has $f - W$ and $V - VAR$ characteristics. In order to set droop curves for the inverters, the network coupling needs to be considered. In a low-voltage grid the coupling impedance is typically dominated by its resistive component whereas at medium-high voltage levels the coupling impedance is dominated by its inductive component. A nice review about voltage droop in

Figure 2.17 is a polar plot representing the effect of voltage magnitude and angle variations on the output active and reactive powers based on the feeder coupling and inverter output impedance [22]. For all cases within figure 2.17, the active and reactive power injection magnitude increases when the voltage magnitude at the output of the inverter, E, is increased. For the inductive case, figure 2.16A, the radius of the reactive power stays constant as the voltage angle between PCC and POC bus is increased whereas the active power injection into the grid is increased significantly. The resistive dominated line in figure 2.17B demonstrates the inverse of the inductive coupled line. A complex coupled transmission line demonstrates that voltage angle difference has a similar effect on both active and reactive power injection. The grey zone within the polar plots of figure 2.17 depicts the applicable operation region in which an inverter would adjust its angle based on its active and reactive power injection capabilities.

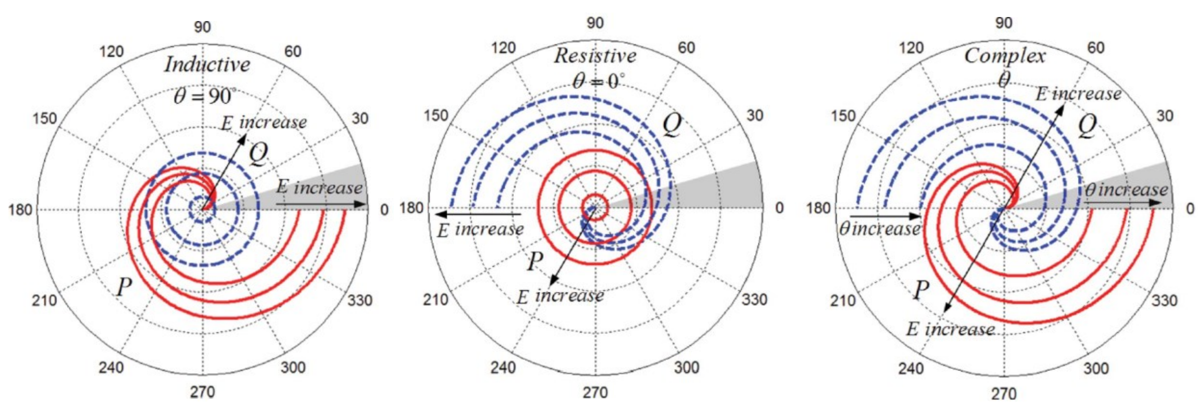

A) *B)* *C)*

Figure 2.17: PQ Polar Plots of: A) inductive coupling, B) Resistive Coupling, C) Complex Coupling [22]

As this thesis is concerned with low-voltage network dynamics, only resistive dominant coupling lines will be considered. Therefore, our *V*-f (droop) control law employed within the single-phase inverters is based on the $V - W$ and $f - VAR$ characteristics at the POC, hence

$$P_{I,B} = Y_{IB}E_I(E_I - E_B\cos(\theta_I - \theta_B)) \tag{2.22}$$

and

$$Q_{I,B} = -Y_{IB}E_BE_I\sin(\theta_I - \theta_B), \tag{2.23}$$

where $P_{i,b}$ and $Q_{i,b}$ denote the active and reactive power injection from the inverter POC to PCC bus. Equations (2.22) and (2.23) demonstrate two things: first, that the active power injected from the inverter into to a stiff network bus strongly depends on the difference between voltage amplitudes of the two oscillators; and second, that the reactive power injection depends strongly on the difference between their respective voltage phase angles. Note the phase-frequency relationship,

$$\Delta\theta_{I,B} = \theta_I - \theta_B = \int(\omega_{inv} - \omega_{grid})dt. \tag{2.24}$$

Due to these aforementioned properties, the droop control laws employed within each inverter are configured as

$$E_{inv} = -m_i(P_{I,B} - P_{I,nom}) + E_{inv}{}^* \tag{2.25}$$

and

$$\omega_{inv} = n_{inv}Q_{I,B} + \ \omega_{inv}{}^*, \tag{2.26}$$

where $E_{inv}{}^*$ is the inverter operating voltage set point for nominal power injections of $P_{inv_{nom}}$ (this nominal power set point is determined by both the generation capacity and the network operator responsible for governing the interconnection requirements); $\omega_{inv}{}^*$ is the nominal operating frequency set point; E_{inv} and ω_{inv} are the output voltage and frequency control signal for the inverter based on their respective droop gains m_{inv} and n_{inv}; and $P_{I,B}$ and $Q_{I,B}$ are the sensed active and reactive output powers, respectively. Furthermore, (2.25) and (2.26) may be written as,

$$\Delta E_{inv} = E_{inv}{}^{*} - E_{inv} = m_{inv}\left(P_{I,B} - P_{inv_{nom}}\right) \tag{2.27}$$

and

$$\Delta\omega_{inv} = \omega_{inv} - \omega_{inv}{}^{*} = n_{inv}Q_{I,B}. \tag{2.28}$$

Thus, providing the following intuition:

The dynamics of a droop-controlled inverter are strictly governed by the droop coefficients and the power flows from the inverter into the network. Any deviation of voltage and frequency from their nominal set point is the result of a power imbalance in the network. Figure 2.19 represents the frequency droop curve for a resistive dominant low-voltage impedance which adheres to equation (2.28). For a low voltage microgrid operation in Volt-Watt (V-W) mode, we propose a piece-wise linear curve where the rate of power curtailment can be made greater for over-voltage conditions than is the case in conventional droop control (where the generator is sensitive to the constant slope droop coefficient). This piece-wise V-W droop curve is illustrated in figure 2.18. In microgrid operation, any load steps will have a large impact on the system stability so the ability for the generators to stay online is crucial.

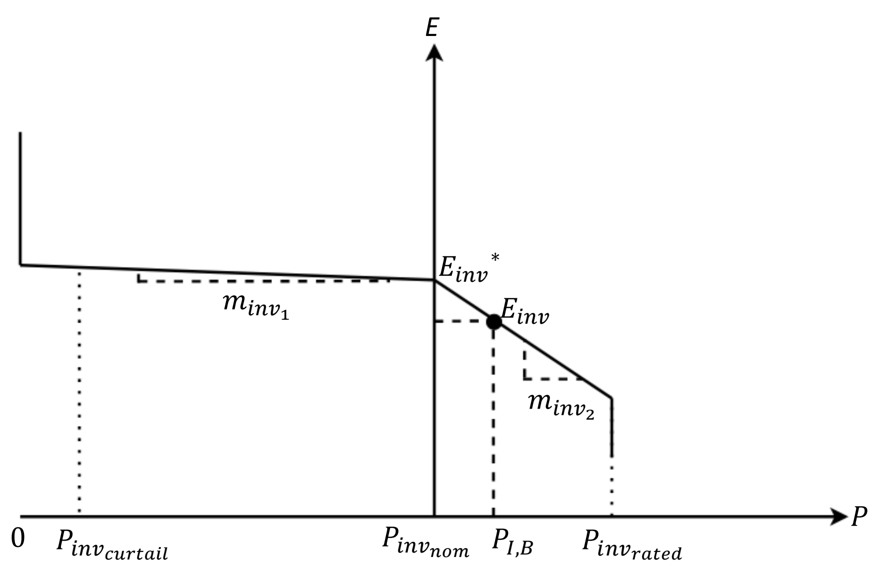

Figure 2.18: V-W Droop Curve

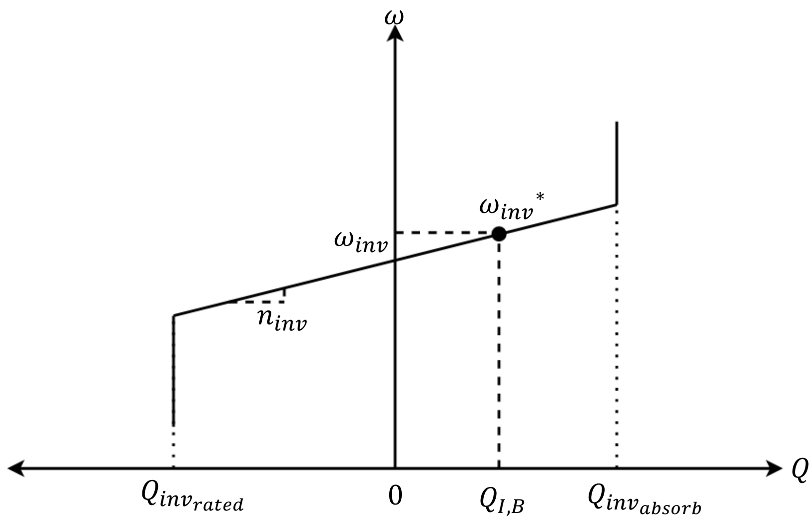

Figure 2.19: f-VAR Droop Curve

When operating in islanded (microgrid) mode, the stiff grid assumption is no longer valid, therefore the conventional droop control methodology has significant effects on the voltage profile throughout the network. The voltage drops in the network as the load increases and hence the generation voltage may also drop due to the conventional droop control. In order to ensure that the voltage is limited to the required operational range, the voltage error must be feedback into the system by measuring the calculated difference between the inverter reference set point voltage and bus voltage [23].This error is then added as positive feedback to the existing voltage feedback signal (2.27) as,

$$\Delta E_{inv} = K_E({E_{inv}}^* - E_B) - m_{inv}\left(P_{I,B} - P_{inv_{nom}}\right). \tag{2.29}$$

The integration of (2.29) provides the control signal to the inverter and may be expressed as

$$\tau_{inv}\frac{dE_{inv}}{dt} = K_E({E_{inv}}^* - E_B) - m_{inv}\left(P_{I,B} - P_{inv_{nom}}\right) \tag{2.30}$$

where K_e is the reference voltage error feedback gain and τ_{inv} captures the delay in the system for the inverter [23]. The droop control strategy employed in the low-voltage microgrid is known as Proportional (Robust) Droop Control and can be found in more detail in [14], [23], [24].The complete structure of the proportional droop control schema is illustrated in figure 2.20.

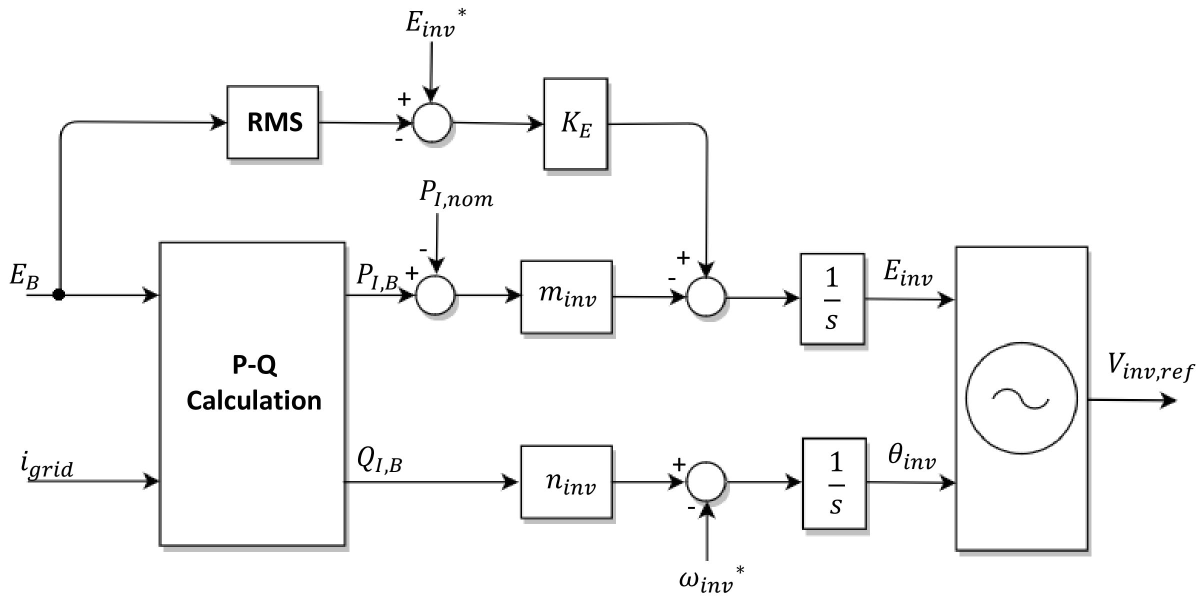

Figure 2.20: Microgrid Proportional Droop Control Schema

2.2.3 Complete Single-Phase Inverter Control Model

A complete grid-interfaced voltage source inverter primary control structure is presented in figure 2.21. The presented primary control structure aggregates the fast acting inner current and voltage control loops represented in figures 2.14 and 2.15 respectively. The final output command to control the inverter H-Bridge switching gates, V^*, is converted to an SPWM signal through a final gain block K_{pwm} . The K_{pwm} block is typically a unity gain block and primarily depicts the change of time domain to digital domain switching signal input command.

The V_{ref}^* reference command to the fast-acting inner multiloop control blocks is generated from the proportional droop control strategy described in section 2.2.2 and based on the aforementioned sensed grid conditions. Note: the primary control strategy presented in figure 2.21 does not account for V_{dc} needed to manage the DC link to couple the DC stage of the inverter input to the PV system. Within this these we assume stiff V_{dc} requirements to allow for the inverter to meet all power flow requirements within its ratings.

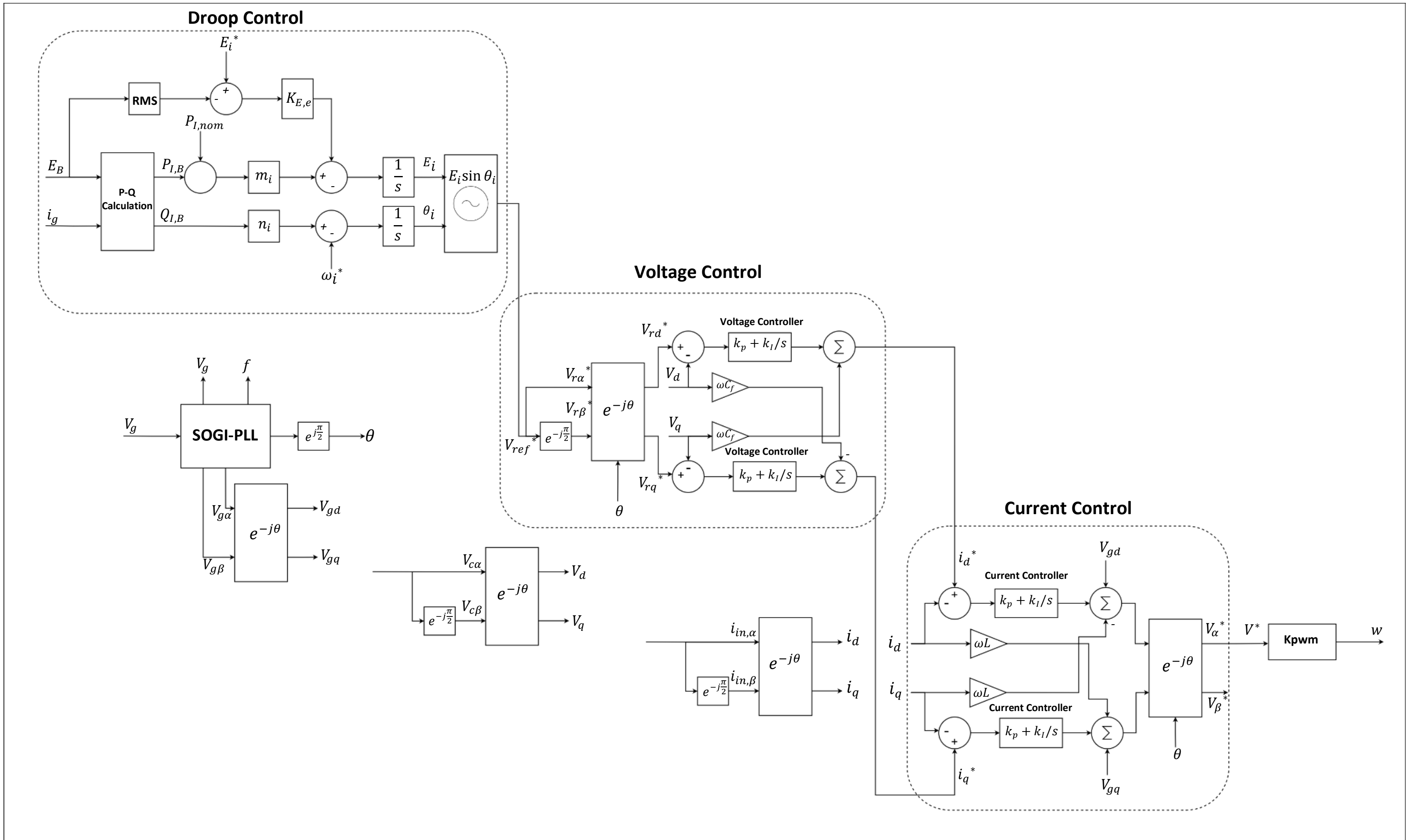

Figure 2.21: Single-Phase Inverter Primary Control Loop Schema

2.3 Synchronization

Inverters have many different capabilities, and are generally classified based on their primary control loops. They are either grid-forming, grid-supporting and/or grid feeding inverters. With droop control being employed, a VSI can serve as either a grid forming or grid supporting inverter. A current source inverter (CSI) is classified as a grid feeding inverter. A grid forming inverter essentially is feeding a standalone network and is responsible for producing and maintaining the voltage and frequency at all buses within the network. If there are multiple droop-controlled inverters within the network, all inverters would contribute to the grid formation process. Their contributions are based on their respective impedances, as seen at their terminals, and their droop coefficients. This means that droop-controlled inverters allocate their individual powers to work cooperatively to achieve a nominal V/f operating point without any centralized communication. This inherent capability in achieving voltage and frequency regulation also allows droop inverters to actively support the grid if the forming requirement is not needed.

Dependent on whether the droop-controlled inverter is a grid-forming inverter or a grid supporting inverter; droop control inverters need a synchronization mechanism. A well designed, fast acting synchronization mechanism is essential for an accurate representation of grid variables to allow for proper inverter control operation. This necessity is further emphasized with the use of the aforementioned *dq* control techniques in which the rotating reference frame has to be synchronized with the grid reference signal with no error. The DER must act according to the grid-state that is obtained via the synchronization mechanism. In modern inverters, this is typically done by a phase-locked-loop (PLL) or some variation of the PLL. The basic concept of a modern synchronization mechanism will be highlighted in this section.

2.3.1 Phase-Locked-Loop (PLL)

The basic structure of the PLL is demonstrated in figure 2.22 and consists of three main components: 1) a phase detector, 2) a Loop filter and 3) a Voltage controlled oscillator (VCO). The principle

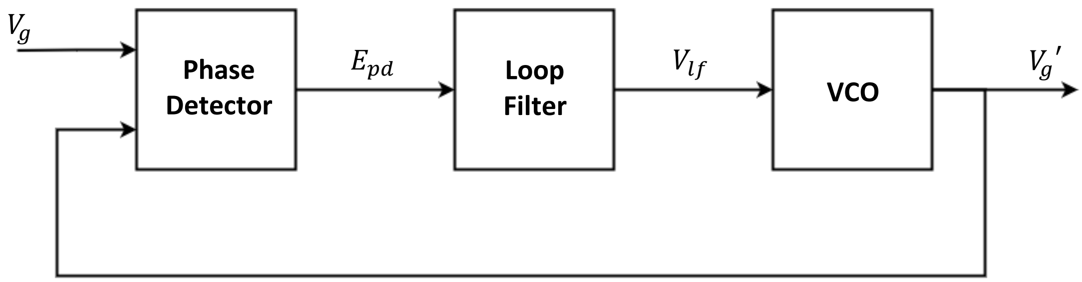

Figure 2.22: Basic PLL Structure

of operation is as follows. The input signal applied to the PLL is the sensed grid voltage at the POC,

$$v_g(t) = V_g \sin(\omega_g t + \phi), \tag{2.31}$$

and the signal generated from the VCO is

$$v_g{}'(t) = V_g{}' cos(\omega_g{}' t + \phi'). \tag{2.32}$$

The phase error signal from the multiplier of the phase detector is

$$\begin{aligned} E_{pd} &= V_g k_{pd} \sin(\omega_g t + \phi)\, cos(\omega_g{}' t + \phi') \\ &= \frac{V_g k_{pd}}{2} \{\sin[(\omega_g - \omega_g{}')t + (\phi - \phi')] + sin[(\omega_g + \omega_g{}')t + (\phi + \phi')]\}. \end{aligned} \tag{2.33}$$

The objective of the loop filter is to remove the high frequency term $\sin[(\omega_g + \omega_g{}')t + (\phi + \phi')]$ leaving the phase detector error term as $E_{pd} = \frac{V_g k_{pd}}{2} \sin[(\omega_g - \omega_g{}')t + (\phi - \phi')]$. If we assume the VCO frequency is well tuned and close to the 60Hz grid frequency, then $\omega_g \approx \omega_g{}'$, and the phase error will be relatively small, $-\frac{\pi}{4} \leq \phi - \phi' \leq \frac{\pi}{4}$. We can therefore linearize the output of the phase detector as

$$E_{pd} = \frac{V_g k_{pd}}{2} (\phi - \phi'), \tag{2.34}$$

thus, providing a small signal linearized model of the phase detector. The variations in the VCO frequency are given by

$$\omega_g{}' = \omega_c + k_{vco}V_{lf}, \tag{2.35}$$

where $\omega_g{}'$ is centered about the VCO center frequency ω_c, V_{lf} is the output volage of the loop filter and hence the DC signal of the phase detector error E_{pd}. Lastly, k_{vco} is the tuning parameter of the VCO frequency. The variations in the VCO's phase are obtained by integrating the VCO's tuning parameter,

$$\phi'(t) = \int k_{vco}V_{lf}\, d\tau. \tag{2.36}$$

We can now create a linearized small signal model of the PLL using the following components:

- Phase Detector: $E_{pd}(s) = \frac{V_g k_{pd}}{2}[\Phi(s) - \Phi'(s)]$, where $\Phi(s)$ and $\Phi'(s)$ are the Laplace transform of the sensed grid phase $\phi(t)$ and output VCO phase $\phi'(t)$;
- Loop Filter: $V_{lf}(s) = k_{lf}\left(1 + \frac{1}{T_i s}\right)E_{pd}(s)$, where T_i is the time constant of the loop filter;
- Voltage Controlled Oscillator: $\Phi'(s) = \frac{1}{s}V_{lf}(s)$, where $V_{lf}(s)$ is the Laplace transform of V_{lf}.

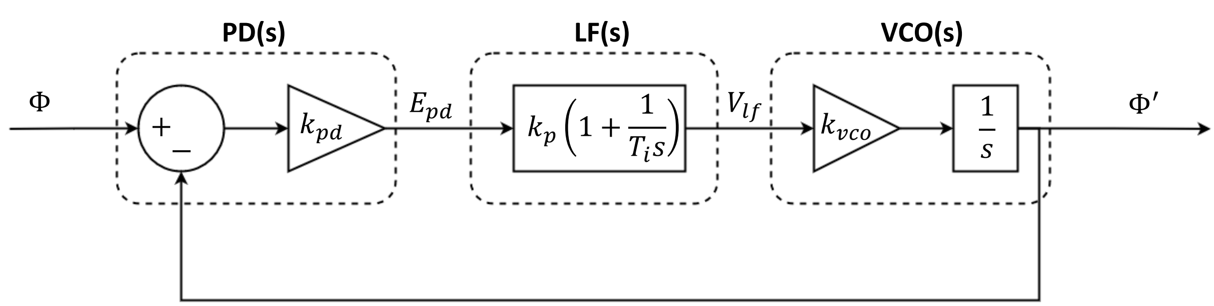

Figure 2.23: Basic PLL Small Signal Model

The open loop phase transfer function of the basic PLL is

$$G_{pll}(s) = PD(s)LF(s)VCO(s) = k_{pd}\, k_p k_{vco}\left(1 + \frac{1}{T_i s}\right)\left(\frac{1}{s}\right) = \frac{Ks + \frac{K}{T_i}}{s^2}, \tag{2.37}$$

where $K = k_{pd}\ k_p k_{vco}$ and is referred to as the PLL gain; the closed loop transfer function is

$$H_{pll}(s) = \frac{\Phi'(s)}{\Phi(s)} = \frac{G_{pll}(s)}{1 + G_{pll}(s)} = \frac{Ks + \frac{K}{T_i}}{s^2 + Ks + \frac{K}{T_i}}, \tag{2.38}$$

and the error transfer function is

$$E_\theta(s) = \frac{E_{pd}(s)}{\Phi(s)} = 1 - H_{pll}(s) = \frac{s^2}{s^2 + Ks + \frac{K}{T_i}}. \tag{2.39}$$

The closed loop transfer function demonstrates that we have a second order system with two complex poles that represent a low pass-filtering characteristic in the detection of the input phase angle [11]. The system characteristics are

$$\omega_n = \sqrt{\frac{K}{T_i}}\ \ \&\ \xi = \frac{\sqrt{KT_i}}{2}. \tag{2.40}$$

Using equation (2.40) we can design the time constant of the PLL to achieve desired response characteristics such as settling time, overshoot, and peak time. There are many other key parameters of the PLL that need to be taken into consideration during the design stage. This includes the frequency hold range, frequency pull-in range, time to pull-in, frequency lock-range, time to lock-in range and pull-out range. These are important parameters that need to be considered in the design of a PLL and are described in great detail in [11], [25]. The focus of this thesis is not on the PLL details, but in its necessary realization to enable the distributed PV study; consequently, a high-level description will suffice.

There is an inherent limitation to PLL in grid applications due to the 50Hz/60Hz grid signal. The majority of PLL applications are in communications systems which operate at much higher frequencies, therefore the assumption that the higher frequency term generated from the PD can be is valid. In the case of grid connected applications the higher frequency term is near the 3db point of the PLL bandwidth and therefore this assumption is no longer valid. The result is the 2nd fundamental of the grid input signal is not fully attenuated by the loop filter. Thus, 2f oscillations exist within the PLL leading to oscillatory frequency and phase estimations. This problem can be mitigated by adjusting the bandwidth of the PLL but this has a deleterious effect on the frequency pull-in range, frequency hold range, etc…. Therefore, direct use of a PLL is not commonly employed within grid connected applications [11]. In order to properly implement a PLL in grid connected applications, another technique must be employed within the phase detector to remove the high frequency term.

2.3.2 Second Order Generalized Integrator Phase-Locked-Loop (SOGI-PLL)

For our purpose, a new PD design is necessary to cancel out oscillations at twice the grid frequency for power grid connected applications. This can effectively be done with the use of an ideal quadrature signal generator (QSG), demonstrated in Figure 2.24. The quadrature signal generation block does not introduce any additional delays in the system, that would modify the time constant and performance of the adjusted PLL.

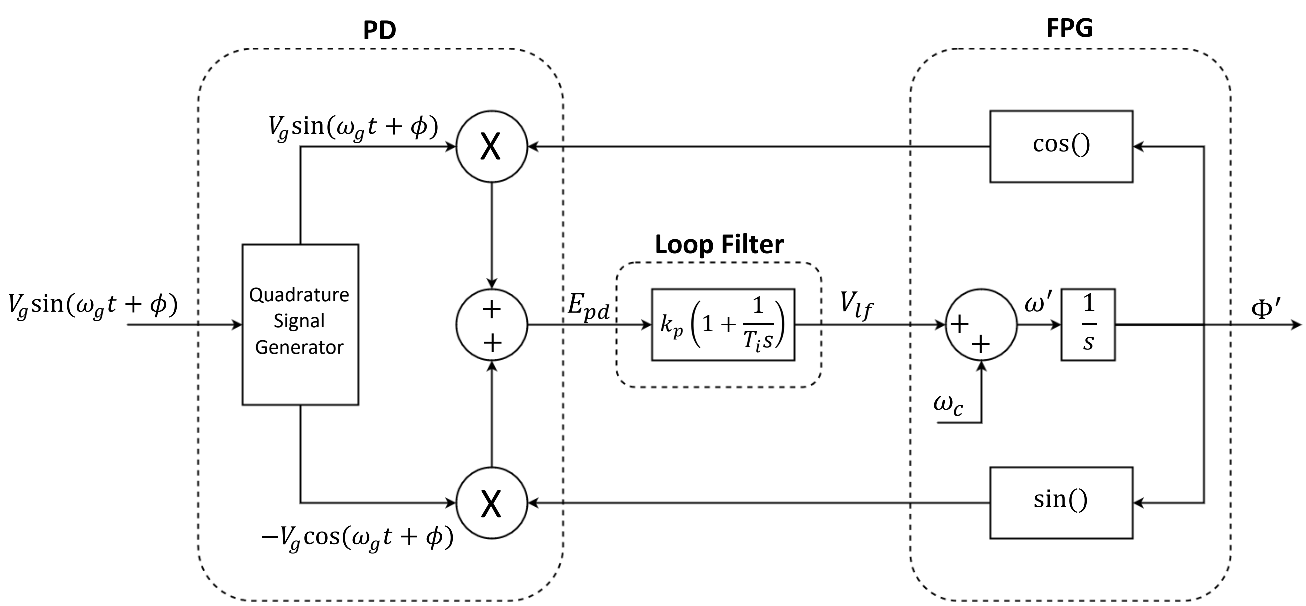

Figure 2.24: Ideal QSG PLL Block Diagram

The error signal is now

$$E_{pd} = V_g \sin(\omega_g t + \phi)\, cos(\omega_g{}'t + \phi') - V_g \cos(\omega_g t + \phi)\, sin(\omega_g{}'t + \phi')$$
$$= V_g \sin[(\omega_g - \omega_g{}')t + (\phi - \phi')]. \tag{2.41}$$

Therefore, when the PLL has achieved frequency synchronization ($\omega_g = \omega_g{}'$) the steady state oscillations cease to exist. The PLL can be tuned to the desired bandwidth as the low bandwidth limitation has now been removed; thus, a system better suited for the needs of grid applications [11].

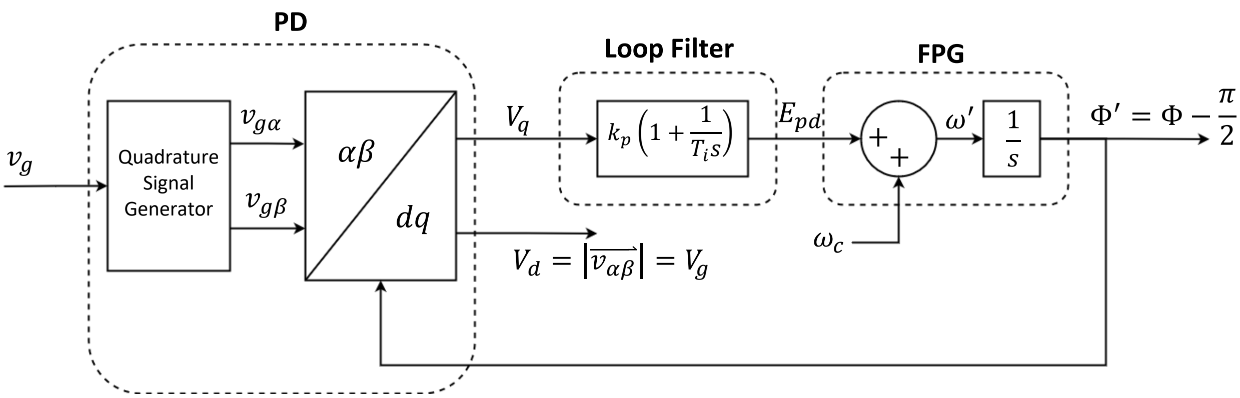

Figure 2.25: Adjusted PLL for Clarke and Park Transform

Figure 2.24 and equation (2.41) may be adjusted to accommodate the Clarke-Park transform, shown in Figure 2.25. The input signal to QSG is (2.31) and the output signal from the PD is

$$\begin{bmatrix} v_{g\alpha} \\ v_{g\beta} \end{bmatrix} = v_g \begin{bmatrix} sin(\Phi) \\ -cos(\Phi) \end{bmatrix} \tag{2.42}$$

$$\begin{bmatrix} V_d \\ V_q \end{bmatrix} = \begin{bmatrix} cos(\Phi') & sin(\Phi') \\ -sin(\Phi') & cos(\Phi') \end{bmatrix} \begin{bmatrix} v_{g\alpha} \\ v_{g\beta} \end{bmatrix}. \tag{2.43}$$

Equation (2.42) into (2.43) yields

$$\begin{bmatrix} V_d \\ V_q \end{bmatrix} = v_g \begin{bmatrix} cos(\Phi') & sin(\Phi') \\ -sin(\Phi') & cos(\Phi') \end{bmatrix} \begin{bmatrix} sin(\Phi) \\ -cos(\Phi) \end{bmatrix} = v_g \begin{bmatrix} sin(\Phi - \Phi') \\ -cos(\Phi - \Phi') \end{bmatrix}. \tag{2.44}$$

As mentioned in section 2.2, the single-phase system is transformed into a dual phase through the use of a virtual projection onto the $\alpha\beta$ axis using the quadrature signal generator. In the case of the PLL, the virtual $\alpha\beta$ grid voltage vector is projected onto the *dq* rotating reference frame rotating at the PLL speed Φ'. When the PLL frequency matches the grid frequency the virtual input grid vector and rotating reference frame are stationary with respect to each other. The PLL then drives the phase difference of the two reference frames to $\frac{\pi}{2}$ and a *dq* axes will then be in perfect quadrature with the virtual grid vector. Based on (2.44) the quadrature axis (V_q) is typically driven to zero allowing the d axis to align and overlap the virtual grid voltage vector in the steady state. Thus, we can extract the grid voltage magnitude information from V_d whereas V_q contains the phase information in quadrature, therefore the phase shift must be compensated for.

The implementation difficulty is how the quadrature signal generator transforms the grid voltage input signal into its $\alpha\beta$ reference frames. There are multiple ways of doing so, including the T/4 transport delay [26], Hilbert Transform and Inverse Park Transform [27], among others. These methods have several drawbacks including high sensitivity to frequency variations and harmonics which result in poor PLL synchronization performance. The most widely employed quadrature signal generator is based on the *second order generalized integrator* (SOGI), shown in Figure 2.26.

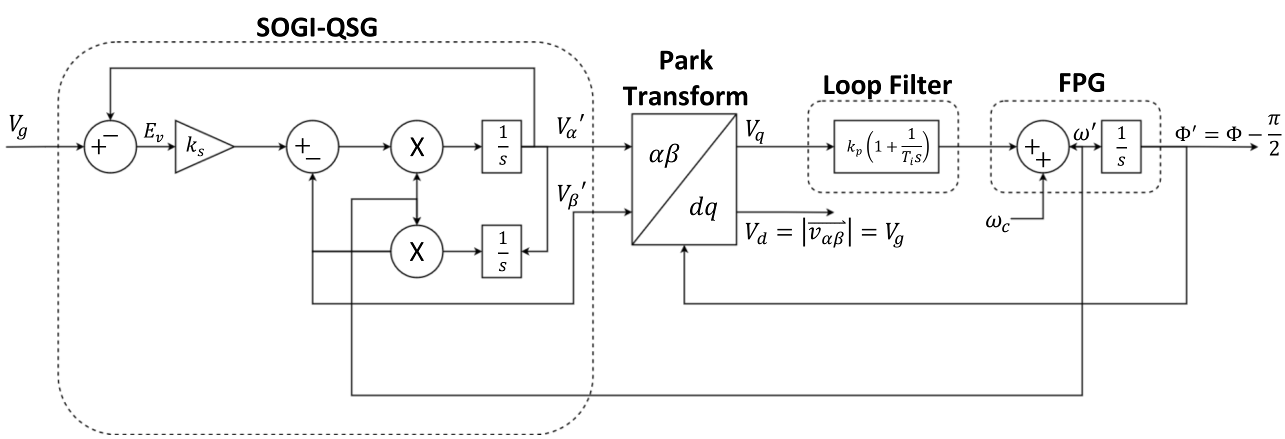

Figure 2.26: SOGI-PLL Block Diagram

The SOGI is an adaptive resonant filter approach allowing only the selected fundamental frequency to pass the SOGI filter while also providing the quadrature generated signal of that component (SOGI-QSG). The transfer functions of the SOGI-QSG are

$$\frac{V_\alpha'(s)}{V_g(s)} = \frac{k_s\omega' s}{s^2 + k_s\omega' s + \omega'^2} \tag{2.41}$$

$$\frac{V_\beta'(s)}{V_g(s)} = \frac{k_s\omega'^2}{s^2 + k_s\omega' s + \omega'^2} \tag{2.42}$$

Bode plots demonstrate that magnitude and phase are tuned solely by the gain k_s. Thus, this filter is suitable for variable frequency applications such as our input grid voltage. The SOGI-QSG bandwidth can be tuned to achieved the desired response across the varying frequencies that the SOGI-PLL will see over the course of its operation. Note that a lower k_s leads to a narrower bandwidth, but very low values of k_s will degrade dynamic performance. Significant work was done in [28] detailing this process and the inner works of the SOGI-QSG, the discussion of the SOGI-PLL will be left kept to a its high-level here.

2.4. Distributed Energy Resource Interconnection and Operation Requirements

Here we discuss the essential technical specifications for the interconnection and interoperability between utility electric power systems (EPSs) and distributed energy resources (DERs). The focus is the recently released IEEE 1547-2018 standard, which has seen major expansion over the earlier versions. Its main emphasis is the installation of DER on radial primary and secondary distribution systems, including network distribution systems. We begin with an overview of the Standard, then discuss abnormal response and ride-through requirements, and finally review voltage and frequency regulation specifications. The current standard does address other technical specifications and requirements regarding integration with area EPS grounding, synchronization, interconnection integrity and so forth, but these will not be discussed in the remainder of this thesis as the most important topics for change within the standard are embedded within regulation and ride-through operation requirements for abnormal area EPS conditions. The later parts of this paper will discuss these topics in more detail and what the drivers are behind them to make the capabilities mandatory in modern DER devices, as well as how the new revision of the IEEE 1547-2018 standard does so.

2.4.1 IEEE-1547 Standard for Interconnection and Interoperability of DER's with Associated Electric Power Systems Interface

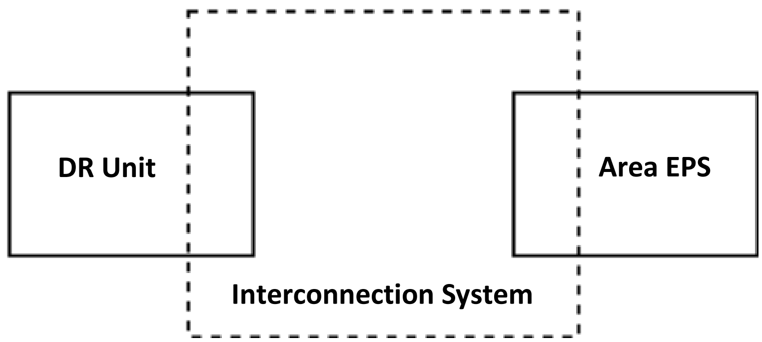

Figure 2.27: Scope of Early IEEE 1547 Standards

The former version of the IEEE 1547 standard was published in 2003. At this time the level of DER penetration was low and utilities did not expect DER to ever reach significant penetration at a regional level. It was therefore assumed that the frequency and voltage at the substation between the distribution and transmission grid would always be close to nominal no matter how these DERs would contribute to the distribution system. The 2003 standard provided the minimum functional technical requirements that were universally needed to ensure a technically sound interconnection. Figure 2.27 demonstrates these minimal requirements through the dashed box only have a minimal overlap on the blocks which represent the entirety of the DER Unit and Area EPS as a whole.

The IEEE 1547-2003 standard was characterized by the "do no harm" principle, providing a series of requirements on how the DER unit should function. The first clause in the general requirements section states that "The distributed resource shall not actively regulate the voltage at the PCC." [1], implying that the DER should always operate at unity power factor. The standard addressed how the DER should respond to Area EPS abnormal conditions, highlighting the response to abnormal voltage and frequency. It is specified that when voltage and frequency are outside of the ranges specified by the ANSI C84.1-1995 standard [29], the DER system shall "cease to energize the Area EPS". Table 2.2 and 2.3 demonstrate the corresponding clearing times for cessation for certain percentages of abnormal voltages and frequencies.

Voltage range (% of base voltage[a])	Clearing time(s)[b]
V< 50	0.16
50 ≤ V< 88	2.00
110 < V < 120	1.00
V ≥ 120	0.16

Table 2.2: IEEE 1547-2003 Response Time to Abnormal Voltage [30]

DR size	Frequency range (Hz)	Clearing time(s)[a]
≤ 30 kW	> 60.5	0.16
	< 59.3	0.16
> 30 kW	> 60.5	0.16
	< {59.8 – 57.0} (adjustable set point)	Adjustable 0.16 to 300
	< 57.0	0.16

Table 2.3: IEEE 1547-2003 Response Time to Abnormal Frequency [30]

In IEEE 1547-2003 there is zero flexibility for voltage regulation and no capability for any low voltage or high voltage ride through (LVRT and HVRT). Furthermore, this version was only applicable to DER units with aggregate capacity of 10MVA or less at the point of common coupling (PCC), interconnected to the EPS at typical primary and/or secondary distribution voltages. With increasing penetration of DER capacity at the grid edge, in particular the growth in residential PV, these interconnection requirements began to create significant grid problems such as: feeder hosting capacity, reverse power flows, local voltage stability, protection requirements, control requirements and impact on overall EPS stability.

The IEEE 1547-2018 standard was developed to both address the problems, and to better exploit DER generation potential. The adjusted scope of the standard is illustrated in Figure 2.28. It specifically addresses the power interface between DER and area EPS. It provides greater detail regarding DER functionality requirements which encompasses the DER unit as a whole and/or the system. This encompassing is demonstrated in figure 2.28 with the increased coverage of the dashed box on the DER block in comparison with that of figure 2.27. Specifically, the new revision adds a well-defined power interface with the Area EPS that encapsulates the bigger picture needs of the BPS. This need is represented by new mandated ride-through and regulation requirements preventing a massive loss of DER in abnormal operation regions of the EPS. This expands the standard from its former narrow focus on distribution system aspects only to one which covers BPS aspects as well. A mandated communication interface highlights how much impact DER have on the EPS today and how much impact they will have in the future. The communication requirement allows Area EPS operators become more proactive operators with mass DER penetration while also relaying aggregated real-time information to BPS operators to ensure overall power system stability and integrity.

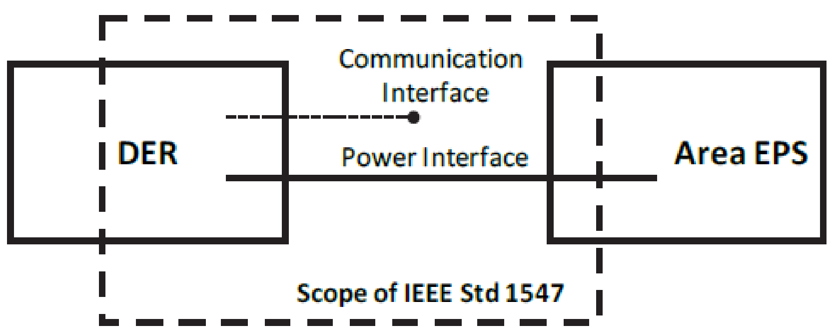

Figure 2.28: IEEE 1547-2018 Scope of Standard [1]

Within the 2018 revision, there are a series of new defined concepts to create consistency in terms of the reference point of applicability, at which the standard applies. The Point of Common Coupling

(PCC) is defined as the point of connection between the area EPS (utility grid) and the local EPS (customer installation), as before. The 2018 revision adds a new reference point of applicability: the point of connection (POC).

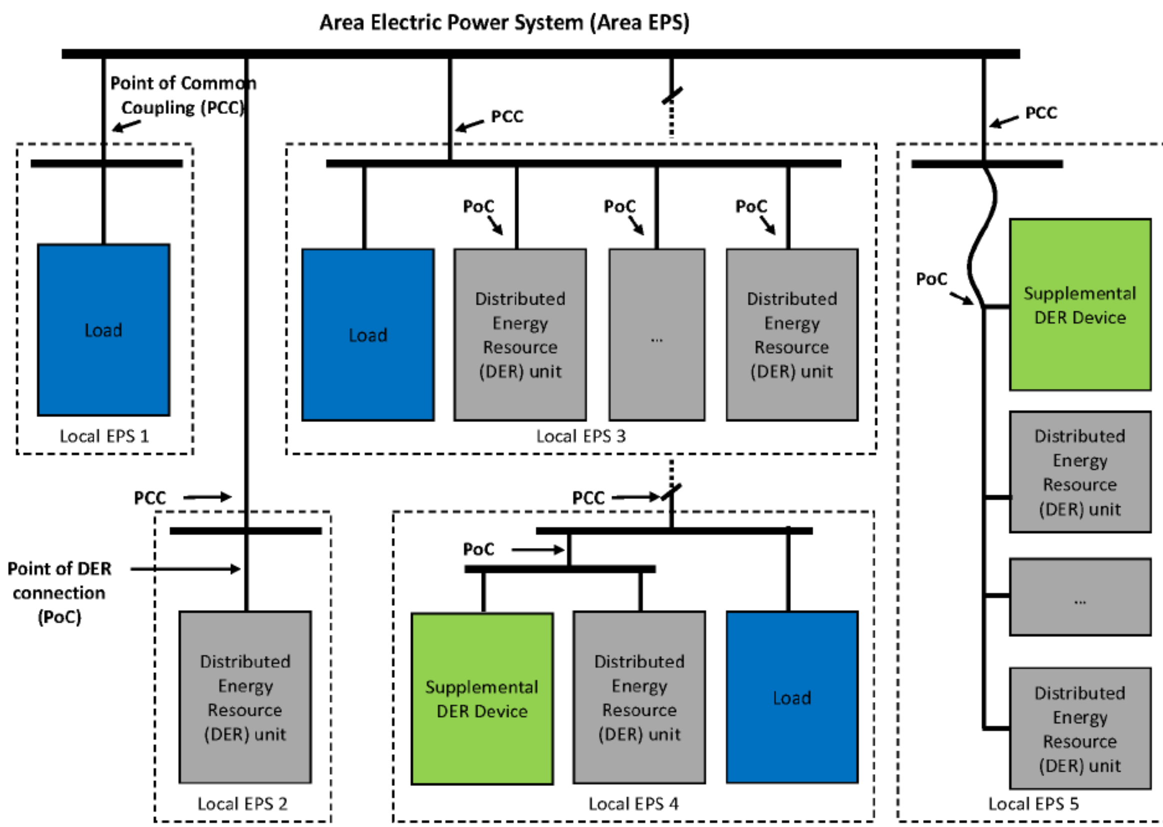

Figure 2.29: IEEE 1547-2018 Reference Points of Applicability Example [1]

The POC is defined as the point where a DER unit OR DER supplemental device is connected in a local EPS. The requirements of the IEEE 1547 standard are to be met at the PCC regardless of any load behavior within the local EPS. The driver behind the broadened reference point of applicability is the tension between utility and DER vendor perspectives. The former has insight into the area EPS and so wants compliance at the PCC, while the latter must accommodate the local EPS and thus wishes compliance at the POC.

Figure 2.29 schematically differentiates between the two reference points. It also introduces supplemental DER devices located at the grid edge. These devices are needed to help any equipment connected within a local EPS meet the requirements of the new standard at the POC or PCC. This is due to the fact that some DER units may not be compliant or there is a need to retrofit some existing systems. These devices consist of capacitor banks, STATCOMS, harmonic filters, protection devices and so forth. Shown in figure 2.29 local EPS 4, a supplemental DER device connected in parallel with the DER unit itself, and shown in figure 2.29 local EPS 5, one is in parallel with the entire DER system. The supplemental DER device is allowing the DER unit itself to meet the new 1547 standard at the POC in local EPS 4 whereas the supplemental device is helping the DER system meet the 1547 standard at the PCC. The point of where the standard physically applies (the POC or PCC) is defined in the standard by a decision tree as described within appendix C For a majority of small scale low-voltage network DER applications, the standard applies at the PoC.

The major discussion point of the new IEEE 1547-2018 revision is the introduction of new mandatory abnormal event ride through and voltage regulation capabilities. The requirement is defined by technology-neutral performance categories that are determined by the authority governing interconnection requirements (AGIR). The AGIR can be a regional reliability coordinator that maintains real-time operating reliability of BPS within a reliability coordinator area. The AGIR is to determine the applicability of the categories to the type of the DER resource due to their impact on frequency and voltage performance of the interconnections and the variability of regional power system. It is therefore the responsibility of the AGIR to quantify impactful DER penetration levels and assign the categories accordingly. These categories are split into regulation (categories A & B) and ride-through categories (I, II & III), as depicted in figure 2.30.

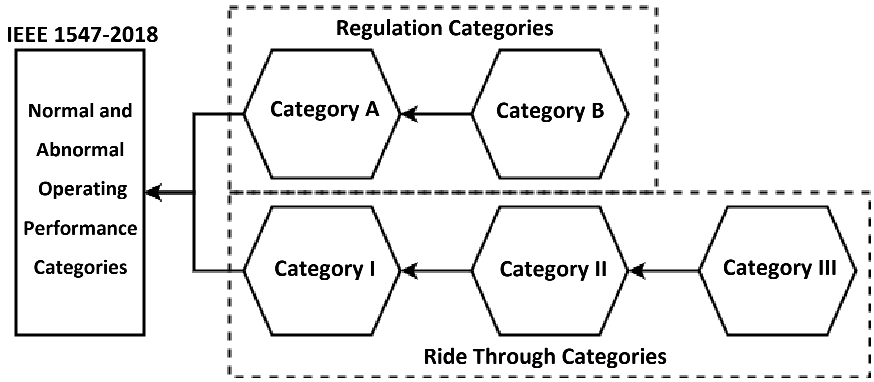

Figure 2.30: IEEE 1547-2018 Performance Categories [1]

2.4.2 IEEE-1547-2018 Abnormal Response and Ride-Through Requirements

Bulk power system operators have concerns regarding reliability issues within the BPS due to aggregate DER that continue tripping at voltage and frequency values that are close to nominal. The IEEE 1547-2003 voltage and frequency tripping specifications can lead to massive losses in DER generation that can create BPS abnormal events. For example, transmission faults can depress voltage over a very large area that and potentially trip large amounts of DER's which would lead to cascading effects in the bulk system, where the frequency and voltage would further deviate from the desired values. As system frequency is common across the entire interconnection and is affected by the balance between load and generation, any loss of DER has an impact on the system frequency unless other resources are sufficient to restore balance. If not, the frequency will deviate further. This will happen whether the DER is on a high-penetration feeder or not. When analyzing frequency behavior, what counts is the regional aggregate capacity of DER and not only the aggregate capacity on the feeder. In order to obtain a balance between protection and security of the BPS, IEEE 1547-2018 mandates both over voltage (OV), under voltage (UV) and frequency tripping requirements and ride-through capabilities.

These capabilities are split into three different categories as summarized in Table 2.4. Categories I, II and III are designed to address the "big picture need" on the bulk power system side and specify voltage and frequency ride through capabilities. These categories are specified by the AGIR because they are intended for, and have implications on, the bulk system. In addition to this, the standard specifies ranges of allowable settings as well as default parameters which are considered as sufficient or “cause no harm” values. These values are similar to that specified by the 2003 standard but if one were to really exploit the benefits of the new revision it is then desirable to adjust the control parameters of some of the functions to meet the utility’s specific needs. Category I just meets the essential bulk system needs but still mandatory none the less. Category II is the preferred option, because it is fully coordinated with the bulk power system needs. Category III goes beyond category II by not only contributing to the bulk system but also enabling areas of very high penetration distribution systems to help with power quality measures. IEEE 1547-2018 provides a series of tables which defines the ranges of shall trip allowable settings for abnormal over voltage (OV), undervoltage (UV) and frequency ride-through capabilities for the DER. These allowable settings are best depicted by figures 2.31-2.34. Operation outside of the defined continuous operation regions demonstrated within figures 2.31-2.34 is deemed as an abnormal operating region/condition in which the abnormal operating performance category would apply.

Category	Objective
I	Abnormal operating performance Category I is based on essential bulk power system (BPS) stability/reliability needs and reasonably attainable by all DER technologies that are in common usage today.
II	Abnormal operating performance Category II covers all BPS stability/reliability needs and is coordinated with existing reliability standards to avoid tripping for a wider range of disturbances of concern to BPS stability.
III	Abnormal operating performance Category III is based on both BPS stability/reliability and distribution system reliability/power quality needs and is coordinated with existing interconnection requirements for very high DER penetration.

Table 2.4: Performance Categories for Response to Area EPS Abnormal Conditions

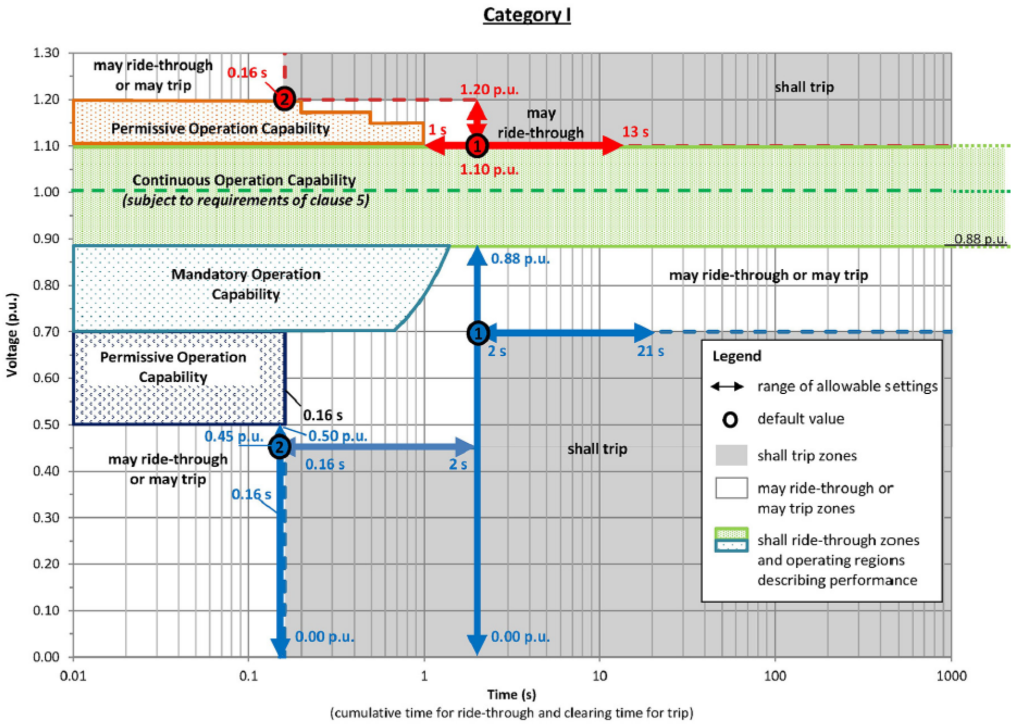

Figure 2.31: IEEE 1547-2018 Category I Voltage Ride Through Requirement [1]

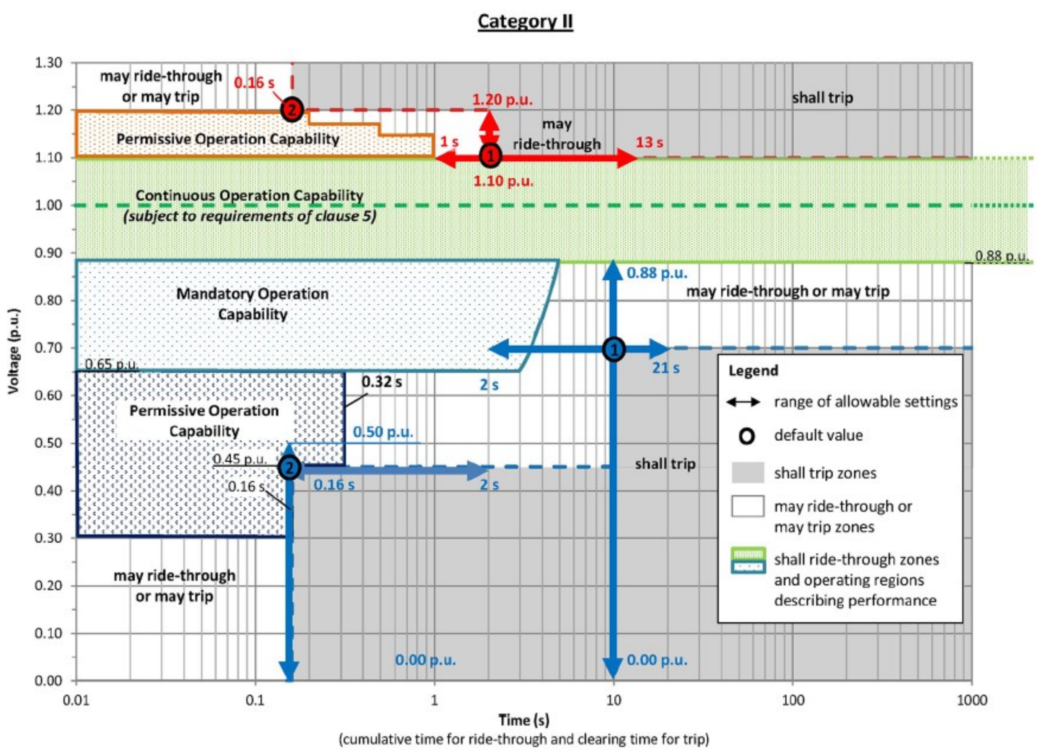

Figure 2.32: IEEE 1547-2018 Category II Voltage Ride Through Requirement [1]

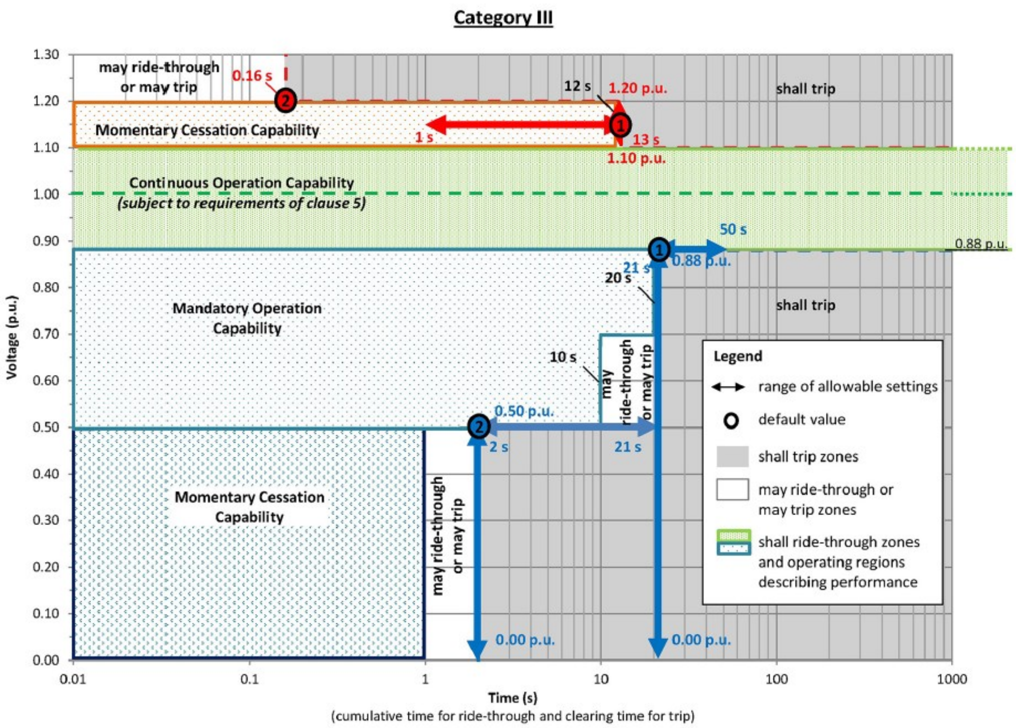

Figure 2.33: IEEE 1547-2018 Category III Voltage Ride Through Requirement [1]

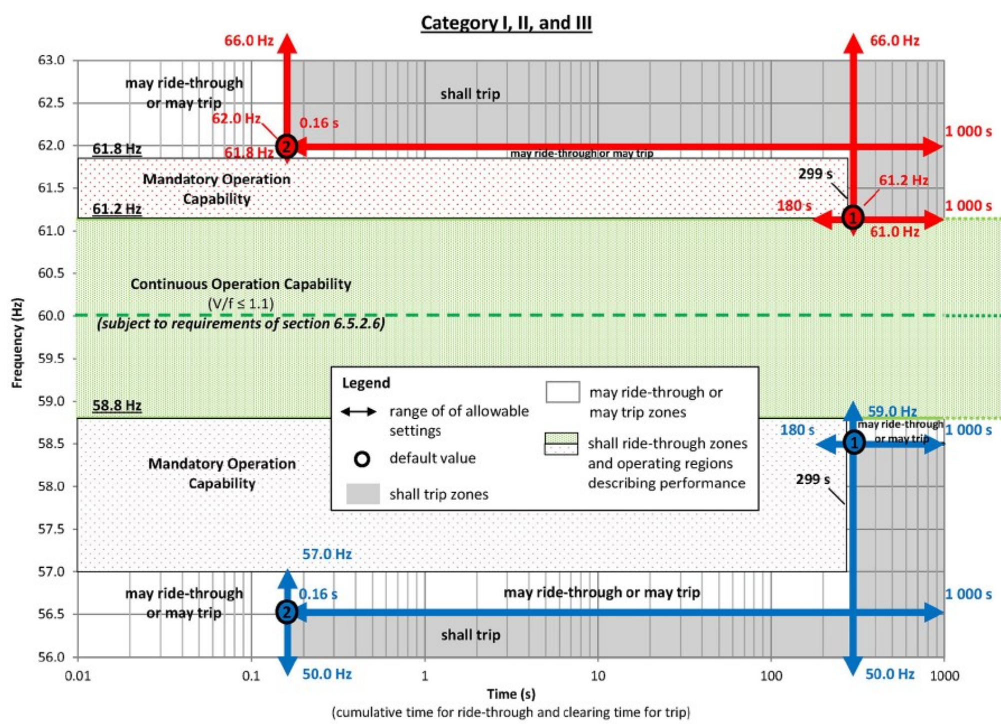

Figure 2.34: IEEE 1547-2018 Category I, II, & III Frequency Ride-Through Requirement [1]

These categories provide disturbance performance terminology which describe how the DER will respond under certain conditions. These figures highlight that permissive operation is required leading to either mandatory operation or momentary cessation. Mandatory operation permits the DER to provide active and reactive current delivery. Momentary cessation is the cessation of energization after disturbance when the evolution of voltage or frequency throughout the defined range establishes whether the DER either cease to energize or restores output to normal. Comparing the categories, we see that the higher the category number the longer and deeper the voltage ride through capability. Categories I and II have sections that provide permissive operation and these are settings that can be adjusted in order to coordinate with existing distribution system. Category III provides the momentary cessation ranges. An important aspect worth mentioning with voltage ride through capability is that the DER must restore output to 80% of pre-disturbance active current within 0.4s. The frequency ride through is similar to the voltage ride through capabilities but the same specification applies to all three categories. The standard allows for a wide range of must-trip settings to accommodate small, isolated grids. These are to be determined at the AGIR's discretion.

These new capabilities give DER considerable flexibility to better support the BPS as DER penetration grows. Furthermore, a mandatory frequency-droop operation is defined to allow the DER to contribute to the local EPS and/or BPS stability. This frequency droop is defined with respect to active power output from the pre-disturbance levels and is based on a frequency excursion beyond a specified droop dead band region defined in table 2.6. Here, *db* stands for dead band, *OF and UF* represent over and under frequency respectively and k_{UF} and k_{OF} represent the droop gains for over and under frequency, respectively. An example implementation of such droop curve is illustrated in figure 2.35. The frequency droop settings defined in table 2.5 are based upon active power injection and will need to be adjusted for low-voltage networks that have transmission lines which exhibit the *f-VAR* relationship as in this study.

Parameter	Default Settings			Ranges of Allowable Settings		
	Category I	**Category II**	**Category III**	**Category I**	**Category II**	**Category III**
db_{OF}, db_{UF} (Hz)	0.036	0.036	0.036	0.017-1.0	0.017-1.0	0.017-1.0
k_{OF}, k_{UF}	0.05	0.05	0.05	0.03-0.05	0.03-0.05	0.02-0.05
$T_{response}$ (s)	5	5	5	1-10	1-10	0.2-10

Table 2.5: IEEE 1547-2018 frequency-droop (frequency-power) parameters [1]

Operation for low-frequency conditions	Operation for high-frequency conditions
$p = \min\limits_{f<60-db_{UF}} \left\{ p_{pre} + \frac{(60 - db_{UF}) - f}{60k_{UF}};\ p_{avl} \right\}$	$p = \max\limits_{f<60+db_{OF}} \left\{ p_{pre} + \frac{f - (60 + db_{OF})}{60k_{OF}};\ p_{min} \right\}$

Table 2.6: IEEE 1547-2018 frequency-droop (frequency-power) operation [X]

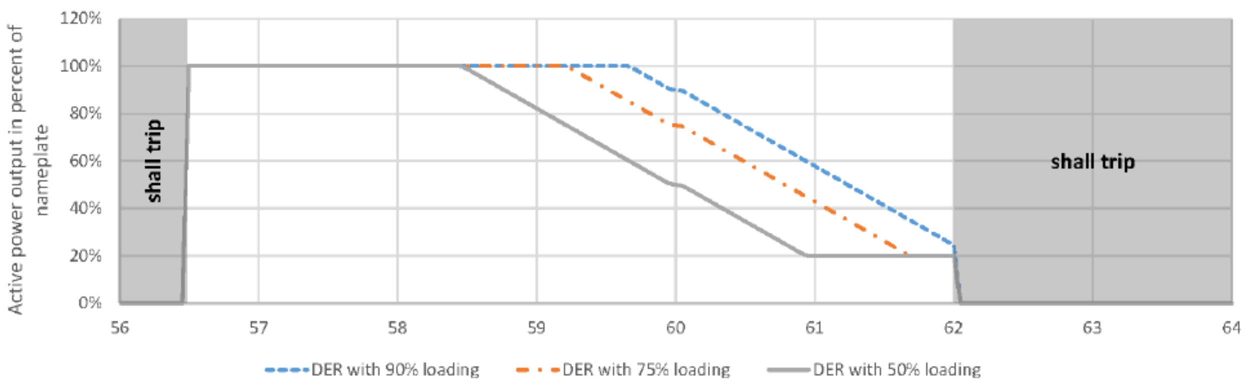

Figure 2.35: Example of Frequency Droop Functionality According to Table 2.5 [1]

This section has described why these ride-through capabilities are needed and what corresponding issues are addressed. Category III provides the highest level of flexibility needed to support the entire BPS system operation as well as the capability of local EPS support and power quality. For a low-voltage network with the capability of disconnecting from the BPS and operating independently, all DER sources should adhere to Category III for the longer ride through capabilities to support such a volatile network. We will consider a Category III dynamic analysis for this thesis.

2.4.3 IEEE 1547-2018 Voltage and Frequency Regulation Specifications

Another important feature in the latest revision in the standard is that the DER "shall be capable" of regulating voltage and frequency. In earlier versions of the standard, it was originally specified as "shall not", but in the 1547-2014 revision it was updated to "may be able". In the 2018 revision, the default settings of the DER are to be set at the do no harm values but it is at the utilities discretion to specify the regulation settings and capabilities to fully exploit the benefits of the DER unit/system. With this being said the newest revision does not define regulation capability but rather defines regulation functionality. Stressing again that the capabilities are determined by the utility as the impact is more on a local level.

The previous section specified DER voltage and frequency ride through capabilities and the reasons for doing so, describing how DER should ride through abnormalities and assist the BPS stability instead of aggravating it. Voltage and frequency regulation capabilities can increase the robustness of the area EPS and further assist the BPS to some extent. For example, if the voltage is beginning to fall or rise above the ANSI limits the DER unit can detect this and inject or absorb reactive VAR's and therefore contributing to local level voltage stability. If the frequency were to deviate from these the DER unit/system could inject more active watts to help increase system frequency stability. If aggregate amounts of DER systems on the local level were all to do the same, it may have a significant impact on BPS frequency stability. The IEEE 1547-2018 revision specifies how the DER should go about contributing active or reactive power during certain ride through areas.

The newest revision divides the functionalities into two categories, shown in table 2.7. Category A covers minimum performance capabilities needed for Area EPS voltage regulation and are reasonably attainable by all DER technologies. Category B covers ALL requirements within Category A and specifies supplemental capabilities needed to adequately integrate DER's in local Area EPS's where the aggregated DER penetration is higher or where the overall DER power output is subject to large frequency variations. Due to the new regulation capabilities having a more prominent effect within the local power network, the local area EPS operator are to specify to which category the DER belongs. Furthermore, the regulation requirements mainly apply to the continuous operation region (demonstrated within figures 33-35) when the voltage is between 0.88 and 1.1 times the nominal voltage level, V_N. The local area EPS can define further requirements for regulation beyond the continuous operation region of the DER to facilitate the stability of the network.

DER Category	Category A	Category B
Voltage regulation by reactive power control		
Constant power factor	Mandatory	Mandatory
Voltage – reactive power mode	Mandatory	Mandatory
Active power- reactive power mode	Not required	Mandatory
Constant reactive power mode	Mandatory	Mandatory
Voltage and active power control		
Voltage – active power (volt-watt) mode	Not required	Mandatory

Table 2.7: IEEE 1547-2018 DER Required Regulation Capabilities [1]

Hosting capacity is an important benefit of the new regulation capabilities as it ultimately can increase in DER. Hosting capacity is a methodology that aims at determining the amount of DER capacity that you can integrate at any given point in any given distribution system. There are many factors that impact hosting capacity which include feeder design and operation, DER location and DER technology. If one were to use advanced DER technology like advanced inverters with voltage-reactive power control capabilities, then the hosting capacity could be increased regardless of feeder and location.

Hosting capacity may be increased as follows. If an inverter is operating with a constant power factor, then it is injecting only active power into the area EPS. If the amount of DER penetration was to increase on the feeder, then the active power injection could become high enough to cause the voltage to exceed the specified ANSI voltage limits hence limiting the capacity and possibly driving the DER to disconnect. If advanced inverters were employed, they could then inject reactive power in the system bringing down the voltage and therefore increasing the hosting capacity. Figures 2.36 and 2.37 specify the minimum reactive power capabilities for DER units that adhere to the IEEE 1547-2018 standard for categories A and B, respectively. Category B allows for the most regulation flexibility within their settings. Due to the power flow characteristics of a low-voltage transmission line, the DER under study must be classified as category B. The DER can then employ our proposed *V-W* droop curve, defined by equation (2.25) and presented in figure 2.38, with droop settings that must then adhere to table 2.8.

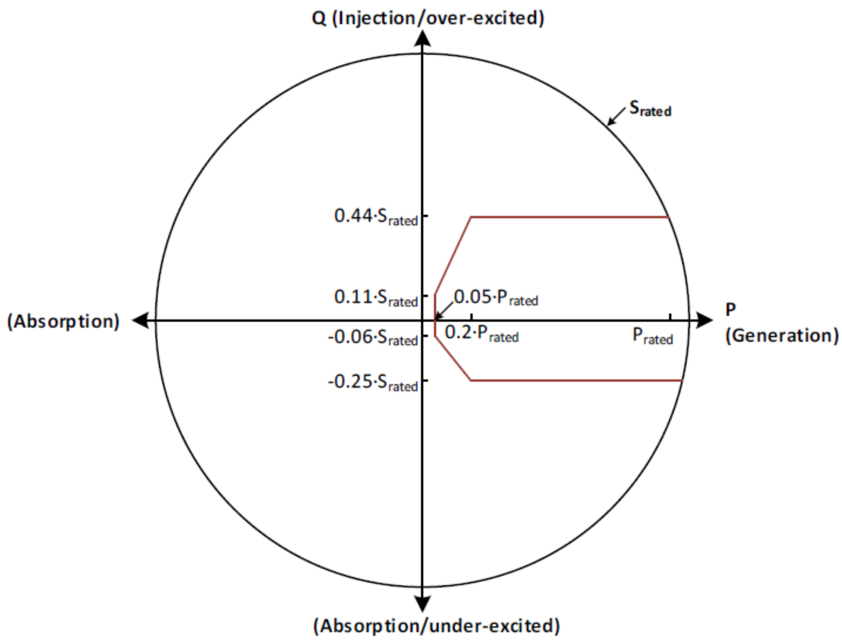

Figure 2.36: Category A Minimum Reactive Power Injection Capability [1]

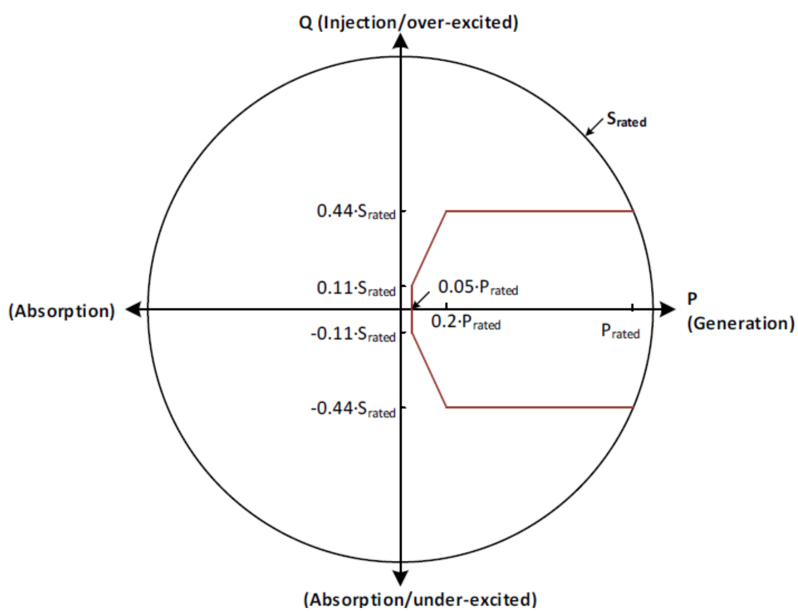

Figure 2.37: Category B Minimum Reactive Power Injection Capability [1]

Voltage-active Power Parameters	Default Settings	Range of Allowable Settings	
		Minimum	Maximum
$\boldsymbol{V_1}$	$1.06V_N$	$1.05V_N$	$1.09V_N$
$\boldsymbol{P_2}$	P_{rated}	N/A	N/A
$\boldsymbol{V_2}$	$1.1V_N$	$V_1 + 0.01V_N$	$1.10V_N$
$\boldsymbol{P_2}$ *(Applicable to DER that can only generate active power)*	The lesser of $0.2P_{rated}$ or P_{min}	P_{min}	P_{rated}
$\boldsymbol{P_2}'$ *(Applicable to DER that can generate and absorb active power)*	0	0	P_{rated}'
Open Loop Response Time	10s	0.5s	60s

Table 2.8: IEEE 1547-2018 Voltage-Active Power Mode [1]

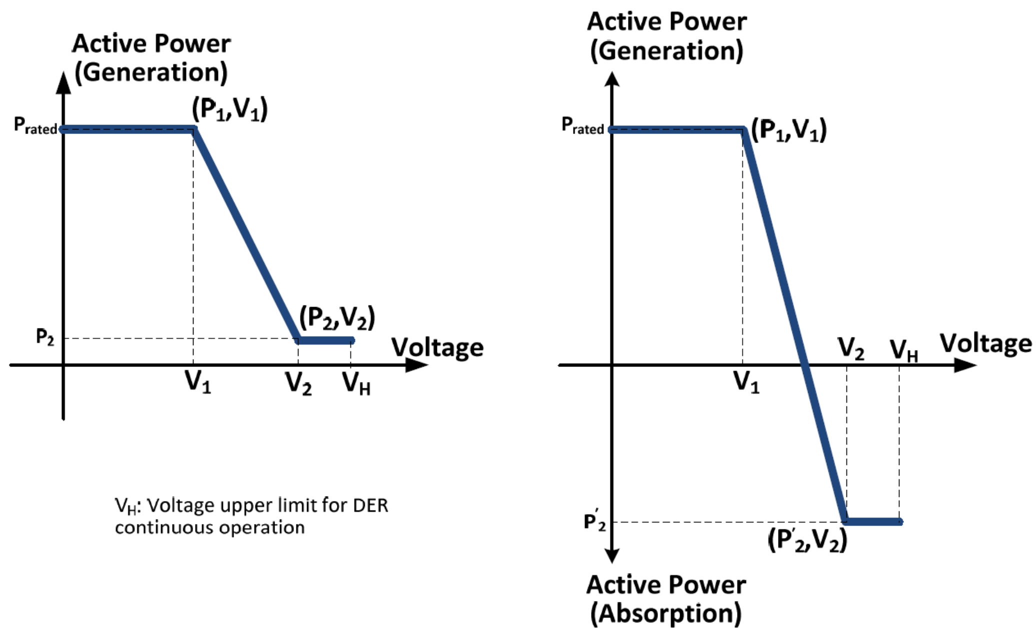

Figure 2.38: IEEE 1547-2018 Voltage-Active Power Suggested Droop Curve Example [1]

In summary, the ideal settings for grid-edge DER within a high penetration low-voltage neighborhood are: 1) category III, abnormal response and ride-through requirements and; 2) category B, voltage and frequency regulation capabilities. We have seen in the previous section that the standard provides an active power frequency droop setting, which the DER must adhere. However, these settings don't apply for prosumers that are located at the grid-edge due to the inherent power flow properties of the resistive dominant line-impedance. Therefore, we must re-apply this context in the terms of reactive power capabilities of the DER unit according to the category B regulation capabilities. This will be addressed in the network dynamic analysis setup in Chapter 3.

CHAPTER 3: Low-Voltage Network Modelling

Chapter 3 will now consider the control dynamics that are associated with prosumers interfacing with the low-voltage network to build on the discussion in Chapter 2, where the latest revision of the interconnection standard and the guiding principles that define allowable limits of operation and flexibility were presented. It is apparent that due to the resistive properties of the inverter output impedance coupled with the feeder line, the droop equations and dynamics differ from those of medium to high voltage DER applications. Furthermore, it is critical in low-voltage networks to adopt the proportional droop control methodology in order to improve the voltage profile of the network and to maintain operation within the defined limits. A low-voltage network is defined as an interconnect operating at 1kV or less. Chapter 3 lays out the ground work for a high penetration low-voltage network dynamic analysis. The dynamics of interconnected prosumers are defined along with loads. Figure 3.1 provides a general schema for the low-voltage network under consideration, a low-density suburban neighborhood of homes with PV generation (shown here as roof-top); utilization transformers connect the primary and secondary distribution feeders.

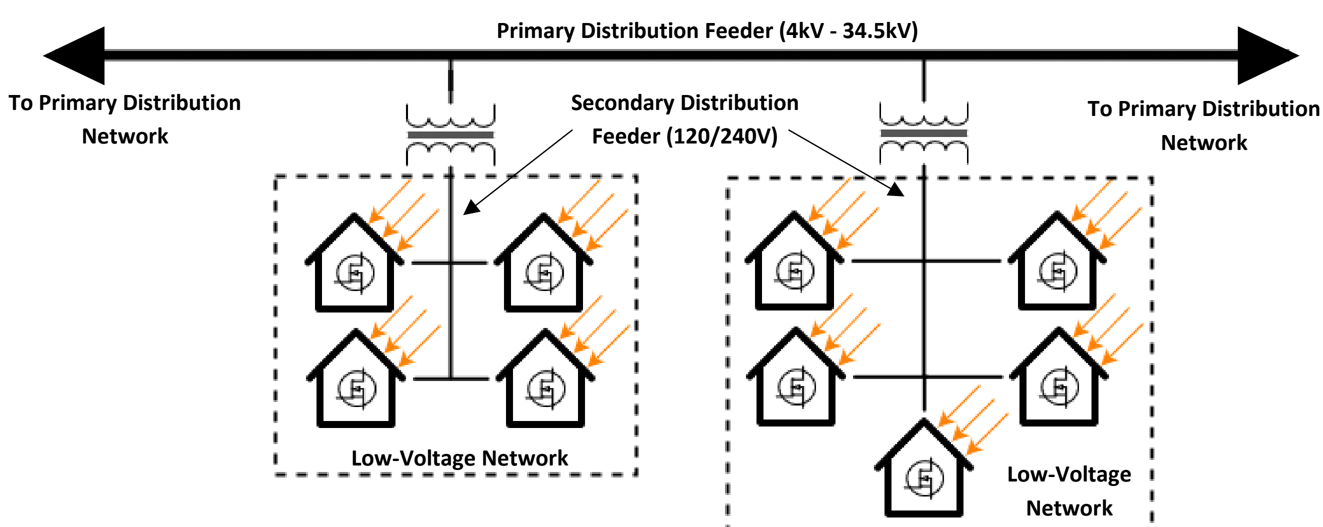

Figure 3.1: Grid Edge Low-Voltage Network Consisting of Prosumers

3.1 Low-Voltage Network Modelling

The objective of this chapter is to effectively model a neighborhood of highly interacting interconnected homes at the grid edge, illustrated by the dashed boxes in figure 3.1. Primary distribution network topologies can vary depending on country and location; urban, suburban or rural. These topologies can be either radial, loop and grid type. In rural and suburban areas in Canada, it is common to see a primary distribution system similar to that demonstrated in Appendix B. The primary distribution system consists of a feeder branching out from the substation to reach the end consumer. This primary distribution system generally consists of three components: feeder, trunk and branch [31]. Depending on geographical location and planned loads on the feeder, the primary distribution voltage level may vary between 4kV to 34.5kV and are typically three-phase. For residential end consumers, it is common to see a single-phase tap (branch or trunk) off one of the three-phases to supply a single resident or a residential neighborhood of 100 homes or less. To service the end consumer, a secondary distribution transformer steps down the voltage to the utilization voltage level and is connected to the customer service entrance. This secondary distribution system is a low-voltage network typically feeding 1-5 or more homes in a rural and suburban setting. It is common to see higher PV penetration in suburban and rural areas which contain the aforementioned combined low and high voltage single-phase feeders.

The scope of studies within this thesis will be kept to a single low-voltage network of prosumers. The model chosen is a low-voltage suburban neighborhood of 4 homes demonstrated in the leftmost dashed box in figure 3.1. This low-voltage microgrid mesh topology is selected as it allows for the greatest load, generation and interconnection diversity to be studied. The four-node mesh shown in figure 3.2 allows a comprehensive annotation, but any number of nodes may be considered in the simulation. For this study, the rooftop PV generation and the loads are aggregated at the distribution panel and are denoted as bus B_k in figure 3.2.

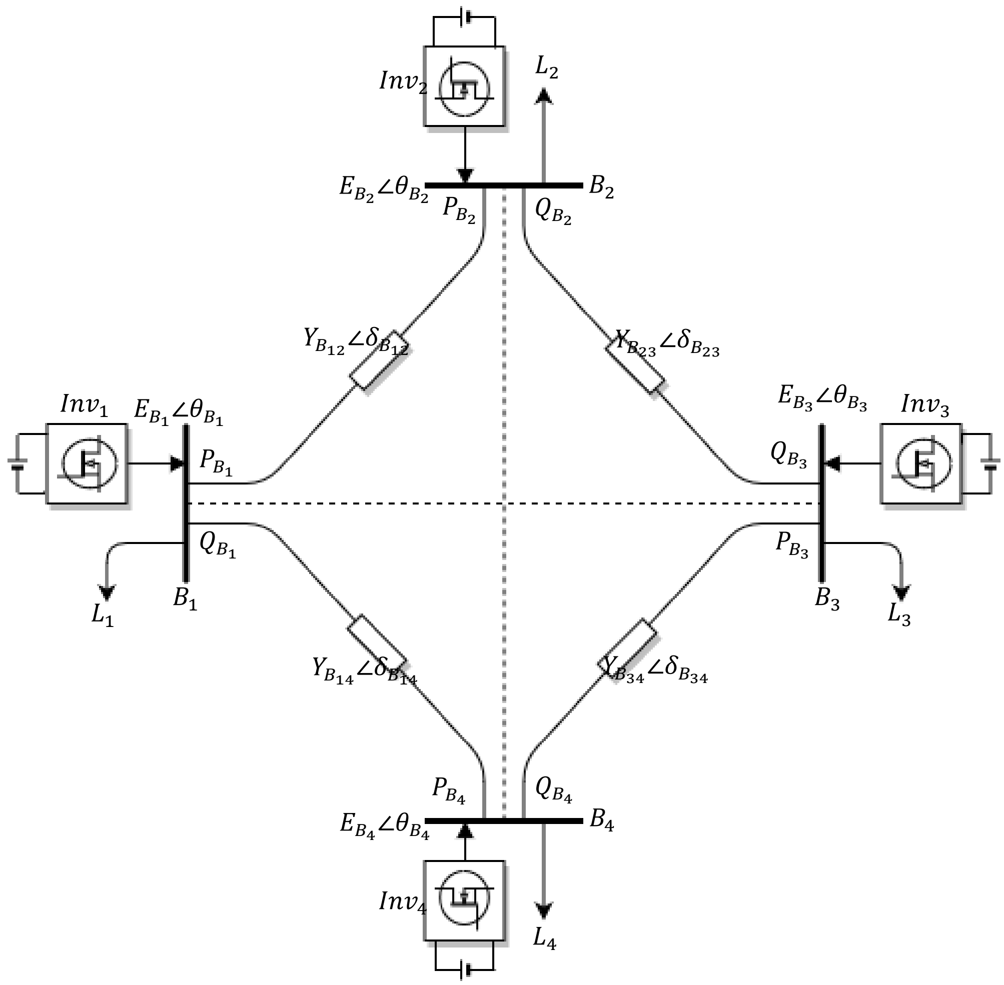

Figure 3.2: Grid-Edge Low Voltage Network Model

For clarity, we use a label-index subscript convention in describing the various quantities of interest: labels will be in upper case and may be followed by an index subscript in lowercase. Thus, I_i refers to the i^{th} inverter while B_k refers to the k^{th} bus. For example, $(\cdot)_{I_i}$ refers to a quantity associated with the i^{th} inverter; $(\cdot)_{I_iB_k}$ denotes the multi-directional coupling between the i^{th} inverter and the k^{th} network bus; $(\cdot)_{I_i,B_k}$ is a directional representation and denotes the flow from the i^{th} inverter to the k^{th} network bus ; and $(\cdot)_{B_{kj}}$ is a nondirectional representation and represents coupling between busses *k* and *j.*

Similar to power flows from the inverter into the bus, as presented in the chapter 2, the power flows within the low-voltage network also depend on the voltage amplitudes and phases on their respective buses. The apparent power required from each bus within the network can be expressed as

$$S_{I_i,B_k} = \sum_{j=1}^{N} E_{B_k} E_{B_j} Y_{B_{kj}} e^{j\left(\theta_{B_k} - \theta_{B_j} + \delta_{B_{kj}}\right)}, \tag{3.1}$$

where the phasors $E_{B_k} e^{j\theta_{B_k}}$ and $E_{B_j} e^{j\theta_{B_j}}$ give the voltage magnitudes and angles at bus *k* and *j*, respectively, and $Y_{B_{kj}} e^{j\delta_{B_{kj}}}$ is the admittance of the secondary feeder transmission line between bus *k* and *j*. Applying a change of variable $\kappa_{kj} = E_{B_k} E_{B_j} Y_{B_{kj}}$ and the transfer of the $j = k$ term out of the sum allows (3.1) to be written as

$$S_{I_i,B_k} = E_{B_k}{}^2 \sum_{j=1}^{N} Y_{B_{kj}} e^{j\delta_{B_{kj}}} - \sum_{\substack{j=1 \\ j \neq k}}^{N} \kappa_{kj} e^{j\left(\theta_{B_k} - \theta_{B_j} + \delta_{B_{kj}}\right)}, \tag{3.2}$$

where the apparent power injection depends on the driving-point admittance of bus *k*, denoted by $Y_{B_{kj}} e^{-j\delta_{B_{kj}}}$ [2]. The driving-point admittance is the sum of all admittances at bus *k*, that is, arising from the local loads and the connected line admittances. The transfer admittance between buses *k* and *j,* given by $Y_{B_{kj}} e^{j\left(\theta_{B_k} - \theta_{B_j} - \delta_{B_{kj}}\right)}$, may be conceptualized as the power flow between these busses. The power injection at bus *k* from the *i^th^* inverter can be given in terms of active and reactive power as

$$P_{I_i,B_k} = \sum_{j=1}^{N} \kappa_{kj} \cos(\theta_{B_k} - \theta_{B_j} + \delta_{B_{kj}}), \tag{3.3}$$

$$Q_{I_i,B_k} = -\sum_{j=1}^{N} \kappa_{kj} \sin\left(\theta_{B_k} - \theta_{B_j} + \delta_{B_{kj}}\right). \tag{3.4}$$

As the phase dynamics of a low voltage network are correlated with the reactive power, the phase dynamics of the i^{th} inverter under resistive dominated coupling may be described by (3.4) in (2.26) as

$$\frac{d\theta_{I_i}}{dt} = \omega_{I_i}{}^* + n_{I_i}\sum_{j=1}^{N} \kappa_{kj} \sin\left(\theta_{B_k} - \theta_{B_j} + \delta_{B_{kj}}\right), \tag{3.5}$$

and the voltage dynamics by (3.3) in (2.30) as

$$\tau_{I_i}\frac{dE_{I_i}}{dt} = K_{I_E}(E_{I_i}{}^* - E_{B_k}) - m_I\left[P_{I_{nom}} - \sum_{j=1}^{N} \kappa_{kj} \cos\left(\theta_{B_k} - \theta_{B_j} + \delta_{B_{kj}}\right)\right]. \tag{3.6}$$

Note that (3.5) and (3.6) assume a static shunt admittance load at each individual bus and is encapsulated within $\tilde{Y}_{B_{kk}}$ term. In order to properly analyze the dynamics within a low-voltage network, more fitting load models are needed with a re-defined driving point admittance term. These will be defined in section 3.3.

The premise of the bus voltage dynamics being governed by equation (3.6) is that the inner voltage control loops are operating on much faster time scale with respect to the droop control loop. Time constants for inner control loops are much smaller than those of the droop control loops. This can be further described by the active and reactive power flow measurement which is performed using a low-pass filter performing a running average. Therefore, the inner and outer control loops within the inverter are considered decoupled and the governing dynamics of the inverter interaction with the low-voltage network are governed by (3.5) and (3.6). This assumption will be carried through the remainder of this thesis in study of interaction between coupled inverters within a network.

Furthermore, the governing dynamics of (3.5) uncover unique phenomena within coupled oscillators and collective synchronization. Thus, allowing us to build further intuition into the interaction of homes within a low-voltage network and broaden the perspective of inverter control design to the local network level scope.

3.2 Coupled Oscillators

A network of coupled inverters employing droop control exhibits unique dynamic behavior. It inherently shows that the frequency dynamics of coupled droop-controlled inverters naturally exhibit the properties of a Kuramoto model [32]. The Kuramoto model was developed to model the phenomenon of collective synchronization of individual oscillators with uniformly distributed natural frequencies around a similar limit cycle. For any system of weakly coupled oscillators, the long-term dynamics are governed by [33].

$$\frac{d\theta_i}{dt} = \omega_i + \sum_{j=1}^{N} \alpha_{ij}(\theta_i - \theta_j)\,. \tag{3.7}$$

Systems with purely sinusoidal coupling can be represented by

$$\frac{d\theta_i}{dt} = \omega_i + \sum_{j=1}^{N} \kappa_{ij}\sin(\theta_i - \theta_j)\ , \tag{3.8}$$

where θ_i is phase angle of oscillator *i* with respect to a stationary reference frame, ω_i is the natural frequency of the oscillator, $\kappa_{ij} \geq 0$ is the coupling gain between oscillators *i* and *j*, and $\sin(\theta_i - \theta_j)$ is the phase interaction function. The system is incoherent until coupling gain $\kappa_{ij} > \kappa_{critical}$ whence the system then becomes synchronous. Properties of such coupling gain are demonstrated in figure 3.3. The significance of this model will now be described with respect to a microgrid network.

Equation (3.5) demonstrates that reactive power flows under the resistive coupling impedance assumption very much resemble the Kuramoto model, as shown in (3.8). Further insight into the Kuramoto model can be developed by writing (3.5) as

$$\frac{d\theta_{I_i}}{dt} = \omega_{I_n} + n_{I_i}\sum_{\substack{j=1 \\ j\neq k}}^{N} \kappa_{kj}\sin\left(\theta_{B_k} - \theta_{B_j} + \delta_{B_{kj}}\right), \tag{3.9}$$

where the natural frequency of the *i^th^* inverter $\omega_{n,i} = \omega_{I_i}^{*} + n_{I_i} E_{B_k}^{2} Y_{B_{kk}} \sin(\delta_{B_{kk}})$ of each inverter (oscillator) depends on the ability for the DER to meet the local demand. This natural frequency is further influenced by the demand/supply required from the network itself which is determined by the network coupling $\kappa_{kj} \sin\left(\theta_{B_k} - \theta_{B_j} - \delta_{B_{kj}}\right)$. The coupling strength, ($\kappa_{kj} = E_{B_k} E_{B_j} Y_{B_{kj}}$ and frequency droop n_{I_i}) between oscillators is characterized by the voltage and coupling impedance magnitudes of the bus along with the droop gains of the inverters within the network. Thus, demonstrating the impact of tuning the droop gain parameters of the inverters within the network. The sinusoidal phase interaction between inverters is further influenced by structure of the network and coupling cable selection of the feeder which will introduces a phase error constant of $\delta_{B_{kj}}$.

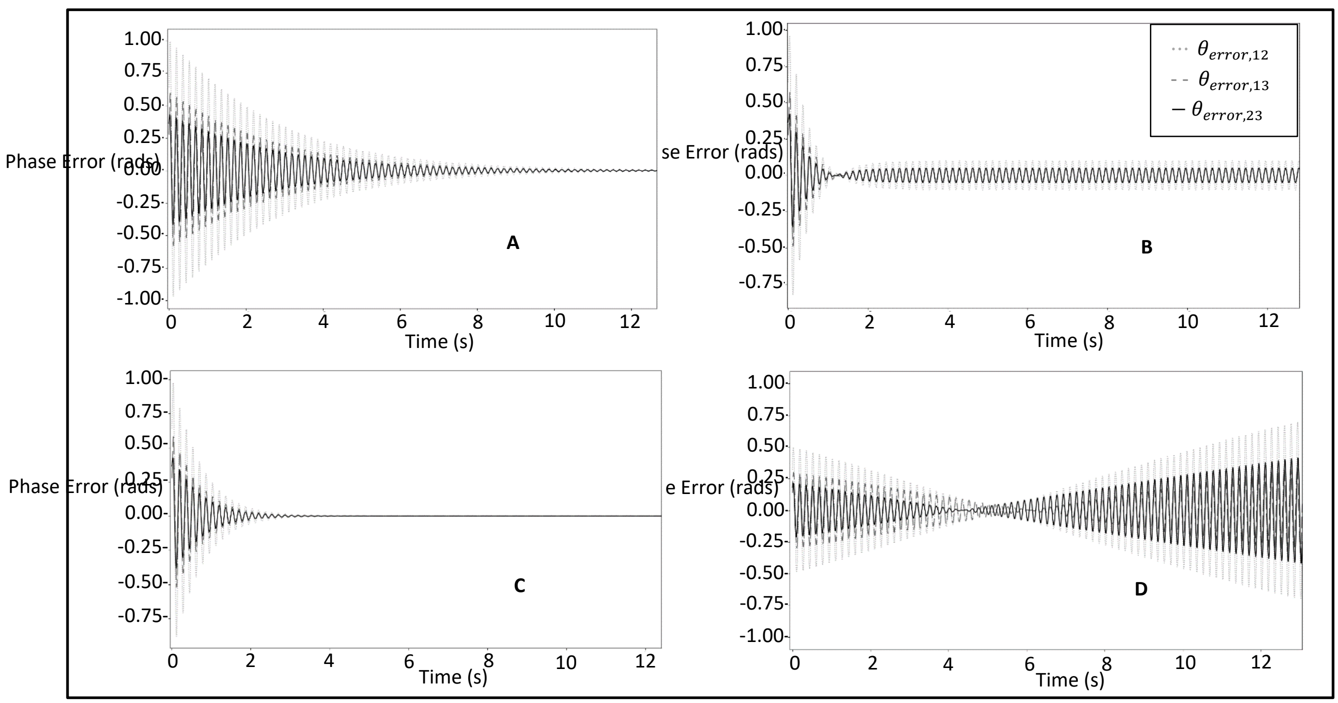

Figure 3.3: The Kuramoto Model Synchronization with Varying Coupling Strength. A: Phase & frequency lock between three oscillators with no phase error and large settling time; B: Phase & frequency lock between three oscillators with phase error with improved settling time; C: Phase & frequency lock between three oscillators with zero phase error and improved settling time; D: Unstable case of oscillator network, no phase lock.

As aforementioned, the droop gain of the inverter, coupling impedance and voltage magnitude play an important role in the coupling strength, synchronization and therefore the stability of the network. Figure 3.3 best highlights this effect of coupling strength using a system of three coupled oscillators. The four plots depicted in figure 3.3 represent the instantaneous phase error (phase angle difference) between three different oscillators that have initial randomly distributed phases in radians. The natural frequency of the oscillators is between 375-380radians/s. The coupled oscillators in figure 3.3 are represented by equation (3.8) where a uniform coupling strength $\kappa_{ij} = \kappa$ is used. Figures 3.3A&C represent $\kappa > \kappa_{critical}$ where the coupled oscillators successfully synchronize and the coupling strength is sufficient enough to drive the phase error to zero amongst oscillators within the system. Figure3.3B represents a weakly coupled system in which $\kappa > \kappa_{critical}$ and frequency entrainment amongst oscillators occur but a constant phase error amongst oscillators exists. Finally, Figure3.3D represents and instable system of coupled oscillators where $\kappa < \kappa_{critical}$ and frequency and phase entrainment does not occur; each oscillator influences one another and frequency grows beyond their natural frequency. These effects will be referenced in context with a low-voltage network and will be studied in chapter 4.

3.3 Low-Voltage Network Load Modelling

Now that we understand the generation dynamics associated with the individual buses of the network, a detailed discussion is needed regarding the necessary load models for low-voltage networks. As previously mentioned, the generation capacity is small and a first order system has low inertia. Therefore, the network is extremely sensitive to the type of loading. It is important to model the loads appropriately to enable realistic analyses of high-penetration neighborhoods. Residential loads, which vary widely, will be the primary concern of this thesis. Figure 3.4 details the variety of load modelling techniques that are used in power systems today. They are broadly categorized into four different classes: (1) static; (2) dynamic; (3) composite; and (4) ANN-based. The specific model implementations are generated based via statistical or heuristic techniques [34]. Load models which model load active and reactive power consumption as a function of voltage and frequency will be highlighted here. The load power voltage and frequency model dependence are required to effectively integrate the load models with the inverter droop control model. The load models described within this section are used in low-voltage network study and demonstrate this dependence.

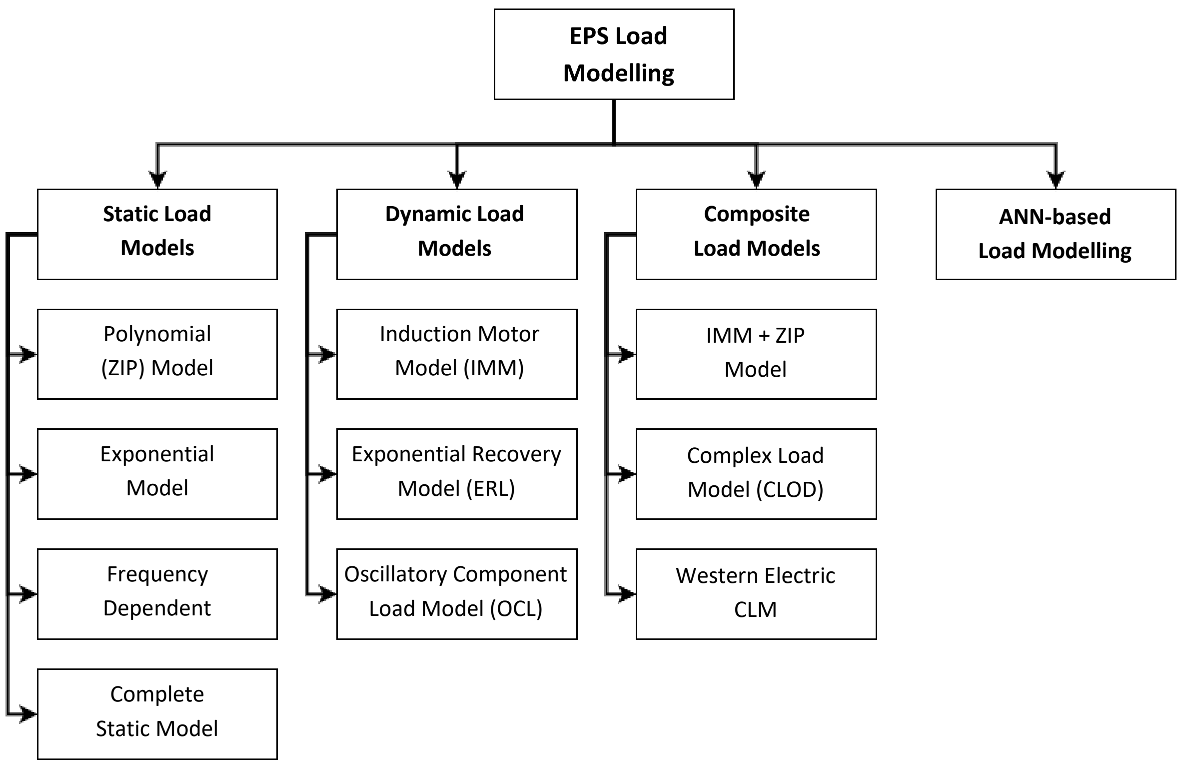

Figure 3.4: Electric Power System Load Model Types [34]

3.2.1 Static Load Models

As shown in figure 3.4, there are four different types of static load models. These are used in both static and dynamic analyses and represent the dependence of the loads on the bus voltage and system frequency. Each are described below.

3.2.1.1 Polynomial (ZIP) Load Model

The polynomial, or ZIP, load model is the simplest of the models and assumes either a constant impedance (Z), current (I) or power demand (P). At a high-level, the constant power model is voltage invariant and allows loads with a stiff voltage characteristic to be represented but it is not appropriate for dynamic analysis for this reason. The constant current model gives a load demand that changes linearly with voltage and is adequate to represent real power demand of resistive loads and mixed motor devices. A constant impedance load, models the load power to the square of the voltage which is representative of some lighting models but does not accurately represent stiff loads. The ZIP polynomial model combines all three load characteristics into one model to obtain a more general voltage characteristic. This consists of weighted sums of the constant impedance, current and power terms such as [2]:

$$P_L = P_0 - \left[a_1 \left(\frac{V}{V_0}\right)^2 + a_2 \left(\frac{V}{V_0}\right) + a_3\right] \tag{3.10}$$

$$Q_L = Q_0 - \left[a_4 \left(\frac{V}{V_0}\right)^2 + a_5 \left(\frac{V}{V_0}\right) + a_6\right] \tag{3.11}$$

where the terms P_0, Q_0 and V_0 are the values at the initial operating conditions (i.e., nominal operation pre-disturbance) and the polynomial parameters $(a_1 - a_6)$ are the model coefficients and the power factor of the load. The P_L and Q_L parameters are the consumed load powers as a function of the voltage and frequency.

3.2.1.2 Exponential Load Models

The exponential static load model represents an exponential power-voltage relationship as

$$P_L = P_0 \left(\frac{V}{V_0}\right)^{n_p} \tag{3.12}$$

$$Q_L = Q_0 \left(\frac{V}{V_0}\right)^{n_q}. \tag{3.13}$$

The parameters of the model are n_p and n_q. If they are set to 0, 1 or 2, the model approximates the constant power, current and impedance respectively.

The exponential load and ZIP load models do not effectively model the load when there is a significant bus voltage drop below 0.7 p.u [2]. In order to create a more effective representation, a piecewise approximation is used where the exponential or polynomial model is used for voltages close to the rated voltage and a constant impedance model is used for voltages below 0.3-0.7 per unit [2].

3.2.1.3 Frequency-Dependent Load Model

The polynomial and exponential load models discussed above depend on voltage only. However, active and reactive power are tied to system frequency. Therefore, we introduce this dependence by multiplying exponential or polynomial load models by a frequency dependent factor, $\left[1 + a_f(f - f_0)\right]$. The term f represents the actual system frequency, f_0 is the nominal (rated) frequency and a_f is the model frequency sensitivity parameter. Tying this frequency dependence with a voltage dependent load model $P(V)$ and $Q(V)$ give,

$$P_L = P(V)\left[1 + k_{pf}\frac{(\Delta f)}{f_0}\right] \tag{3.14}$$

$$Q_L = Q(V)\left[1 + k_{qf}\frac{(\Delta f)}{f_0}\right], \tag{3.15}$$

where k_{pf} and k_{qf} are the frequency sensitivity parameters, $\Delta f = f - f_0$. $P(V)$ and $Q(V)$ represent the voltage dependent load characteristic associated with the type of load where the ZIP model (3.10) and (3.11) or the exponential load model (3.12) and (3.13) can be used.

3.2.1.4 Complete Static Load Model (EPRI LOADSYN)

A more complete static load model can be created by combining the previous models. As recommended by the IEEE task force on load representation for dynamic performance [35] [36], this is given as

$$\frac{P_L}{P_{frac}P_0} = K_{pz}\left(\frac{V}{V_0}\right)^2 + K_{pi}\frac{V}{V_0} + K_{pc} + K_{p1}\left(\frac{V}{V_0}\right)^{n_{pv1}}\left[1 + k_{pf1}(\Delta f)\right] + K_{p2}\left(\frac{V}{V_0}\right)^{n_{pv2}}\left[1 + k_{pf2}(\Delta f)\right], \tag{3.16}$$

where,

$$K_{pz} = 1 - \left(K_{pi} + K_{pc} + K_{p1} + K_{p2}\right), \tag{3.17}$$

and P_{frac} is the fraction of the bus load represented by the static model [35] [36]. The complete reactive load model is similarly

$$\frac{Q_L}{Q_{frac}Q_0} = K_{qz}\left(\frac{V}{V_0}\right)^2 + K_{qi}\frac{V}{V_0} + K_{qc} + K_{q1}\left(\frac{V}{V_0}\right)^{n_{qv1}}\left[1 + k_{qf1}(\Delta f)\right] + K_{q2}\left(\frac{V}{V_0}\right)^{n_{qv2}}\left[1 + k_{qf2}(\Delta f)\right], \tag{3.18}$$

where

$$K_{qz} = 1 - \left(K_{qi} + K_{qc} + K_{q1} + K_{q2}\right) \tag{3.19}$$

and

$$Q_0 \neq 0. \tag{3.20}$$

3.2.2 Dynamic Load Models

Static load models ignore transients and their response to a voltage step change at the PCC can be treated as instantaneous [34]. Static load models have inherent limitations as they do not capture the inertial response and frequency recovery of motors. Dynamic load models are critical to accurately model power system behavior as their response is based on the previous state and current input. Without the use of dynamic load models, we cannot effectively study the inter-area oscillations that can lead to voltage and frequency stability issues in distribution networks. These oscillation effects are more prominent at the grid-edge due to the low-inertia generation sources and can lead to severe volatility within the low-voltage network. It is known that induction motor loads typically consume anywhere from 55 to 70% of the total energy supplied by a power system [2]. Therefore, the dynamics attributed to motor loads are the most significant aspects of dynamic characteristics of system loads. Here we describe the three dynamic load models referenced in figure 3.4.

3.2.2.1 Exponential Recovery Load Model (ERL)

The ERL model was developed to capture the real and reactive power response to a step change in voltage at the PCC. ERL attempts to model the behavior of induction motors and thermostat-controlled devices on the power system and are relatively accurate on the time scale of seconds. The behavior defined in [37]describes when the bus experiences a voltage step, the induction motor slips cannot change instantaneously so the aggregate load appears static. The load then recovers to a steady state level after a settling time of T_p has passed. Minutes after the disturbance, the voltage tap changers on transformers will then address any voltage level deviation and recover the system to the nominal operation point. This action is on the time scale of minutes and could lead voltage overshoot if certain loads were shed beforehand. The advantage to inverters operating with voltage regulation capabilities will allow the network to address these corrections on a much faster time scale compared to traditional distribution networks.

The general load model assumes an exponential recovery to a steady state value and is captured by the following differential equations,

$$T_P \frac{dx_P}{dt} + x_P = P_s(V) - P_T(V) \tag{3.21}$$

$$P_L = x_P + P_T(V) \tag{3.22}$$

$$T_Q \frac{dx_Q}{dt} + x_Q = Q_s(V) - Q_T(V) \tag{3.23}$$

$$Q_L = x_Q + Q_T(V) \tag{3.24}$$

The generic form for the ERL is of $T_P \frac{dx_P}{dt} + x_P = N(V)$ where $N(V) = P_s(V) - P_T(V)$. The function $P_s(V)$ is an exponential static load function and could have the form of those mentioned within section *3.2.1*. $P_T(V)$ defines fast transient changes in the load and is the dynamic load response. Typically, $P_s(V) =$

$P_0\left(\frac{V}{V_0}\right)^{\alpha_s}$ and $P_T(V) = P_0\left(\frac{V}{V_0}\right)^{\alpha_T}$. The notation is similar for reactive power. The remaining parameters of the ERL model may generally be described as follows: $(\cdot)_L$ depicts active/reactive power response; $x_{(\cdot)}$ represents active/reactive power recovery state variable and; $T_{(\cdot)}$ denotes the load recovery time constant. The decomposition of the ERL response of equations (3.21) and (3.22) are demonstrated in figure 3.5. Detailed information about the ERL model and its derivation are found in [36] [37] [38]. The ERL model has the inherent drawback of being a first order system (thus neglecting oscillations) and being uncorrelated with system frequency. The following two dynamic models will address such issues.

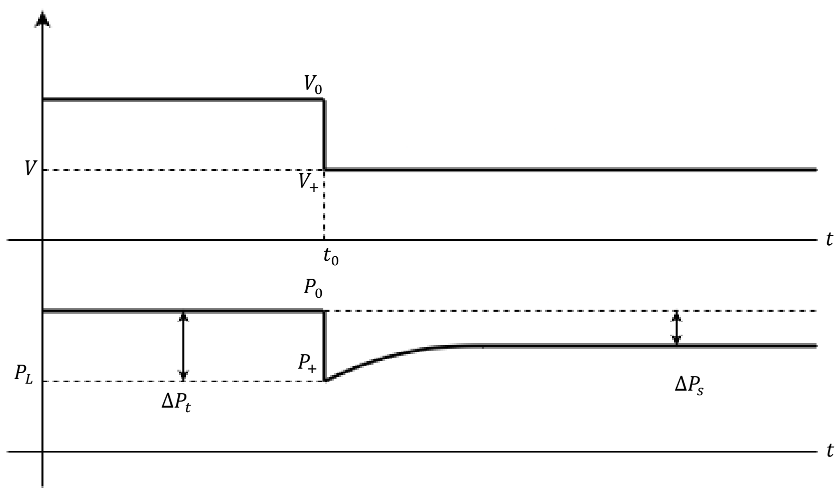

Figure 3.5: Exponential Recovery Load Model Response [38]

3.2.2.2 Oscillatory Component Load Model (OCL)

The aforementioned ERL model is a first order model that represents only static and exponential recovery components and cannot model a damped oscillatory component. Loads that are dominated by induction machines have an inertial mass and therefore will oscillate under a step voltage change due to the instantaneous imbalance. In a low-voltage network, inertial oscillations at different buses also have the potential to resonate and must be accounted for in the loads. The oscillatory component load model (OCL) has been recently proposed to address this gap and serves as an extension of the ERL [34]. Figures 3.6(a) and (b) show the ECL and OCL model fit results, respectively, to a voltage step change for a load that was fit to the model based on measured bus data in [34]. The OCM model is seen to reasonably well capture measured oscillatory load response whereas the ERL model is shown to neglect it completely. The value that the OCM provides is a uniform load power voltage and frequency dependent dynamic load model that can be fit to many different types of inertial loads.

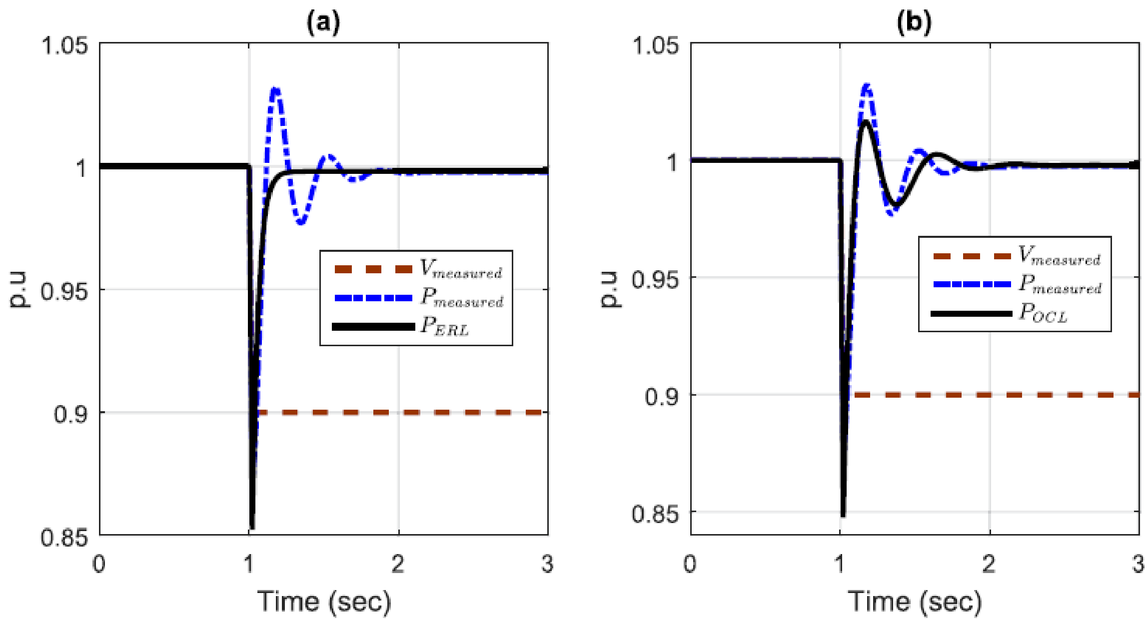

Figure 3.6: Oscillatory Component Model Simulated Disturbance with Active Power Response a) ERL fit. b) OCL Model Fit. [34]

The OCL model uses a standard second order differential equation to characterize the load and is of the following form.

$$\frac{d^2x(t)}{dt^2} + 2\xi\omega_0\frac{dx(t)}{dt} + {\omega_0}^2x(t) = f(t), \tag{3.25}$$

where ξ is the system damping and $|\xi| < 1$, ω_0 represents the system natural frequency and $x(t)$ denotes the system response. The OCL model uses (3.25) to extend the ERL equations (3.21) - (3.24) as

$$P_L(t) = P_s(V) + K_{P_{exp}}x_{P_{exp}}(t) + K_{P_{osc}}x_{P_{osc}}(t) \tag{3.26}$$

$$T_P \frac{dx_{P_{exp}}(t)}{dt} + x_{P_{exp}}(t) = \frac{d\tilde{V}(t)}{dt} \tag{3.27}$$

$$\frac{d^2 x_{P_{osc}}(t)}{dt^2} + 2\xi_P \omega_{0P} \frac{dx_{P_{osc}}(t)}{dt} + {\omega_{0P}}^2 x_{P_{osc}}(t) = \frac{d\tilde{V}(t)}{dt} \tag{3.28}$$

$$Q_L(t) = Q_s(V) + K_{Q_{exp}} x_{Q_{exp}}(t) + K_{Q_{osc}} x_{Q_{osc}}(t) \tag{3.29}$$

$$T_Q \frac{dx_{Q_{exp}}(t)}{dt} + x_{Q_{exp}}(t) = \frac{d\tilde{V}(t)}{dt} \tag{3.30}$$

$$\frac{d^2 x_{Q_{osc}}(t)}{dt^2} + 2\xi_Q \omega_{0Q} \frac{dx_{Q_{osc}}(t)}{dt} + {\omega_{0Q}}^2 x_{Q_{osc}}(t) = \frac{d\tilde{V}(t)}{dt} \tag{3.31}$$

where $P_L(t)$ and $Q_L(t)$ represent the active and reactive power response; $T_{(\cdot)}$ demonstrates the delay; $x_{(\cdot)_{exp}}(t)$ and $x_{(\cdot)_{osc}}(t)$ depicts the state variables corresponding to exponential and oscillatory recovery, respectively; and $K_{(\cdot)_{(\cdot)}}$ represents the weighted coefficients of the oscillatory and exponential responses. $\tilde{V}(t)$ represents the RMS voltage and $P_S(V)$ represents the static load model dependency, which is typically the exponential load model as used in the ERL. Further examples of the OCL model fit in comparison to the ERL model fit in field measurement studies can be found in [34]. A drawback to the proposed OCM is the maturity of such model, many different load parameters are needed to be fit to such model. There is plenty of work to be performed fitting the OCM model to well-known inertial loads commonly seen within residential, commercial and industrial loads before use in stability studies. The OCM will be left to its basic principle here and will not be analyzed within the low-voltage network stability study due to the lack of parameters detailing residential loads.

3.2.2.3 Induction Motor Model (IMM)

The OCL captures the inertial representations in the load steps at an aggregate level represented at the bus. In order to model the response to the granularity required for the low-voltage networks, it is important to understand and model the dynamics of the induction motor directly. This granularity is required to allow for a more in-depth analysis on the inertial effects of rotating machine-based loads on a low-voltage network. The IEEE task force for load representation for dynamic performance has made recommendations for induction machine modelling [39] but has noted that there is an inherent frequency suppression limitation in such models. This makes the IMM models in [39] [40] appropriate for most grid dynamic studies but insufficient for low-voltage network studies in which the frequency sensitivity is much higher. In the case of a low-voltage network microgrid, the frequency stability must be accounted for and inertial effects must be studied with great detail.

The dynamics between single-phase and three-phase induction machines vary significantly due to the internal winding structure of such motors. The spatial separation of windings in a three-phase motor makes it much easier to produce a starting torque and hence start an induction machine. In a single-phase motor, the spatial separation of each three phases does not exist, therefore the theory and hence dynamics are completely different. The theory involved in single-phase induction machines is *rotating field theory* and is detailed in [41]. In a single-phase motor, it is required to transform a single-phase system to a two-phase system in order to produce a starting torque to rotate the motor. This two-phase system is structured as a main and auxiliary winding within a single-phase induction motor. On the auxiliary winding, a starting capacitor is responsible for transforming the single-phase input 90 degrees out of phase with respect to the main winding to produce a starting torque. This transformation and other inefficiencies involved in rotating field theory result in a large starting torque and hence starting current. This starting torque is significantly larger than that of a three-phase motor and must be accounted for within a low-voltage network study due to its inherent sensitivity.

Due to the aforementioned nature of the single-phase induction machine, the objective of this section is to detail a more granular model that addresses the larger impact of starting current and the additional machine frequency component required for the low-voltage network dynamic analysis. A typical model for a single-phase induction motor is presented in figure 3.7, based on the work done in [42] this model is used for the characterization of single-phase air conditioner compressor.

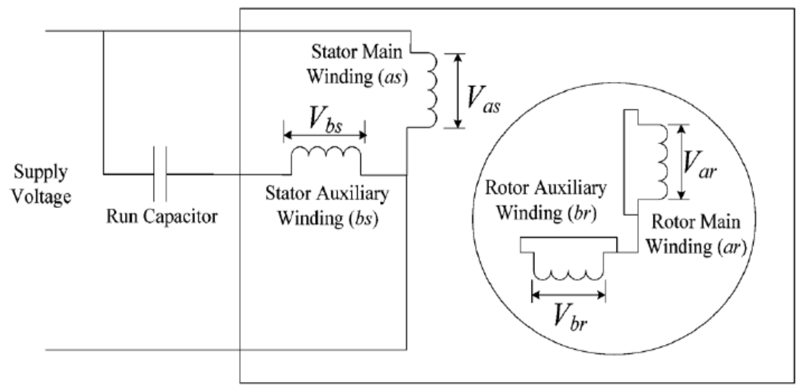

Figure 3.7: Single-Phase Induction Motor Model [42]

The single-phase induction motor with a main and auxiliary winding is an example of an unsymmetrical two-phase induction motor. The two-phase induction motor is unsymmetrical due to the main and auxiliary winding containing different turn ratios leading to a difference in magnitude in main and auxiliary voltage vector magnitudes. The auxiliary winding's main function is to start the rotation of the motor. These two windings are in space quadrature with one another but due to their asymmetry they have different number of turns and winding distributions. The layout of the machine is illustrated in figure 3.8.

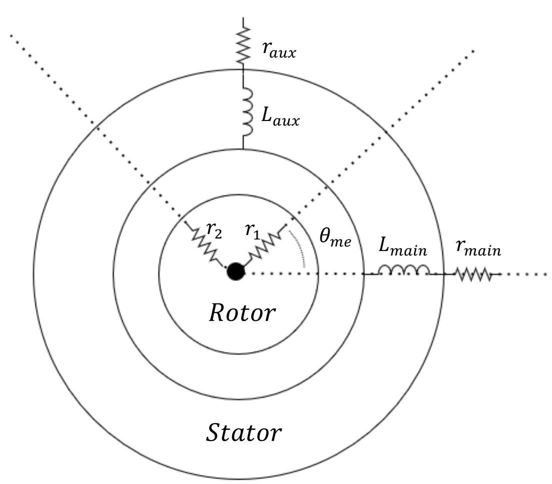

Figure 3.8: Single-Phase Induction Rotor & Stator Axes

The flux linkage and current relationship between the stator and rotor main and auxiliary windings is given by,

$$\begin{bmatrix}\lambda_{main}\\ \lambda_{aux}\\ \lambda_{r1}\\ \lambda_{r2}\end{bmatrix}=\begin{bmatrix}L_{main} & 0 & \mathcal{L}_{main,r1}(\theta_{me}) & \mathcal{L}_{main,r2}(\theta_{me})\\ 0 & L_{aux} & \mathcal{L}_{aux,r1}(\theta_{me}) & \mathcal{L}_{aux,r2}(\theta_{me})\\ \mathcal{L}_{main,r1}(\theta_{me}) & \mathcal{L}_{aux,r1}(\theta_{me}) & L_r & 0\\ \mathcal{L}_{main,r2}(\theta_{me}) & \mathcal{L}_{aux,r2}(\theta_{me}) & 0 & L_r\end{bmatrix}\begin{bmatrix}i_{main}\\ i_{aux}\\ i_{r1}\\ i_{r2}\end{bmatrix}. \tag{3.32}$$

Were $L_{(\cdot)}$ represents self-inductance of the subscripted winding, $\mathcal{L}_{(\cdot)}(\theta_{me})$ is the mutual inductance between the respective subscripted windings and are a function of the rotor angle θ_{me}. The rotor angle represents the spatial position of the rotor axis with respect to the fixed stator axis. Assuming a sinusoidal distribution of air-gap flux, the mutual inductances between the main winding and the rotor can be represented as,

$$\mathcal{L}_{main,r1}(\theta_{me}) = L_{main,r1}cos(\theta_{me}) \tag{3.33}$$

$$\mathcal{L}_{main,r2}(\theta_{me}) = -L_{main,r2}sin(\theta_{me}). \tag{3.34}$$

Where $L_{main,r(\cdot)}$ is the amplitude of the mutual inductance between the two subscripted windings. A similar representation applies with the auxiliary winding of the motor. The voltage equations of the single-phase induction machine are defined in terms of winding currents and flux linkages between the stator and rotor winding as,

$$\begin{bmatrix}\frac{d\lambda_{main}}{dt}\\ \frac{\lambda_{aux}}{dt}\\ \frac{\lambda_{r1}}{dt}\\ \frac{\lambda_{r2}}{dt}\end{bmatrix}=\begin{bmatrix}v_{main}\\ v_{aux}\\ v_{r1}\\ v_{r2}\end{bmatrix}-\begin{bmatrix}R_{main} & 0 & 0 & 0\\ 0 & R_{aux} & 0 & 0\\ 0 & 0 & R_r & 0\\ 0 & 0 & 0 & R_r\end{bmatrix}\begin{bmatrix}i_{main}\\ i_{aux}\\ i_{r1}\\ i_{r2}\end{bmatrix}. \tag{3.35}$$

The electro-magnetic torque is induced by the air gap flux and the rotor winding currents to drive the motor shaft against the counter load torque is given by,

$$T_e = \left(\frac{Poles}{2}\right)\begin{bmatrix}-L_{main,r}(i_{main}i_{r1}\sin(\theta_{me}) + i_{main}i_{r2}\cos(\theta_{me})) + \\ L_{aux,r}(i_{aux}i_{r1}\cos(\theta_{me}) - i_{aux}i_{r2}\sin(\theta_{me}))\end{bmatrix}. \tag{3.36}$$

The machine rotor acceleration equation is based on the power balance between the electric torque and the mechanical torque (including friction and windage losses). The rotor acceleration equation is represented by

$$J\frac{d\omega_r}{dt} = P_{L,e} - P_{L,m}. \tag{3.37}$$

The terms $P_{L,e}$ and $P_{L,m}$ represent the electromechanical induced power and the mechanical power of the mechanical output shaft, respectively. The parameter *J* represents the machine inertial constant. The mechanical power is defined by

$$P_{L,m} = \omega_r T_m, \tag{3.38}$$

where the mechanical torque T_m is recommended by the IEEE task force for load representation and dynamic performance [X] to be modelled as

$$T_m = \mathrm{A}\left(\frac{\omega_r}{\omega_{r0}}\right)^2 + B\frac{\omega_r}{\omega_{r0}} + C + D\left(\frac{\omega_r}{\omega_{r0}}\right)^{am} \tag{3.39}$$

with

$$\mathrm{C} = 1 - (\mathrm{A} + B + D). \tag{3.40}$$

To model the electromechanical power consumed by the motor $P_{L,e}$, we use the electro-magnetic torque developed by the machine with the stator electrical frequency ω_s to get

$$P_{L,e} = \omega_s T_e. \tag{3.41}$$

$$s = \frac{d\theta_r}{dt} = \frac{\omega_s - \omega_r}{\omega_s} \tag{3.42}$$

The slip speed, *s*, between the rotor and stator is represented by (3.42). Note, the work performed in [42] [41] provides a well detailed breakdown of a single-phase induction machine and should be used as reference.

The drawback with the single-phase induction motor machine model is the complexity involved in calculating the consumed load power. The issue with the integration of such machine model within the low-voltage network model is that there isn't a clearly defined voltage-frequency active-reactive load power consumption relationship. This further emphasizes the value of the oscillatory control model and the need for advancing the research in developing standardized OCM load model parameters to accurately encapsulate the dynamics of single and three phase induction machines. Thus, allowing for more accurate and in-depth stability studies to be performed.

The frequency-voltage dependent load model dependence will now be demonstrated within the context of the complete grid-edge low voltage network model.

3.4 Complete Grid Edge Low Voltage Network Model

Section 3.1 described the dynamics of inverter-based generation sources within the low-voltage network and defined the mathematical representation of how the generation sources are coupled together. The equations that defined the dynamics were given by (3.5) and (3.6). Since (3.5) and (3.6) assumed a static shunt admittance load (i.e., the driving point admittance) at each individual bus denoted by $\tilde{Y}_{B_{kk}}$, in order to properly analyze the dynamics within a low-voltage network, the more fitting load models defined in section 3.3 need to be incorporated in this treatment. For reactive power flow, we therefore re-express (3.5) as

$$\frac{d\theta_{I_i}}{dt} = \omega_{I_i}{}^* + n_{I_i}(Q_{L,B_k} + Q_{B_k,network}) \tag{3.44}$$

where,

$$Q_{B_k,network} = E_{B_k}{}^2 \sum_{\substack{j=1 \\ j\neq k}}^{N} Y_{B_{kj}} \sin\left(\delta_{B_{kj}}\right) + \sum_{\substack{j=1 \\ j\neq k}}^{N} \kappa_{kj} \sin\left(\theta_{B_k} - \theta_{B_j} + \delta_{B_{kj}}\right), \tag{3.45}$$

denotes the power exported to the remaining nodes within the low-voltage network; $Q_{L_{B_k}}$, the reactive load connected to bus *k*, replaces the shunt admittance reactive power demand ${E_{B_k}}^2 Y_{B_{kk}} \sin(\delta_{B_{kk}})$ with our developed load consumption models presented in section 3.3. For example, using the frequency dependent load model from (3.13),

$$Q_{L_{B_k}} = Q_0 \left(\frac{V}{V_0}\right)^{n_q}. \tag{3.46}$$

Similarly, for active power flow (3.6) is re-expressed as

$$\tau_{I_i} \frac{dE_{I_i}}{dt} = K_{I_E}({E_{I_i}}^* - E_{B_k}) - m_{I_i}[P_{I_{nom}} - (P_{L,B_k} + P_{B_k,network})]. \tag{3.47}$$

where

$$P_{B_k,network} = {E_{B_k}}^2 \sum_{\substack{j=1 \\ j \neq k}}^{N} Y_{B_{kj}} \cos(\delta_{B_{kj}}) + \sum\nolimits_{\substack{j=1 \\ j \neq k}}^{N} \kappa_{kj} \cos\left(\theta_{B_k} - \theta_{B_j} + \delta_{B_{kj}}\right) \tag{3.48}$$

represents the active power exported to the remaining nodes within the low-voltage network. Similar to (3.44), the shunt admittance active power demand ${E_{b_k}}^2 Y_{b_{kk}} \cos(\delta_{b_{kk}})$ is replaced by $P_{L_{B_k}}$, the active load connected to bus *k*, found with our developed load consumption models presented in section 3.3. For example, using the frequency dependent load model from (3.14),

$$P_{L_{B_k}} = P_0 \left(\frac{V}{V_0}\right)^{n_p}. \tag{3.49}$$

Within this low-voltage network simulation, we re-emphasize our assumption that the time constant of the droop control loop is much larger than that of the inner control loops. Therefore, the droop control loop provides the governing control dynamics that are critical to network stability; the dynamics associated with inner current and voltage control can be neglected due to the separation of time scales. Hence, we have re-expressed (3.5) and (3.6) as (3.47) and (3.44) to allow for the low-voltage network model to accommodate different loads within the network which explicitly have a voltage/frequency to active/reactive power relationship.

In summary, section 3.4 has described the dynamics needed to investigate low-voltage network operation in greater detail. The generation and load interaction dynamic equations at each bus within the low-voltage network have been defined. The resemblance between a low-voltage network of droop-controlled inverters and coupled inverters described by the Kuramoto model was uncovered. Thus, allowing the development of further intuition on the interaction of droop-controlled inverters within a network and the potential significance of the droop control gain design. Lastly, we defined the low-voltage network model of interconnected droop-controlled inverters within a secondary grid network in which we adjusted the network power flow equations to accommodate for any load models which have a clearly defined voltage/frequency-active/reactive power relationship. Chapter 4 will test various network scenarios with various load models to explore this developed intuition and the effects of different loads on the low-voltage network. Based on the impact of loading within the network, the developed intuition allows us to investigate whether the coupling impedance of the line and topology of the network may improve the stability of the network and potentially make the network more resilient to disturbances.

CHAPTER 4: Low-Voltage Network Dynamic Performance

Based upon the concepts and theory developed in the preceding chapters, we have designed a low-voltage distribution system stability analysis tool for high penetration residential neighborhood dynamic analysis. The generation sources within the network are residential PV systems which adhere to the IEEE 1547-2018 standard. The loads within the network are built upon the active/reactive power to voltage/frequency relationships developed in chapter 3. The load models employed within the simulation environment are at the user's discretion but they have the capability to model the most common residential loads such as lighting, electronic, heating and induction motor-based loads.

Chapter 4 will present the software architecture of the low-voltage simulation tool along with a low-voltage network stability study on different transient scenarios. We will analyze different network topologies and their effect on the dynamic stability with respect to the transient disturbance test cases. All generation sources on the network adhere to the IEEE 1547-2018 specifications and will be tested against the various performance category requirements. The objective of the analysis is to test the resilience of the low-voltage network with the added flexibility in the 1547-2018 standard. Furthermore, the impact of coupling and different types of loading on the network will be closely examined to demonstrate the sensitivity of the network due to the lack of inertia associated with inverter interfaced generation.

4.1 Low-Voltage Secondary Network Simulations

In this section, a secondary low-voltage network of interconnected homes is tested for voltage, angle and frequency stability. The interconnection under study is indicated by the leftmost dashed box low-voltage network in figure 3.1 and figure 4.1.

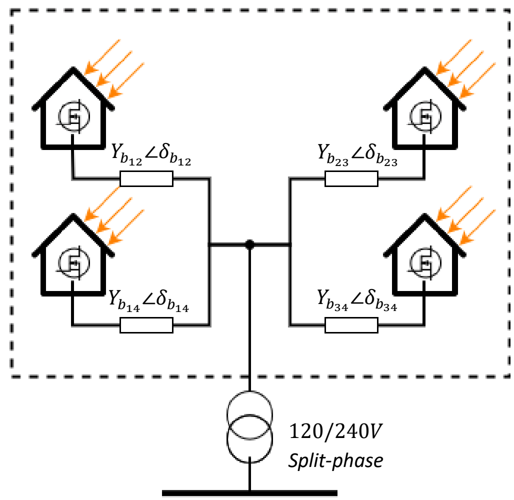

Figure 4.1: Low-Voltage Secondary Test Network

At the utilization voltage level, it is common to see 200A service #2/0 copper or #4/0 all aluminum (AAC) or aluminum clad conductors. The conductors interconnecting the homes in this study will be the aforementioned AAC cables with per unit coupling impedance demonstrated in table 4.1; based on an estimated cable length of 1000 feet (300m). Typically, a secondary low-voltage network will be interconnected on the secondary tap of the secondary low-voltage network step-down transformer. The secondary voltage is at the utilization level and is typically a split-phase 120/240V system in North America; the chosen base voltage of the network. The network is sized based on a required 200A service entry per house.

Feeder Line Impedances	Impedance (X) p.u.	Admittance (Y) p.u.	Ampere Rating (A)
Network 1 (#4/0 AAC)	$0.1885 + j0.05$ $(0.195\angle 14.83)$	$4.957 + j1.313$ $(5.128\angle 14.83)$	310

Table 4.1: Per-Unit Low Voltage Network Coupling Impedance

The low-voltage network simulation generation capacity per house is demonstrated in table 4.2. The apparent power rating is based around the average North American rooftop PV installation size, estimated to be 6.6kW/system [43]. Based on the IEEE 1547 standard, DER is required to have a rated reactive power injection/absorption capability of 0.44% of the nameplate apparent power rating. Furthermore, the droop gains for the individual DER systems were calculated based on the voltage and frequency requirements set forth by IEEE 1547-2018 standard and the theory and concepts discussed in chapter 2.2.2. Chapter 2 introduced a nominal active power injection set point, $P_{I_{nom}}$. The nominal active power injection setting allows for greater DER flexibility within a low-voltage network microgrid. This set point is selected to be 70% of the nameplate rated active power. Table 4.3 depicts the inverter-based DER generation settings of the low-voltage network under test, demonstrating the power rating of each inverter in p.u. and the dual-slope droop curve settings. The voltage feedback gain K_{I_E} will be tested with two different settings: 0 and 10. Each inverter in the system will have their nominal voltage reference set point $E_I{}^*$ set to 1.0 p.u. and frequency reference set point $\omega_I{}^*$ set at 377 radians/second (60Hz). As indicated by figure 4.1, the network topology under test is the commonly used star topology in secondary networks. The generation trip settings will be turned off within this study but the output of generation will be limited to their respective power ratings. This will provide a more complete view of the new ride-through capabilities that are required for DER in the context of a low-voltage network microgrid.

Bus/Injection Capabilities	**Apperent Power Rating (S_{B_k}/ $S_{B_k(p.u.)}$)**	**Active Power Rating (P_{B_k})**	**Reactive Power Rating (Q_{B_k})**
Bus 0 (B_0)	5.92kVA / 0.1184	5.0kW	2.2kVAR
Bus 1 (B_1)	8.19kVA / 0.1638	7.5kW	3.3kVAR
Bus 2 (B_2)	6.0kVA / 0.12	5.5kW	2.42kVAR
Bus 3 (B_3)	10.925kVA / 0.2185	10kW	4.4kVAR
Total:	**31.035kVA / 0.6207**	**28kW**	**12.32kVAR**

Table 4.2: Low Voltage Microgrid Generation Capacity

Generation Droop Settings	**P_{rated} (p.u.)**	**Q_{rated} (p.u.)**	K_{I_E}	m_{I_1}	m_{I_2}	n_{I_1}	m_{I_2}
Bus 0 (b_0)	0.1	0.044	0 , 10	$\frac{-0.15}{P_{1,nom}}$	$\frac{-0.3}{P_{1,nom}-P_{1,rated}}$	$\frac{2.75}{Q_{1,rated}}$	$\frac{1.75}{Q_{1,rated}}$
Bus 1 (b_1)	0.15	0.066	0 , 10	$\frac{-0.15}{P_{2,nom}}$	$\frac{-0.3}{P_{2,nom}-P_{2,rated}}$	$\frac{2.75}{Q_{2,rated}}$	$\frac{1.75}{Q_{2,rated}}$
Bus 2 (b_2)	0.11	0.0484	0 , 10	$\frac{-0.15}{P_{3,nom}}$	$\frac{-0.3}{P_{3,nom}-P_{3,rated}}$	$\frac{2.75}{Q_{3,rated}}$	$\frac{1.75}{Q_{3,rated}}$
Bus 3 (b_3)	0.2	0.088	0 , 10	$\frac{-0.15}{P_{4,nom}}$	$\frac{-0.3}{P_{4,nom}-P_{4,rated}}$	$\frac{2.75}{Q_{4,rated}}$	$\frac{1.75}{Q_{4,rated}}$
Total:	**0.56**	**0.2464**	-	-	-		-

Table 4.3: Low-Voltage Microgird Droop Parameter Settings

4.2 Low-Voltage Network Simulation Architecture

The software has been designed with a component-based architecture allowing for ease of use and expandability of the core application to include further transmission, generation and load sources. Figure 4.2 demonstrates the software architecture of the low-voltage simulation tool that has been developed to date.

To run the simulation, the user must define the BusSetting.py and Simulation.py files, indicated in figure 4.2. The BusSettings.py file is responsible for defining the bus objects which aggregates the loads and generation at the PCC; the point responsible for connecting the end-utilization with the secondary distribution network. Furthermore, a network object is required to define the bus coupling and coupling impedances. The Simulation.py file is responsible for instantiating the required objects from BusSettings.py and defining the network simulation run function. The network simulation run function defines the simulation environment which contains: simulation length, disturbance function, disturbance function execution time, desired network response return variables, load powers and the end load plotting.

An abstract low-voltage network plotter class is available to allow the user to plot network bus voltages, frequency and load powers versus time with ease. An IEEE 1547-2018 plotter class inherits the LV network plotter class and extends the graphing capabilities. This allows the user to plot network frequency and bus voltage against the IEEE1547-2018 category I-III requirements to visualize for any violation. In accordance with the IEEE1547-2018 standard, different inverter classes are available that adhere to the low-voltage and frequency ride through capabilities which contain the disconnection settings and ride-through capabilities in accordance with the standard. The loads currently available for use within the simulation tool are those presented in Chapter 3.

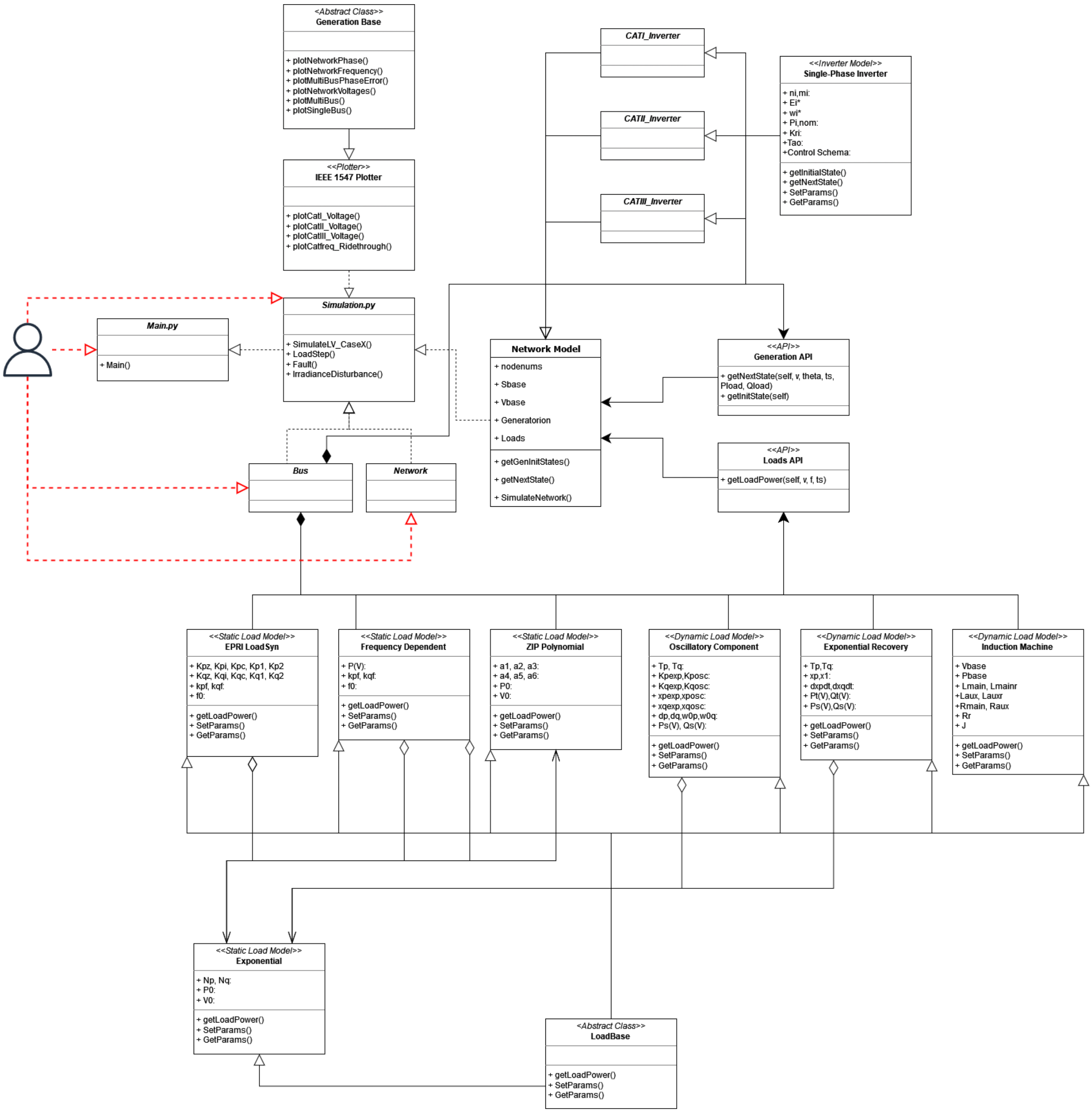

Figure 4.2: Low-Voltage Distribution Network Simulation Architecture

4.3 Frequency Dependent Load Step Disturbance Analysis

A low-voltage network test is run based on the theory developed in Chapter 3 and settings displayed in tables 4.2 and 4.3. The first low-voltage network test case employs a static frequency dependent load model from section 3.2.1.3. The parameters from the frequency dependent load model are obtained from the research composed in [44] [39] .Each bus within the network has an aggregated static frequency dependent load along with an inverter interfaced PV generation source. The network bus load settings are demonstrated in table 4.4.

Bus Number	Exponential Frequency Dependent Initial Load				Exponential Frequency Dependent Load Step			
-	Time (s)	Parameters	Load Power		Time (s)	Parameters	Load Power	
-	-	n_p, n_q, k_{pf}, k_{qf}	P_L	Q_L	-	n_p, n_q, k_{pf}, k_{qf}	P_L	Q_L
0	0	1.2, 2.7, 0.7, -2.3	0.05	0.0136	1.5-2.4	1.2, 2.7, 0.7, -2.3	0.12	0.015
1	0	1.2, 2.7, 0.7, -2.3	0.1	0.0254	2.4-3.5	1.2, 2.7, 0.7, -2.3	0.12	0.03
2	0	1.2, 2.7, 0.7, -2.3	0.05	0.0136	3.5-4.0	1.2, 2.7, 0.7, -2.3	0.15	0.02
3	0	1.2, 2.7, 0.7, -2.3	0.1	0.0372	4.0-4.8	1.2, 2.7, 0.7, -2.3	0.105	0.0272

Table 4.4: Frequency Dependent Static Load Test Case 1

Initially, the generation sources on the network are synchronized to the utility grid and the grid state is in a normal operation state at a voltage of 1.0 p.u. and frequency of 60Hz. At time t=0 seconds, the network goes from grid connected mode to microgrid/islanded mode instantaneously. The initial frequency dependent loads on the network at time t=0 seconds is demonstrated by column 2 in table 4.4. Beginning at time t=1.5 seconds the network experiences an instantaneous load step disturbance at each bus on the network according to table 4.4. At each bus, the load models maintain the same load parameters but increase their active and reactive loading, demonstrated in column 3 in table 4.4.

The inverters active and reactive power, voltage, frequency, instantaneous phase and referenced phase responses are captured at each bus and displayed in figures 4.3-4.8, 4.11, 4.12 and 4.15-4.19. The loading and load response is captured at each bus and illustrated in figures 4.9-4.10 and 4.13-4.14. The inverter voltage and frequency responses are plotted in reference to the IEEE 1547-2018 Category III requirements are demonstrated in figures 4.3-4.8.

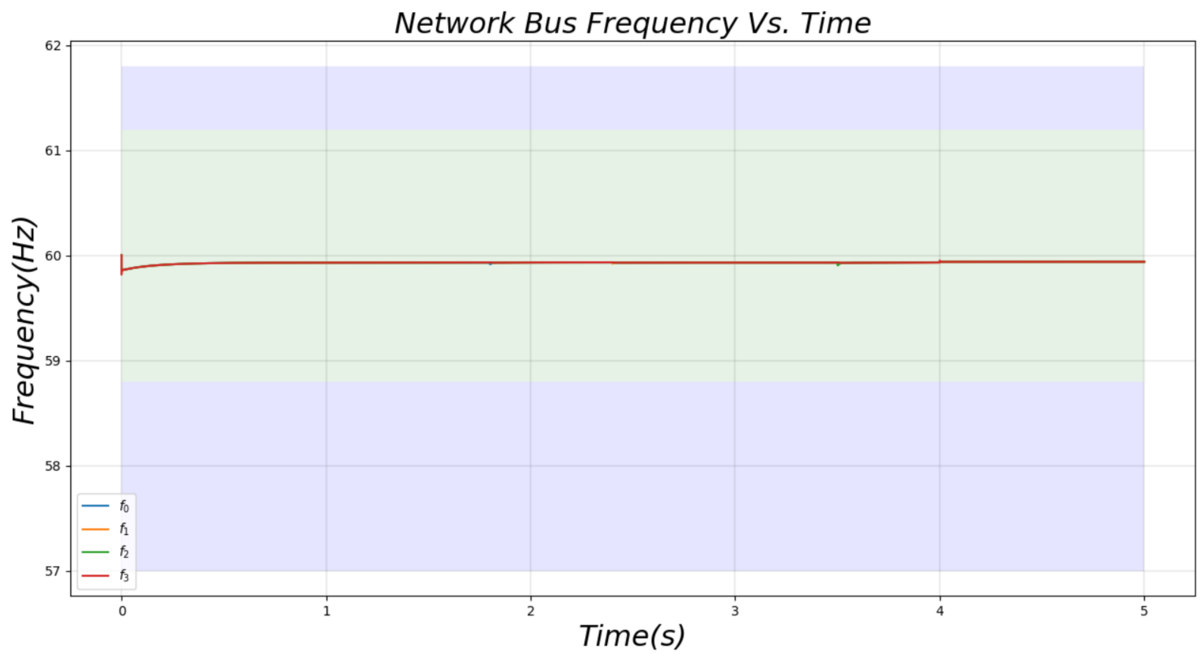

Figure 4.3: Frequency Dependent Static Load Test Case 1 Response Plotted Against IEEE 1547-2018 Category III Ride-Through Requirements Frequency Response

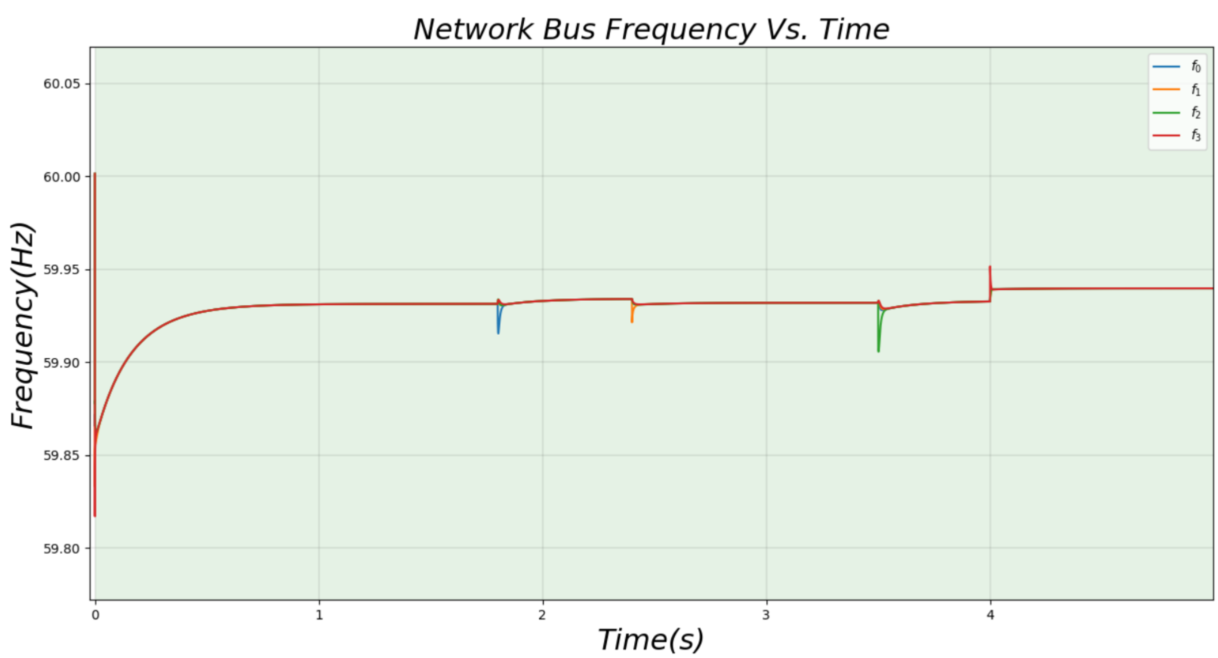

Figure 4.4: Frequency Dependent Static Load Test Case 1 Response Plotted Against IEEE 1547-2018 Category III Ride-Through Requirements

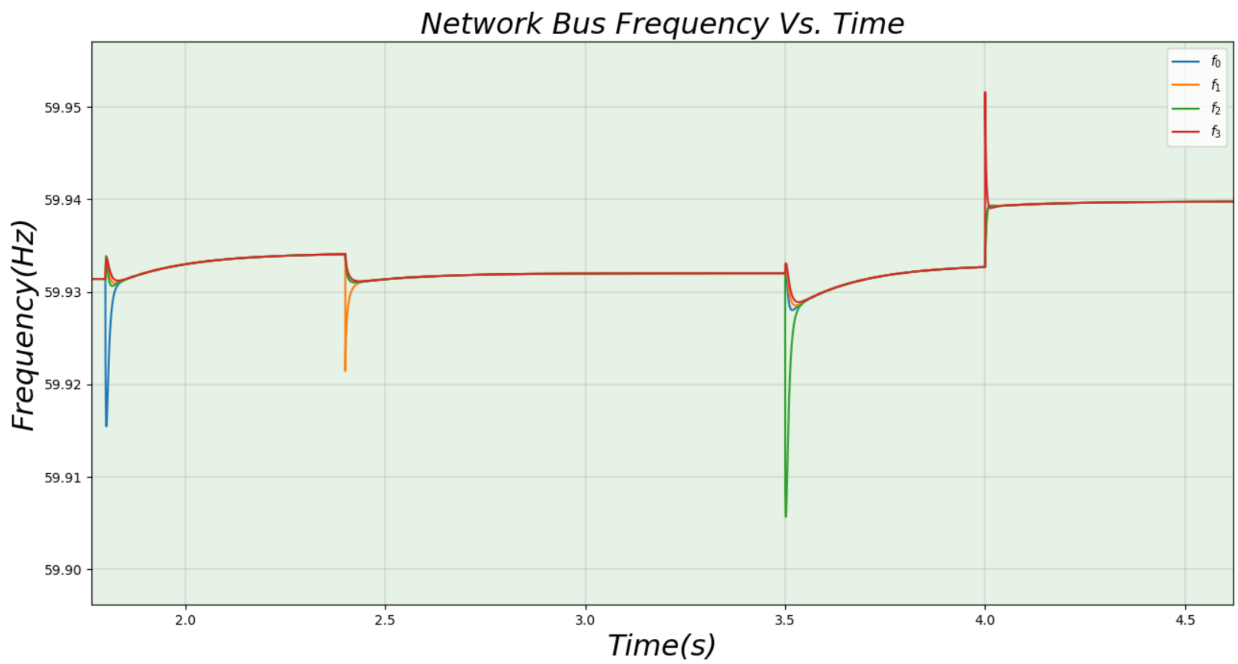

Figure 4.5: Frequency Dependent Static Load Test Case 1 Response Plotted Against IEEE 1547-2018 Category III Ride-Through Requirements Frequency Response Zoom

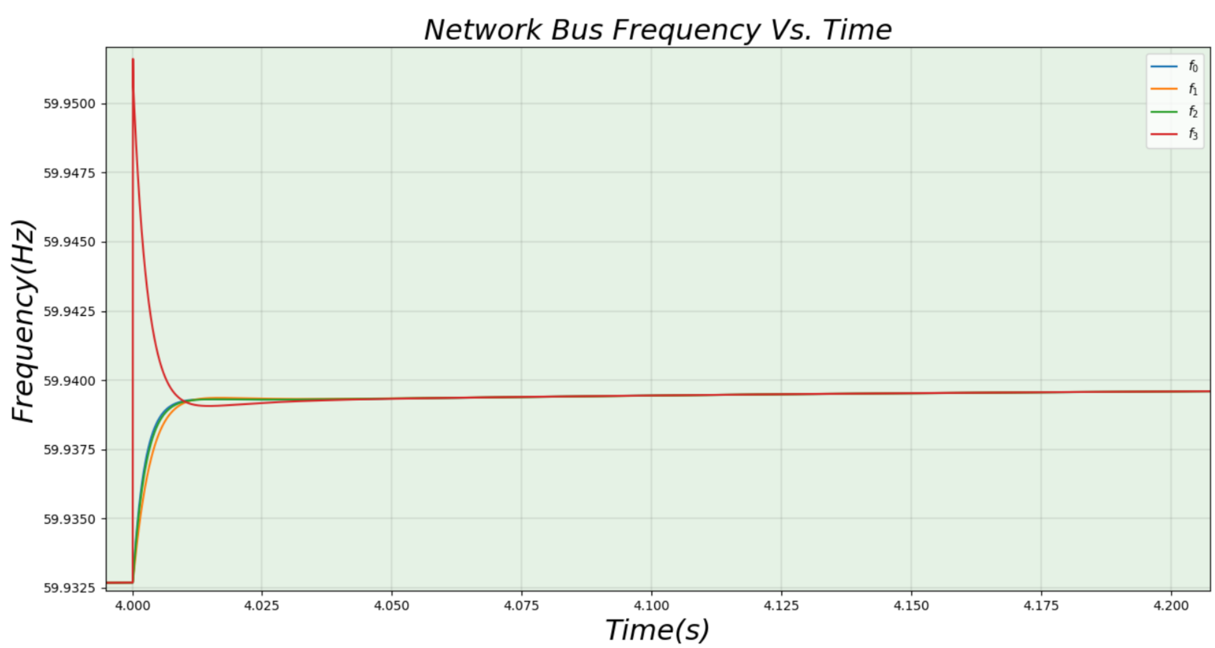

Figure 4.6: Frequency Dependent Static Load Test Case 1 Response Plotted Against IEEE 1547-2018 Category III Ride-Through Requirements Frequency Response @ 4.0seconds Zoom

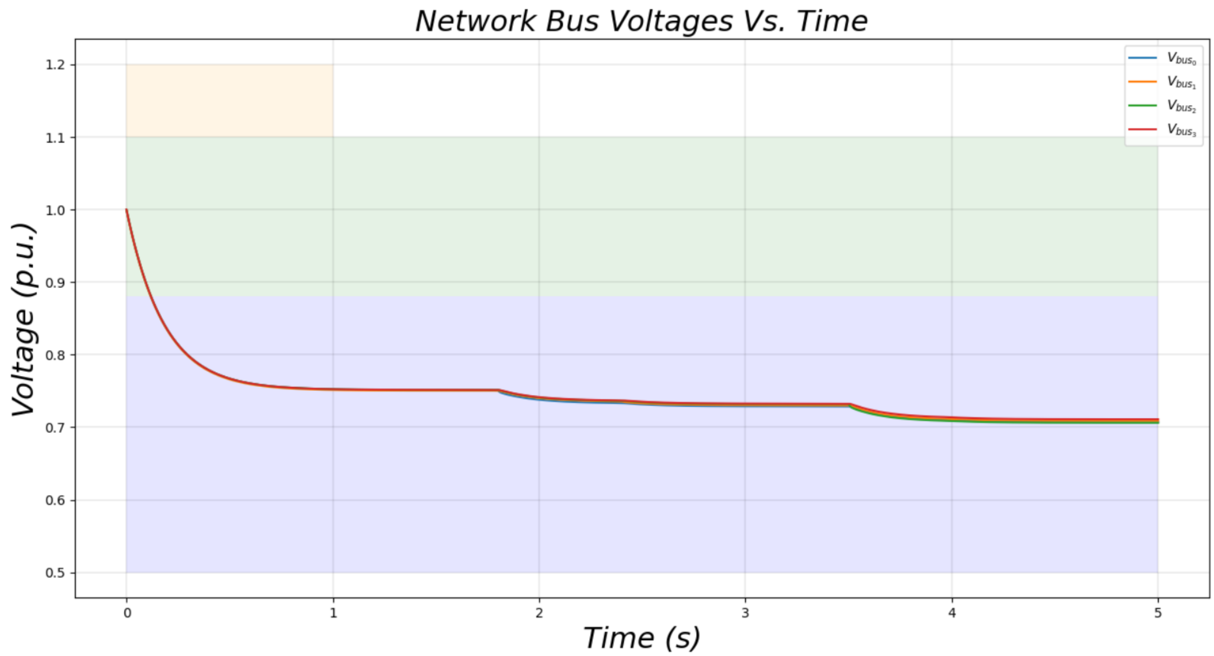

Figure 4.7: Frequency Dependent Static Load Test Case 1 Response Plotted Against IEEE 1547-2018 Category III Ride-Through Requirements Voltage Response

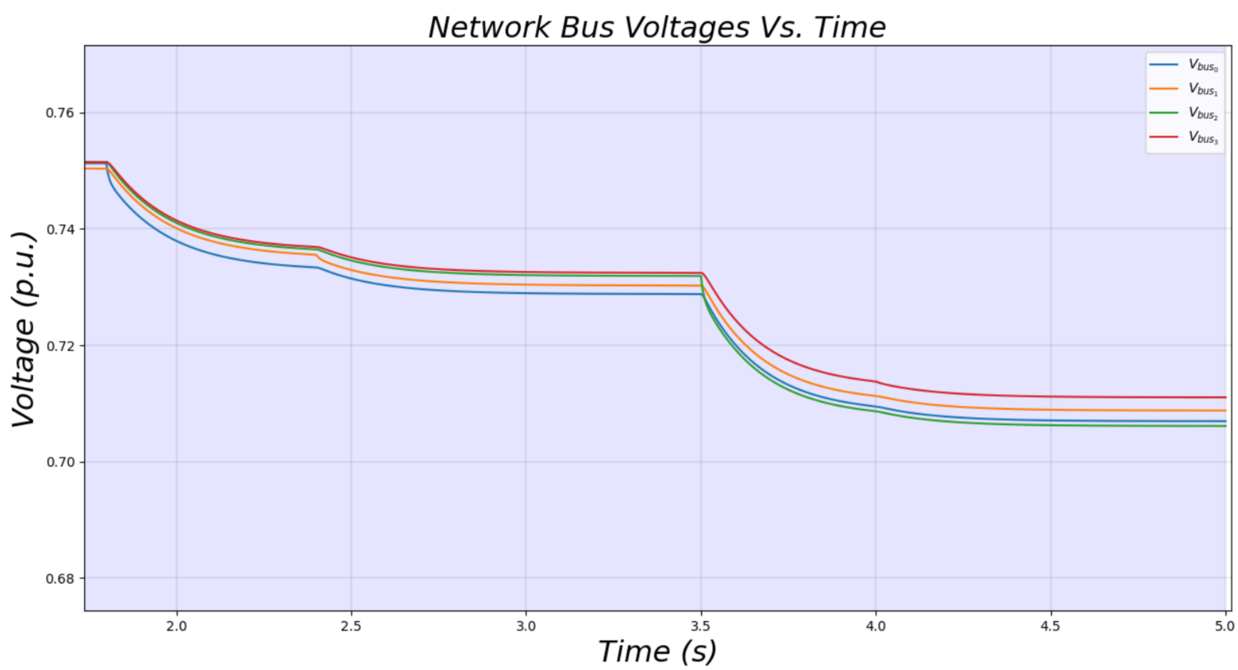

Figure 4.8: Frequency Dependent Static Load Test Case 1 Response Plotted Against IEEE 1547-2018 Category III Ride-Through Requirements Voltage Response Zoom

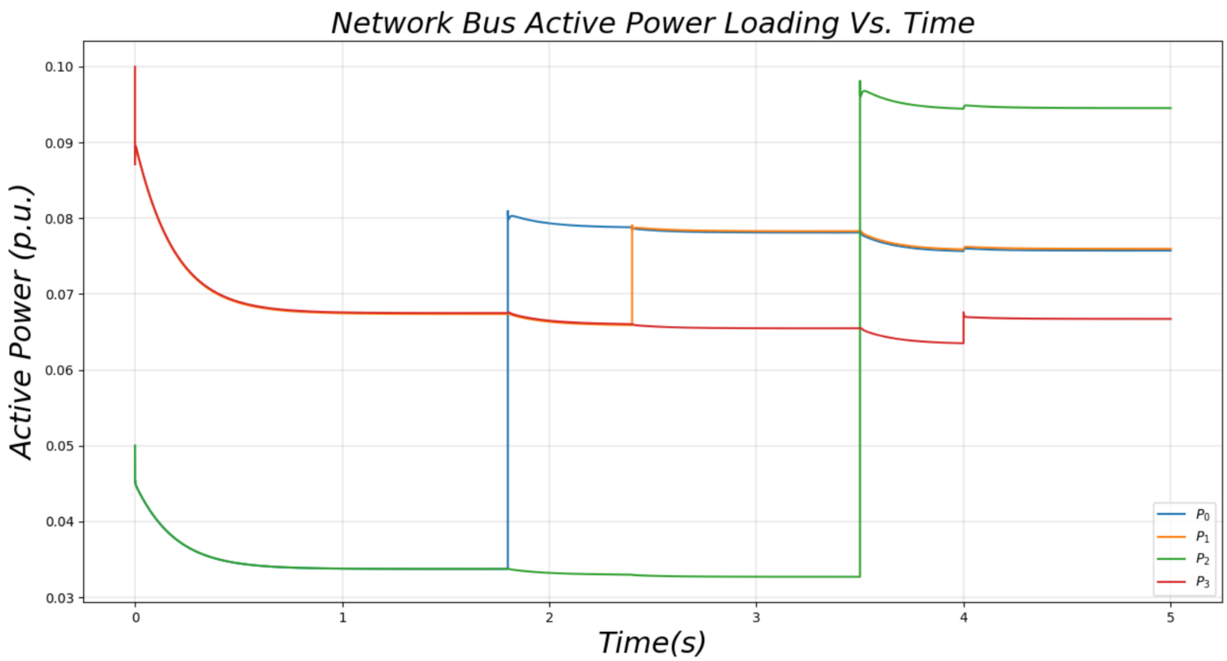

Figure 4.9: Frequency Dependent Static Load Test Case 1 Inverter Active Power Load Response

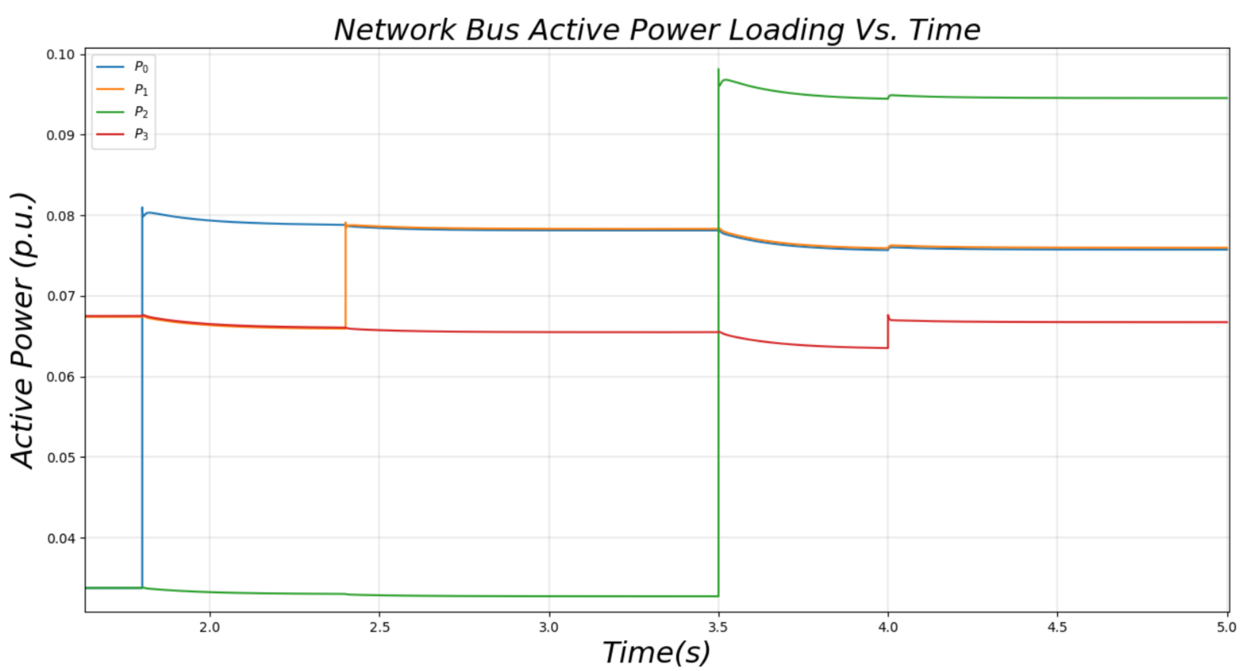

Figure 4.10: Frequency Dependent Static Load Test Case 1 Inverter Active Power Load Response Zoom

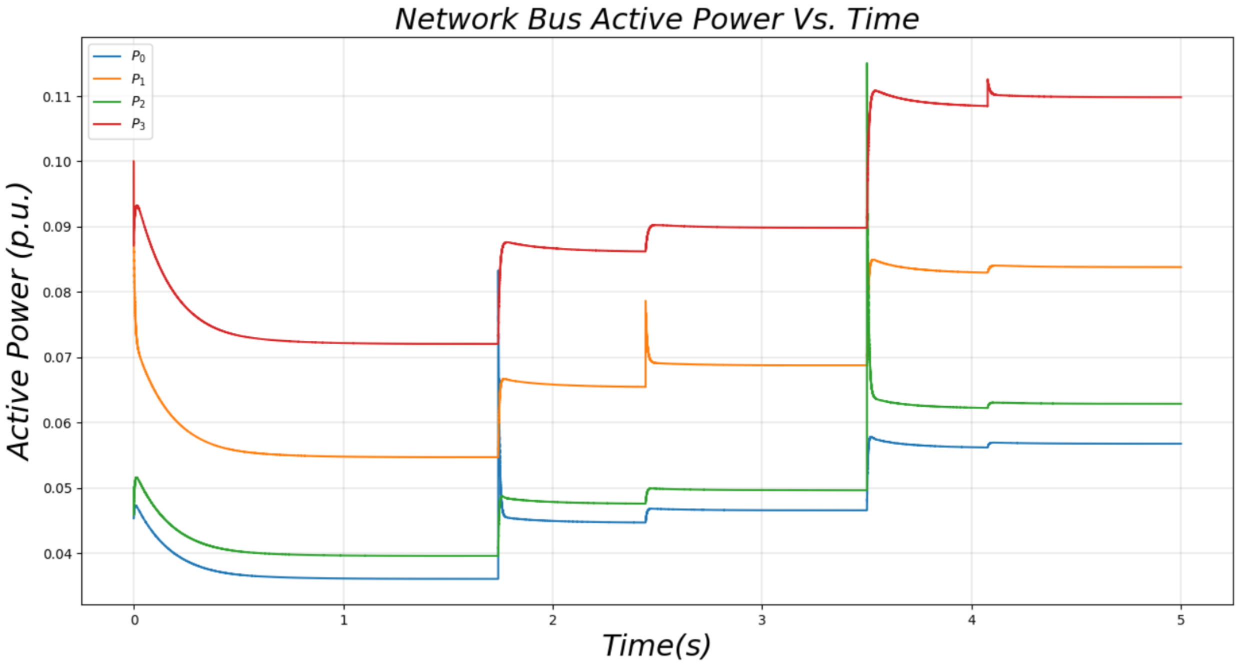

Figure 4.11: Frequency Dependent Static Load Test Case 1 Inverter Active Power Response Zoom

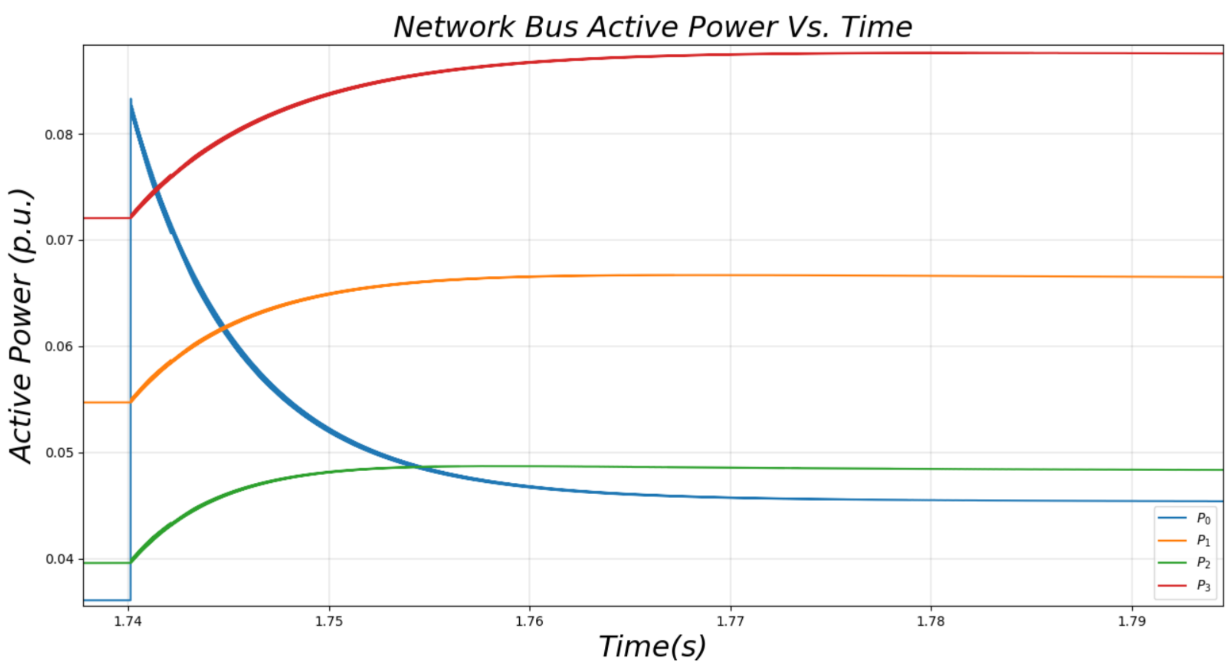

Figure 4.12: Frequency Dependent Static Load Test Case 1 Inverter Active Power Response Response Zoom

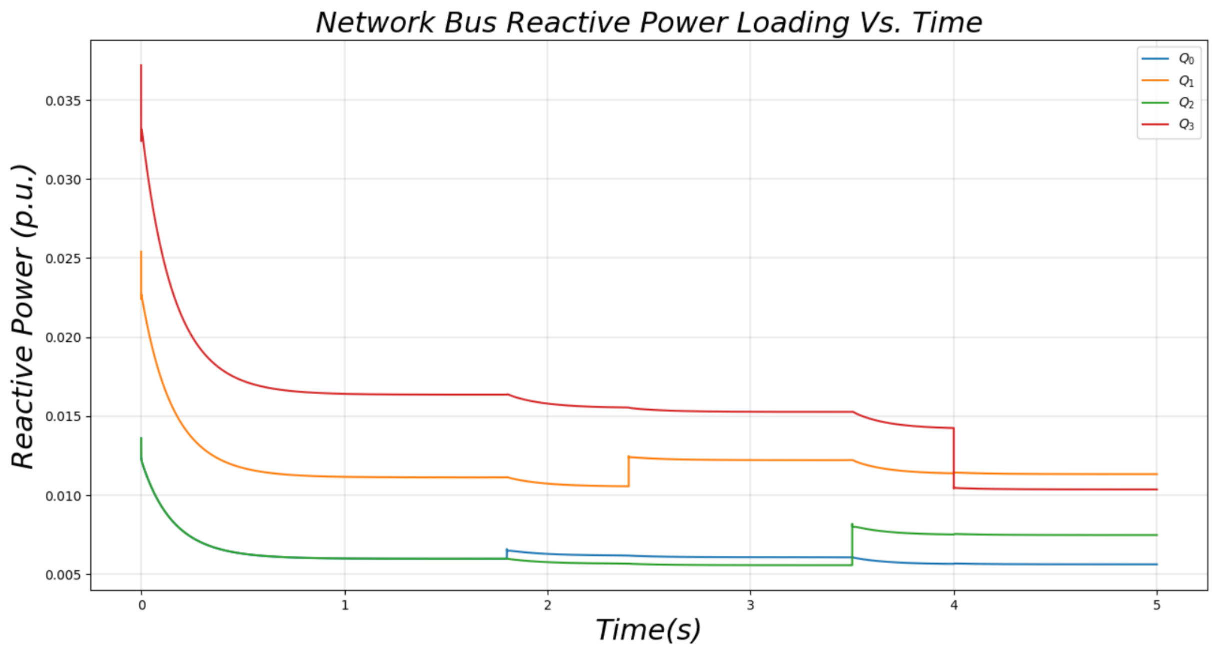

Figure 4.13: Frequency Dependent Static Load Test Case 1 Inverter Reactive Power Response Response

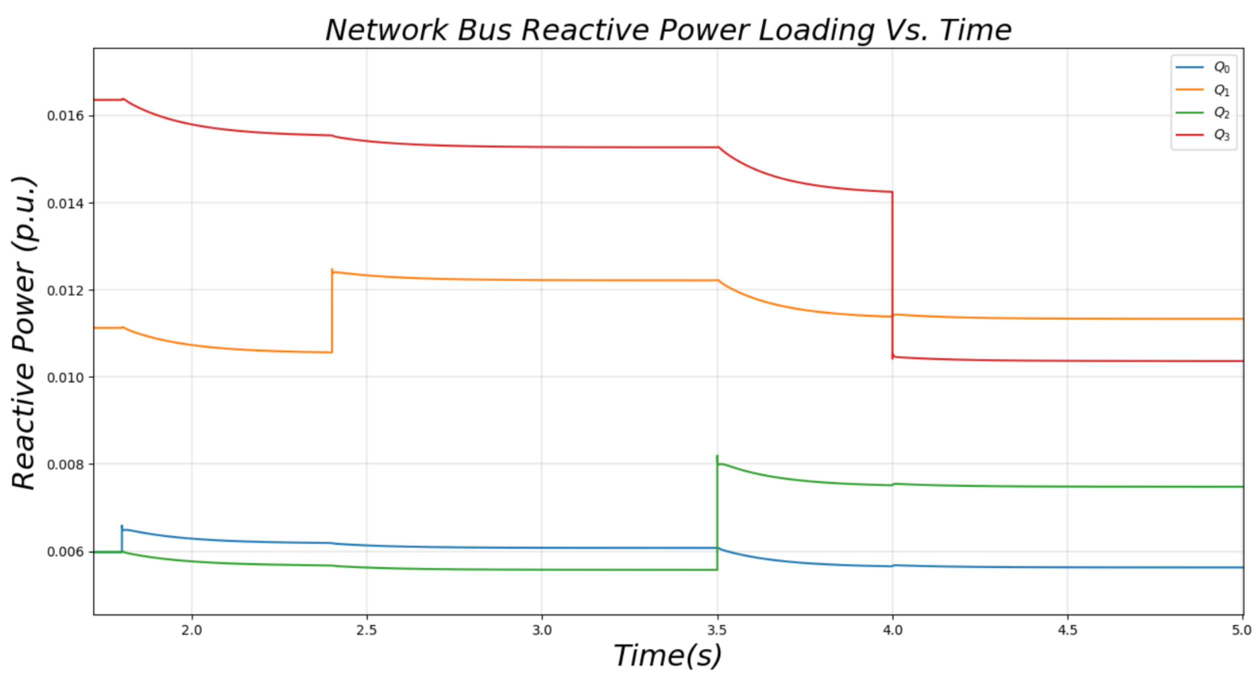

Figure 4.14: Frequency Dependent Static Load Test Case 1 Inverter Reactive Power Response Response Zoom

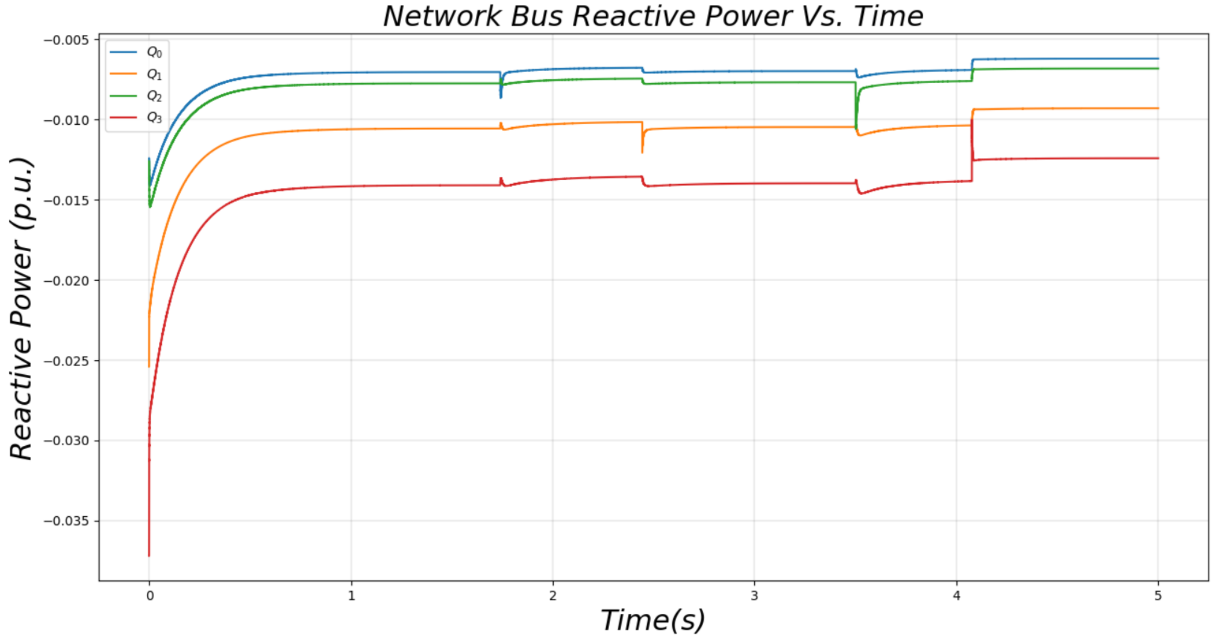

Figure 4.15: Frequency Dependent Static Load Test Case 1 Inverter Reactive Power Response Response

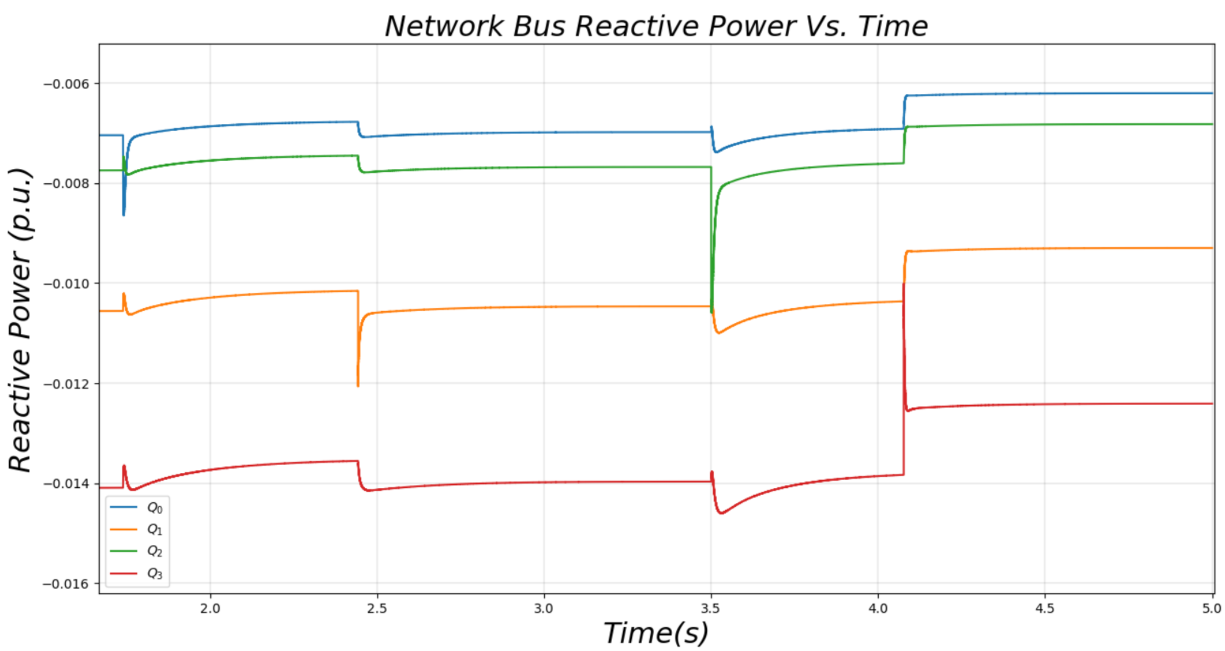

Figure 4.16: Frequency Dependent Static Load Test Case 1 Inverter Reactive Power Response Response Zoom

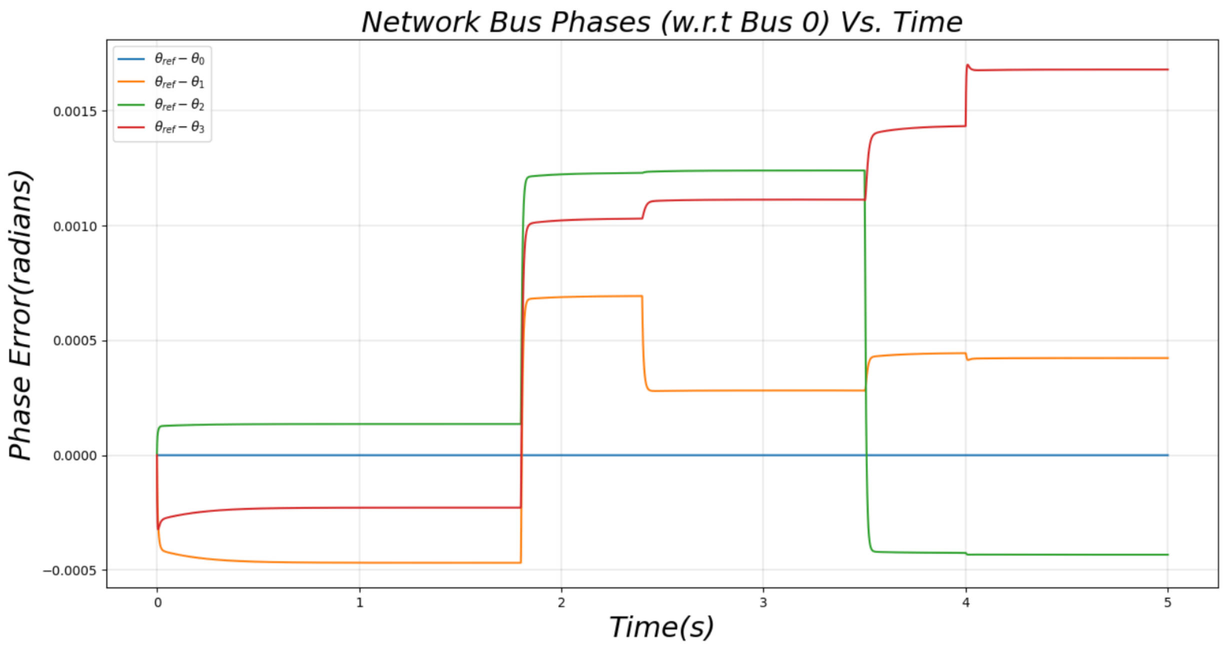

Figure 4.17: Frequency Dependent Static Load Test Case 1 Inverter Phase Response Response

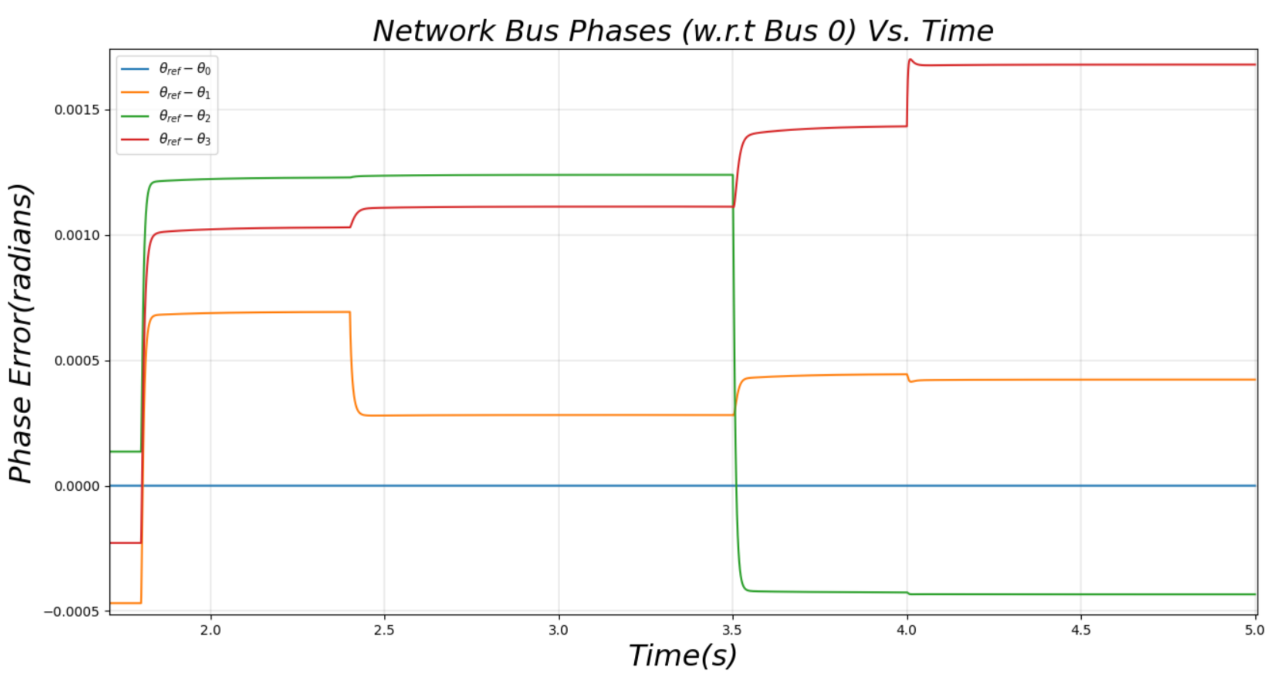

Figure 4.18: Frequency Dependent Static Load Test Case 1 Inverter Phase Response Response Zoom

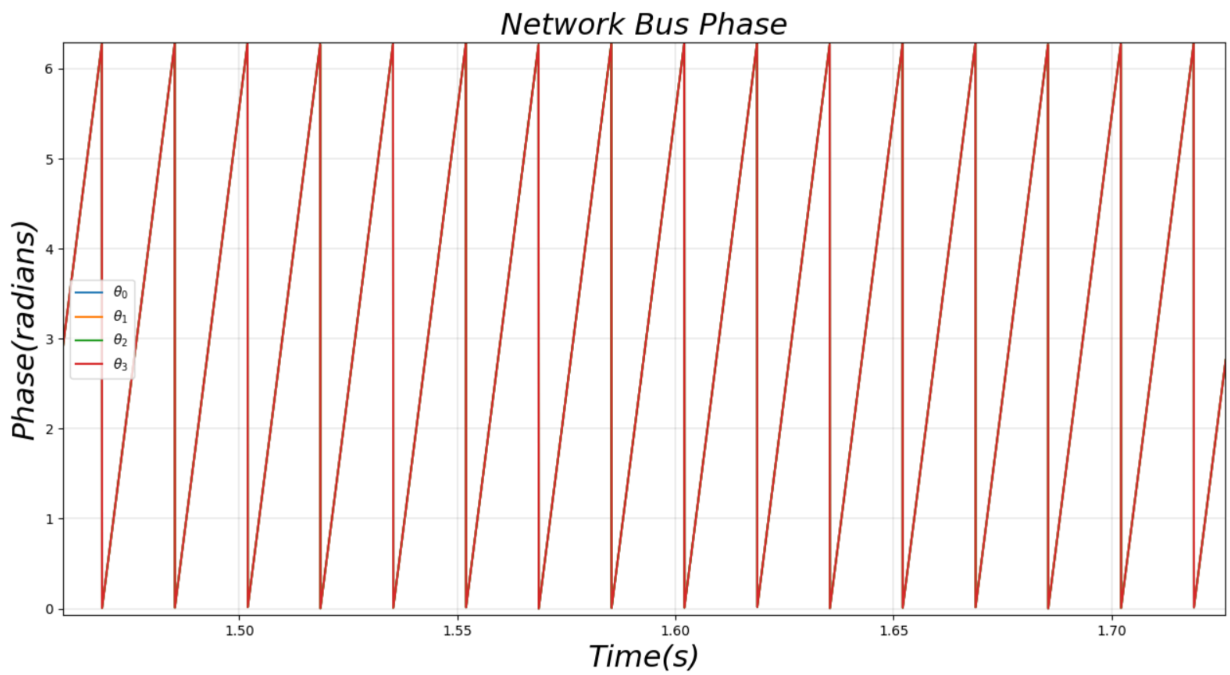

Figure 4.19: Frequency Dependent Static Load Test Case 1 Inverter Instantaneous Phase Response

Based on the frequency dependent loading in accordance with table 4.4, the low-voltage network under test is able to maintain intact. Upon entrance of islanded mode at t=0 seconds, the DERs maintain synchronization and settle to a frequency of approximately 59.925Hz at 0.6 seconds. This is based on the DERs reactive loading experienced at their respective buses and exported/ imported requirements from the other buses on the network. Based on the initial network loading, the voltage falls well below the continuous operation region defined by the IEEE 1547-2018 Category III requirements and the network is now in an alert state. The low-voltage network is still intact at this point but requires restorative action. At t=1.5 seconds, the network begins to experience a series of load steps which further aggravates the voltage level. Although the network is still intact, without any restorative control being taken, the voltage level maintains well below the continuous operation region. Based on the most tolerant IEEE1547-2018 ride-through capability, Category III, the DERs will begin disconnected from the network after t > 5 seconds. Thus, aggravating the loading event further pushing the system into either an emergency or an in-extremis state if loads are not shed. At this point the low-voltage network would be declared as a system not-intact. A fast-acting secondary control system would be required to take action on the setpoints of the droop controlled DERs within the network in order for voltage stability to be maintained.

In order to address the voltage stability in the network, the proportional droop control voltage feedback gains K_{I_E} are adjusted. The same test is performed on the network with a voltage feedback gain K_{I_E} of 10 on each inverter within the network. The performance of the low-voltage network with the adjusted voltage feedback gains are illustrated within figure 4.20-4.34. Figures 4.20-4.25 represent the low-voltage network voltage and frequency response plotted against the IEEE 1547-2018 Cat-III requirements. The low-voltage network remains intact and operating within the continues operation region as a result of the droop voltage feedback gain adjustment. Further disturbances within the network do not affect the stability of the system and the network maintains a normal operational state throughout the simulation.

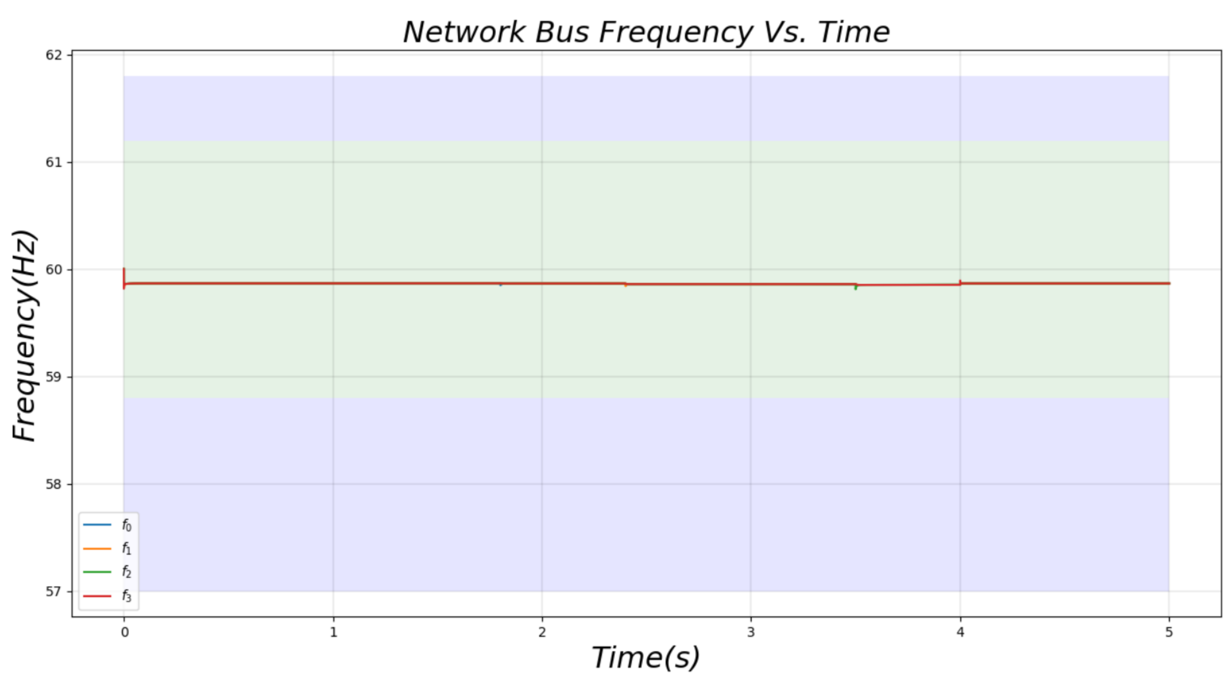

Figure 4.20: Frequency Dependent Static Load Test Case 1 Response Plotted Against IEEE 1547-2018 Category III Ride-Through Requirements Frequency Response (Ke=10)

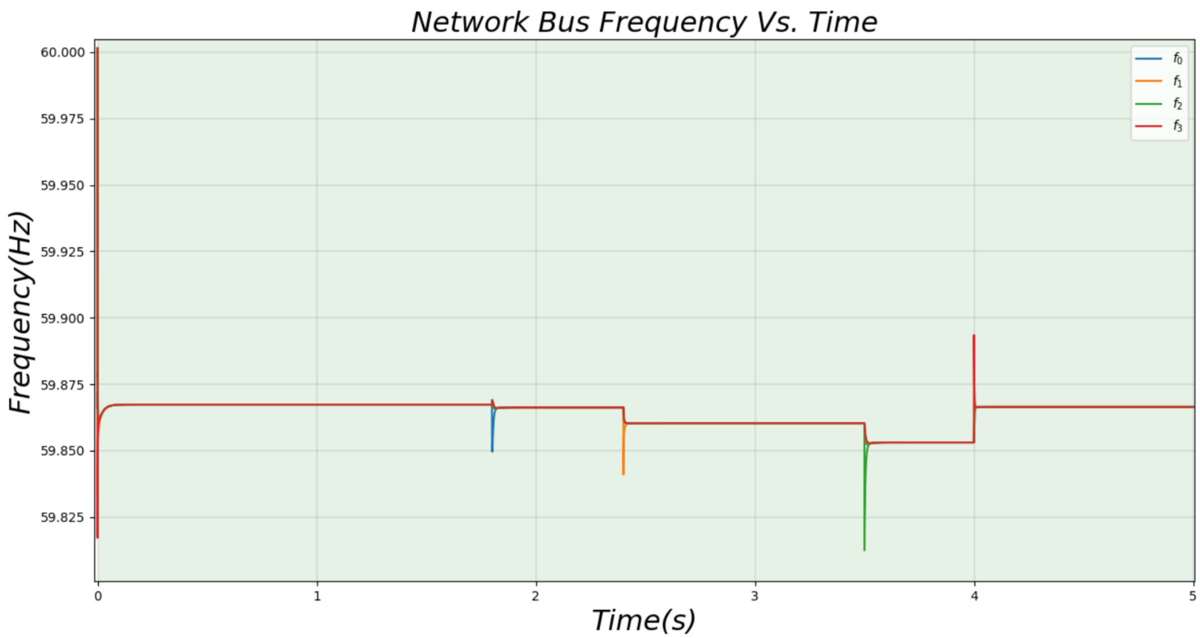

Figure 4.21: Frequency Dependent Static Load Test Case 1 Response Plotted Against IEEE 1547-2018 Category III Ride-Through Requirements Frequency Response (Ke=10) Zoom 1

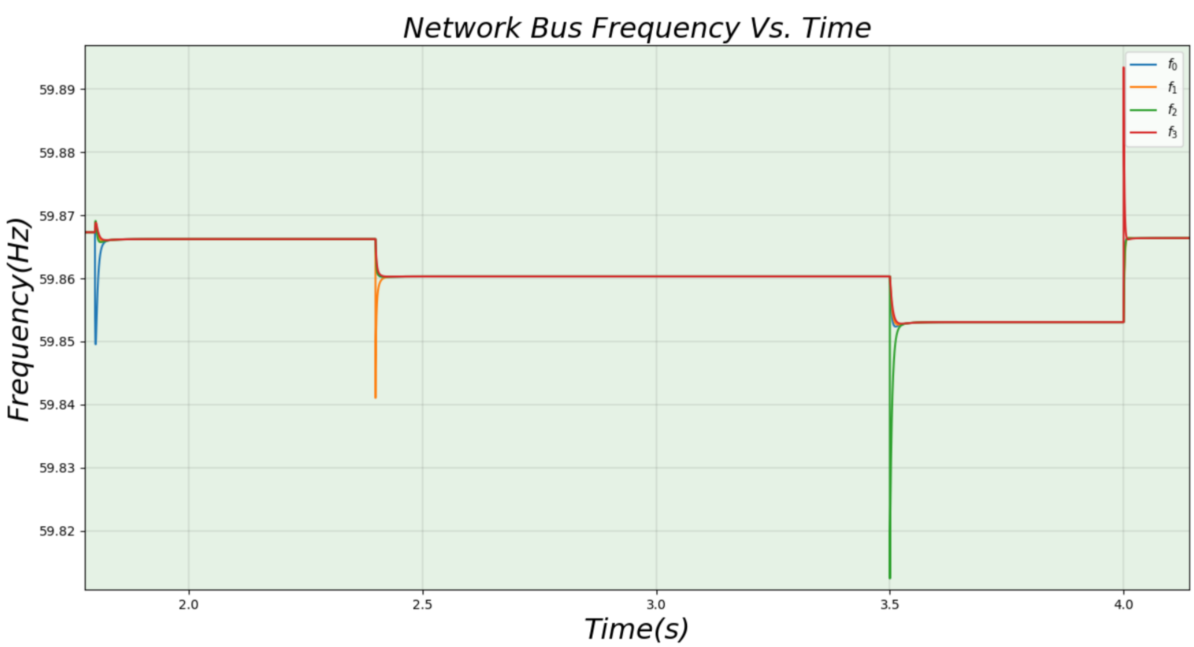

Figure 4.22: Frequency Dependent Static Load Test Case 1 Response Plotted Against IEEE 1547-2018 Category III Ride-Through Requirements Frequency Response (Ke=10) Zoom 2

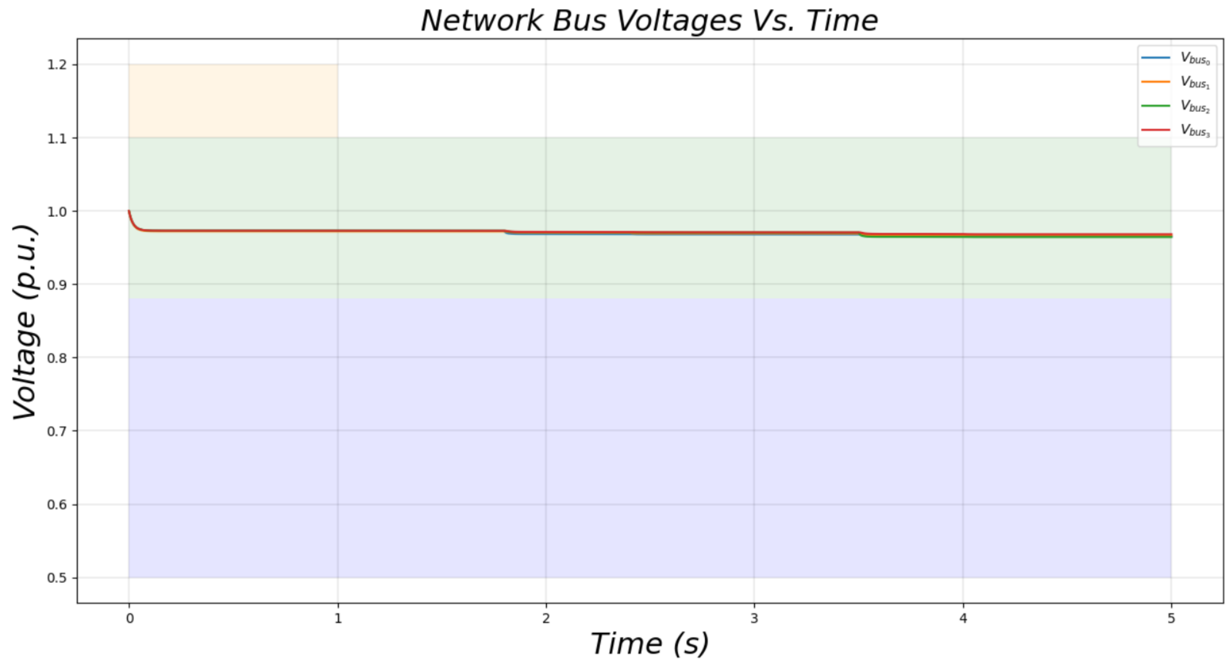

Figure 4.23: Frequency Dependent Static Load Test Case 1 Response Plotted Against IEEE 1547-2018 Category III Ride-Through Requirements Voltage Response (Ke=10)

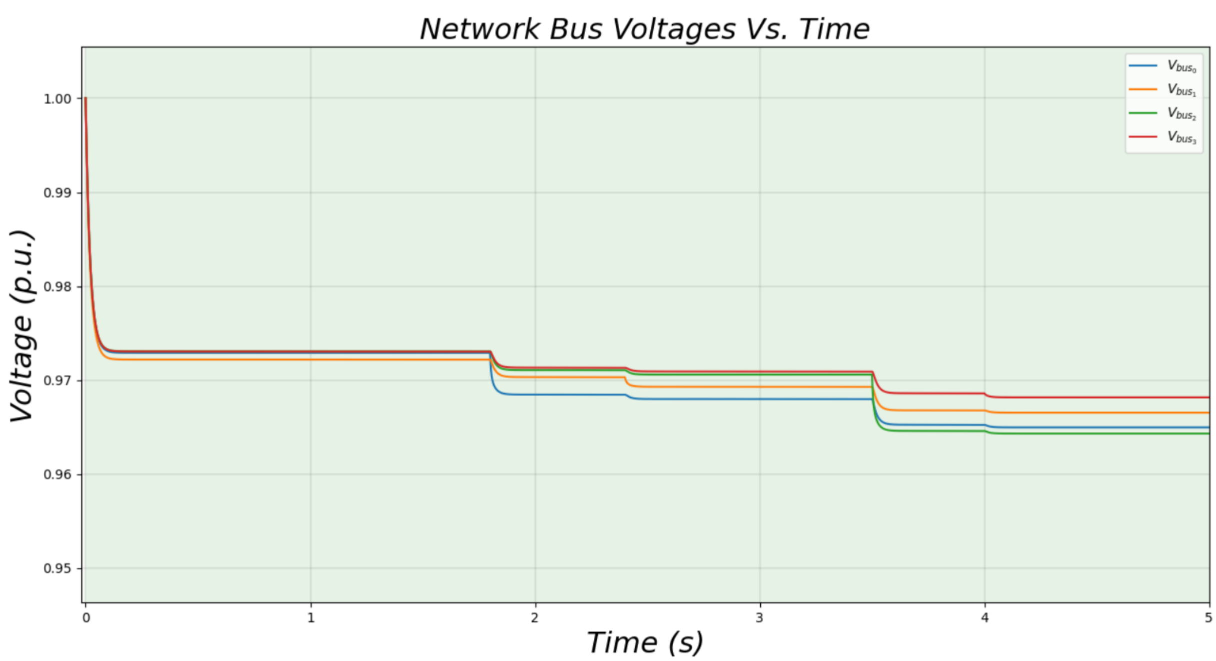

Figure 4.24: Frequency Dependent Static Load Test Case 1 Response Plotted Against IEEE 1547-2018 Category III Ride-Through Requirements Voltage Response (Ke=10) Zoom 1

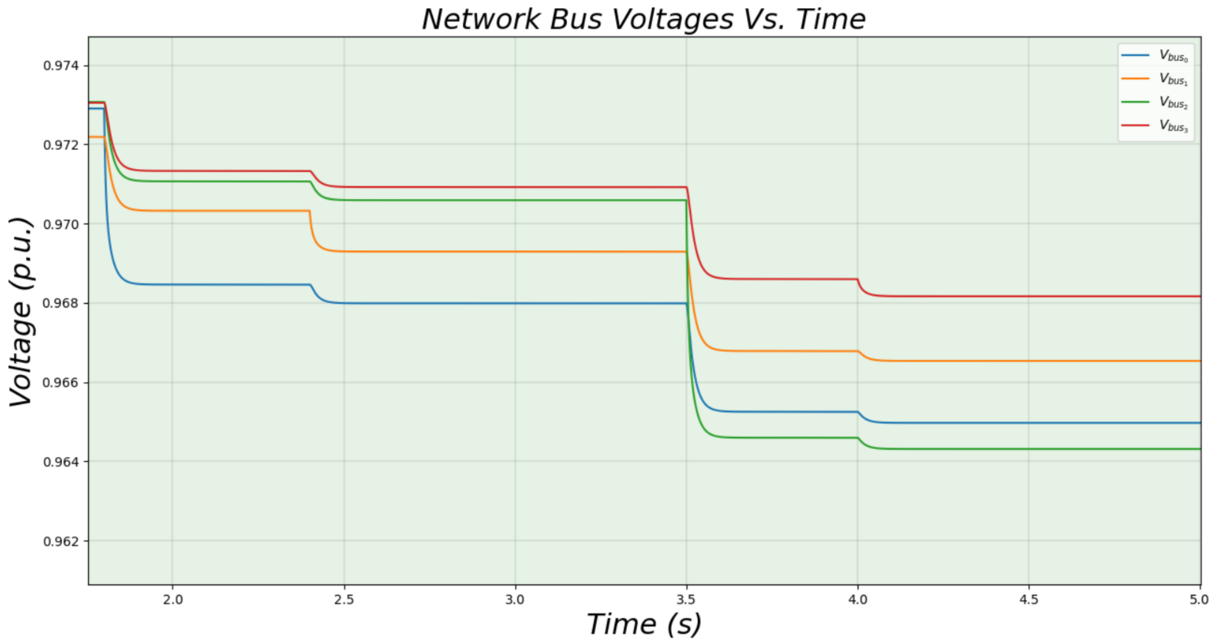

Figure 4.25: Frequency Dependent Static Load Test Case 1 Response Plotted Against IEEE 1547-2018 Category III Ride-Through Requirements Voltage Response (Ke=10) Zoom 2

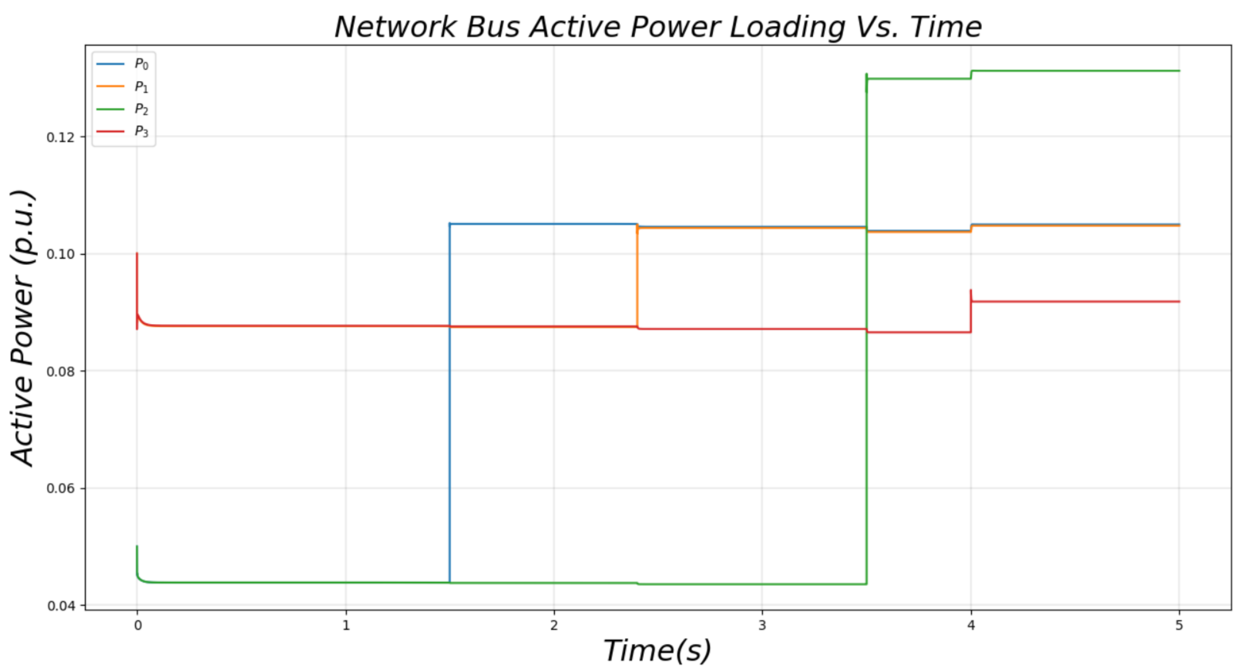

Figure 4.26: Frequency Dependent Static Load Test Case 1 Active Power Load Response (Ke=10)

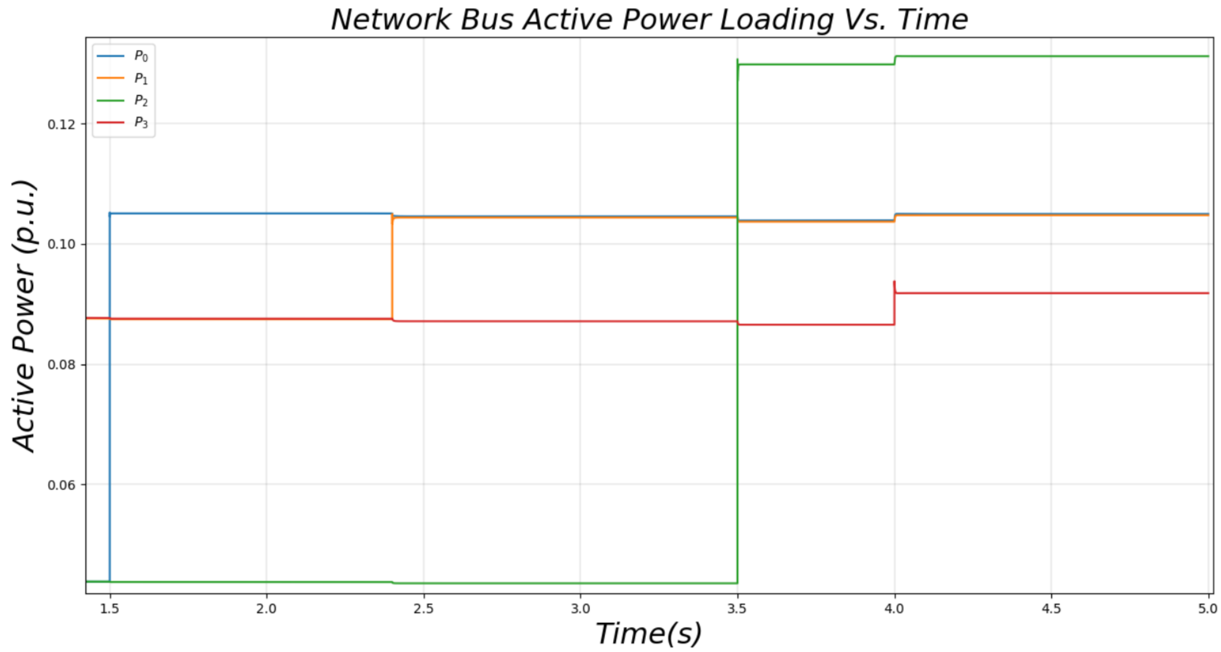

Figure 4.27: Frequency Dependent Static Load Test Case 1 Active Power Load Response (Ke=10) Zoom

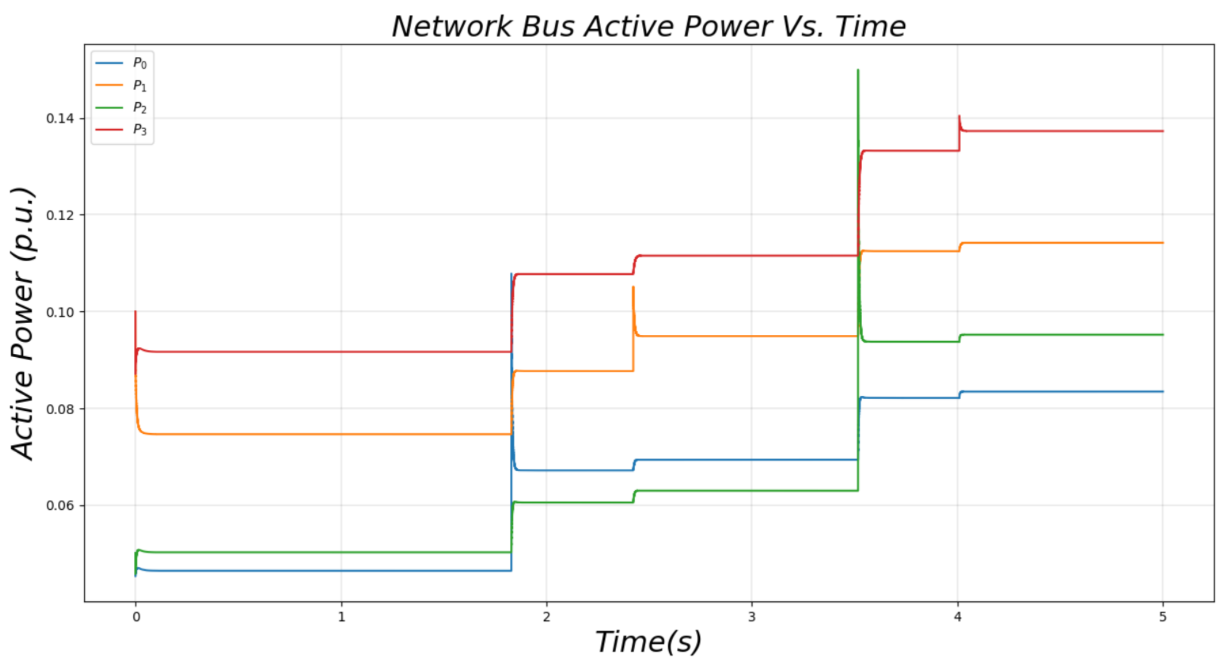

Figure 4.28: Frequency Dependent Static Load Test Case 1 DER Active Power Response (Ke=10)

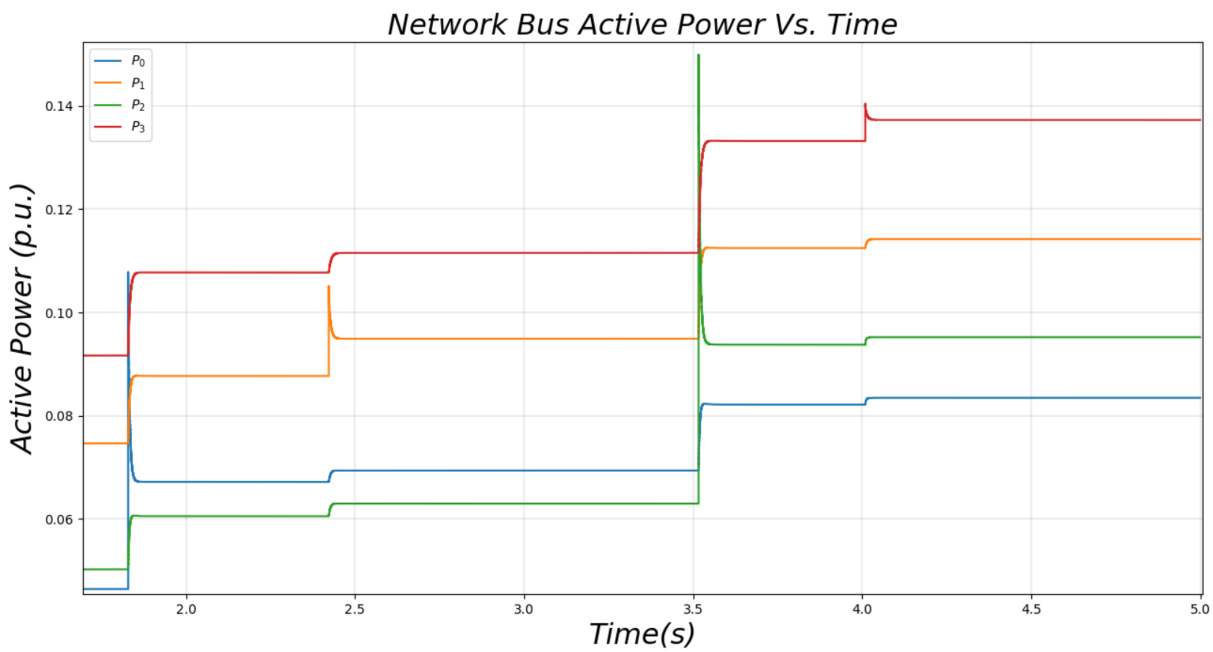

Figure 4.29: Frequency Dependent Static Load Test Case 1 DER Active Power Response (Ke=10) Zoom

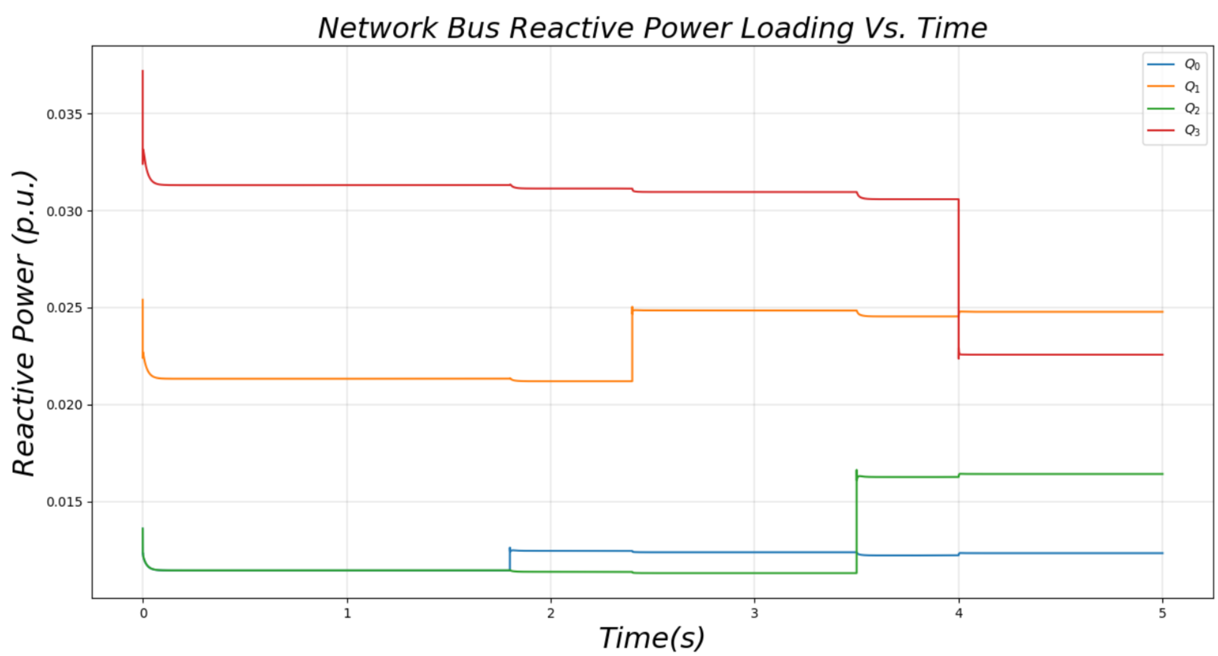

Figure 4.30: Frequency Dependent Static Load Test Case 1 Rective Power Load Response (Ke=10)

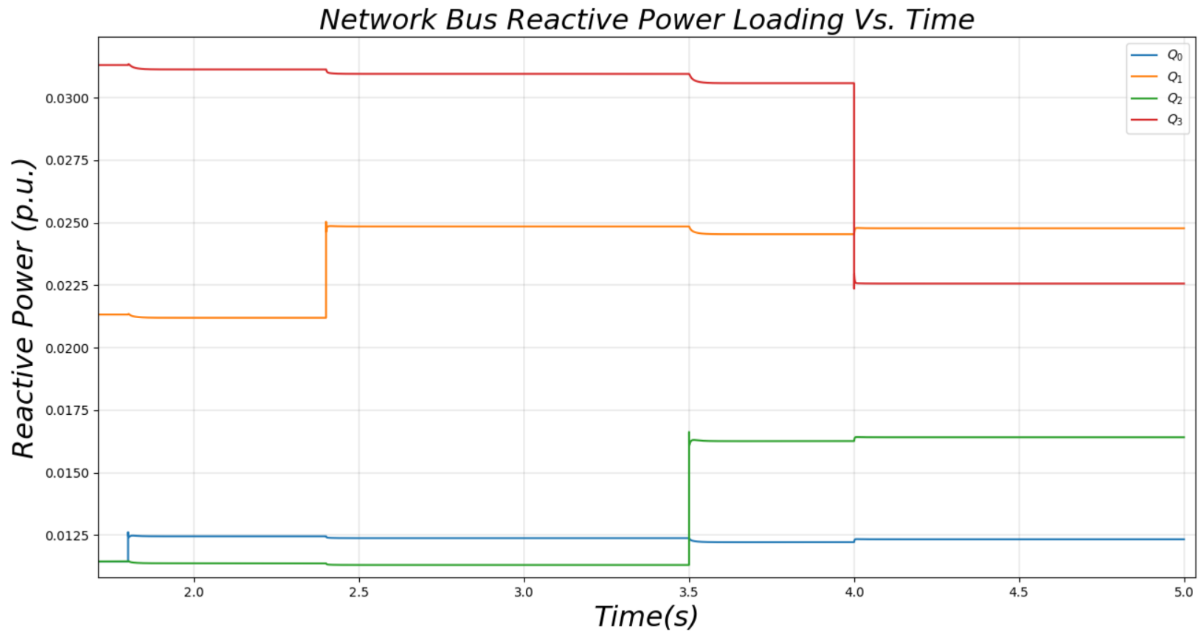

Figure 4.31: Frequency Dependent Static Load Test Case 1 Rective Power Load Response (Ke=10) Zoom

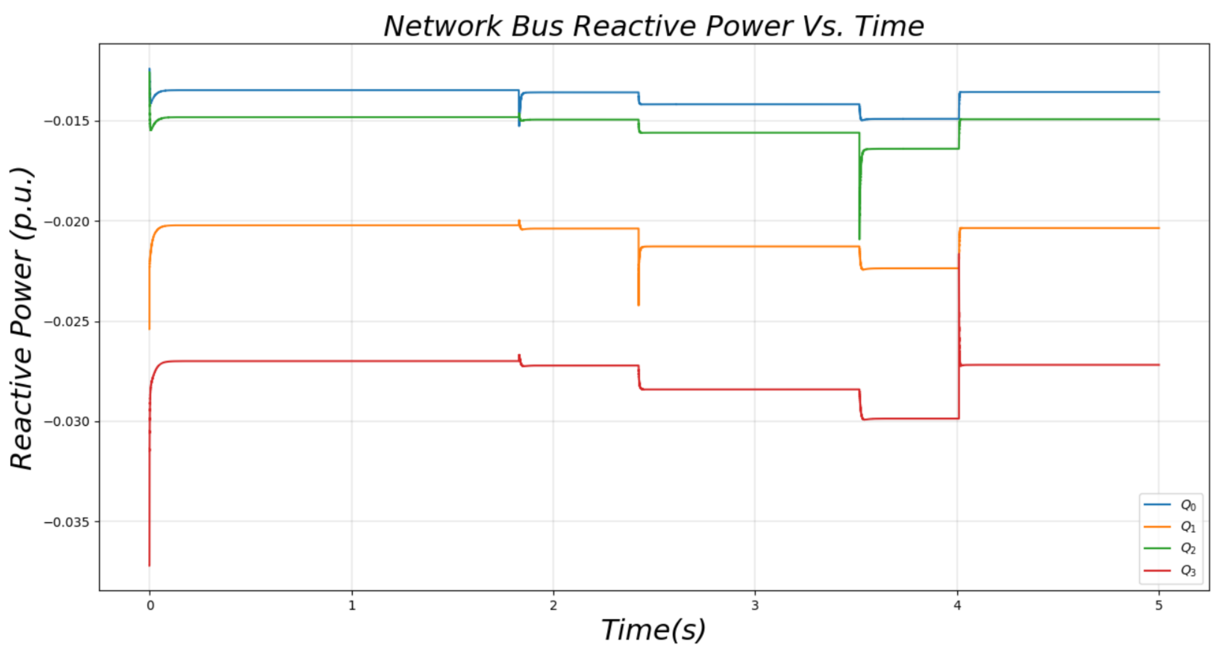

Figure 4.32: Frequency Dependent Static Load Test Case 1 DER Rective Power Load Response (Ke=10)

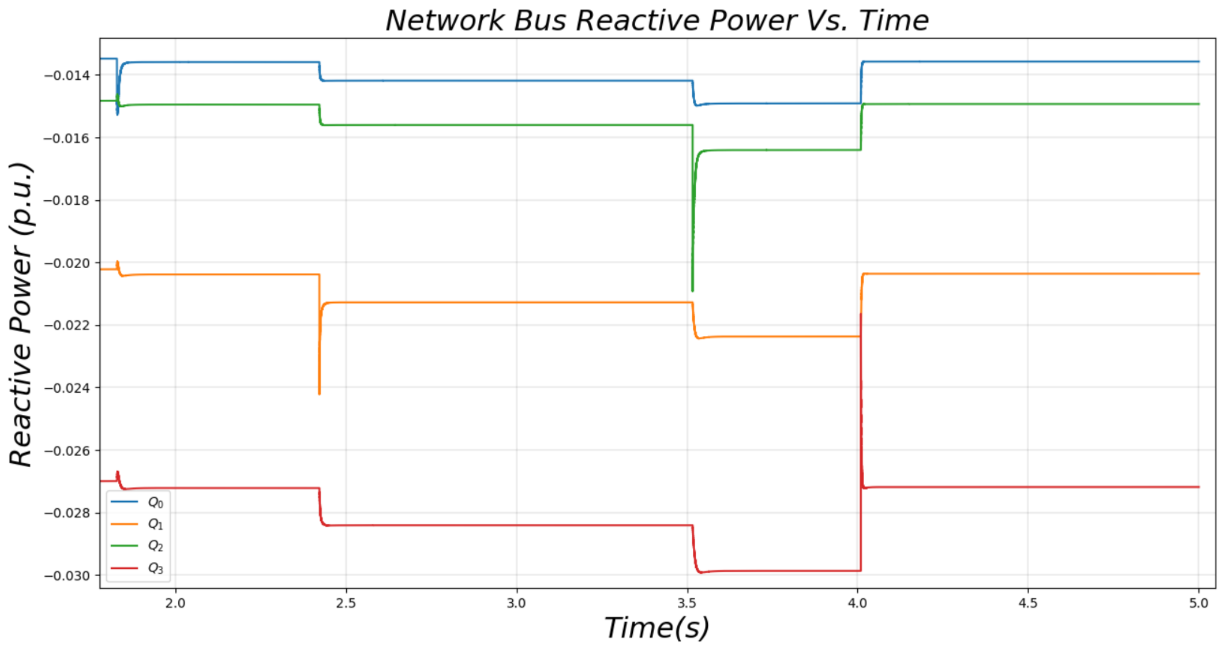

Figure 4.33: Frequency Dependent Static Load Test Case 1 DER Rective Power Load Response (Ke=10) Zoom

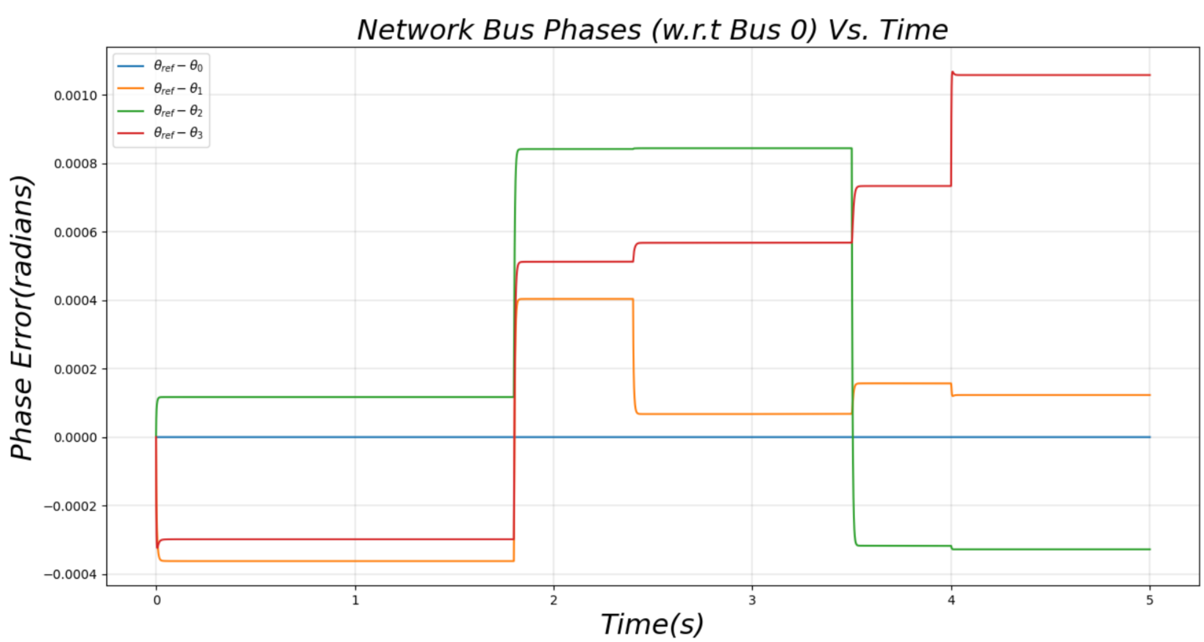

Figure 4.34: Frequency Dependent Static Load Test Case 1 DER Phase Response (Ke=10)

Figures 4.26-4.34 demonstrate a significant difference in the active/reactive loading and DER active/reactive output power in response to the adjustment of the proportional droop control gain adjustment. Demonstrated in the DER active output power response with $K_{I_E} = 10$ in figure 4.29 in comparison to figure 4.11 with $K_{I_E} = 1$ response, the active power output is higher at each bus on the network. The increase in voltage gain leads to a more prominent voltage feedback error signal resulting in additional voltage compensation at the output of each DER on the network. The loads on the network are dominated by the exponential voltage terms in equations (3.12) and (3.13). Thus, a larger active power consumption of each load based on the voltage profile of the network; displayed in figure (4.9) and (4.30). Similarly, the reactive loading is also a function of the network voltage profile and the result of the feedback gain adjustment increased the reactive loading and output of the DER's. Therefore, the reactive loading results in a lower network frequency ranging between 59.85-59.875 Hz in comparison to $K_{I_E} = 1$ frequency response ranging between 59.93-59.935 Hz. In summation, the adjusted voltage droop gain results in a more robust low-voltage network in which the voltage profile is maintained within the continuous operation region and the system maintains nominal operation and intact with load disturbances on the network.

4.4 EPRI Load Syn Disturbance Analysis

As indicated in section 3.2.1.4, the EPRI Load Syn model is the weighted sum of multiple exponential and frequency dependent loads attached to the PCC. In a low-voltage network, the PCC can be seen as the distribution panel which aggregates the loads of the interconnected home. Thus, allowing for a more complete load model to be used within the low-voltage network simulation. Maintaining the same DER generation and interconnect settings from tables 4.2, 4.3 and 4.4 in section 4.1, we proceed to test the low-voltage network with a load model that encapsulates multiple loads at each distribution panel in the network. The parameters for the EPRI LoadSyn model are taken from the work done in [35] and are demonstrated in table 4.5.

EPRI LoadSyn Initial Load							
Bus	**Time (s)**	**Active Power Parameters**	**Reactive Power Parameters**	**Rated Power**		**Load Power**	
-	-	$K_{pz}, K_{pi}, K_{pc}, K_{p1,}K_{p2}.$ $k_{pf1}, k_{pf2}, n_{pv1}, n_{pv2}$	$K_{qz}, K_{qi}, K_{qc}, K_{q1,}K_{q2}.$ $k_{qf1}, k_{qf2}, n_{qv1}, n_{qv2}$	$\boldsymbol{P_R}$	$\boldsymbol{Q_R}$	$\boldsymbol{P_L}$	$\boldsymbol{Q_L}$
0	0	0.3, 0, 0, 0.2, 0.5, 1, 1.9, 1.0, 0.1	-0.1516, 0, 0, 0.4845, 0.672, -2.8, 1.2, 3.0, 0.5	0.1	0.044	0.05	0.0136
1	0	0.3, 0, 0, 0.2, 0.5, 1, 1.9, 1.0, 0.1	-0.1516, 0, 0, 0.4845, 0.672, -2.8, 1.2, 3.0, 0.5	0.15	0.066	0.10	0.0254
2	0	0.3, 0, 0, 0.2, 0.5, 1, 1.9, 1.0, 0.1	-0.1516, 0, 0, 0.4845, 0.672, -2.8, 1.2, 3.0, 0.5	0.11	0.0484	0.05	0.0136
3	0	0.3, 0, 0, 0.2, 0.5, 1, 1.9, 1.0, 0.1	-0.1516, 0, 0, 0.4845, 0.672, -2.8, 1.2, 3.0, 0.5	0.2	0.088	0.1	0.0372
Total:		-	-	0.56	0.2464	0.3	0.0898
EPRI LoadSyn Load Step							
Bus	**Time (s)**	**Active Power Parameters**	**Reactive Power Parameters**	**Rated Power**		**Load Power**	
-	-	$K_{pz}, K_{pi}, K_{pc}, K_{p1,}K_{p2}.$ $k_{pf1}, k_{pf2}, n_{pv1}, n_{pv2}$	$K_{qz}, K_{qi}, K_{qc}, K_{q1,}K_{q2}.$ $k_{qf1}, k_{qf2}, n_{qv1}, n_{qv2}$	$\boldsymbol{P_R}$	$\boldsymbol{Q_R}$	$\boldsymbol{P_L}$	$\boldsymbol{Q_L}$
0	1.5-2.4	0.3, 0, 0, 0.2, 0.5, 1, 1.9, 1.0, 0.1	-0.1516, 0, 0, 0.4845, 0.672, -2.8, 1.2, 3.0, 0.5	0.1	0.044	0.09	0.015
1	2.4-3.5	0.3, 0, 0, 0.2, 0.5, 1, 1.9, 1.0, 0.1	-0.1516, 0, 0, 0.4845, 0.672, -2.8, 1.2, 3.0, 0.5	0.15	0.066	0.12	0.03
2	3.5-4.0	0.3, 0, 0, 0.2, 0.5, 1, 1.9, 1.0, 0.1	-0.1516, 0, 0, 0.4845, 0.672, -2.8, 1.2, 3.0, 0.5	0.11	0.0484	0.08	0.02
3	4.0-4.8	0.3, 0, 0, 0.2, 0.5, 1, 1.9, 1.0, 0.1	-0.1516, 0, 0, 0.4845, 0.672, -2.8, 1.2, 3.0, 0.5	0.2	0.088	0.15	0.0272
Total:		-	-	0.56	0.2464	0.515	0.0922

Table 4.5: EPRI LoadSyn Static Load Test Case

Similar to the tests performed in section 4.3, the generation sources on the network are synchronized to the utility grid and the grid state is in a normal operation state at a voltage of 1.0 p.u. and frequency of 60Hz. At time t=0 seconds, the network goes from grid connected mode to microgrid/islanded mode instantaneously. The initial EPRI loadsyn loads on the networks are demonstrated by rows 4-7 and columns 7-8 in table 4.5. Beginning at time t=1.5 seconds, the network experiences an instantaneous load step disturbance at each bus on the network according to table column 2 rows 12-15 in table 4.5. At each bus, the load models maintain the same load parameters but increase their active and reactive loading, demonstrated in column 6 in table 4.5. The following results are obtained.

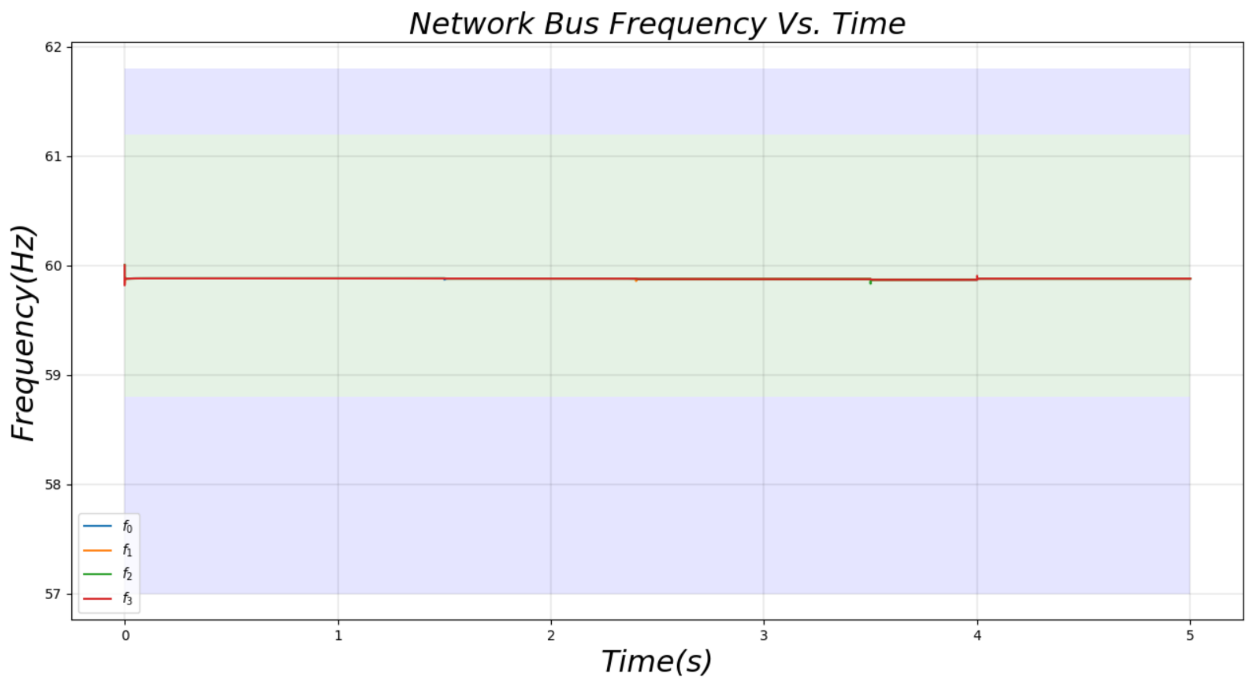

Figure 4.35: EPRI LoadSyn Model Network Frequency Response (Ke=10)

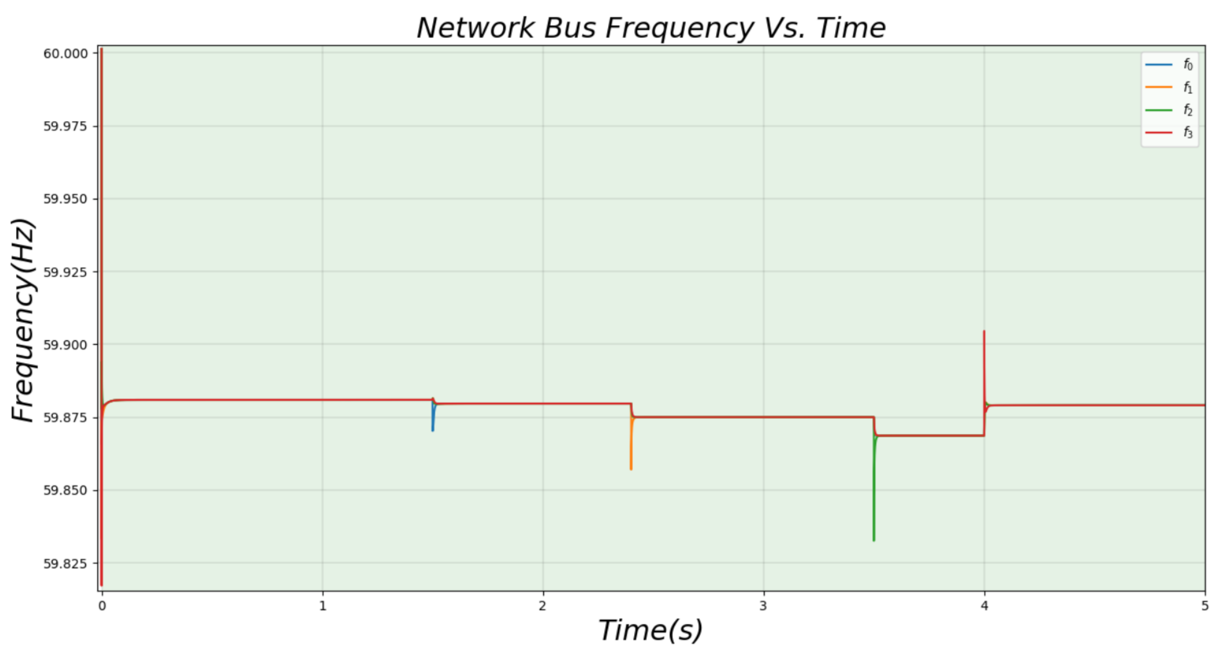

Figure 4.36: EPRI LoadSyn Model Network Frequency Response Zoom (Ke=10)

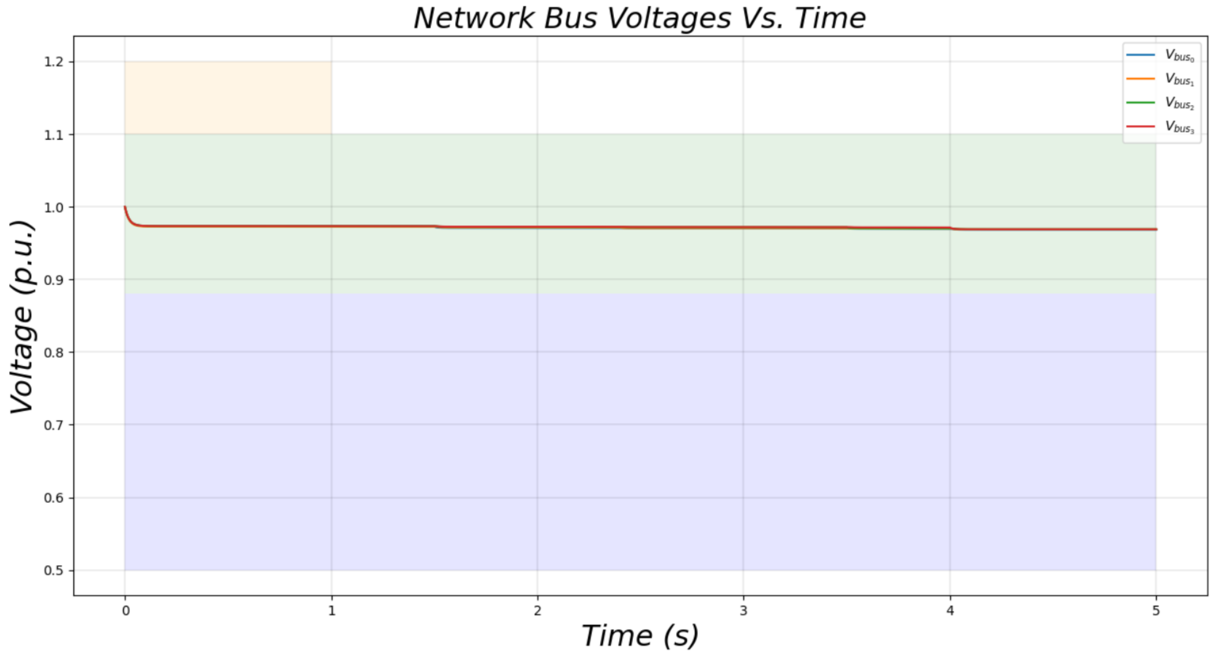

Figure 4.37: EPRI LoadSyn Model Network Voltage Profile (Ke=10)

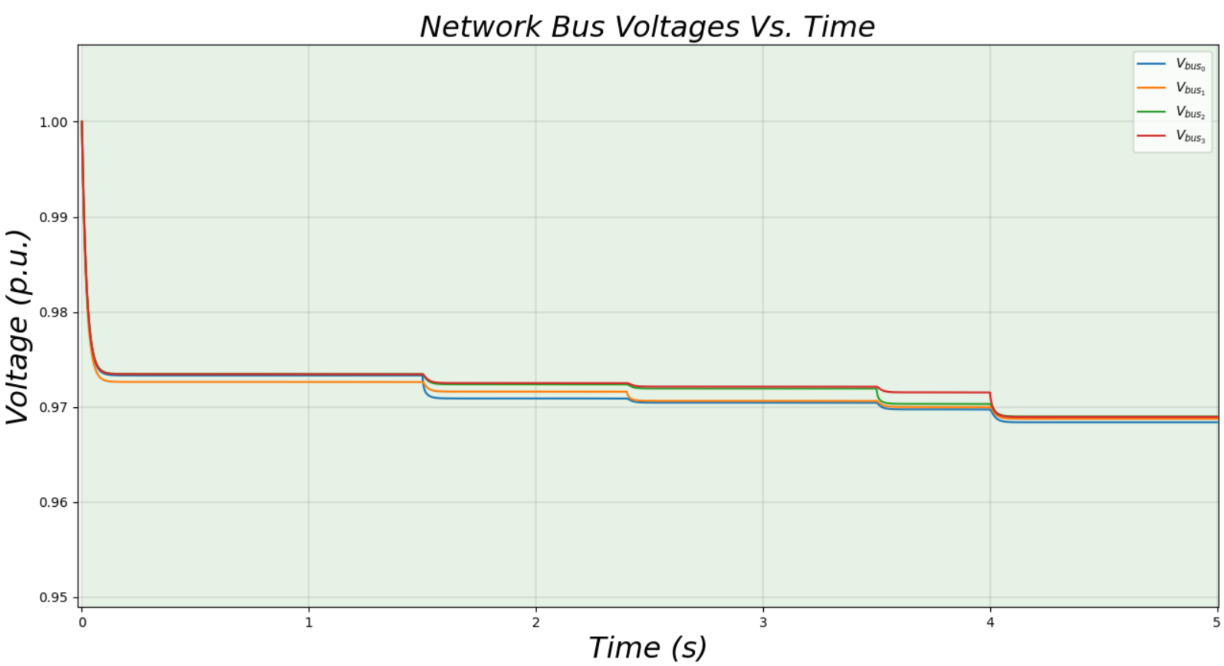

Figure 4.38: EPRI LoadSyn Model Network Voltage Profile Zoom (Ke=10)

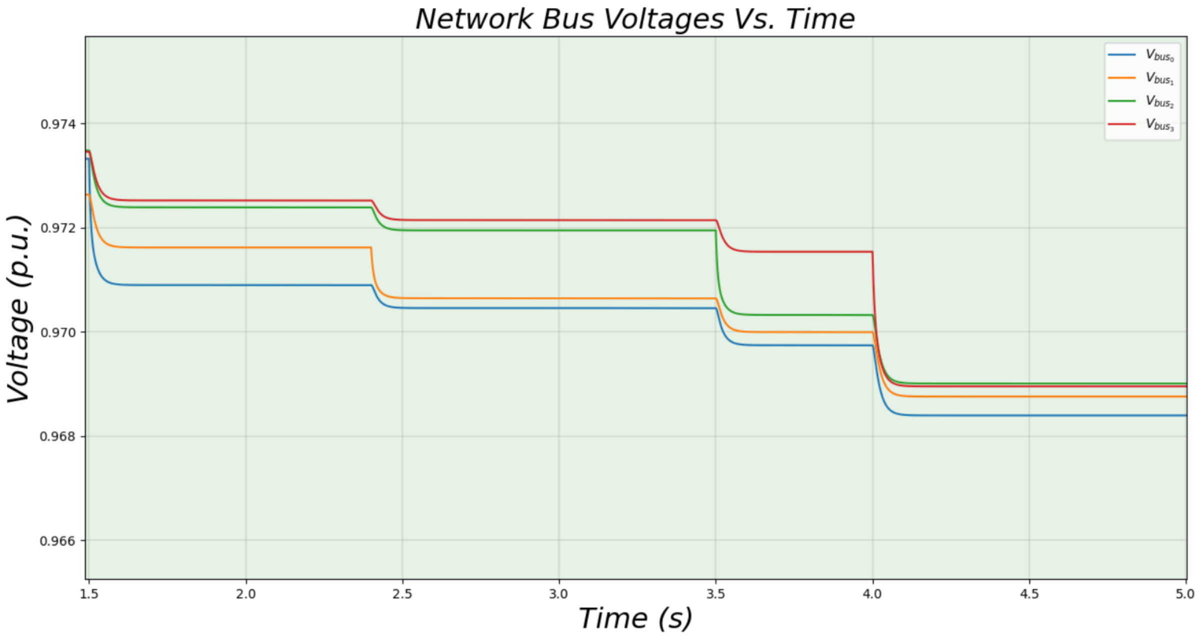

Figure 4.39: EPRI LoadSyn Model Network Voltage Profile Load Zoom (Ke=10)

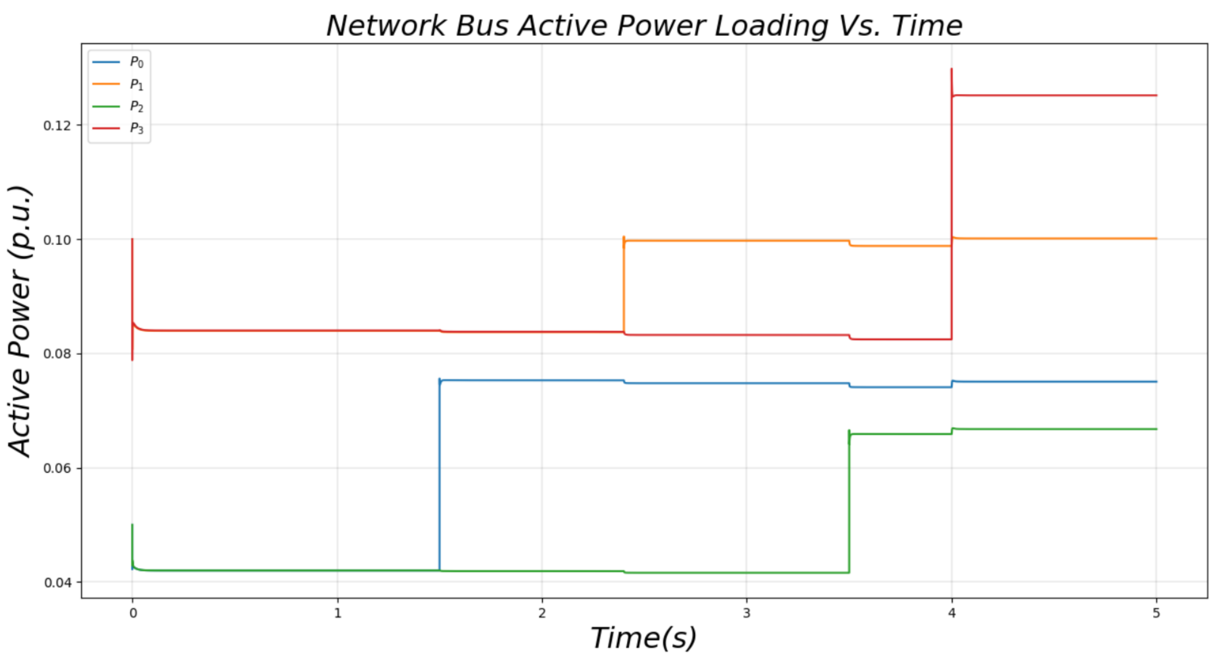

Figure 4.40: EPRI LoadSyn Low-Voltage Network Bus Load Powers (Ke=10)

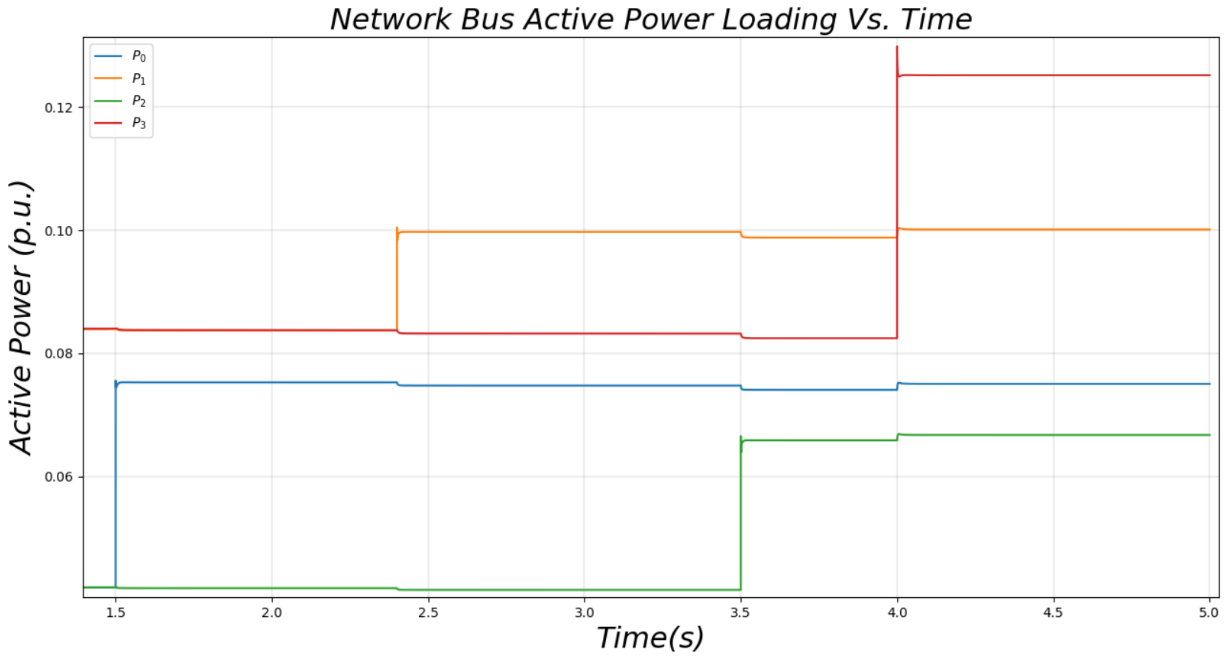

Figure 4.41: EPRI LoadSyn Low-Voltage Network Bus Load Powers Zoom 2 (Ke=10)

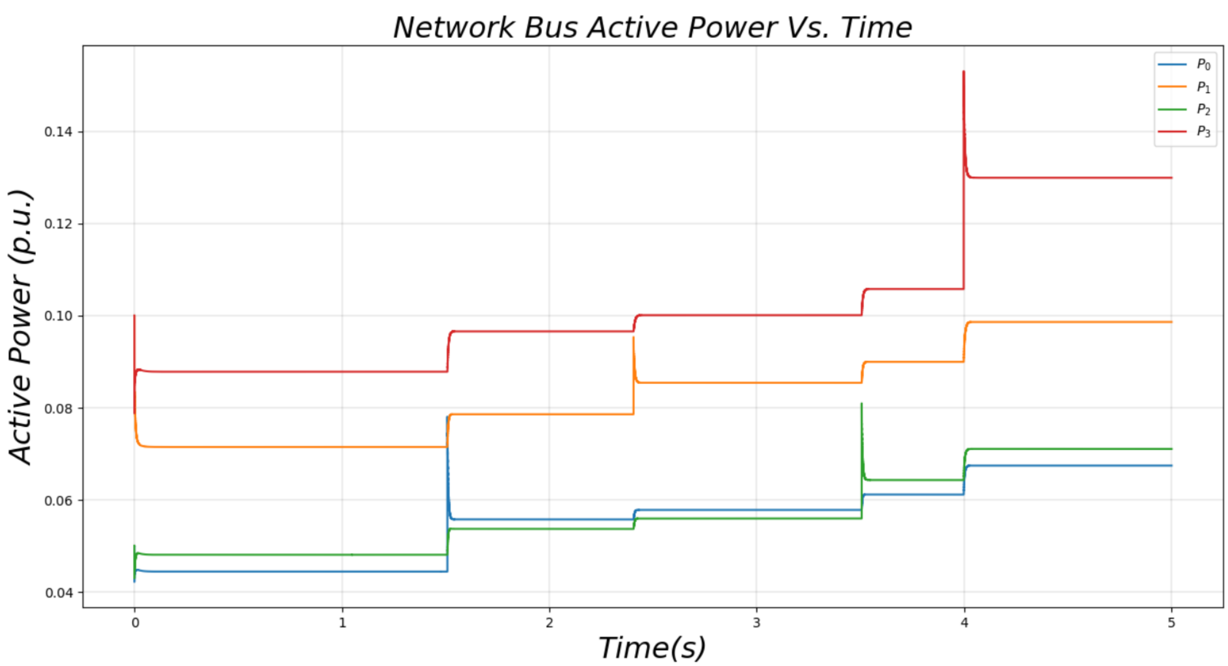

Figure 4.42: EPRI LoadSyn Model Bus Active Power Injections (Ke=10)

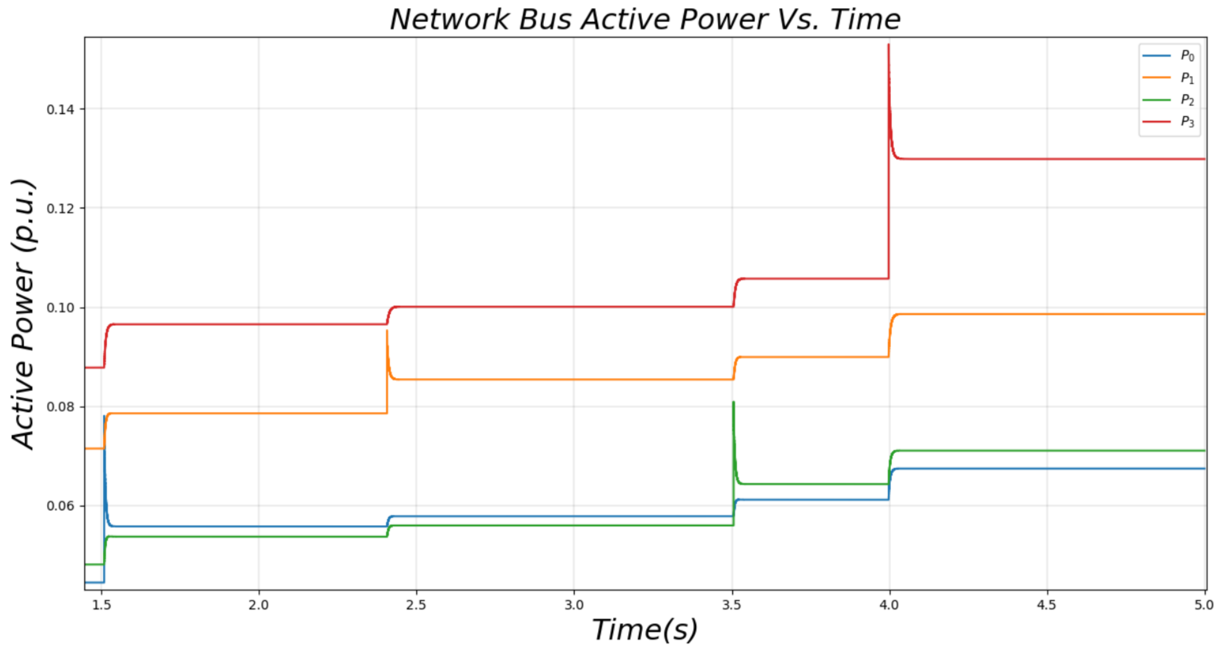

Figure 4.43: EPRI LoadSyn Model Bus Active Power Injections Load Step Zoom (Ke=10)

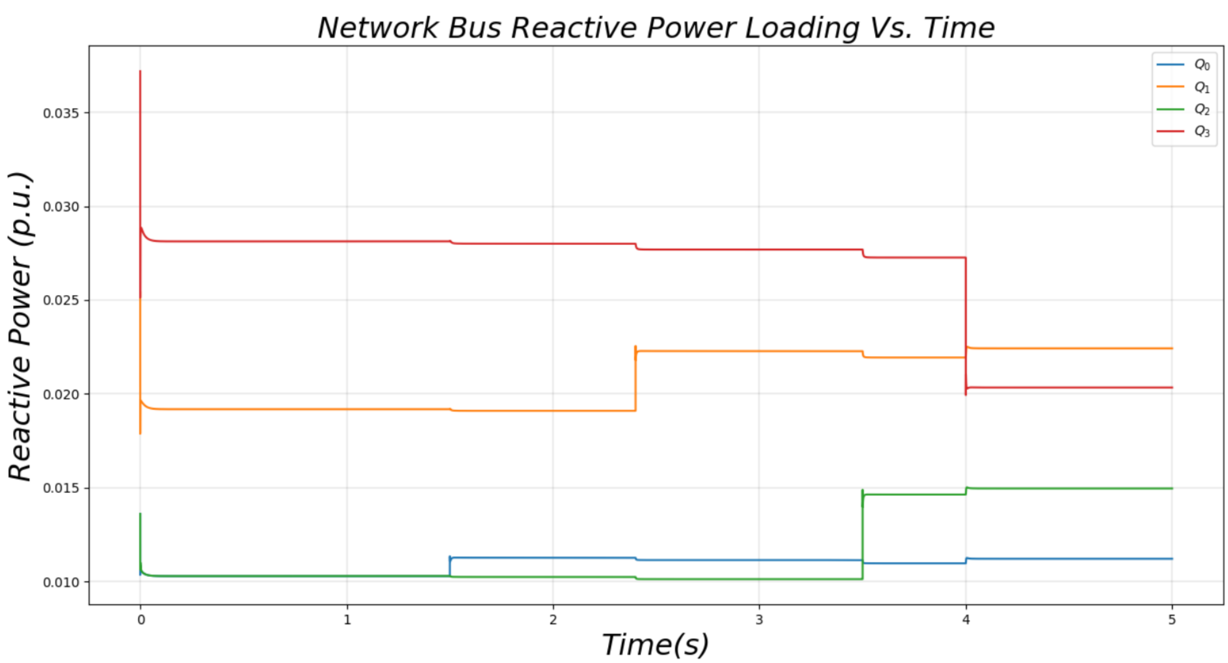

Figure 4.44: EPRI LoadSyn Model Bus Reactive Power Loading (Ke=10)

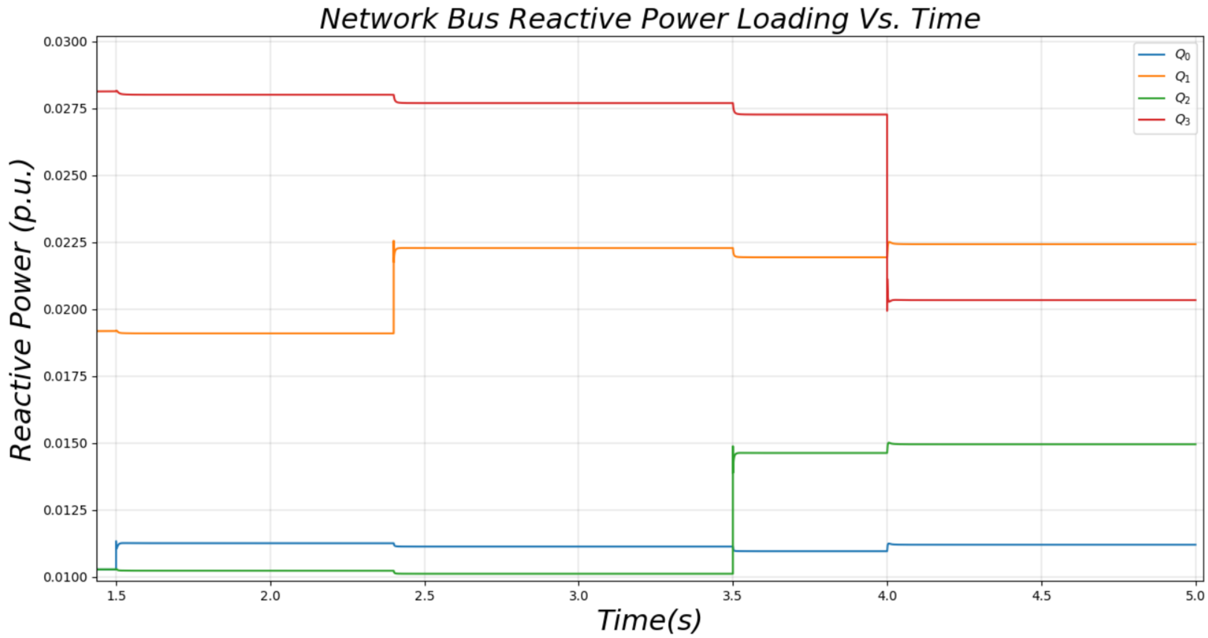

Figure 4.45: EPRI LoadSyn Model Bus Reactive Power Loading Zoom (Ke=10)

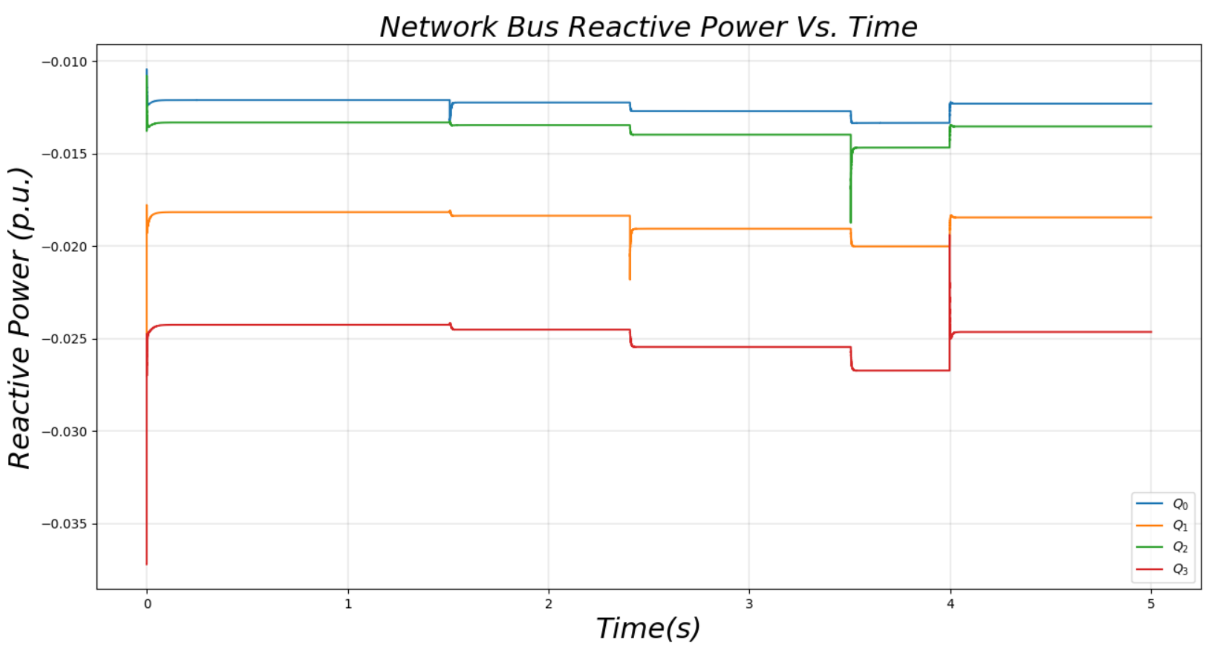

Figure 4.46: EPRI LoadSyn Model Bus DER Reactive Power Injection (Ke=10)

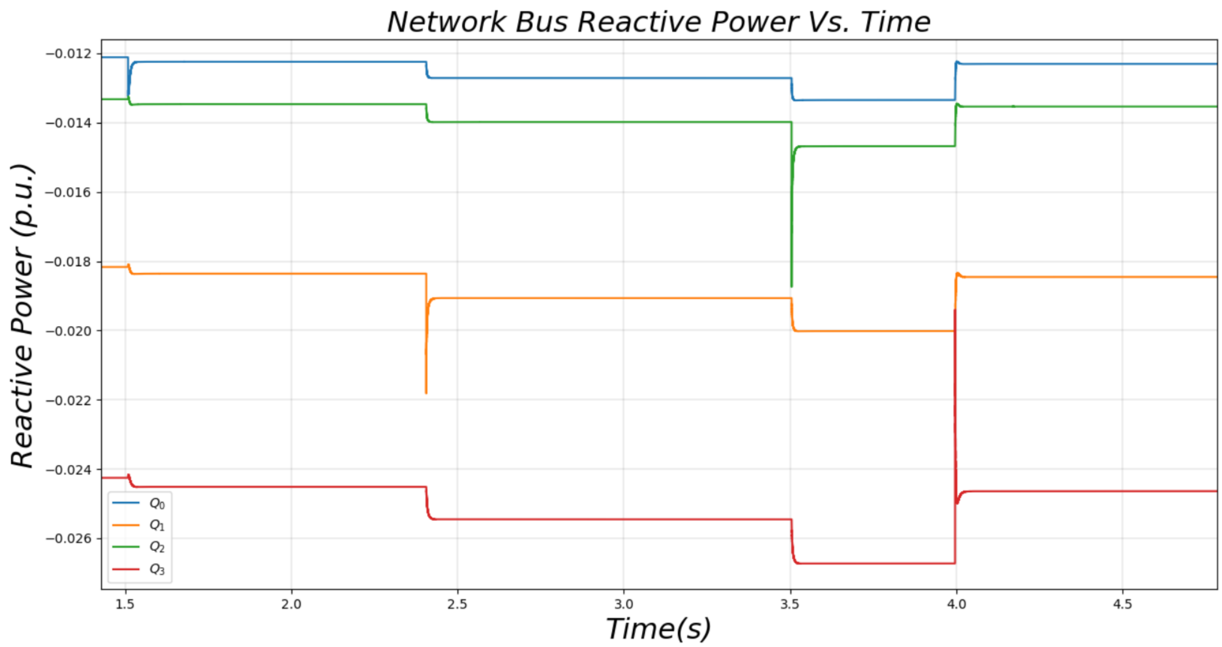

Figure 4.47: EPRI LoadSyn Model Bus DER Reactive Power Injection Zoom (Ke=10)

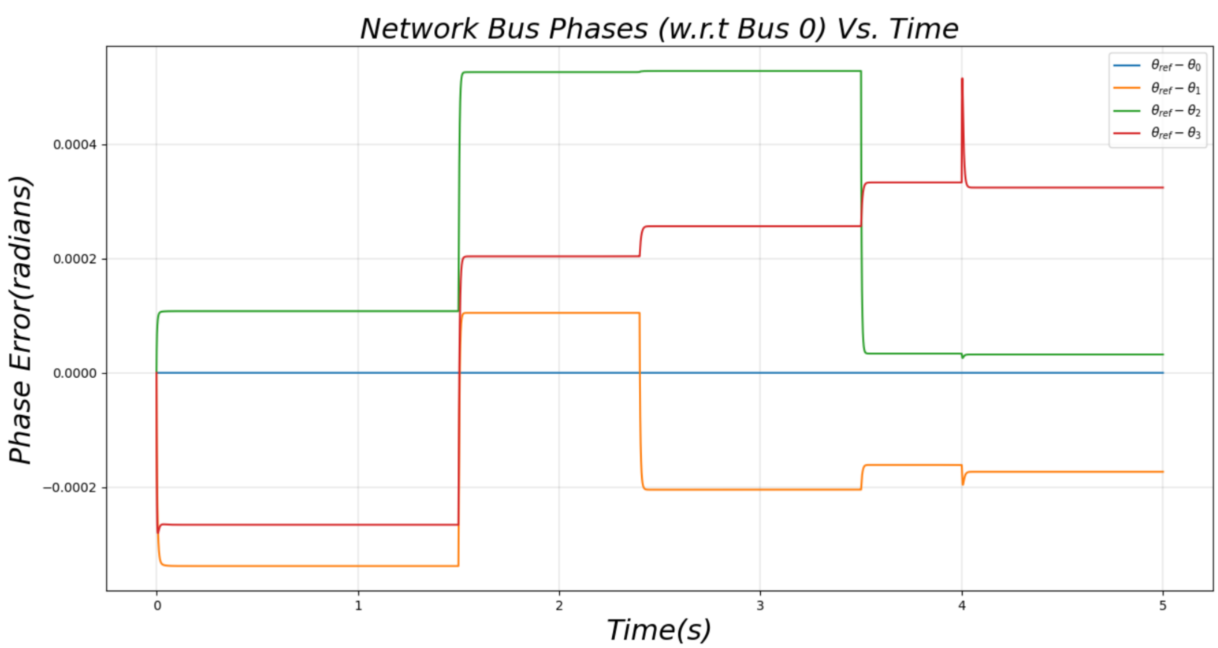

Figure 4.48: EPRI LoadSyn Model DER Phase Response to Load Step Distrubances (Ke=10)

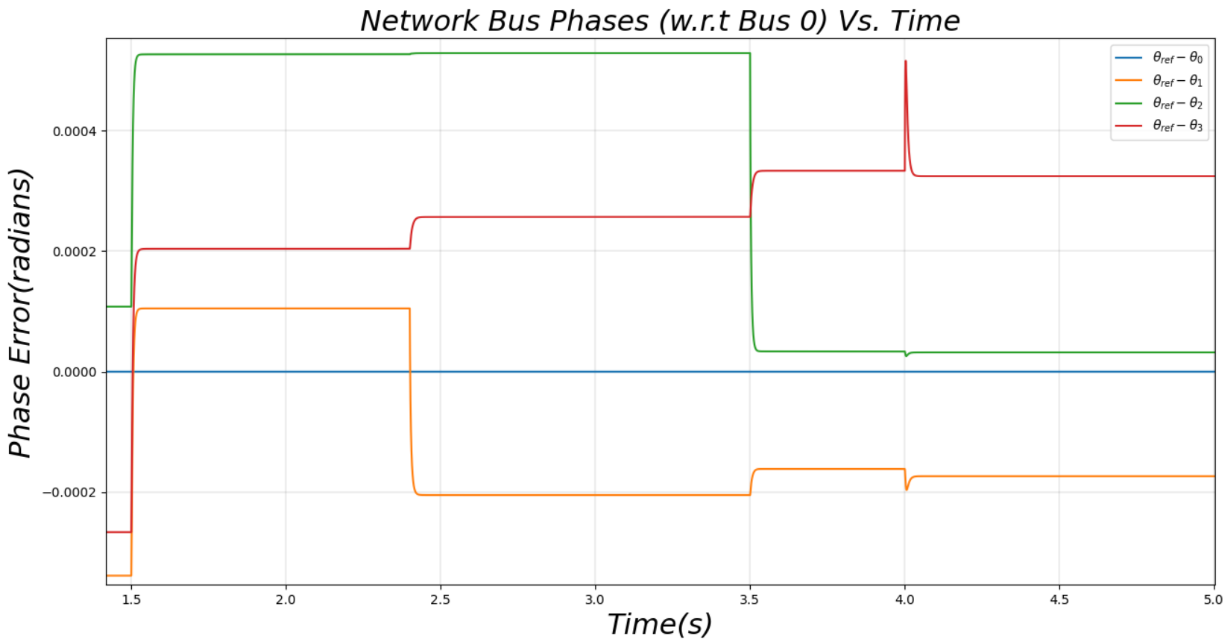

Figure 4.49: EPRI LoadSyn Model DER Phase Response to Load Step Distrubances (Ke=10)

The results of the low-voltage network simulation are presented in figures 4.35-4.49 with a proportional droop voltage feedback gain of $K_{I_E} = 10$. This section omits the results for voltage droop feedback gain $K_{I_E} = 1$ due to the similarity in response to that of section 4.3 figures 4.3-4.19. The low-voltage network within this simulation is intact, stable and within its normal operation state despite the load disturbances experienced on the network. Figure 4.39 depicts the impacts of loading on the low-voltage network voltage profile. At $t = 1.5\ seconds$, the low-voltage network experiences the first load step at bus 0 as indicated by the active/reactive power loading in figures 4.40 and 4.44. As a result, the voltage profile of the network falls to a new steady state based on the individual DER settings at each bus on the network. The voltage at bus 0 experiences the largest voltage drops within the network due to the load step experienced at its PCC bus. The other DER on the network also experience this load step despite the load on bus 0 being within bus 0s DER rated power; the load is shared amongst all DERs within the network. Based on the work proven in [23], the DER share their load based on their respective droop gains and coupling impedance. As the load steps increase on each bus within the network the voltage response at each bus experiences a similar response to bus 0 based on the respective loads at each bus.

The frequency of the network is stable and synchronization of DER within the network are maintained throughout each load disturbance. A stable operating frequency based on the loading on the networks is maintained around 59.875Hz. At each reactive load step, there is a brief frequency disturbance at each bus in the network due to droop controller adjusting their respective phase response. This is illustrated by the frequency, phase and reactive power responses in figures 4.36, 4.44 and 4.49. Due to the coupling strength of the interconnections in the network, the droop controlled DER maintain synchronization and frequency stability.

4.5 Exponential Recovery Load Disturbance Analysis

The low-voltage network is now tested against the exponential recovery dynamic load model. As discussed in section 3.2.2.1, the ERL model is responsible for modelling the dynamic response for thermostat-controlled loads on the power system. Within the low-voltage network, this load model is responsible for capturing a residential HVAC system. The ERL load model parameters employed within this simulation are from the work done in [37] [38], where the load parameters are fitted to measured voltage and frequency responses on a residential distribution system bus. The ERL model has a large time constant and exhibits a response on the time scale of minutes; the simulation time is adjusted accordingly.

Similar to sections 4.3-4.4, the DER generation and interconnect settings from tables 4.2, 4.3 and 4.4 are maintained. At t = 0 seconds, the generation sources on the network are synchronized to the utility grid and the grid state is in a normal operation state at a voltage of 1.0 p.u. and frequency of 60Hz. At time t=0 seconds, the network goes from grid connected mode to microgrid/islanded mode instantaneously. The initial loads on the network during disconnection are EPRI loadsyn static loads with minimal loading on the network and are demonstrated by the initial load section of table 4.6.

Initial Load							
Bus	**Time (s)**	**Active Power Parameters**	**Reactive Power Parameters**	**Rated Power**		**Load Power**	
-	-	$K_{pz}, K_{pi}, K_{pc}, K_{p1,} K_{p2}.$ $k_{pf1}, k_{pf2}, n_{pv1}, n_{pv2}$	$K_{qz}, K_{qi}, K_{qc}, K_{q1,} K_{q2}.$ $k_{qf1}, k_{qf2}, n_{qv1}, n_{qv2}$	***P_R***	***Q_R***	***P_L***	***Q_L***
0	0	0.3, 0, 0, 0.2, 0.5, 1, 1.9, 1.0, 0.1	-0.1516, 0, 0, 0.4845, 0.672, -2.8, 1.2, 3.0, 0.5	0.1	0.044	0.05	0.0136
1	0	0.3, 0, 0, 0.2, 0.5, 1, 1.9, 1.0, 0.1	-0.1516, 0, 0, 0.4845, 0.672, -2.8, 1.2, 3.0, 0.5	0.15	0.066	0.10	0.0254
2	0	0.3, 0, 0, 0.2, 0.5, 1, 1.9, 1.0, 0.1	-0.1516, 0, 0, 0.4845, 0.672, -2.8, 1.2, 3.0, 0.5	0.11	0.0484	0.05	0.0136
3	0	0.3, 0, 0, 0.2, 0.5, 1, 1.9, 1.0, 0.1	-0.1516, 0, 0, 0.4845, 0.672, -2.8, 1.2, 3.0, 0.5	0.2	0.088	0.1	0.0372
Total:		-	-	0.56	0.2464	0.3	0.0898
Exponential Recovery Load Steps							
Bus	**Time (s)**	**Active Power Parameters**	**Reactive Power Parameters**	**Rated Power**		**Load Power**	
-	-	$x_{p0}, T_p, \alpha_t, \alpha_s$	$x_{q0}, T_q, \beta_t, \beta_s$	***P_R***	***Q_R***	***P_L***	***Q_L***
0	1.5-240	0.2, 127.6, 2.26, 0.38	0.03, 75.3, 5.22, 2.68	0.1	0.044	0.08	0.02
1	300-600	0.2, 127.6, 2.26, 0.38	0.03, 75.3, 5.22, 2.68	0.15	0.066	0.1	0.03
2	700-1000	0.2, 127.6, 2.26, 0.38	0.03, 75.3, 5.22, 2.68	0.11	0.0484	0.08	0.03
3	1000-1800	0.2, 127.6, 2.26, 0.38	0.03, 75.3, 5.22, 2.68	0.2	0.088	0.105	0.0272
Total:		-	-	0.56	0.2464	0.515	0.0922

Table 4.6: Exponential Recovery Load Test Case

Beginning at time t=1.5 seconds, the network begins to experience instantaneous load step disturbances at each bus on the network according to the exponential recovery load steps load power column in table 4.6. At each bus, the load models maintain the same load parameters but increase their active and reactive loading. The voltage and frequency response of the low-voltage network in accordance to the load disturbances in table 4.6 are displayed in figures 4.50-4.53 and are plotted against the IEEE 1547-2018 Cat-III requirements. The network results are demonstrated first for a proportional droop control gain $K_{I_E} = 1$ in figures 4.50-4.58 and $K_{I_E} = 10$ in figures 4.59-4.67.

The low-voltage network simulation is run for approximately 30 minutes to capture the full effects of the ERL. Due to the ERL modelling HVAC loads, induction motor-based loads, the reactive power response is much more prominent in comparison to the static load models in section 4.3-4.4. Thus, a greater impact on the system frequency as indicated by figures 4.50 & 4.51.

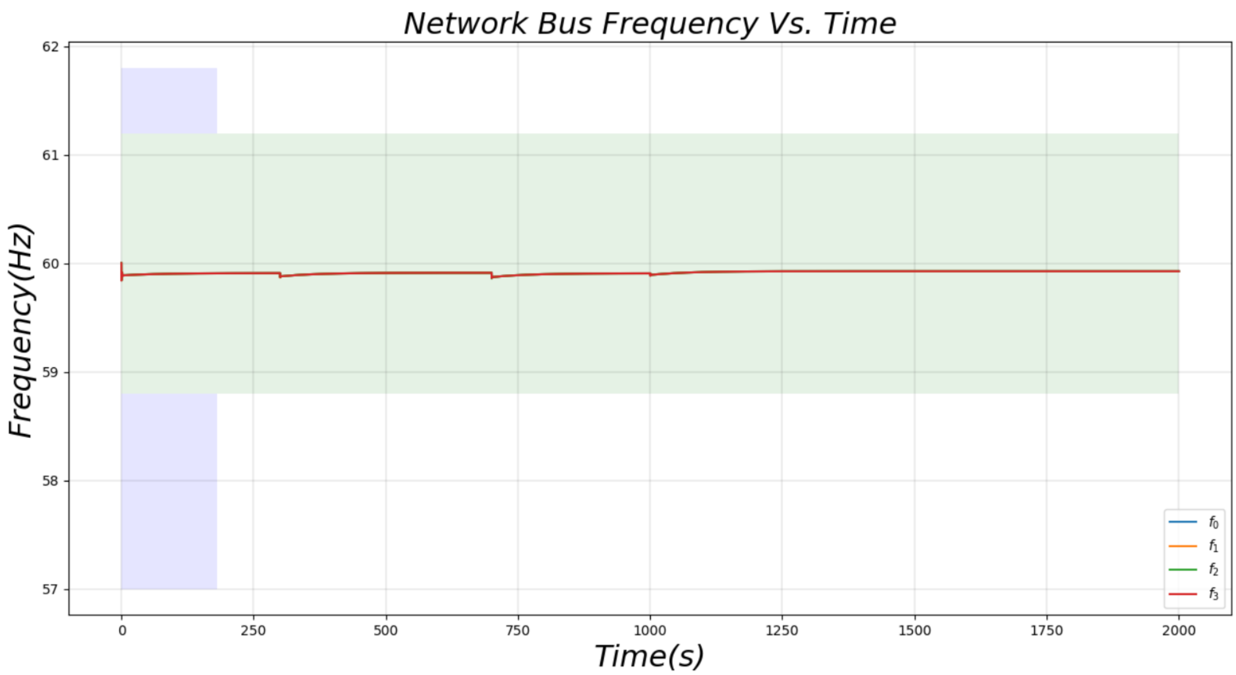

Figure 4.50: ERL Model Network Frequency Response (Ke=1)

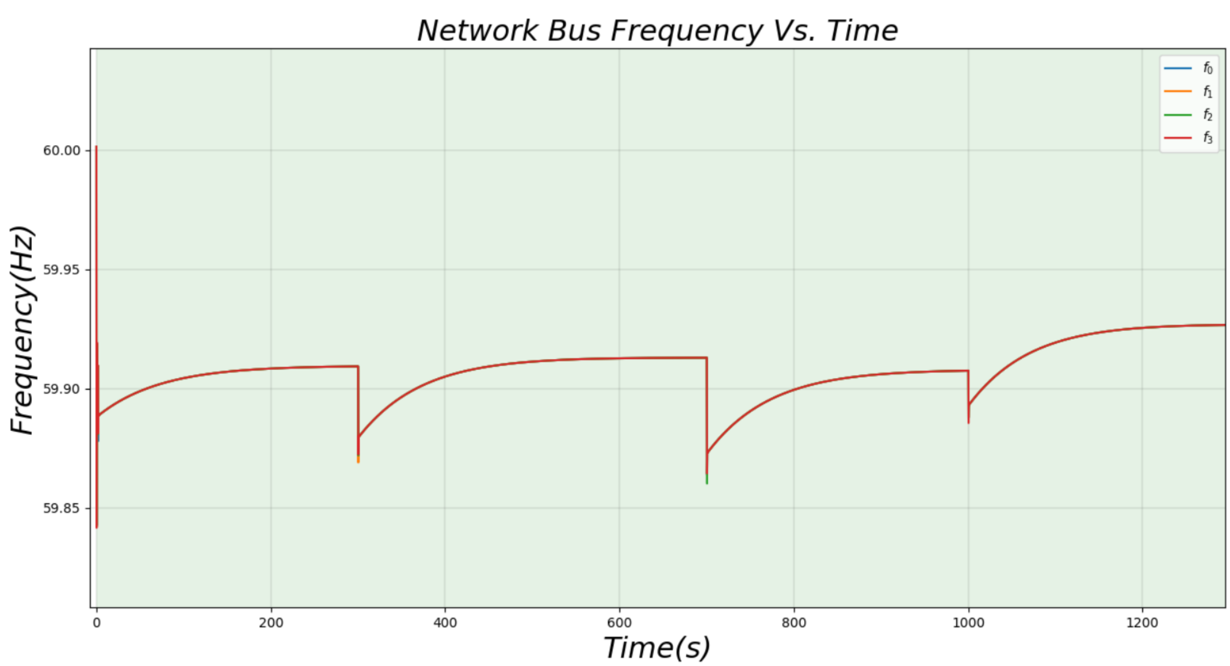

Figure 4.51: ERL Model Network Frequency Response Zoom (Ke=1)

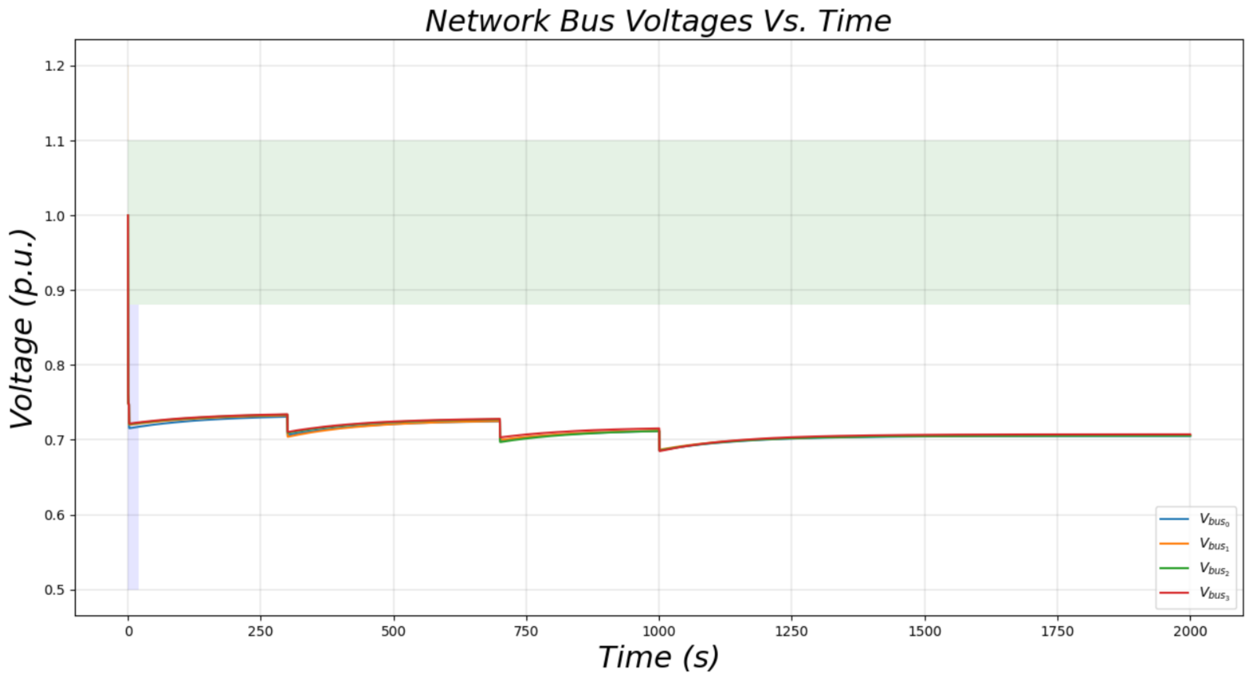

Figure 4.52: ERL Model Network Voltage Response (Ke=1)

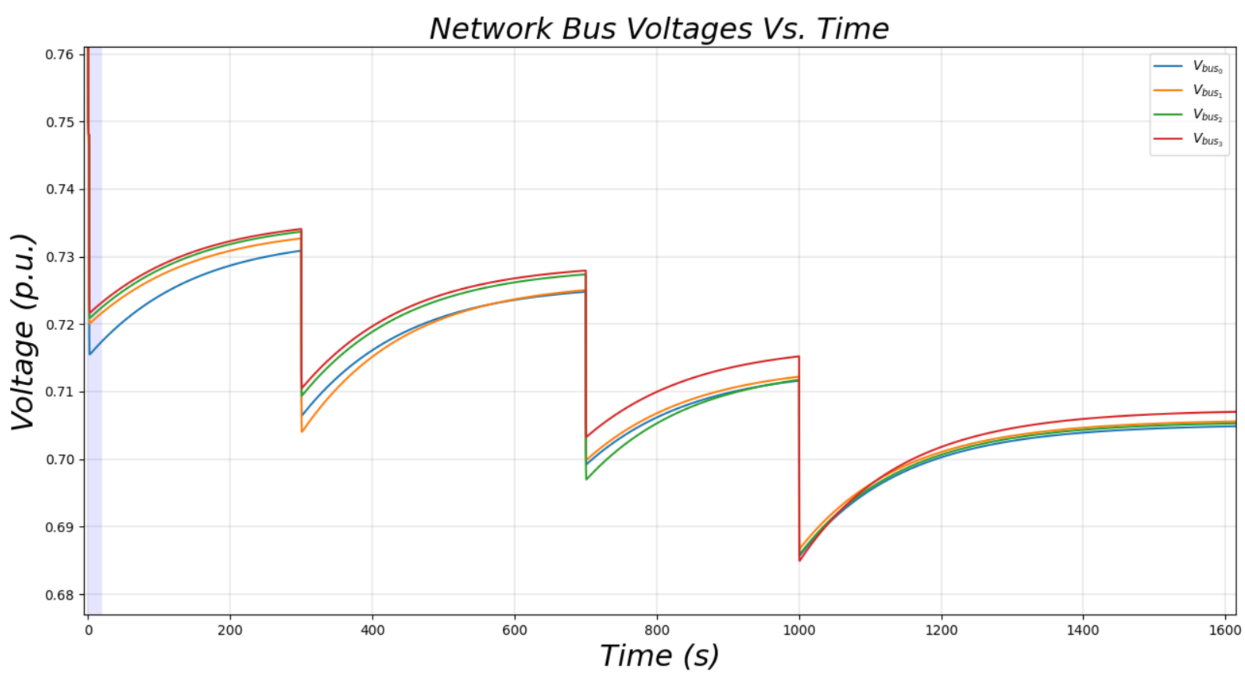

Figure 4.53: ERL Model Network Voltage Response (Ke=1)

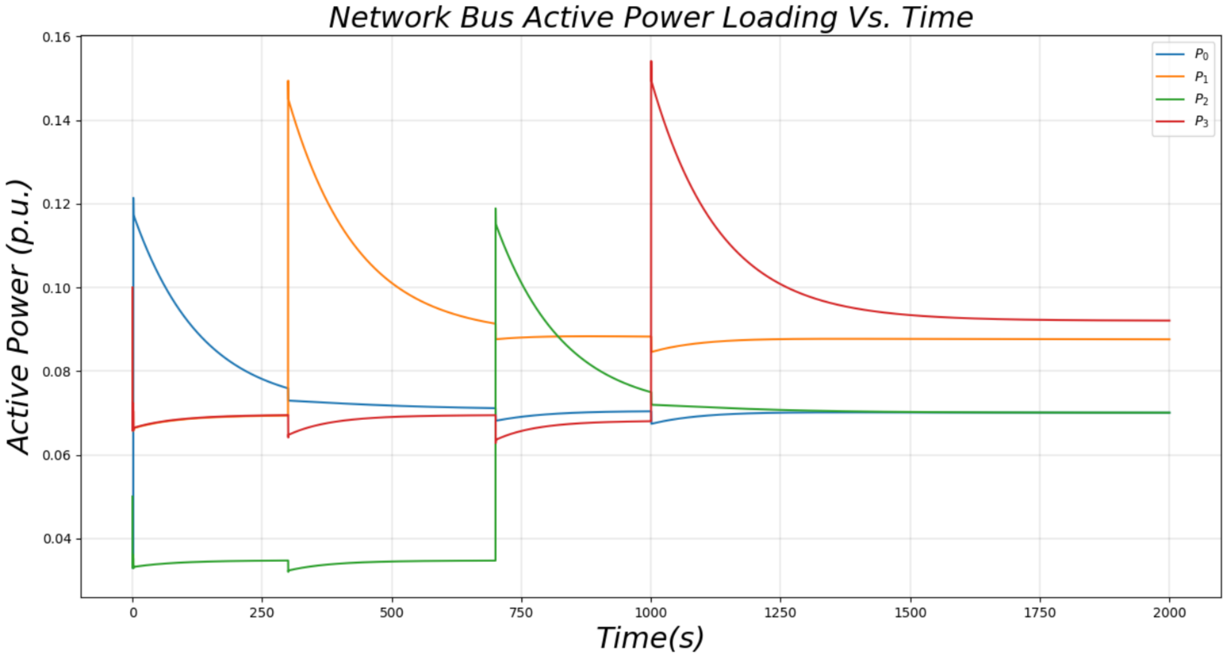

Figure 4.54: ERL Model Network Active Power Loading (Ke=1)

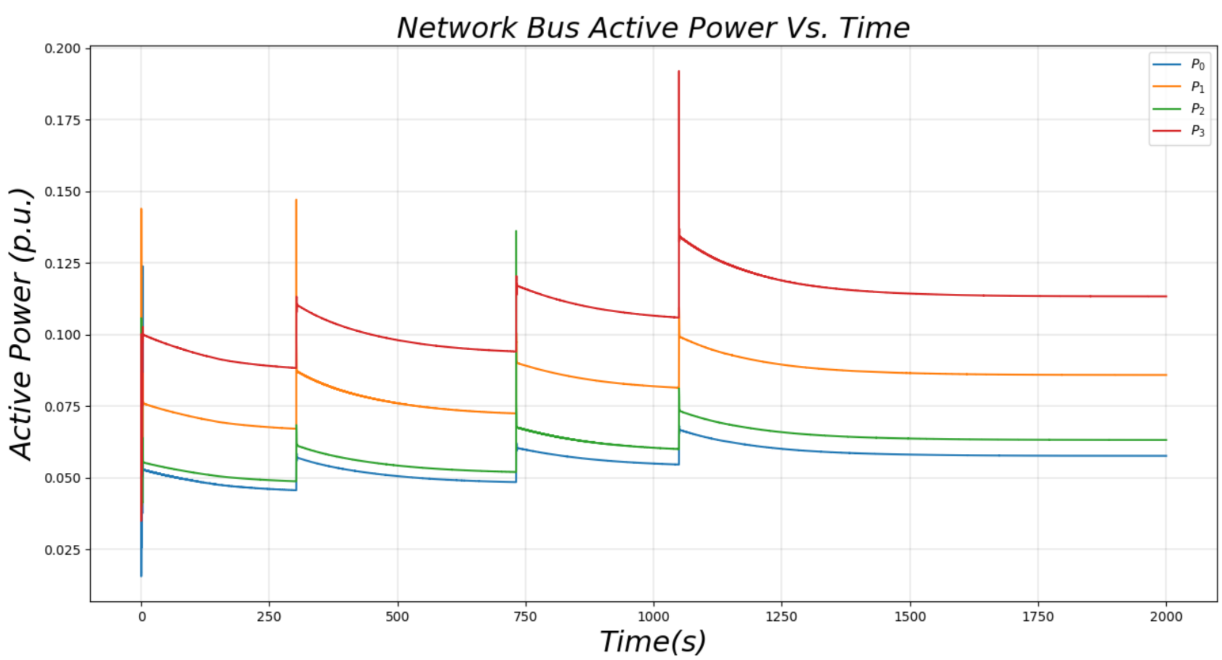

Figure 4.55: ERL Model Network Active Power DER Generation (Ke=1)

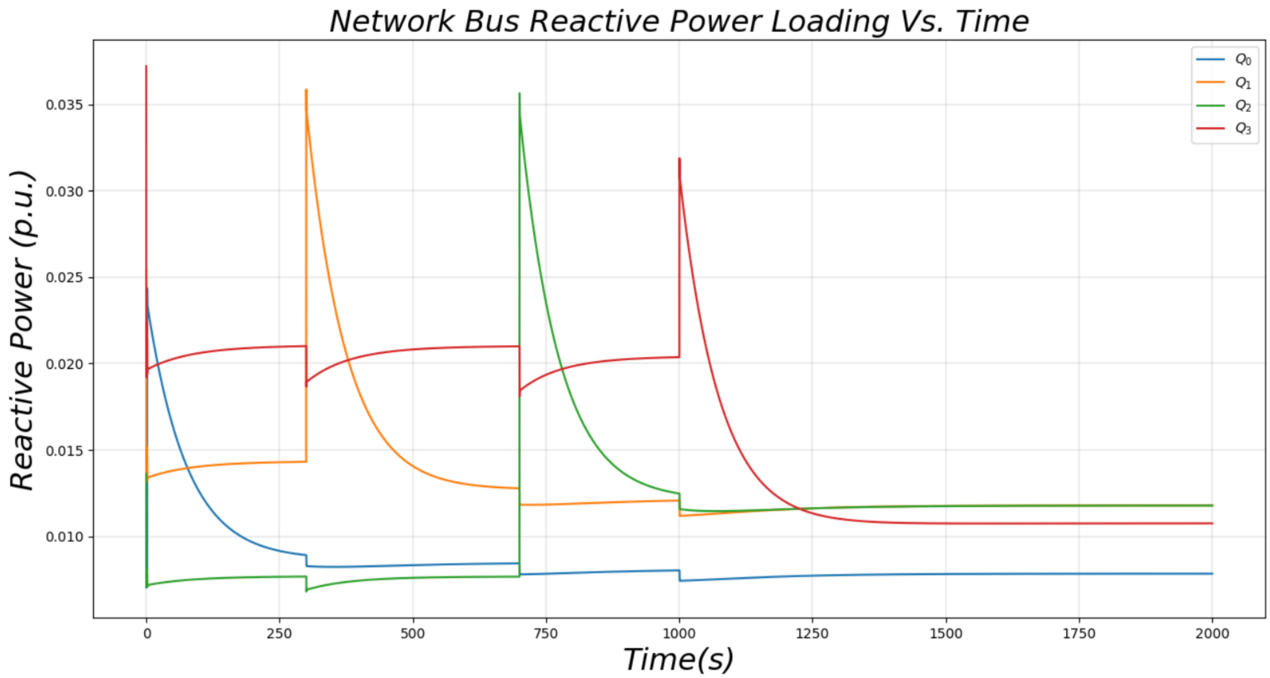

Figure 4.56: ERL Model Network Reactive Power Loading (Ke=1)

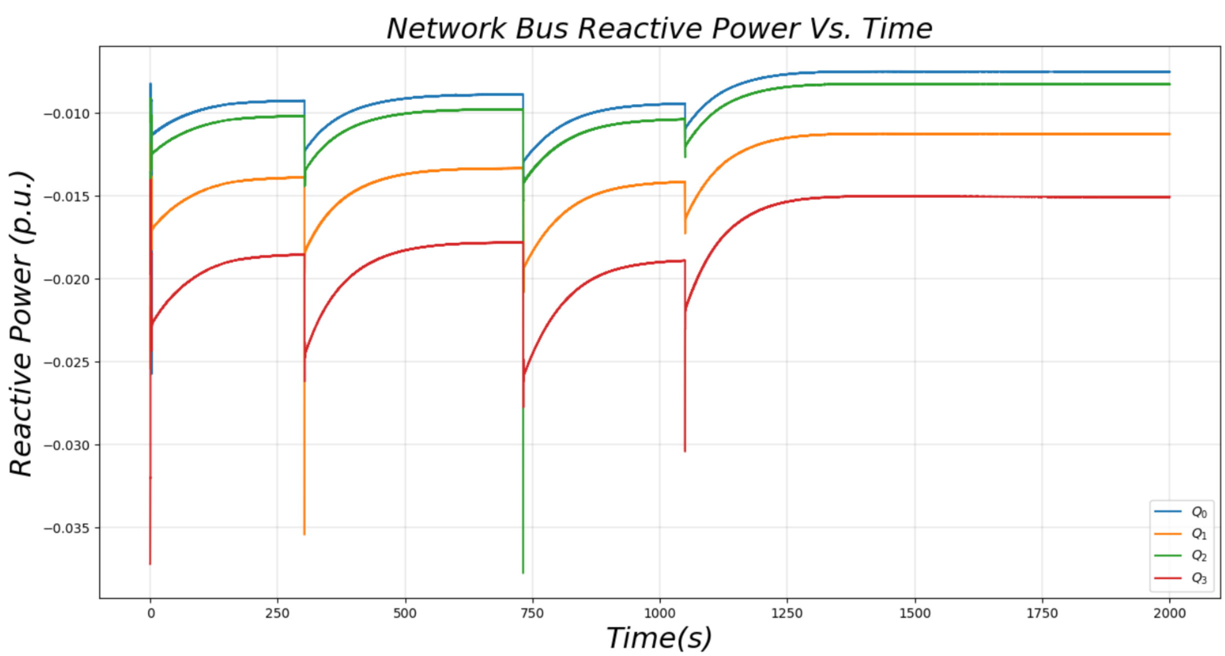

Figure 4.57: ERL Model Network Reactive Power DER Generation (Ke=1)

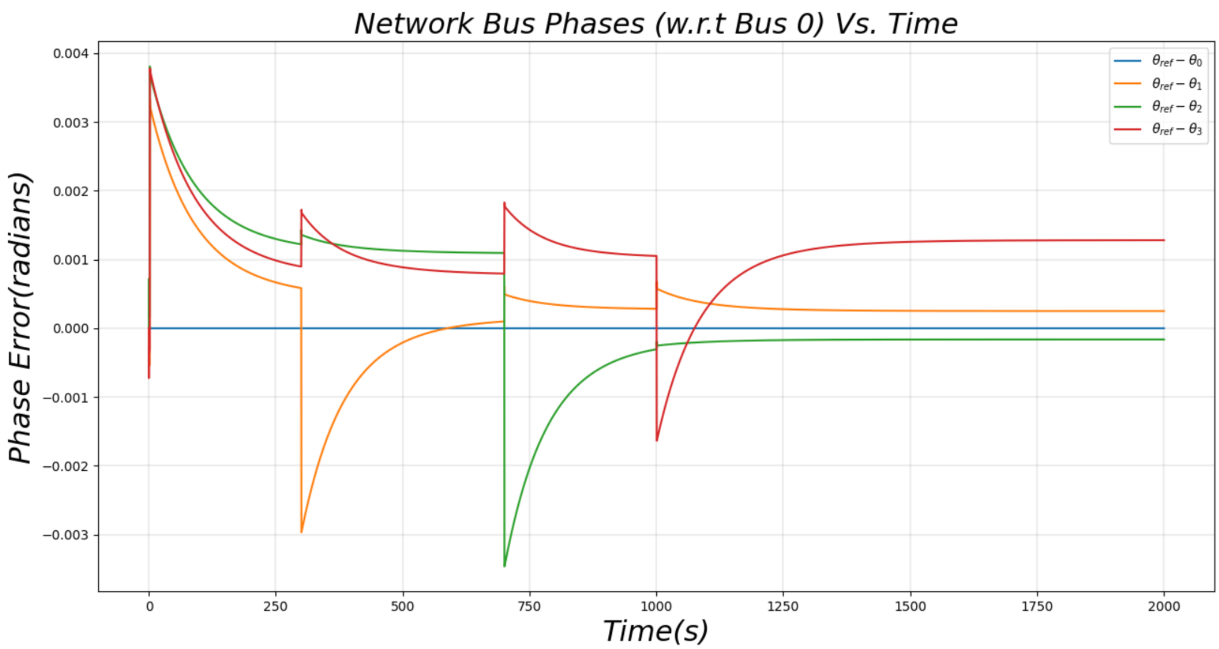

Figure 4.58: ERL Model Network Active DER Phase Response (Ke=1)

Based on figures 4.50 & 4.51, the system frequency stabilizes at 59.925Hz after the final ERL disturbance on bus 3. Despite the load disturbances on the system, the frequency remains in the continuous operation region according to IEEE1547-CATIII requirements and is a nominal (normal) operation state. Frequency being correlated to the reactive power loading on the network, figure 4.57 demonstrates that the load is shared amongst each DER on the network in accordance to their respective droop coefficients. Note the reactive power injection is negative (indicating injection and not absorption) due to the power transfer properties of a resistive dominated DER to network coupling impedance; correlated with the theory presented in section 2.2.2. Despite the disturbances on the network, the frequency of the DER's on the network maintain synchrony due to the strong coupling impedance of the transmission lines.

However, the voltage stability of the network is compromised based on the ERL loading experienced and a feedback gain coefficient $K_{I_E} = 1$. Indicated by figures 4.52 & 4.53, the voltage falls well below the continuous operation region of 0.88 p.u. The IEEE 1547-2018 CAT III LVRT requirements state that the voltage mandatory operation region (0.5-0.88 p.u.) must be maintained for a maximum of 20 seconds. Due to the time constant of the ERL, the voltage profile of the network and individual buses violate these LVRT requirements and would be required to disconnect from the network. In the mandatory operation region, the system is intact but operating within an emergency state. If no corrective action is taken the state would transition into the in-extremis state. The system would be declared as no longer intact due to the rapid loss of DER that would result if no load shedding or other restorative actions are taken.

In order to address the voltage stability in the network, the proportional droop control voltage feedback gains K_{I_E} are adjusted. The same test is performed on the network with a voltage feedback gain K_{I_E} of 10 on each inverter within the network. The performance of the low-voltage network with the adjusted voltage feedback gains are illustrated within figure 4.59-4.67.

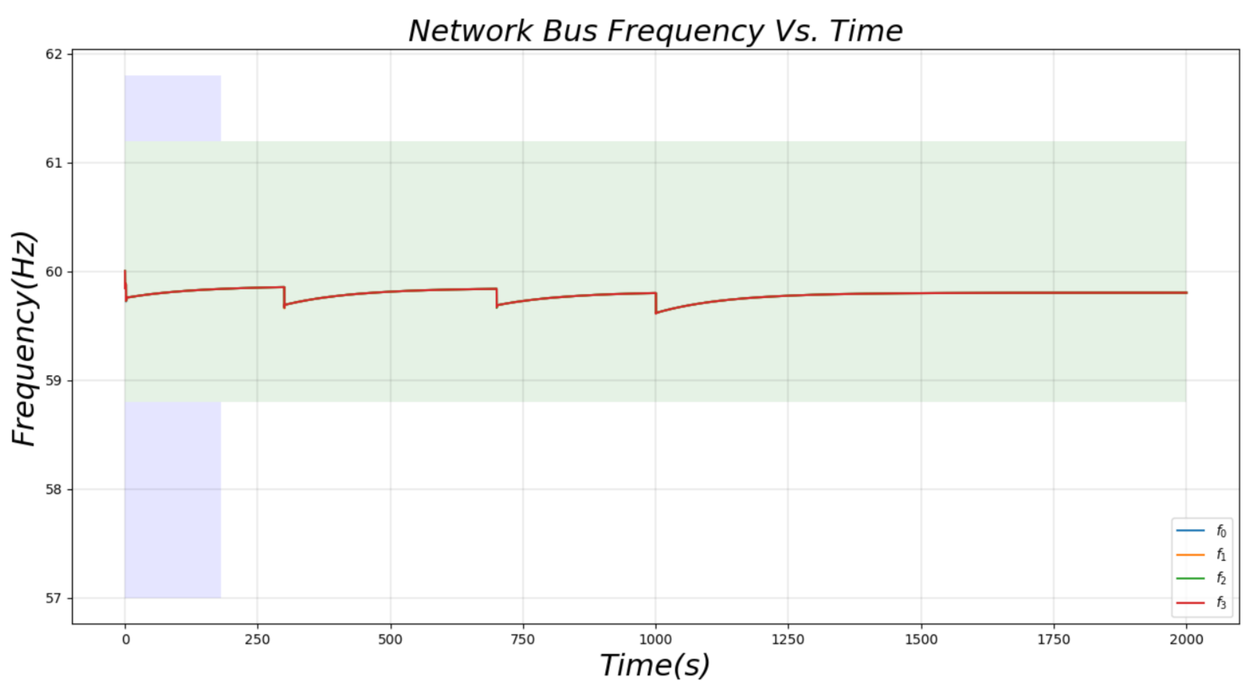

Figure 4.59: ERL Model Network Frequency Response (Ke=10)

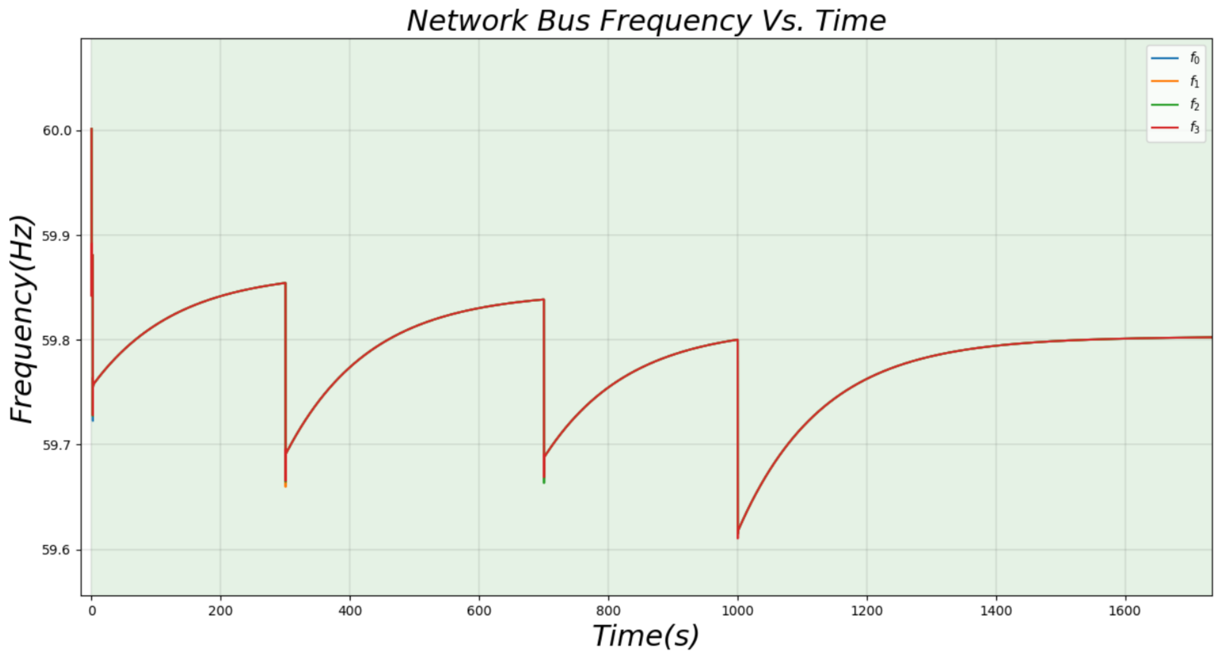

Figure 4.60: ERL Model Network Frequency Response Zoom (Ke=10)

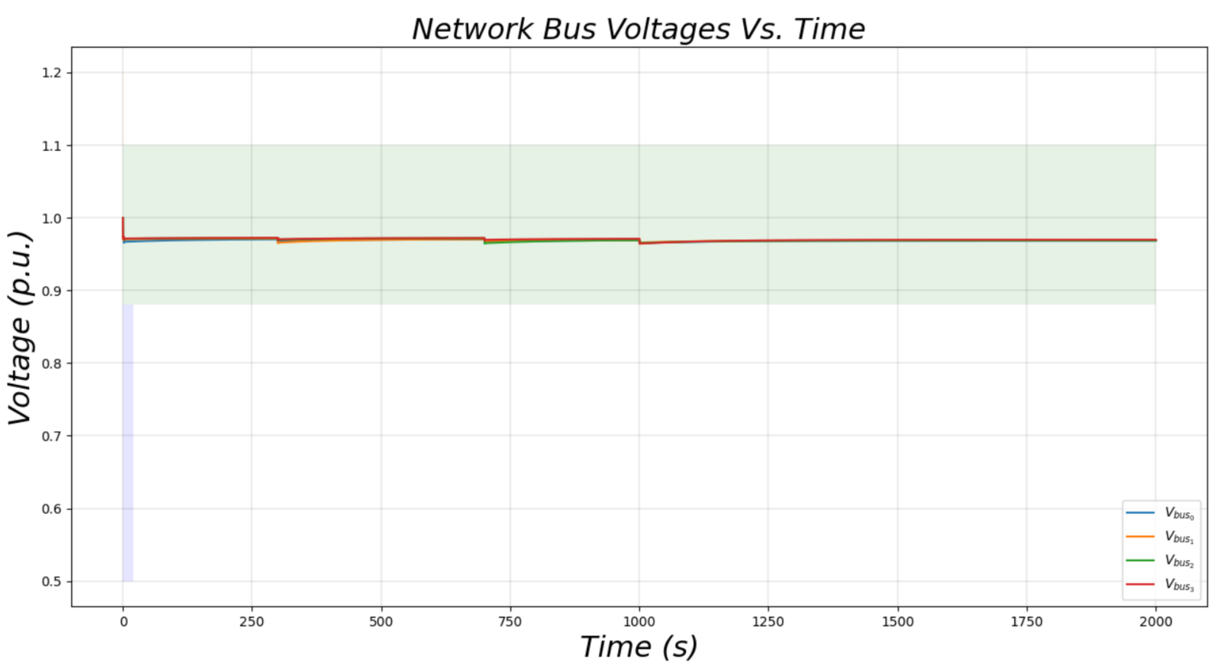

Figure 4.61: ERL Model Network Voltage Response (Ke=10)

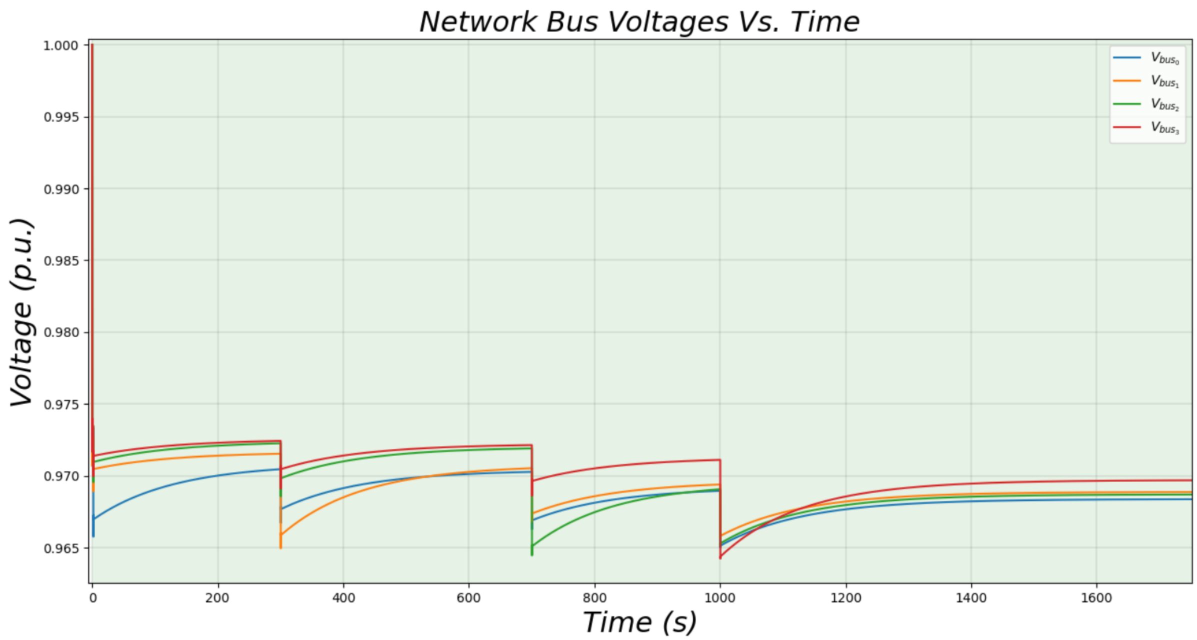

Figure 4.62: ERL Model Network Voltage Response Zoom (Ke=10)

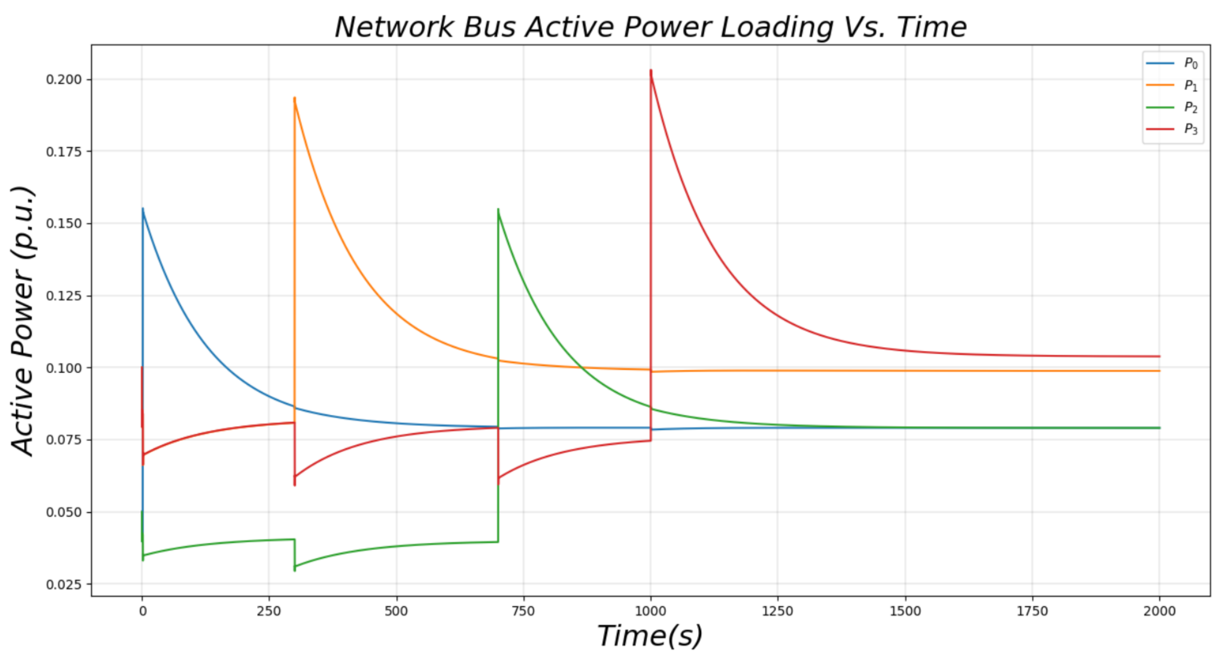

Figure 4.63: ERL Model Network Active Power Loading (Ke=10)

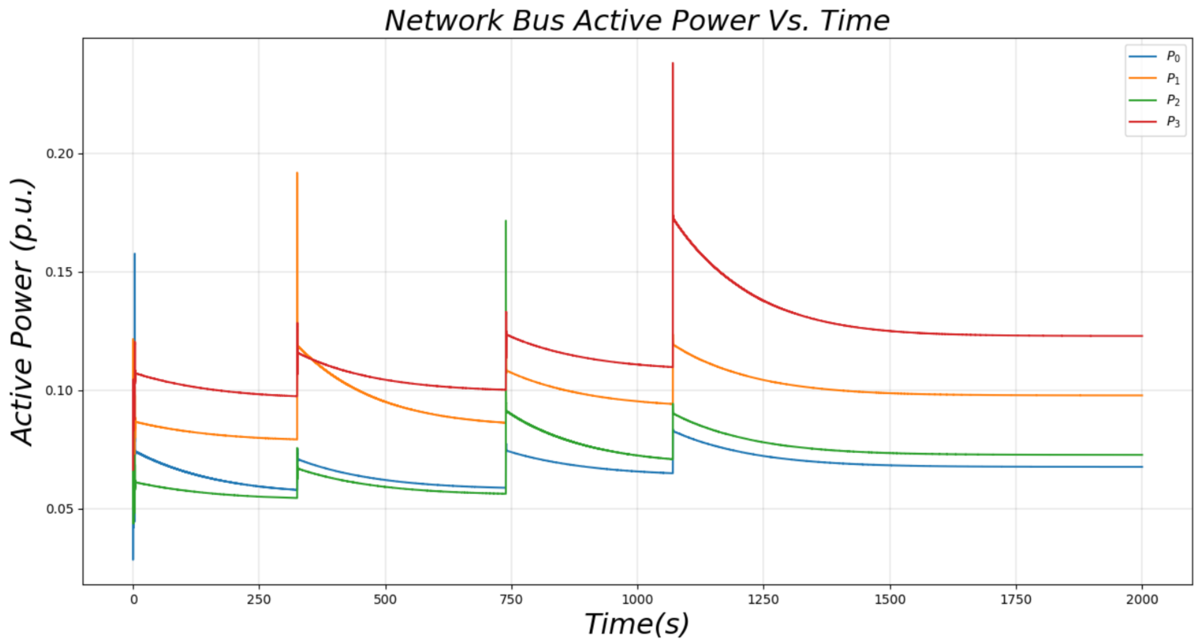

Figure 4.64: ERL Model Network Active DER Active Power Injection (Ke=10)

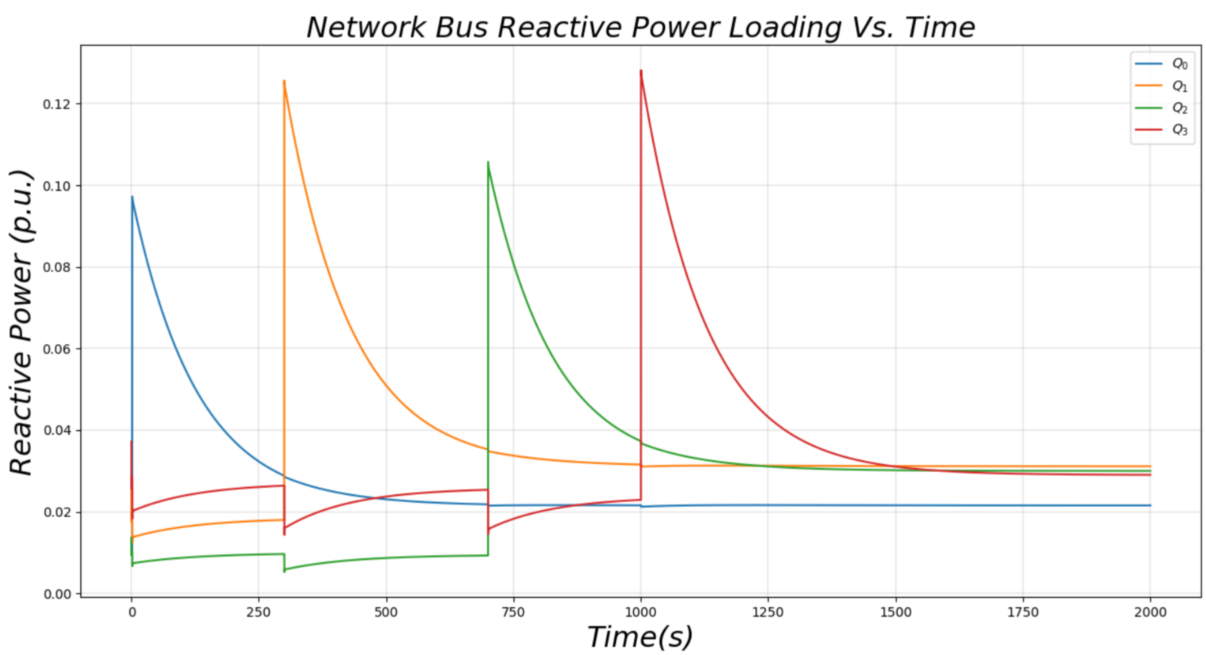

Figure 4.65: ERL Model Network Reactive Power Loading (Ke=10)

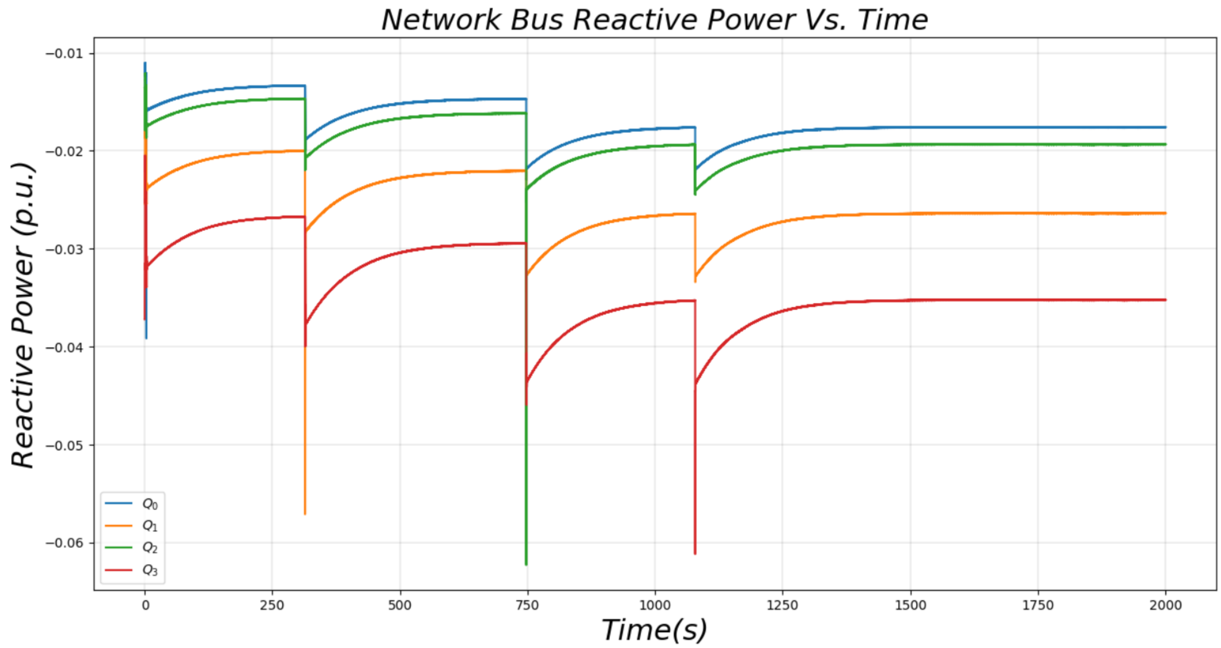

Figure 4.66: ERL Model Network Reactive Power Loading (Ke=10)

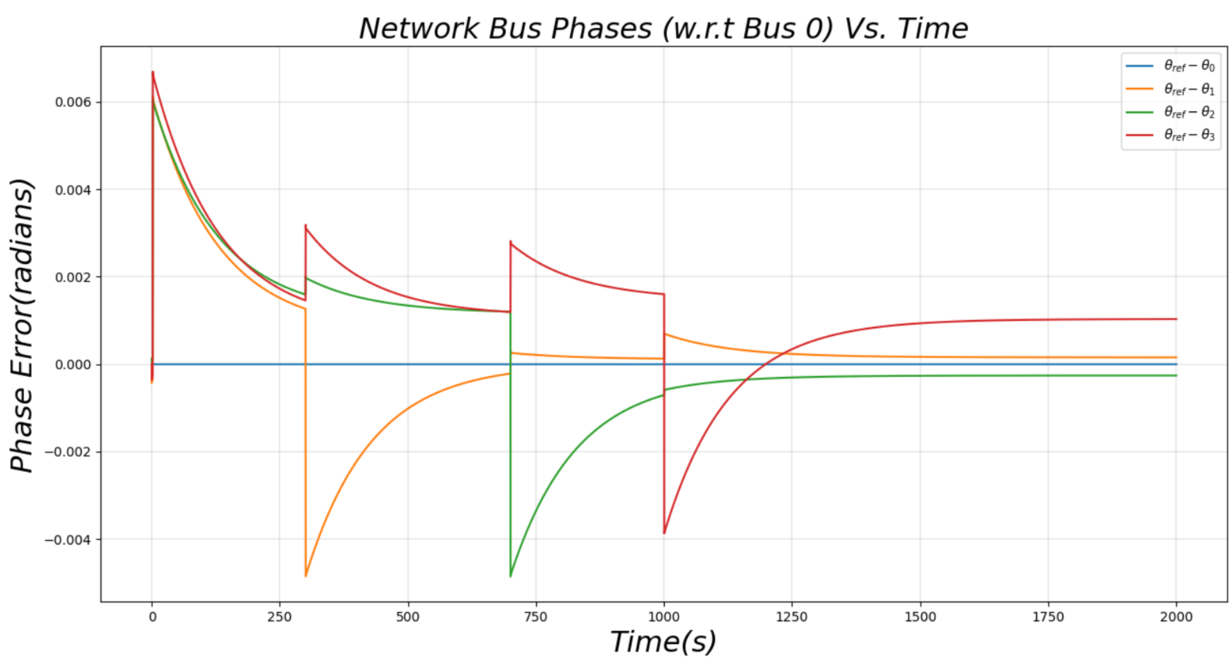

Figure 4.67: ERL Model Low-Voltage Network Phase Response (Ke=10)

Similar to the results obtained in sections 4.3-4.4, a higher voltage feedback gain results in stable network operation regardless of the contingency. In response to the gain adjustment, the active and reactive power consumption at each bus is increased, demonstrated by figures 4.64 & 4.66 in comparison with figures 4.55 & 4.57. The increase in reactive loading further results in the system frequency to settle to 59.8Hz in comparison of 59.9Hz with $K_{I_E} = 1$. This result is due to the static and transient load terms in (3.21) - (3.24) inheriting the exponential voltage characteristics of (3.12) and (3.13). Furthermore, the load is shared amongst the DERs on the network in proportion to their ratings and droop gains.

In summation, the adjusted voltage droop gain results in a more robust low-voltage network. The voltage profile is maintained within the continuous operation region and the microgrid is able to maintain intact and operating within its nominal (normal) state; based on the tested static and dynamic loads. Voltage stability is the major concern for low-voltage network microgrid operation. This sensitivity can be compensated for with DER's implementing a negative voltage feedback loop with feedback error gain K_{I_E}. The tradeoff is the network energy consumption profile is increased drastically due to the load power voltage bus voltage dependence. Feedback gain K_{I_E} needs more consideration in the design of low-voltage microgrids based on the DER capacity and expected loading on the network. In the absence of any voltage feedback (i.e., conventional droop control) the low-voltage network is unstable and the DERs are unable to maintain synchrony amongst each other. These results are demonstrated in Appendix B.

CONCLUSION

The work performed in this thesis has demonstrated an approach to modelling a low-voltage network of interconnected single-phase residential homes. The DERs within each home are modelled through the governing droop control dynamics of the grid interfacing single-phase inverter. The droop control loop is modified with the proportional droop control strategy which allows the DERs to compensate for the drop in voltage proportional to the load as a result of conventional droop control. Using the power terms required within the droop control loop, a relationship with the DERs and loads on the low-voltage network is established. This relationship is defined by the quasi-static network power flow equations which encapsulate the coupling between network buses through their respective voltage magnitude and phase.

Furthermore, the power flow network equations account for a shunt admittance load at each bus to depict the behavior of local loads directly connected to the bus. This study proposes to redefine the shunt admittance load with load models that have an active/reactive-voltage/frequency relationship. Thus, allowing the implementation of more advanced load models into the network to capture the prosumer load behavior at the grid-edge accurately. The load models incorporated within the developed simulation tool are static and dynamic load models such as: ZIP, Exponential, Frequency dependent, EPRI LoadSyn, Exponential Recovery Load, Oscillatory Controlled Load and Single-phase induction machine load. Throughout the work performed in this thesis, it was identified that there is a large gap to be addressed in the modelling of direct consumer loads specifically with dynamic load models such as the ERL, OCL and single-phase induction machine loads. Most stability studies use aggregated load parameters modelled at the primary distribution bus and not the secondary.

It was established that the relationship between interconnected droop-controlled inverters exhibit the Kuramoto phenomena. Allowing a deeper intuition to be developed about coupled DERs within a low-voltage network and their interaction. This can further describe the phenomena in which droop-controlled DERs essentially behave as phase-locked loops as derived in [45]. This phenomenon helps describe the ability for the droop-controlled inverters to maintain synchronization throughout a series of network contingencies. Furthermore, this intuition can assist in the design phase of microgrid low-voltage networks considering the role network topology, transmission line, control coefficients and reactive loading have on frequency stability of the network.

A software architecture was proposed in which a software tool has been developed to encapsulate the aforementioned theory and interaction between distributed generation interfaces and loads on a secondary low-voltage network. The developed low-voltage network tool provides a means for testing a grid-edge low-voltage network against various inverter control designs, network topologies, voltage, frequency and angle stability as well as other transient analysis cases. The low-voltage network was designed in accordance to the newly defined ride-through and regulation capabilities mandated by the IEEE 1547-2018 standard. The simulation tool was then assembled with distributed generation in accordance to the average rooftop PV installation size in North America, typical secondary distribution transmission cables, common secondary network interconnect topology and load model parameters fit to residential load data.

As a result of the simulation performed on a secondary low-voltage network microgrid, it was determined that proportional droop control is a necessary requirement for independent (islanded) operation of a secondary distribution interconnect of residential homes. In the case of no voltage feedback, the network does not maintain synchrony amongst DER’s and voltage, frequency and angle stability collapse immediately. Furthermore, with unity voltage error feedback within the proportional droop control loop the network can maintain intact but the ride through requirements of IEEE1547-2018 standard would cause the DERs to begin disconnecting from the network leading to further aggravation of the disturbance event and collapse of the network if no restorative action is taken. In order to mitigate such effects, one can tune the voltage feedback gain in order to compensate for the drop in network voltage. Thus, leading to a more proportional and stable network regardless of the load disturbance experienced. In conclusion of the study, the secondary low-voltage network primary concern is the voltage stability of the network as there are no voltage compensation devices operated on the secondary distribution system and therefore a concern of the connected DERs. Frequency stability is an added concern but due to the coupling effects and proportional droop control, the network exhibits a coherent response with strong angle stability. Although, more work is needed to test the frequency stability with detailed inertial load models.

Future Work

The future direction of the proposed research is to fit low-voltage secondary loads to the presented load models. A strong emphasis is taken on load models which encapsulate the inertial effects of loads such as the OCM and single-phase induction AC motor models. Furthermore, the DC link and PV power point optimization control is needed to appropriately capture the effects of generation disturbances, ramping and curtailment of power from the PV system. The software simulation tool that was developed needs to be adjusted to handle cases in which the load consumption exceeds the generation capacity of the local connected DER unit. The issue found was that the bus dynamics are strictly governed by the DERs primary control loop and in the event in which the DER is operating at its maximum rated power, the voltage and phase dynamics of the bus then become controlled by the load. Therefore, this needs to be accounted for accordingly to capture further power flow and coupling effects within the network. Finally, the simulation tool needs validation tested against a ground truth secondary low-voltage network of loads and DERs implementing proportional droop control.

REFERENCES

[1] P. IEEE Standards Coordinating Committee 21 on Fuel Cells, 1547-2018 - IEEE Standard for Interconnection and Interoperability of Distributed Energy Resources with Associated Electric Power Systems Interfaces, IEEE, 2018.

[2] J. W. B. &. J. R. B. Jan Machowski, Power System Dynamics: Stability and Control 2nd Edition, John Wiley & Sons, Ltd., 2008.

[3] P. Kundur et al., "Definition and classification of power system stability IEEE/CIGRE joint task force on stability terms and definitions,," *IEEE Transactions on Power Systems,* vol. 19, pp. 1387-1401, 2004.

[4] Working Group C4.601, "Review of On-line Dynamic Security Assessment Tools and Techniques," CIGRE Publication, 2007.

[5] A. K. K. a. M. N. R. Rao, "A brief review on multilevel inverter topologies," *2017 International Conference on Data Management, Analytics and Innovation (ICDMAI),* vol. doi: 10.1109/ICDMAI.2017.8073508., pp. 187-193, 2017.

[6] A. Bughneda, M. Salem, A. Richelli, D. Ishak and S. Alatai, "Review of Multilevel Inverters for PV Energy System Applications," *Energies 2021, 14 (6), 1585,* vol. https://doi.org/10.3390/en14061585, 2021.

[7] S. A. P. A. M. C. w. L. a. H.-J. K. Ronak A. Rana, "Review of Multilevel Voltage Source Inverter Topologies and Analysis of Harmonics Distortions in FC-MLI," *Electronics,* vol. 1329, no. 0.3390/electronics8111329 , p. 8, 2019.

[8] A. O. R. D. K. a. P. S. M. Pamujula, "Cascaded 'H' Bridge based Multilevel Inverter Topologies: A Review," *2020 International Conference for Emerging Technology (INCET),* no. 10.1109/INCET49848.2020.9154031, pp. 1-7, 2020.

[9] P. N. K. V. P. a. J. P. A. Tatu, "Review of modulation schemes for loss analysis in inverters," *2012 Nirma University International Conference on Engineering (NUiCONE),* no. 0.1109/NUICONE.2012.6493279., pp. 1-5, 2012.

[10] P. S. U. S. C. a. V. B. B. D. Atkar, "Control of seven level cascaded H-Bridge inverter by hybrid SPWM technique," *2016 IEEE International Conference on Power Electronics, Drives and Energy Systems (PEDES),* no. 10.1109/PEDES.2016.7914435., pp. 1-6, 2016.

[11] M. L. P. R. R. Teodorescu, Grid Converters for Photovoltaic and Wind Power Systems, John Wiley & Sons, Ltd., 2011.

[12] H. K. a. K.-H. Kim, "Filter design for grid connected PV inverters," *2008 IEEE International Conference on Sustainable Energy Technologies,* no. 10.1109/ICSET.2008.4747165, pp. 1070-1075, 2008.

[13] H. Z. F. L. F. L. C. L. a. B. L. X. Zhang, "An LCL-LC power filter for grid-tied inverter," *2013 IEEE International Conference of IEEE Region 10 (TENCON 2013),* no. 10.1109/TENCON.2013.6718873., pp. 1-4, 2013.

[14] T. H. Q.C. Zhong, Control of Power Inverters in Renewable Energy & Smart Grid Integration, John Wiley & Sons, Ltd., 2013.

[15] K. Z. W. Z. a. L. Z. X. Su, "Proportional-resonant current control of single-phase grid-tied PV inverter system," *CICED 2010 Proceedings,* pp. 1-4, 2010.

[16] P. A. S. S. P. G. R. S. P. a. D. K. P. M. A. Waghmare, "Proportional resonant control technique for grid interfacing of multilevel inverter," *2018 International Conference on Power, Instrumentation, Control and Computing (PICC),* vol. 10.1109/PICC.2018.8384759., pp. 1-6, 2018.

[17] N. Güler, "Proportional Resonant and Proportional Integral Based Control Strategy for Single Phase Split Source Inverters," *2020 9th International Conference on Renewable Energy Research and Application (ICRERA),* vol. 10.1109/ICRERA49962.2020.9242690, pp. 510-514, 2020.

[18] S. H. X. C. a. Y. X. B. Li, "A simplified DQ-frame current controller for single-phase grid-connected inverters with LCL filters," *2017 20th International Conference on Electrical Machines and Systems (ICEMS),* vol. 10.1109/ICEMS.2017.8056053, pp. 1-5, 2017.

[19] Y. W. S. L. a. F. Z. C. Hu, "State-space model of an inverter-based micro-grid," *2018 3rd International Conference on Intelligent Green Building and Smart Grid (IGBSG),* vol. 10.1109/IGBSG.2018.8393525, pp. 1-7, 2018.

[20] M. A. B. R. L. H. <. K. U. S. Tayab, "A Review of Droop Controlled Techniques for Microgrid," *Renewable and Sustainable Energy Reviews,* vol. 76, pp. 717-727, 2017.

[21] D. C. R. a. D. N. Gaonkar, "Frequency and voltage droop control of parallel inverters in microgrid," *2016 2nd International Conference on Control, Instrumentation, Energy & Communication (CIEC),* vol. 10.1109/CIEC.2016.7513771., pp. 407-411, 2016.

[22] M. C. J. M. J. M. G. a. Z. Q. W. Yao, "Design and Analysis of the Droop Control Method for Parallel Inverters Considering the Impact of the Complex Impedance on the Power Sharing," *IEEE Transactions on Industrial Electronics,* vol. 58, pp. 576-588, 2011.

[23] Q. Zhong, "Robust Droop Controller for Accurate Proportional Load Sharing Among Inverters Operated in Parallel," *IEEE Transactions on Industrial Electronics,* vol. 60, pp. 1281-1290, 2013.

[24] Q. Z. a. Y. Zeng, "Universal Droop Control of Inverters With Different Types of Output Impedance," *IEEE Access,* vol. 4, pp. 702-712, 2016.

[25] A. Blanchard, Phase-Locked Loops: Application to Coherent Receiver Design, Wiley, 1976.

[26] T. L. V. T. M. N. T. M. Q. D. a. L. X. C. T. H. Van, "Application of the Phase Shift Full Bridge Converter for the Single-Phase Full-Bridge Inverter to Improve the Output of the Renewable Energy," *2021 3rd International Conference on High Voltage Engineering and Power Systems (ICHVEPS),* pp. 419-424, 2021.

[27] MicroSemi, "Park, Inverse Park and Clarke, Inverse Clarke Transformations MSS Softare Implementation," 2013.

[28] M. M. a. J. M. G. S. Golestan, "Second order generalized integrator based reference current generation method for single-phase shunt active power filters under adverse grid conditions," *4th Annual International Power Electronics, Drive Systems and Technologies Conference,* pp. 510-517, 2013.

[29] National Electrical Manufacturers Association, " Electric Power Systems and Equipment-Voltage Ratings (60 Hertz) - ANSI C84.1-1995 (R2005)," American National Standards Institute, Inc., 2005.

[30] IEEE Standards Coordinating Committee, "IEEE Standard for Interconnection and Interoperability of Distributed Energy Resources with Associated Electric Power Systems Interfaces 2003," IEEE, 2003.

[31] A. Remier, "BC Hydro - Electric Distribution System Cost of Service Study," Reimer Consulting Group Inc. , 2010.

[32] S. Strogatz, "From Kuramoto to Crawford: Exploring the onset of Synchronization in Populations of Coupled Oscillators," *Physica D 143,* 2000.

[33] C. A. R. S. Gupta S, "Kuramoto model of synchronization: equilibrium and nonequilibrium aspects," *Journal of Statistical Mechanics: Theory and Experiment,* vol. 2014, 2014.

[34] A. N. M. M. A. J. Y. a. V. T. E. S. N. Raju Paidi, "Development and Validation of a New Oscillatory Component Load Model for Real-Time Estimation of Dynamic Load Model Parameters," *IEEE Transations On Power Delivery,* vol. 35, no. 2, pp. 618-629, 2020.

[35] IEEE Task Force on Load Representation for Dynamic Performance, "Standard Load Models for Power Flow and Dynamic Performance Simulation," *IEEE Transactions on Power Systems,* vol. 10, no. 3, pp. 1302-1313, 1995.

[36] Z. W. J. W. B. M. H. B. a. D. Z. A. Arif, "Load Modeling—A Review," *IEEE Transactions on Smart Grid,* vol. 9, no. 6, pp. 5986-5999, 2018.

[37] D. K. a. D. J. Hill, "Modelling and identification of nonlinear dynamic loads in power systems," *IEEE Transactions on Power Systems,* vol. 9, no. 1, pp. 157-166, 1994.

[38] D. J. Hill, "Nonlinear dynamic load models with recovery for voltage stability studies," *IEEE Transactions on Power Systems,* vol. 8, no. 1, pp. 166-176, 1993.

[39] IEEE Task Force on Load Representation for Dynamic Performance, ""Bibliography on load models for power flow and dynamic performance simulation," *IEEE Transactions on Power Systems,* vol. 10, no. 1, pp. 523-538, 1995.

[40] D. G. L. a. C. C. Y. D. S. Brereton, "Representation of Induction-Motor Loads During Power-System Stability Studies," *Transactions of the American Institute of Electrical Engineers. Part III: Power Apparatus and Systems,* vol. 76, no. 3, pp. 451-460, 1957.

[41] C. K. J. S. D. U. A.E. Fitzgerald, Electric Machinery, 2003.

[42] V. V. J. U. a. J. H. E. Y. Liu, "Transient model of air-conditioner compressor single phase induction motor," *2014 IEEE PES General Meeting | Conference & Exposition,* p. 1, 2014.

[43] K. W. R. M. D. Feldman, "H1 2021 Solar Industry Update," *NREL/PR-7A40-80427,* 2021.

[44] J. V. M. S. Z. D. K. Y. S. M. V. a. S. S. L. M. Korunović, "Recommended Parameter Values and Ranges of Most Frequently Used Static Load Models," *IEEE Transactions on Power Systems,* vol. 33, no. 6, pp. 5923-5934, 2018.

[45] Q. Z. a. D. Boroyevich, "A droop controller is intrinsically a phase-locked loop," *IECON 2013 - 39th Annual Conference of the IEEE Industrial Electronics Society,* pp. 5916-5921, 2013.

[46] D. A. Engler, "Applicability of Droops In Low Voltage Grids," *DER Journal NO. 1,* 2005.

APPENDIX A: Conventional Droop Control Test

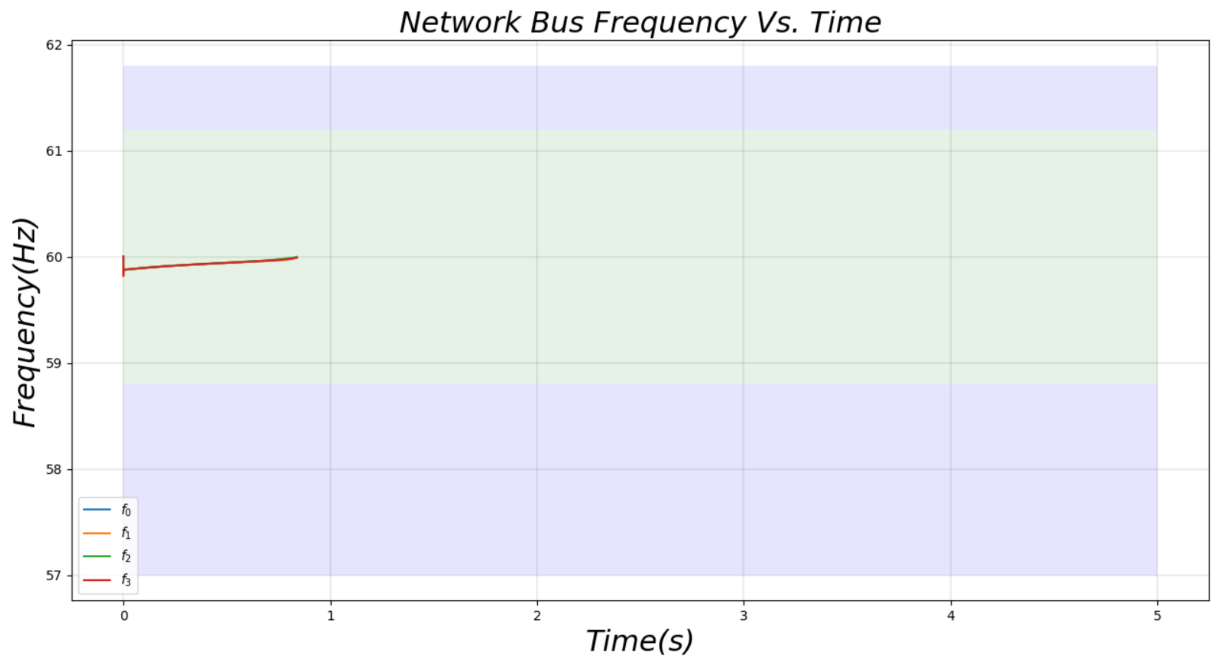

Figure A1: Frequency Dependent Static Load Test Case 1 Response Plotted Against IEEE 1547-2018 Category III Ride-Through Requirements Frequency Response (Ke=0)

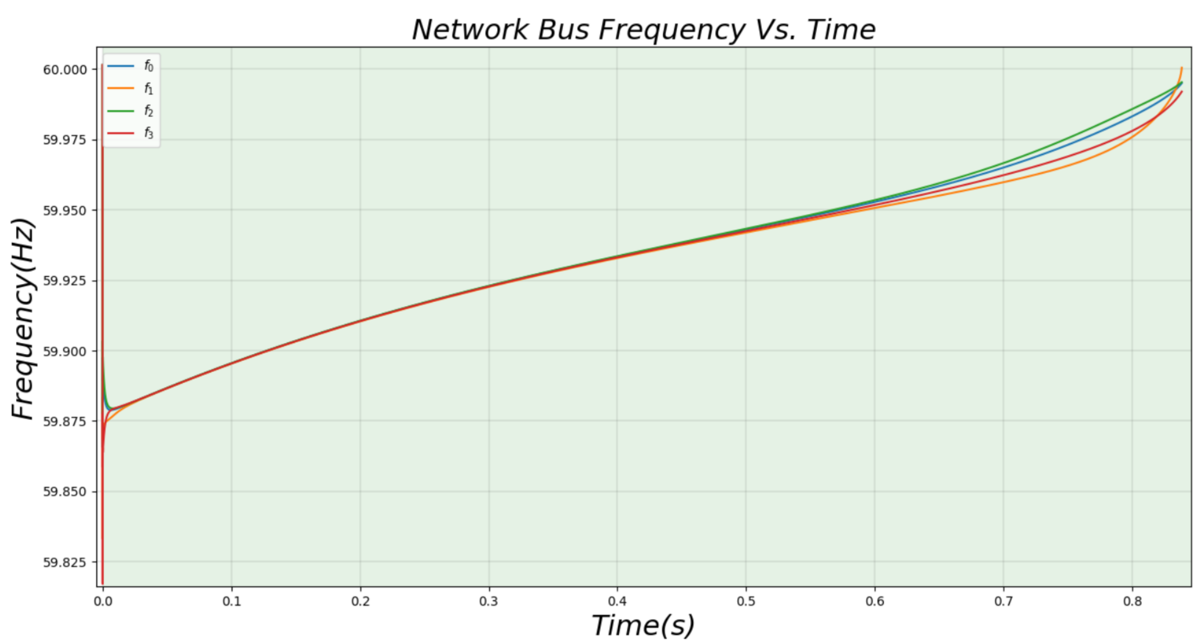

Figure A2: Figure 4.4: Frequency Dependent Static Load Test Case 1 Response Plotted Against IEEE 1547-2018 Category III Ride-Through Requirements (Ke=0)

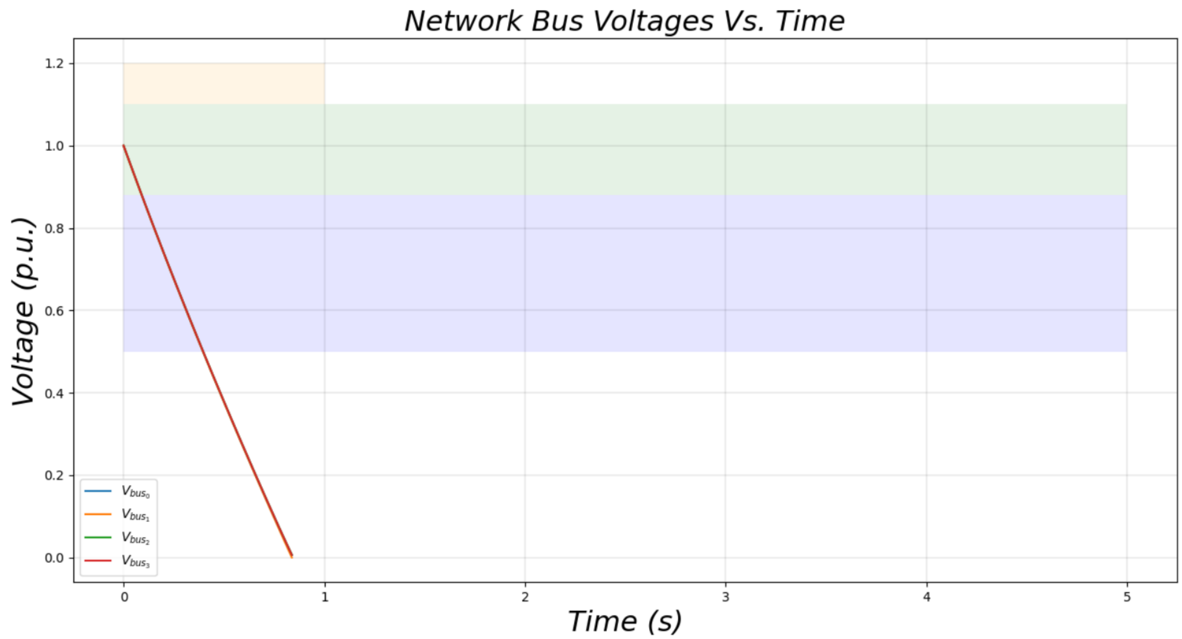

Figure A3: Frequency Dependent Static Load Test Case 1 Response Plotted Against IEEE 1547-2018 Category III Ride-Through Requirements Voltage Response (Ke=0)

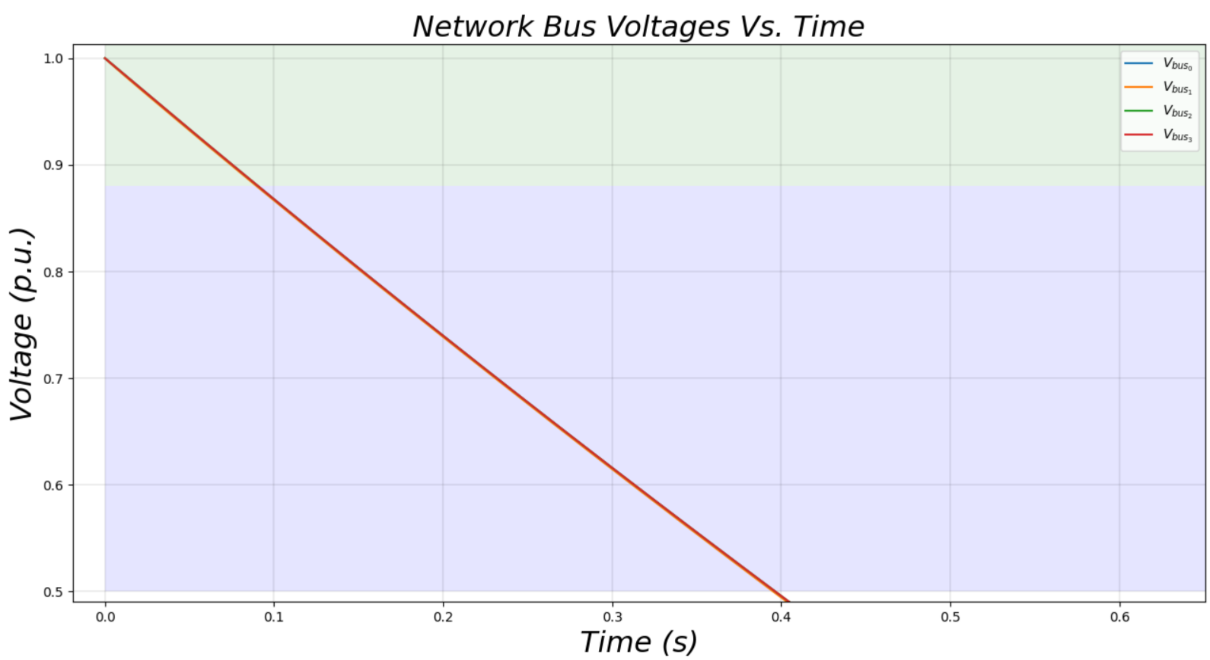

Figure A4: Frequency Dependent Static Load Test Case 1 Response Plotted Against IEEE 1547-2018 Category III Ride-Through Requirements Voltage Response (Ke=0)

APPENDIX B: Standard Primary Distribution System

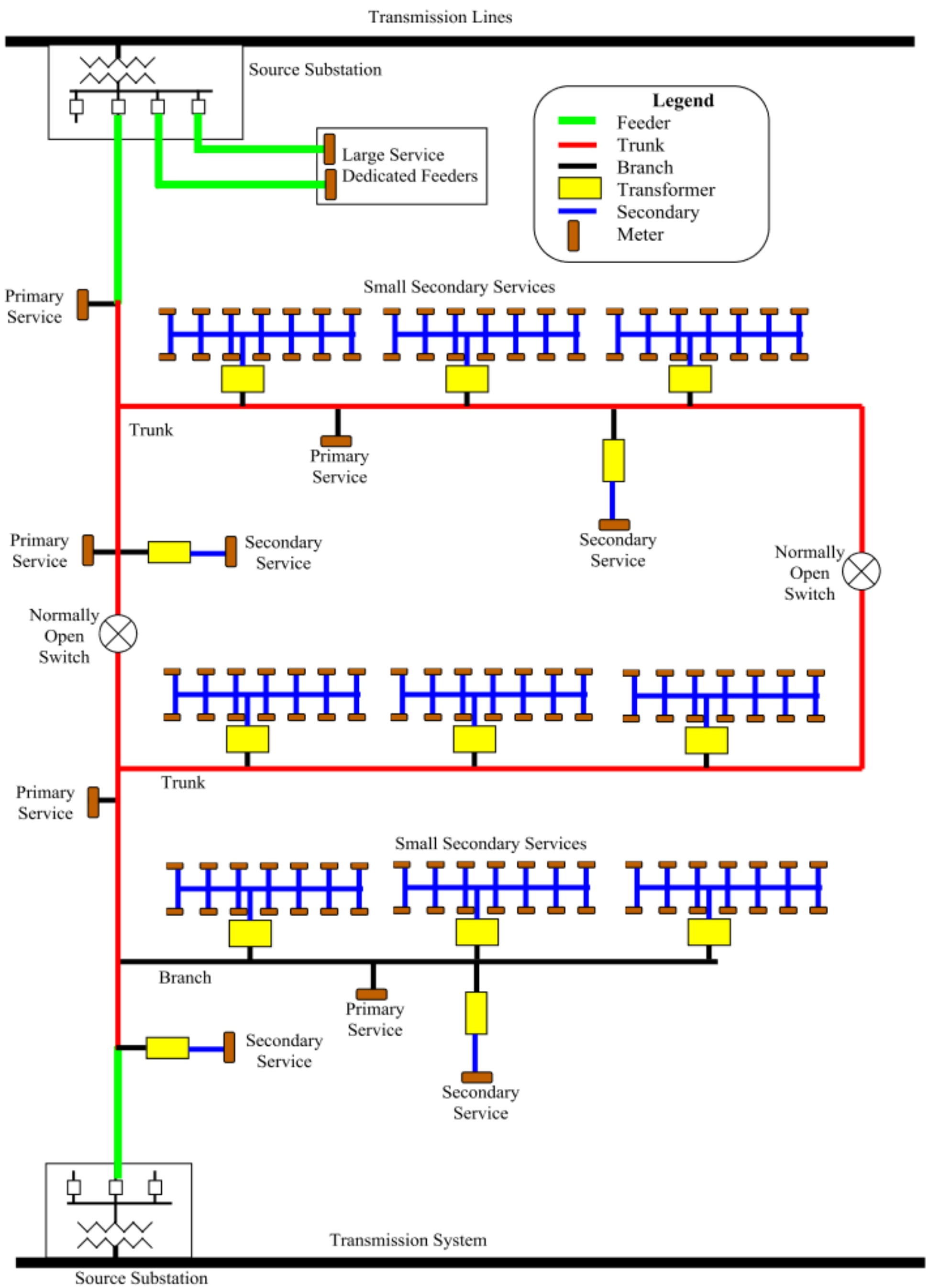

Figure B1: Common Primary Distribution System Located in British Columbia, Canada [31]

APPENDIX C: IEEE 1547-2018 DER Decision Tree

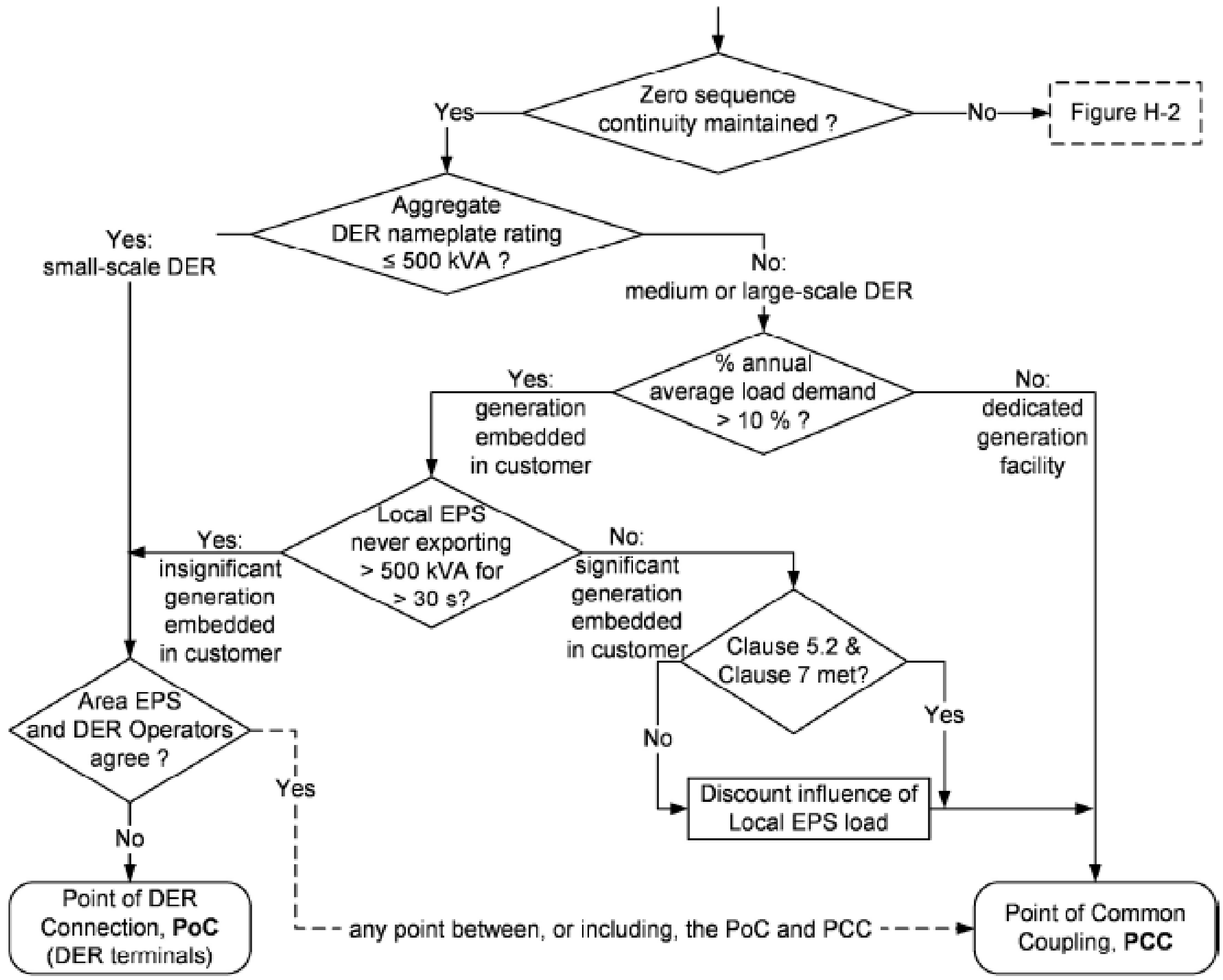

Figure C1: Decision Tree for Reference Point Of Applicability for Local EPS where Zero Sequence Continuity is Maintained [1]

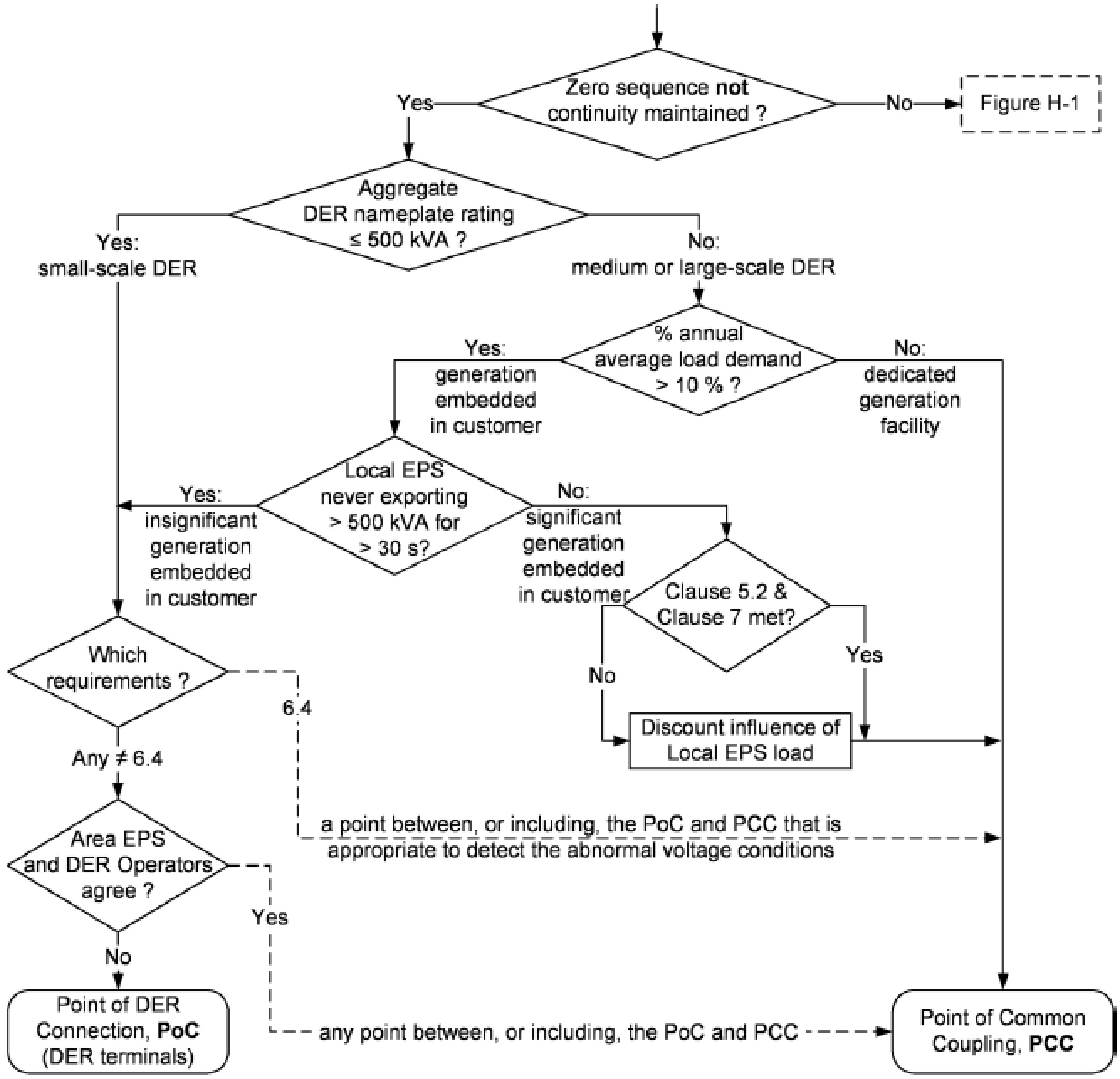

Figure C2: Decision Tree for Reference Point Of Applicability for Local EPS where Zero Sequence Continuity is Not Maintained [1]